Newcastle University

University Research Centre for Catalysis and Intensified Processing

Oxygen flux through unmodified and modified $La_{0.6}Sr_{0.4}Co_{0.2}Fe_{0.8}O_{3-\delta}$ hollow fibre membranes and application to methane oxidation

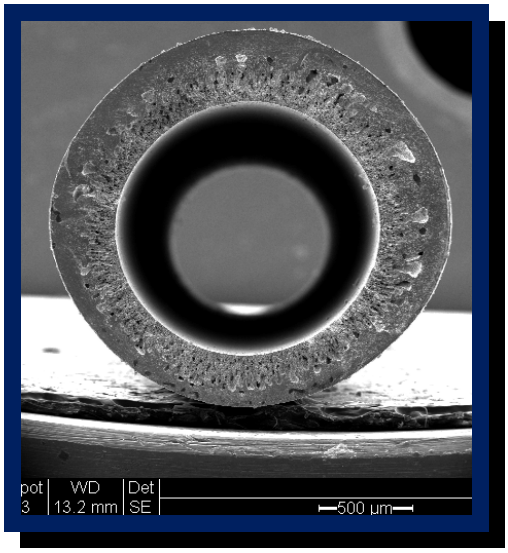

A thesis submitted in part fulfilment of the requirements for the degree of Doctor of Philosophy in Chemical Engineering and Materials Advanced at the University of Newcastle upon Tyne.

by

Serbia M. A. Rodulfo-Baechler

May, 2012

Abstract

Improved catalytic routes could help to transform the exploitation of the large worldwide natural gas reserves, whose principal component is methane. They transform methane into more valuable chemicals and fuels through carbon dioxide reforming of methane (CDRM), steam reforming of methane (SRM) and partial oxidation of methane (POM). These reactions facilitate the formation of syngas, which is subsequently converted to fuels through the Fischer-Tröpsch synthesis. Mixed Ionic and Electronic Conducting (MIEC) membrane reactors are of interest because they have the potential to produce high purity oxygen from air at lower costs and provide a continuous oxygen supply to reactions or/and industrial processes, and hence avoid sourcing the pure oxygen from air by conventional cryogenic separation technology. In addition, the MIEC ceramic membrane shows the ability to carry out simultaneous oxygen permeation and hydrocarbons oxidation into single compact ceramic membrane reactor at high temperature. This can reduce the capital investment for gas-to-liquid (GTL) plants and for distributing hydrogen.

This study compares the oxygen release and oxygen uptake obtained through a $La_{0.6}Sr_{0.4}Co_{0.2}Fe_{0.8}O_{3-\delta}$ hollow fibre membrane (referred as LSCF6428-HFM) under an Air/He gradient at 850°C and 900°C. The separation and quantification of these two processes permitted the determination of the oxygen incorporated into LSCF6428 structure and the development of a model for apparent overall rate constant using the molar flow of the oxygen at the inlet and outlet in different side of membrane (i.e. shell side and lumen side). The results show that the oxygen flux is enhanced by rising helium flow rates, this is due to an increased driving force for oxygen migration across the membrane and also the air flow determines the oxygen amount that permeates across the membrane. In addition, the oxygen flux improves at higher temperatures, due to its dependence on bulk oxygen diffusion and the

oxygen surface reaction rates. The temperature increase improves the mobility of the lattice oxygen vacancies and also the concentration of lattice oxygen vacancies in the perovskite. The impact of surface modification was also studied by coating Co_3O_4 and 5%Ni-LSCF6428 catalysts on the shell side surface of the LSCF6428 hollow fibre membrane for oxygen permeation. It was found that the oxygen flux significantly improved under Air/He gradient for catalyst-coated LSCF6428-HFM. However, under continuous operation conditions over a long time both the unmodified and the modified perovskite LSCF6428-HFM reactors suffered segregation of metal oxides or redistribution of metal composition at the surface membrane, although the bulk LSCF6428 membrane stoichiometry did not change.

The apparent overall rate constants for oxygen permeation of the Co_3O_4/LSCF6428-HFM and 5%Ni/LSCF6428-HFM were enhanced 3-4 fold compared to unmodified LSCF6428-HFM. Comparison of both modified HFM reactors revealed that the apparent overall rate constants for Co_3O_4/LSCF6428-HFM were 2 fold higher than those obtained for 5%Ni-LSCF6428/HFM. According to the distribution of total oxygen permeation residence for unmodified and modified LSCF6428-HFM reactor, the oxygen permeation rate is limited by surface exchange on the oxygen lean side or lumen side ($\boldsymbol{R}_{ex}^{''}$) at 850°C and 900°C and the contribution of bulk diffusion on the oxygen permeation rate increased with a rise in the temperature (900°C).

The methane oxidation reaction was studied in unmodified and modified 5%Ni-LSCF6428/LSCF6428 hollow fibre membrane in reactors at 850°C. The results suggest that catalytic pathways in methane oxidation depended upon flow operation modes, oxygen concentration, H_2 treatment and on the type of catalyst.

The performances in methane conversion of LSCF6428-HFM and 5%Ni/LSCF6428-HFM modules facilitated the formation of $SrCO_3$ because of the reaction of CO_2 with segregated strontium oxide.

Statement of Originality

The work presented in this thesis was carried out in the Laboratory of Applied Catalysis and Solid State Electrochemistry, School Chemical Engineering and Advanced Material, Merz Court, Newcastle upon Tyne from October 2006 to November 2009, under the supervision of Prof. Ian Metcalfe.

All the work is my own, except where stated otherwise, and has not been submitted for any degree at this or any other university.

Acknowledgements

Let me begin by thanking my supervisor, *Professor Ian Metcalfe* for his help, encouragement and valuable advice on the development of this work and also for giving me the opportunity to work in his Group.

I would like to acknowledge the *University of Newcastle upon Tyne* for financial support (EPSRC).

Next, I would like to send my thanks to *Dr. Alan Thursfield* and *Dr. Danai Poulidi* for daily supervision on the laboratory. Thanks to *Simon, Salah and Craig,* for advise commentary and creating friendship at the office and laboratory.

I am also grateful to the fantastic staff team of the Newcastle University for their high quality service, particularly to *Justine* and *Angela* in the reception, to *Stewart, Rob Simon* and *Iain* at the workshop. Great thanks to *Daniel* and *Vicent* for sorting out lots of electronic and computer troubles out from the gas chromatograph and to *Pauline* for scanning electron microscopy analysis, *Katie* and *Maggie* for X-Ray Diffraction analysis.

I would also like to extent my gratitude to *Professor Malcolm L. H. Green FRS* (University of Oxford) and *Professor Bernardo Fontal* (University of Los Andes) for his valuable and relevant technical comments that significantly improved the writing of this manuscript.

I am also grateful to the internal examiner *Professor Subipta Roy* (Newcastle University) and the external examiner *Dr. Klaus Hellgardt* (Imperial College London) for their helpful suggestions to improve this manuscript.

I would also like to thank my family. In particular, *my mum; brothers* and *sister* for their invaluable support and motivating words at the difficult moments. I would like to give thanks to *my husband* for his advice, discussions and friendship. I would like to specially acknowledge *my daughter* who always gives me motivating words, help and friendship.

Also, I would like to thank *Mrs. Lorna Boal* (nurse), *Dr. James* and *Dr. Mc Gregor* for their motivating words to continue writing up my thesis at very difficult moments with my daughter's disease.

Finally, I must say thanks to *God* and *all non-mentioned people* that directly or indirectly contributed to the happy end of this work…. THANK YOU VERY MUCH indeed.

Dedication

My father *Pedro* who passed away before this task was begun, may God bless him and my mother *Edith* for her advice, support and encouragement during all my life. You are the best parents.

My beloved grandparents *Magdalene* (Oma) and *Ernes*t (Opa) thanks for your faith in me, may God bless their.

My sister and brothers: *Barbara, Pedro Santos* and *Swen* their support *and* for teaching me that I should never surrender.

My loving Daughter *Sindy*, whose love, support, understanding and patience, became an essential part of my life. Without her sacrifice with the many hours put into this degree, I could not have ever finished this work. My husband *Sergio* for his support during this time

Every thought we think is creating our future.

Louise L. Hay

General content

Figure content

Chapter 3

Chapter 4

Chapter 5

Appendix II

Appendix III

Appendix V

Table content

Appendix III

Notation

Abbreviations

SMR	*Steam methane reforming*
CMR	*CO_2 methane reforming*
CPO	*Catalytic partial oxidation*
ATR	*Auto thermal reforming*
OCM	*oxidative coupling of methane*
SOE	*selective oxidation of ethane to ethylene*
POM	*partial oxidation of methane*
PSA	*pressure swing adsorption*
VSA	*vacuum swing adsorption*
GTL	*gas-to-liquid*
MIEC	*mixed ionic and electronic conducting*
LSCF6428	*perovskite-type $La_{0.6}Sr_{0.4}Co_{0.2}Fe_{0.8}O_{3-\delta}$*
HFM	*hollow fibre membrane*
SEM	*scanning electron microscopy*
XRD	*X-ray diffraction*
EDX	*energy dispersive X-ray analysis*
PESf	*Polyethersulfone binder*
NMP	*1-methyl-2-pyrrolidinone*
PVP	*poly (vinylpyrrolidone)*
ALHS	*air-lumen-side, helium-shell side*
ASHL	*air-shell side, helium-lumen side*
MSAL	*4% CH_4/He -shell side, air- lumen side*
MLAS	*4% CH_4/He -lumen side, air- shell side*

Symbol	Description	Unit
A	Area membrane	cm^2
C_i	Concentration of defect i	
C_h	Electron hole concentration	
C_v	Oxygen vacancy concentration	
dA	Differential of area membrane	
$dC_i(x)/dx$	Concentration gradient of species (i) at distance (x)	
$dC_j(x)/dx$	Concentration gradient of species (j) at distance (x , z and t	
d_{hkl}	Interplanar spacing of the crystal planes of indices (hkl)	
dl	Differential of the hollow fibre length	
dn'_{o2}	Differential mole oxygen outlet in lumen side	
dn_{O2}	Differential mole oxygen outlet in shell side	
$\tilde{D}$	Chemical diffusion coefficient	$m^2\ s^{-1}$
D_V	Diffusion coefficient of oxygen vacancies	$cm^2\ s^{-1}$
D_i	Effective diffusivity of defect i	$cm^2\ s^{-1}$
D_h	Electron hole bulk diffusion coefficient	$cm^2\ s^{-1}$
D_a	Ambipolar diffusion coefficient	$9.3x10^{-6}\ cm^2s^{-1}$
D_v^0	Pre-exponential coefficient of D_v	$1.58x10^{-2}cm^2s^{-1}$
E_a	Activation energy	$kJ.\ mol^{-1}$
E_D	Activation energy for D_v	$kJ.\ mol^{-1}$
F	Faraday constant	$C\ mol^{-1}$
ΔG	Gibbs energy of the reaction	$kJ\ mol^{-1}$
$2h^{\bullet}$	Electron hole	
ΔH	Enthalpy of the reaction	$J\ mol^{-1}$
J_i	Transport flux of defect i mol $cm^{-2}\ s^{-1}$	$mol\ cm^{-2}\ s^{-1}$
k	Rate constant	$\mu mol^{\ s-1}\ bar^{-1}\ cm^{-2}$

k_f	*Forward reaction rate constants for the surface reactions*	*c atm$^{0.5}$s^{-1}*
k_r	*Reverse reaction rate constants for the surface reactions*	*mol cm^{-2} s^{-1}*
l	*Length variable of hollow-fibre membrane module*	*cm, mm*
L	*Membrane thickness*	*mm or cm*
$n_{O2\ in}$	*Molar flow of the oxygen at the inlet in the shell side*	*µmol s^{-1}*
$n_{O2\ out}$	*Molar flow of oxygen at the outlet in the shell side*	*µmol s^{-1}*
n'_{O_2out}	*Molar flow of the oxygen outlet in the lumen side*	*µmol s^{-1}*
n'_{N_2out}	*Molar flow of the nitrogen outlet in the lumen side*	*µmol s^{-1}*
n'_{N_2out} **/ 4**	*Correction term for gas phase oxygen transport through the membrane*	
n	*Number of hollow fibres*	
n_t	*Mole total in the shell side*	*µmol*
n'_t	*Mole total in the lumen side*	*µmol*
n	*Integer (the order of reflection or diffraction)*	
O^{2-}	*Lattice oxygen*	
O_O^x	*Lattice oxygen in the perovskite structure*	
O_2	*Molecular oxygen*	
$O_{2\ permeation}$	*Oxygen permeation*	*µmol cm^{-2} s^{-1}*
$O_{2\ uptake}$	*Oxygen uptake*	*(µmol s^{-1})*
$O_{2\ release}$	*Oxygen release*	*(µmol s^{-1})*
P	*Pressure total*	*atm*
P'_{O_2}	*High-pressure side*	
P''_{O_2}	*Low-pressure side*	
R	*Gas constant*	*8.3145 Jmol^{-1}k^{-1}*
r_a	*Ionic radius of the A-site cation*	
r_b	*Ionic radius of the B-site cation*	
r_o	*Outer radius of the hollow fibre*	*mm or cm*

r_{in}	*Inner radius of the hollow fibre*	*mm or cm*
R_e	*Reynolds number*	
$R_{ex}^{'}$	*Resistance by exchange reaction at the shell side*	
$R_{ex}^{''}$	*Resistance by exchange reaction at the lumen side*	
R_{diff}	*Resistance by bulk diffusion*	
R_t	*Total permeation resistance*	
S_A	*Superficial active membrane area*	*7.6 cm^2*
SCO	*Selectivity of carbon monoxide*	
SCO_2	*Selectivity of carbon dioxide*	
SC_2H_4	*Selectivity of ethylene*	
SC_2H_6	*Selectivity of ethane*	
SH_2	*Selectivity of hydrogen*	
ΔS	*Entropy of the reaction*	*J $mol^{-1}K^{-1}$*
t	*Tolerance factor*	
T	*Temperature*	*K or °C*
t_i	*Transport number of defect i*	
$V_0^{\bullet\bullet}$	*Oxygen vacancies*	
$\nabla\mu_k$	*Gradient in chemical potential for each individual charge carrier* k	
$\nabla\phi$	*Gradient in electrical potential*	
$\nabla\eta_k$	*Electrochemical potential gradient*	
x	*Membrane thickness variable*	*cm, mm*
x_0	*Mole fraction oxygen*	
XCH_4	*Conversion of methane*	
Z_k^2	*Charge number*	
Z_i	*Charge number of defect i*	

Greek Letters

Symbol	*Description*	*Unit*
μ_{O_2}	*Chemical potential of gaseous oxygen*	
$\mu_{V_O^{\bullet\bullet}}$	*Chemical potential of oxygen vacancy*	
$\mu_{e'}$	*Chemical potential of electrons*	
$\mu_{h^{\bullet}}$	*Chemical potential of electron holes*	
λ	CuK_{α} *radiation,*	*1.54060 Å*
$\sigma_{e'}$	*Partial conductivity of electrons*	
σ_{h}	*Partial conductivity of electron holes*	
$\sigma_{V_O^{\bullet\bullet}}$	*Partial conductivity of oxygen vacancies*	
σ_{el}	*Partial electronic conductivity*	
σ_{ion}	*Partial ionic conductivity*	
σ_{k}	*Conductivity of charge carriers* k	
θ	*Crystal at angle*	
δ	*Oxygen incorporated into the membrane*	

Superscripts

Symbol	*Description*
'	*Shell side*
''	*Lumen side*

Subscripts

Symbol	*Description*
A	*A site cation*
B	*B site cation*
$diff$	*Bulk diffusion*
ex	*Exchange reaction*
e	*Electron*

h	*Electron hole*
k	*Carrier*
in	*Inlet*
i, j	*Hole, proton or vacancy*
ion	*Ion*
V	*Vacancy*
out	*Outlet*
O_2	*Oxygen*
t	*Total*

Chapter 1.

Introduction

I. Research background

In this chapter is given a general overview about the conversion of the fossil fuels (such as coal, crude oil and natural gas) and describes new alternatives for oxygen and syngas production. In addition, the objectives and organization of the thesis are presented.

1.1. Introduction

Currently in the world, 99% of the energy employed comes from fossil fuels, which are non-renewable resources **[1]**. They are formed from the organic remains of dead plants and animals that were deposited at the bottom of seas, lakes, etc. These sediments need millions of years at high temperatures and high pressures to decompose and transform into gas (methane), oil and coal (carbon), which are the fossil fuels. The provisions of fossil fuel resources are limited, they are being consumed very fast **[1]**.

Coal: is the most abundant fossil fuel and supplies 25% of the primary energy consumed worldwide and was the first raw material or feedstock used at an industrial level. Current research is seeking new technologies to convert coal into synthetic liquid fuels that is cleaner (less sulphur) than coal. Due to the rapid growth of the chemical industry in the 20th century and the products of coal combustion there has been an increase of harmful effects on the environment. For this reason liquid hydrocarbons (from crude oil) which are cleaner and cheaper is preferred over coal **[1]**.

Petroleum: provides 38 % of the total world energy and is a mixture of many different hydrocarbons that may also contain oxygen, and traces of sulphur and nitrogen. Typically found in crude oil are alkanes (paraffins), alkenes (olefins) and cycloalkanes (naphthenes and other aromatics), and in lower amounts sulphur-organic compounds, nitrogen-organic

compounds, oxygen-organic compounds and metal containing porphyrins or non-porphyrin metal complexes of V and Ni. Crude oil is often found at great depths in the earth's crust **[2]**.

Crude oil refining is a series of processes for upgrading crude mixtures of hydrocarbons into commercial chemical feedstocks such as diesel fuel, gasoline, jet fuel and lubricants **[3]**. The first process in crude oil refining is fractional distillation (which is used to separate the different hydrocarbons according to their differing boiling points. Hydrocarbons vary in boiling points, from below room temperature to over 600 °C). The distillation process provides products such as: light gases, gasoline, fuel oils, solvents, motor oils, fats, paraffins, candle wax and asphalt. Subsequently, other processes that employ different physical and chemical processes, such as: reforming, hydrogenation, hydrocracking and hydrodesulphurisation are used to give the desired products. **Figure 1.1** is shows the different processes typically used a petroleum refinery **[3]**.

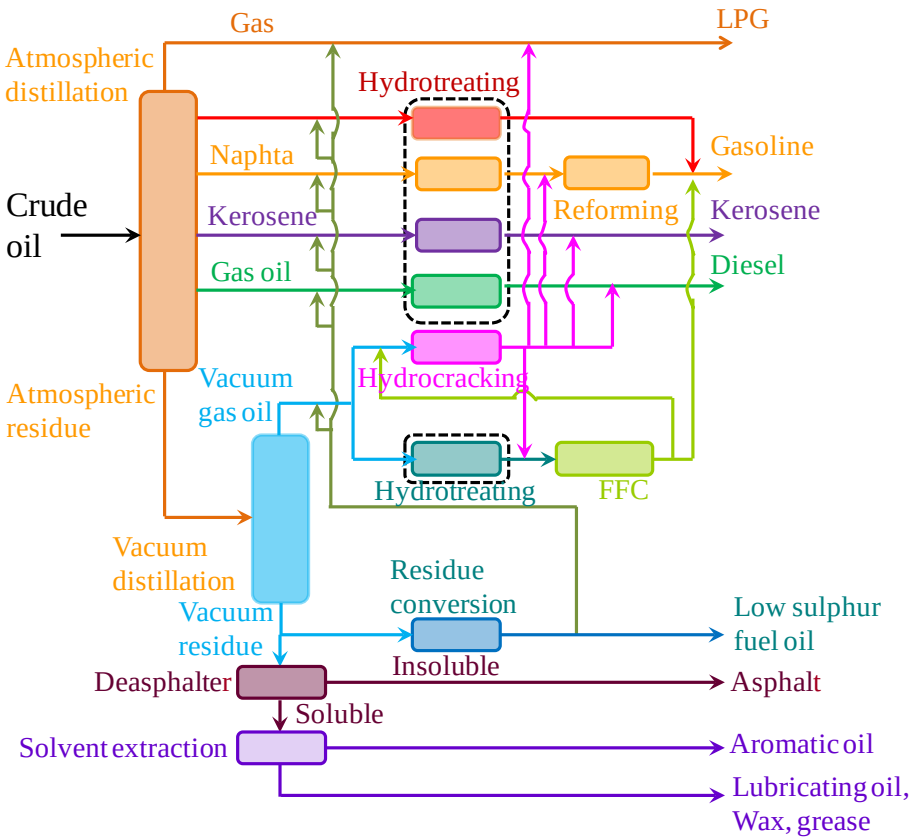

Figure 1.1 Diagram of different processes used in the petroleum refinery **[3]**.

The cracking process is very complex, and involves the breaking –up of heavy molecular weight hydrocarbons into lighter hydrocarbon molecules. Such processes require high temperature, high pressure and various catalysts to produce a variety of fuels that are used mainly in transport as gasoline, and diesel and as jet fuel **[3]**.

The fossil fuel ***natural gas*** (mainly methane) can be found together with crude petroleum and it is often burned in flares. Since 1970 natural gas has been used as an energy source where methane, the major component, is used for heating and some is converted to higher added value chemicals. Currently in the production of syngas (a mixture of carbon monoxide and hydrogen) and pure hydrogen, uses natural gas because it is plentiful. The syngas is used to generate hydrocarbon fuels and the production costs are much lower than for other carbon sources such as naphtha, biomass and coal. However, it is expected by some that in future decades biomass and coal will become the main fossils fuel energy sources because biomass is renewable and a cleaner coal fuel technology will become available **[2, 4]**. The most important processes for producing syngas and pure hydrogen are the following:

I. Steam methane reforming (SMR) is the most widely used commercial process for production of syngas and hydrogen. It is based in the reaction of hydrocarbons (methane) with water (steam). High temperatures (700-1100) °C, are used to overcome the endothermic reaction to produce a mixture of hydrogen and carbon monoxide **[5, 6]**.

$$CH_4 + H_2O \leftrightarrow CO + 3H_2 \qquad \Delta H^{\circ}_{298} = 206\ (kJ/mol) \quad \text{Endothermic Reaction} \quad (1.1)$$

$$CO + H_2O \leftrightarrow CO_2 + H_2 \qquad \Delta H^{\circ}_{298} = -41\ (kJ/mol) \quad \text{Exothermic Reaction} \quad (1.2)$$

However, some of the reactant species can be decomposed at operation temperature and deposited on the catalyst surface as thick layer of inactive carbon (coke). The carbon formation on nickel-based catalysts used in steam reforming, produces serious operational problems and catalyst deactivation. Munster and Grabkelg [**5**] studied the kinetics of the

steam reforming of methane with catalysts containing iron, nickel, and iron-nickel alloys. They proposed that during the steam reforming of methane there is a sequence of two reactions:

$$CH_4 \leftrightarrow C + 2H_2 \qquad \Delta H^{\circ}_{298} = 75\ (kJ/mol) \qquad \text{Endothermic Reaction} \qquad (1.3)$$

$$C + H_2O \leftrightarrow CO + H_2 \qquad \Delta H^{\circ}_{298} = 131(kJ/mol) \qquad \text{Endothermic Reaction} \qquad (1.4)$$

They concluded that on the nickel catalysts, the rate-determining step is the deposition of carbon on the catalyst surface.

Steam reforming is a mature technology and exhibits the highest efficiencies of current economically available hydrogen production methods; around 65% to 70% [**6**]. The production operation cost for steam methane reforming process was reported by Mcglocklin [**6**], see **figure 1.2**. They found that the main costs correspond to the operation (63%) and raw material (19%) whilst the total utility and equipment costs showed lower contribution (18 %).

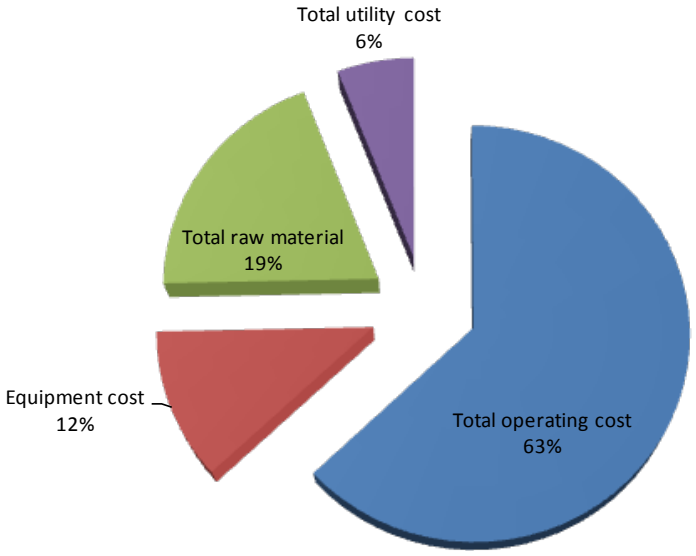

Figure 1.2 Total product cost analysis for steam methane reforming **[6]**

II. CO_2 **Methane reforming (CMR) or dry reforming of methane** is other option for syngas production. It is an endothermic process which is combined with water gas shift

(WGS) reaction for the reforming of natural gas **[5, 8, 9]**. The dry reforming (1.5) and water gas shift (WGS) (1.6) reactions are given below:

$$CH_4 + CO_2 \leftrightarrow 2CO + 2H_2 \qquad \Delta H^{\circ}_{298} = 247\ (kJ/mol) \quad \text{Endothermic Reaction} \quad (1.5)$$

$$CO + H_2O \leftrightarrow CO_2 + H_2 \qquad \Delta H^{\circ}_{298} = 41\ (kJ/mol) \quad \text{Endothermic Reaction} \quad (1.6)$$

The main disadvantage of dry reforming of methane is the significant formation of coke that is subsequently deposited on the catalyst surface, which reduces the useful lifetime of the catalyst. The large formation of coke occurs during methane decomposition (1.7) and Boudouard reactions (1.8), which are given below:

$$CH_4 \leftrightarrow C + 2H_2 \qquad \Delta H^{\circ}_{298} = 75\ (kJ/mol) \quad \text{Endothermic Reaction} \quad (1.7)$$

$$CO + CO \leftrightarrow C + CO_2 \qquad \Delta H^{\circ}_{298} = -172\ (kJ/mol) \quad \text{Exothermic Reaction} \quad (1.8)$$

During CO_2 methane reforming, methane is mixed with carbon dioxide and fed to the CMR reactor. This stream and steam are subsequently fed to the WGS reactor to assist the increase of H_2 production. The dry reforming of methane is not a mature technology, whose main costs are associated to the total operating and equipment costs (83 %), according to Mcglocklin [6], see **figure 1.3**.

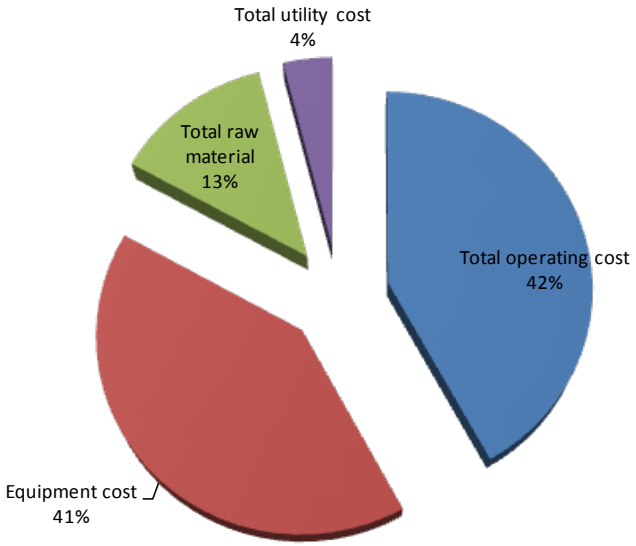

Figure 1.3 Total product cost analysis for CO_2 methane reforming (CMR) **[6]**

III. **Catalytic partial oxidation of methane (CPOM)** requires catalysts that have high selectivity for the partially oxidized product and low selectivity for complete combustion and careful control of reaction conditions, especially the temperature **[8].** Below is given the two main reactions (1.9 and 1.10) involved in the partial oxidation of methane.

$$CH_4 + \tfrac{1}{2}O_2 \leftrightarrow CO + 2H_2 \qquad \Delta H^{\circ}_{298} = -38\ (kJ/mol) \quad \text{Exothermic Reaction} \qquad (1.9)$$

During the second step, the carbon monoxide reacts with water to form carbon dioxide and more hydrogen (WGS reaction) at temperatures around 200°C

$$CO + H_2O \leftrightarrow CO_2 + H_2 \qquad \Delta H^{\circ}_{298} = -41\ (kJ/mol) \quad \text{Exothermic Reaction} \qquad (1.10)$$

Partial oxidation reforming of methane is a much faster process than steam reforming, however it produces less hydrogen per unit of similar fuel. Note that the main cost for this process corresponds to the total operation (70 %); see **figure 1.4** [**6**].

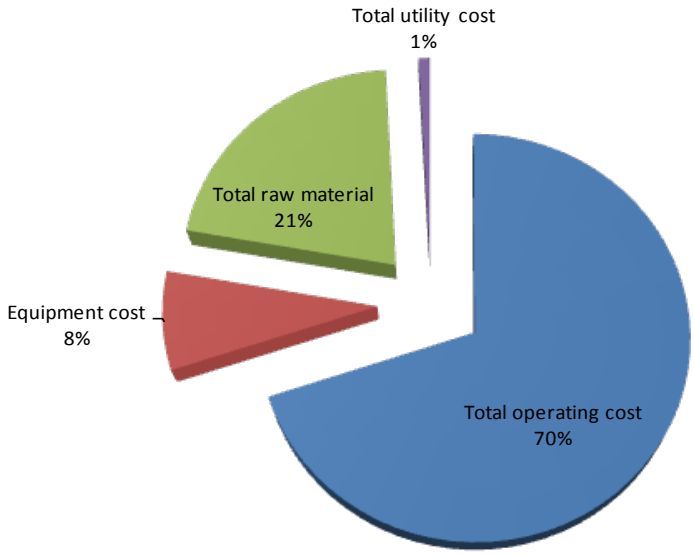

Figure 1.4 Total product cost analysis for catalytic partial oxidation of methane (CPOM) [6**].**

IV. Auto thermal reforming (ATR) is considered to be one of the most effective process to produce a H_2/CO rich product that combines catalytic partial oxidation (CPO) with catalytic steam reforming (SR) **[5, 8, 9, 11].**

During the auto thermal reforming, the hydrocarbon (CH_4) reacts with a mixture of oxygen and water to produce a reformate stream containing hydrogen. The total process is more energy efficient, because the heat produced from the exothermic partial oxidation reaction can be used by the endothermic steam reforming reaction.

$$CH_4 + 1\tfrac{1}{2}O_2 \leftrightarrow CO + 2H_2O \qquad \Delta H^{\circ}_{298} = -520\ (kJ/mol)$$ Exothermic Reaction (1.11)

$$CH_4 + H_2O \leftrightarrow CO + 3H_2 \qquad \Delta H^{\circ}_{298} = 206\ (kJ/mol)$$ Endothermic Reaction (1.12)

The last step requires a water gas shift (WGS) reaction, where the CO reacts with H_2O (steam) to produced CO_2 and H_2.

$$CO + H_2O \leftrightarrow CO_2 + H_2 \qquad \Delta H^{\circ}_{298} = -41\ (kJ/mol)$$ Exothermic Reaction (1.13)

Auto thermal reforming technologies decrease the process size, cost, and start up time of the conventional steam reforming plants, whose total operating cost is 68% (see **figure 1.5**) [**6**].

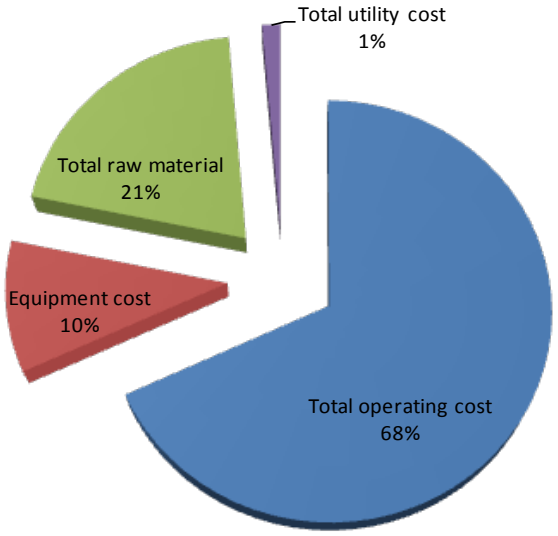

Figure 1.5 Total product cost analysis for auto thermal reforming (ATR) [**6].**

1.2. Novel alternatives for oxygen and syngas production

Many years ago it was recognized that oxygen and oxygen-enriched air are important for medical applications and many industrial processes **[12, 13]**. Examples include the oxidation of NH_3 to NO, the regeneration of fluid-catalytic-cracking catalyst and hydrocarbon oxidation reactions such as partial methane oxidation and methane oxidative coupling. The current method for obtaining pure oxygen on a large scale is by cryogenic air separation (fractional distillation of liquefied air), PSA (pressure swing adsorption) and VSA (vacuum swing adsorption). The first process, cryogenic air separation, utilizes low temperatures and elevated pressures that make it very expensive (118 $/Ton), see **figure 1.6** [**14, 15**], because it is energy intensive, although it produces 99.5% pure oxygen. The other processes, PSA and VSA, require less energy but produce lower purity oxygen (90-93%) **[2]**. In recent years, membrane technology has been suggested as an alternative for producing high purity oxygen from air at lower cost. This is a ceramic metal oxide membrane that due to its mixed ionic and electronic conducting (MIEC) characteristics provides a way for oxygen production. The main advantage of MIEC materials is that, at temperatures of the order of 700-1000 ˚C, oxygen ions can be transported through the membrane from high to low oxygen chemical potential difference via lattice oxygen vacancies. Simultaneously, electrons move in the opposite direction by hopping between the multivalent metal ions, permitting only oxygen ion incorporation into the oxygen vacancy sites. This allows the theoretical selectivity to oxygen to be 100% **[16]**. Air Products reported [**18-20**] the development of ion transport membrane module for pure O_2 production at high temperature. This oxygen unit requires 48% less capital cost and saves 68% of energy compared to cryogenic air separation unit. In **figure 1.6** are compared different technologies for oxygen separation processes [**14, 15**].

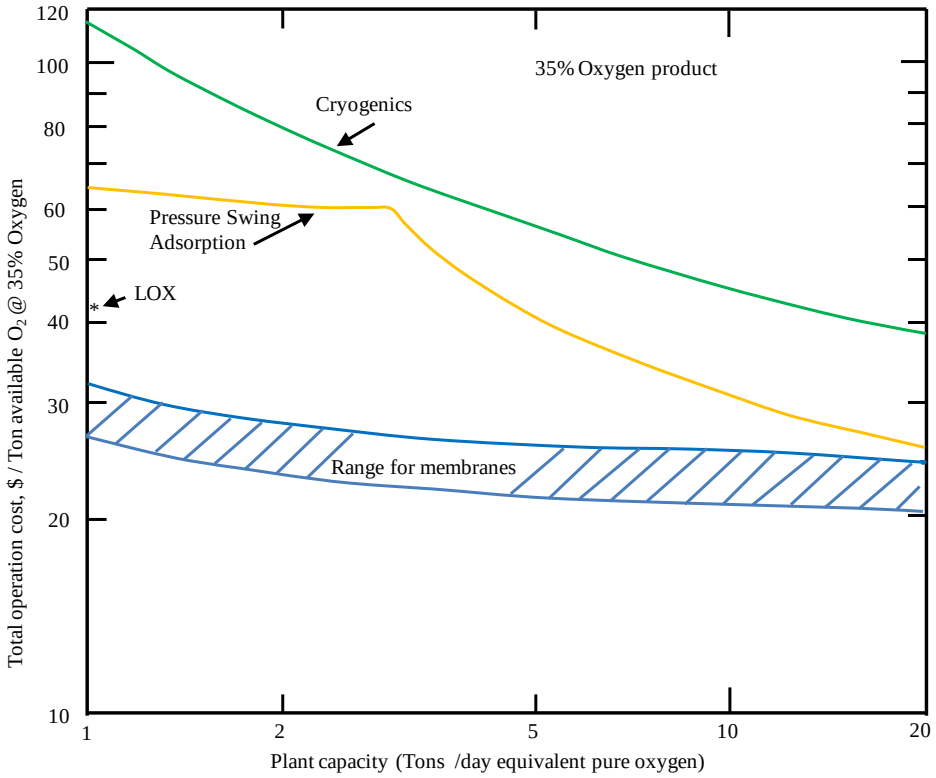

Figure 1.6 Total operation cost against plant capacity for oxygen separation process **[14, 15].**

In addition, the MIEC ceramic membrane has the potential advantage that it could be integrated syngas process into a single compact ceramic membrane reactor lead to high-purity oxygen separation and high temperature syngas processes.

This can reduce the capital investment for gas-to-liquid (GTL) plants and for distributing hydrogen **[20-22]** and can be used for oxygen production in many industrial processes which require a continuous oxygen supply. For example, the oxidation of hydrocarbons such as oxidative coupling of methane to C_2 (OCM), selective oxidation of ethane to ethylene (SOE) and partial oxidation of methane to syngas (POM), etc **[20-24]**. On the other hand, Air Products reported that the second phase of program for reducing the syngas plant cost by more than 30% was completed [**25**].

The mixed-conducting membrane of interest in this work is based on the perovskite-type $La_{0.6}Sr_{0.4}Co_{0.2}Fe_{0.8}O_{3-\delta}$ (hereafter LSCF6428) hollow fibre membrane as it shows highly

mobile electrons and mobile oxygen ions with good chemical stability in comparison with other lanthanum cobaltite materials, as reported by Teraoka *et al.* **[26-28**].

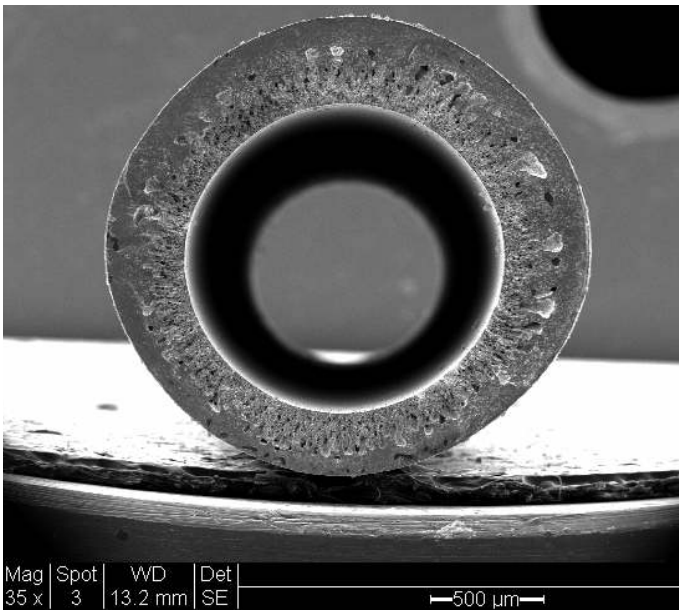

Figure 1.7 SEM image cross section of the LSCF6428-HFM. Membrane supplied by Prof. Li and co-workers, Imperial College London.

In addition such MIEC membranes show the ability to carry out simultaneous oxygen separation and hydrocarbon oxidation reactions according to Hsieh and Yang **[11, 12]**. A cross-section SEM image of LSCF6428 hollow fibre membrane is given in **figure 1.2**

This image shows an inner diameter close to 1 mm and an outer diameter of 1.5 mm. It can be noted that two layers are present: a dense outer skin one and an inner finger like layer (**figure 1.2**) **[29-32].**

There are two main factors that govern the performance of the MIEC membranes with respect to oxygen permeation: Processes occurring at the surface and diffusion of the oxygen vacancies within the bulk of the membrane **[33]**. The hollow fibre $La_{0.6}Sr_{0.4}Co_{0.2}Fe_{0.8}O_{3-\delta}$ membrane, exhibits a number of advantages such as:

1. Combining oxygen separation and supply. Therefore, reducing the units for

operation and the overall operation cost **[20, 22]**.

2. They can be fabricated with thin wall thickness of the order of 250 µm, compared to ca. 1000 µm for conventional membrane geometries; this reduces bulk diffusion resistance **[34, 35]**.

3. High surface area per unit volume (7.6 cm^2) of the membrane reactor compared to disc-shape (5 cm^2). It has been found that modification of the membrane surface with catalysts can promote the rate of surface reactions. Therefore the oxygen permeation rate is improved when the surface reaction is limiting the process **[36]**.

4. It has a chemical stability for different ranges of pH and organic solvents. This is very important, because it permits the use of strong acid and alkali treatments for cleaning the membrane **[37]**.

5. It has a high thermal stability which indicates that it can be used in processes such as gas separation at high temperatures **[37]**.

6. They can be linked with chemical reactions, because they can act as a membrane separating the products from the reactants and/or can act as a catalyst **[37]**. The mechanical stability is usually high compared to organic membranes. This is important for processes at high pressures **[37]**.

1.3. Objective

The overall aims of this research are to improve the oxygen permeation of LSCF 6428 hollow fibre membranes and study the performance of the LSCF6428 membranes reactor in the production of syngas (CO and H_2). Develop and analyze a new approach for oxygen separation and syngas generation simultaneously employing LSCF6428 membrane architecture.

The specific objectives of this research are to:

1. Determine the oxygen permeation of the LSCF6428 hollow fibre membranes without catalysts under different operations conditions as effect of feed flow rate, effect of flow patterns at 850°C and 900°C. The approach is based on the measurements of oxygen permeations under oxygen partial pressure gradients (i.e., varying helium and air flow rates). It is expected that oxygen permeation flux increases as the sweep flow rate and temperatures rise [**29, 32**]. It is anticipated that counter-current and co-current flow patterns show comparable oxygen permeation at high temperature [**29**].
2. Investigate the stability and oxygen incorporated into the unmodified LSCF6428 membrane reactor during long time of operation at 850°C. The difference between the oxygen release obtained in lumen side and oxygen uptake measurement in shell side during experiment gives the oxygen incorporated into LSCF6428 structure. The assessment of the membrane stability is carried out by varying the oxygen flux during operation time and also the characterizations of the membrane pre- and post-operation. According to the literature, the oxygen flux for LSCF6428 membrane could vary after long time of operation [**38, 39**]. It is also expected the incorporation of oxygen into the LSCF6428 structure since this perovskite-type phase is enriched in oxygen vacancies [**25**].
3. Develop a model for determining the overall apparent rate constants for two different flow patterns (i.e., co-current and counter-current modes of operations). The model used to calculate the overall rate constant for oxygen flux operation assumes plug flow in the gas phase, steady state condition and a flux expression whereby the flux depends upon an overall rate constant and the local oxygen partial pressure difference across the membrane. It is anticipated that the model can be used to predict overall rate constants for LSCF6428-HFM at different helium flow rates.

4. Determine the effect of surface modification by different catalysts on the shell side of the LSCF6428 membrane in oxygen permeation under an oxygen chemical potential difference at 850°C and 900°C. The LSCF6428 shell surface membrane was coated with Co_3O_4 or 5%Ni-LSCF6428 catalysts and evaluated under air/He gradients. It is envisaged that the deposition of catalysts on the shell side membrane improves the oxygen flux rate [**40**].
5. Investigate the performance and the role of the catalyst on the LSCF6428 membranes in the partial oxidation of methane. The LSCF6428 membrane-coated Ni nanoparticles are evaluated in the partial oxidation of methane by using air on lumen side and methane on shell side. It is determined the methane conversion and the oxygen flux during the dual catalytic and separation processes. According to the literature, it is anticipated that the conversion of methane and CO selectivity follow an opposite trend [**16**].

1.4. Organization of the thesis

This thesis is divided into the following seven chapters

Chapter One

In this chapter is given a general overview about the conversion of the fossil fuels (such as coal, crude oil and natural gas) and describes new alternatives for oxygen and syngas production. In addition, the objectives and organization of the thesis are presented.

Chapter Two

A brief overview of the perovskite structure is described; the defect chemistry mechanism and stability of these and related materials are given. The theory of the oxygen permeation through mixed ionic-electronic conducting (MIEC) ceramic membranes is presented.

Chapter Three

This chapter describes the fundamentals of the catalyst preparation methods, module assembly, catalytic surface modification, catalytic reaction conditions and finally, the instrumental and principal fundaments of various techniques used to determine the structure, morphology and texture of the membrane.

Chapter Four

This chapter provides information about the oxygen release and oxygen uptake behaviour from unmodified LSCF6428 hollow fibre membrane reactor. In addition, the effect of the various operating parameters on the membrane reactor performance (i.e. modes of gas operation (co-current and counter- current and temperature) are discussed. Also, the calculation are made of the apparent overall reaction rate constants and total permeation

resistance for both modes of operation of the unmodified LSCF6428 hollow fibre membrane at 850°C and 900°C.

Chapter Five

The data are presented for the oxygen release, oxygen uptake, oxygen permeation and apparent overall rate constants and distribution of total permeation resistance obtained from LSCF 6428 hollow fibre membrane modified with cobalt and nickel catalyst at different temperatures. In addition, these results are compared with results obtained with unmodified LSCF6428 hollow fibre membrane (**Chapter 4**).

Chapter Six

This chapter provides the results of partial methane oxidation from 5%Ni/LSCF6428 hollow fibre membrane chapter. Also, the apparent overall rate constants of the partial methane oxidation for different gas compositions and operating conditions are described.

Chapter Seven

Finally, overall **c**onclusions and recommendations for future works are discussed.

1.5. Reference

[1] R.H. Perry, D. W. Green and J. O. Maloney, Perry's Chemical Engineers' Handbook, ed. Seventh, International edition, **1997**, Section 27.

[2] C. H. Bartholomew and R.J. Farrauto, "Fundamentals of Catalytic processes", Second edition, Wiley-Interscience, Chap. 6, **2006,** 339.

[3] G. Martino, P. Courty, C. Marcilly, Handbook of Heterogeneous Catalysis (G. Ertl, H. Knozinger, J. Weitkamp, Eds). Wiley-VCH, Weinheim, 4, **1997**, 1818.

[4] T.G. Kaufmann, A. Kaldor, G.F. Stuntz, M.C. Kerby and L.L. Ansell, Catal. Today, 62, **2000**, 77.

[5] P. Munster and J. J. Grabke, J. Catal., 72, **1981**, 279**.**

[6] K. H. Mcglocklin, Economic analysis of various reforming techniques and fuel sources for hydrogen, Alabama, USA, **2006**, 65-68.

[7] J. R. Rostrup-Nielsen. "Catalytic Steam Reforming in Catalysis", Science and Technology, eds. J. R. Anderson and M. Boudart. Springer- Verlag, New York, **1984**.

[8] J. R. Rostrup-Nielsen, J. Schested, and J. K. Norshov. Adv. Catal., 47: **2002**, 65.

[9] J. R. Rostrup-Nielsen and J. H. Bak Hansen, J. Catal., **1993**, 144:38.

[10] J. Haber, "Selective Oxidation – Heterogeneous", Encyclopedia of Catalysis. Ed. I. Horvath, Wiley- Interscience, Hoboken, NJ, **2003**, 141.

[11] L. M. Aparicio, J. Catal. 165, **1997**, 262.

[12] D. Kang, S. Srinivasan, R. Rhorogood and E.Foster, US Patent 5 516359; **1996**.

[13] P. N. Dyer, S.L. Russek, and D. M. Taylor, **2000**,134, 21.

[14] A. Gollan and M. Kleper, "The economics of oxygen enriched air production via membranes, A/G Technology Corporation, Needhan, Massachusetts, 02194. USA, Proceedings from the Sixth Annual Industrial Energy Technology Conference Volume I, Houston, TX, April 15-18, **1984**.

[15] R. W. Baker, Ind. Eng. Chem. Res. 41, **2002,** 1393.

[16] W. Jin, S. Li, P. Huang, N. Xu, J. Shi and Y. S. Lin, J. Membr. Sci, 166**, 2000**, 13.

[17] X. Tan, Z. Pang, K. Li, J. Membr. Sci., 310, **2008**, 550–556.

[18] S. Liu, G. R. Gavalas, J. Membr. Sci. 246, **2005**, 103–108.

[19] P.A. Armstrong, E. P. Foster, H. H. Gunardson, ITM oxygen for gasification. In SPE/PS-CIM/CHOA International Thermal Operations and Heavy Oil Symposium; Society of Petroleum Engineers: Calgary, Alberta, Canada, **2005**.

[20] B. Steele, C. R. Acad. Sci. Paris, t. 1, Srie II c., **1998**, 533.

[21] H. Wang, S. Werth, T. Schiestel and J. Caro. Angew. Chem., 117, **2005**, 7066.

[22] H.J.M. Bouwmeester, A.J. Burggraaf, in: P.J. Gellings, H.J.M. Bouwmeester, Eds., CRC "Handbook of Solid State Electrochemistry", CRC Press, Boca Raton, FL, **1997**, Chap. 14.

[23] F.T. Akin, Y.S. Lin, J. Membr. Sci. 209, **2002**, 457.

[24] S. Liu, X. Tan, K. Li, R. Hughes, Catal. Rev., 43 (1–2), **2001**, 147.

[25] Air Separation Technology Ion Transport Membrane (ITM), www. Airproducts.com.

[26] Y. Teraoka, H. M. Zhang, S. Furukawa, and N. Yamazoe, Chemistry Letters, **1985**, 1743.

[27] L. W. Tai, M. M. Nasrallan, and H. U. Anderson, J. Solid State Chem. , 118, **1995**, 117.

[28] S. Xu, W. J. Thomson, Ind. Eng. Res., 37, **1998,** 1290.

[29] X. Tan, Y. Liu and K. Li, AIChE Journal, 51, **2005**, 1991.

[30] X. Tan and K. Li Ind. Eng. Res. 45**, 2006,** 142.

[31] A. Thursfield and I. Metcalfe, J. Mater. Chem. 14, **2004,** 2475.

[32] A. Thursfield and I. Metcalfe, J. Solid Electrochem. 10**, 2006,** 604.

[33] H.J.M. Bouwmeester, A. J. Burggraaf, in A. J. Burggraaf, Dense ceramic membranes for oxygen separation, in: A.J. Burggraaf, L. Cot (Eds.), Fundamentals of Inorganic Membrane Science and Technology, Elsevier, Amsterdam, **1996,** pp. 435-528.

[34] K. Li, X. Tan and Y. Liu, J. Membr. Sci. 272, **2006**, 1.

[35] X. Tan, Yutie Liu and K.Li nd. Eng. Chem. Res. 44, **2005**, 61.

[36] S.M. Murphy, D. A. Slade, K.J. Nordheden, S.M. Stagg-Williams, J. Membr. Sci. 277 (1-2), **2006,** 94.

[37] M. Mulder, Basic principles of membrane technology, Netherdands, kluwer, Academic publishers. **1996.**

[38] Y. Zeng, Y. S. Lin and S. L. Swartz, J. Membr. Sci. 150, **1998**, 87.

[39] J. A. Lane; S. J. Benson,D. Waller,J. A. Kilner. **Solid State Ionics**, 121, **1999**, 201

[40] Thursfield and I. Metcalfe, J. Membr. Sci. 288, **2007,** 175.

Chapter 2

Literature survey

1. Literature survey

A brief overview of the perovskite structure is described; the defect chemistry mechanism and stability of these and related materials are given. The theory of the oxygen permeation through mixed ionic-electronic conducting (MIEC) ceramic membranes is presented.

2.1. Overview of the perovskite structure.

In recent years Mixed ionic and Electronic Conducting (MIEC) membranes have attracted attention since the commercialization of the chemical reactors based on these membranes. They can provide a clean, efficient and economic route to separate oxygen from air. The success of this technology could possibly revolutionize the chemical industry where pure oxygen is required, such as in the partial oxidation of methane (POM) **[1, 2]** and the oxidative coupling of methane (OCM) **[3-6]**. Furthermore, this technology can be also employed in medical applications and for oxygen generators **[7, 8]**.

Perovskite-type families of metal oxides have been extensively studied as MIEC membranes. The ideal perovskite (ABO_3) has a cubic close-packed structure (**figure 2.1**) where the cation with a large ionic radius (alkaline earth or a rare earth ion) has 12 coordination to oxygen atoms and occupies A-sites, whilst cations with smaller ionic radius (d-block transition metals) have 6 coordination and occupy B-sites (see **figure 2.1**) **[9, 10]**. "A" and "O" form a cubic closest packing, whilst "B" is contained in the octahedral voids in the packing. Goldschmidt introduced the tolerance factor **(*t*)** to determine the distortion degree of the cubic structure of perovskite **[9]**.

This term is defined as: $t = \frac{r_a + r_o}{\sqrt{2}(r_b + r_o)}$ (2.1)

Where, r_a, r_b and r_o are the ionic radii of the A-site cation, B-site cation and oxygen anion respectively. When the tolerance factor is the unit 1 then the structure is cubic and when $t < 1$ the structure is distorted to a lower symmetry (e.i. tetragonal, orthorhombic, and rhombohedral, etc). Thus, the incorporation of different elements into the perovskite structure can form ideal or distorted structures depending on the tolerance factor **[9]**.

Perovskite are interesting materials for practical applications since they exhibit useful electrical, optical, magnetic and catalytic properties that have been applied in a wide range of technologies **[9, 10]**.

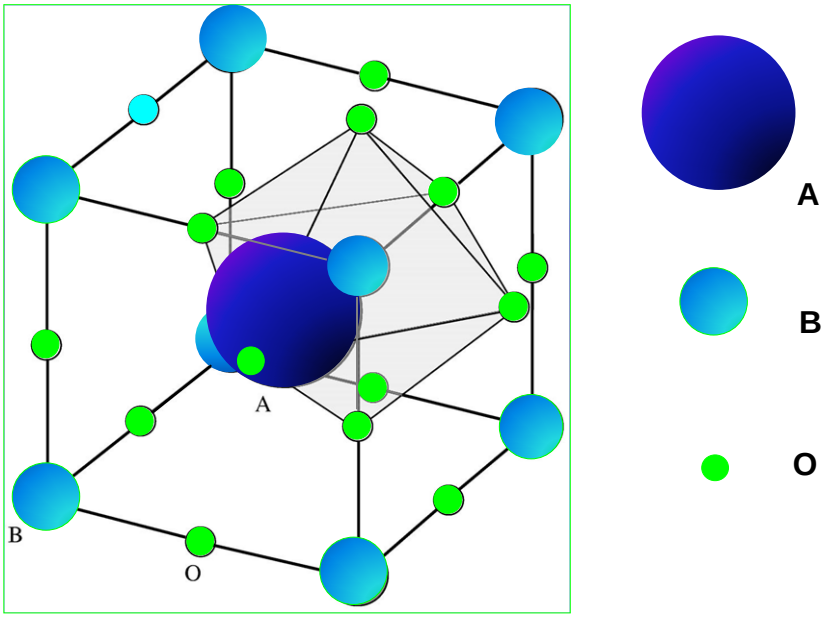

Figure 2.1 Ideal perovskite structure (ABO_3) **[9]**.

A pioneering study of oxygen permeation through perovskite type oxides was carried out by Teraoka *et al*. **[11]**. It was found that the $La_{1-x}Sr_xCo_{1-y}Fe_yO_{3-\delta}$ series showed oxygen permeation and occurred with increasing Co and Sr content due to the oxygen vacancies created in the crystal structure. In addition, they observed that the oxygen permeation rate was directly proportional to temperature.

Further study by Teraoka *et al*. on the oxygen permeation through $Ln_{1-x}A_xCo_{1-y}B_yO_{3-\delta}$ (**Ln**

= La, Pr, Nd, Sm, Gd; **A** = La, Na, Ba, Sr, Ca and **B** = Co, Cr, Fe, Mn, Ni, Cu) showed that lanthanide metal site substitution with metal ions of decreasing ionic radius improved oxygen permeation. When the **A** site is replaced by the above mentioned cation the rate of oxygen flux rose in the order: Ba>Ca>Sr>Na>La. The **B** site substitution, on the other hand, increased oxygen permeation with decreasing ionic radius **[12]**.

In a subsequent study, Anderson **[13]** and Mizusaki **[14]** found that $Ln_{1-x}A_xBO_3$ perovskite, where **B** is selected from Cr, Mn, Fe or Co and **A** is a divalent alkali-earth cation, increases the concentration of oxygen vacancies with the substitution of alkali-earth ion. It was proposed that two different sites for oxygen were present for perovskite-type $La_{1-x}Sr_xCoO_{3-\delta}$ ($\boldsymbol{x = 0.5}$ and $\boldsymbol{x = 0.7}$). In the basal plane of the square pyramid are 4 oxygens and one more at the apex while the oxygen vacancies are between the square pyramid layers (see **figure 2.2**)

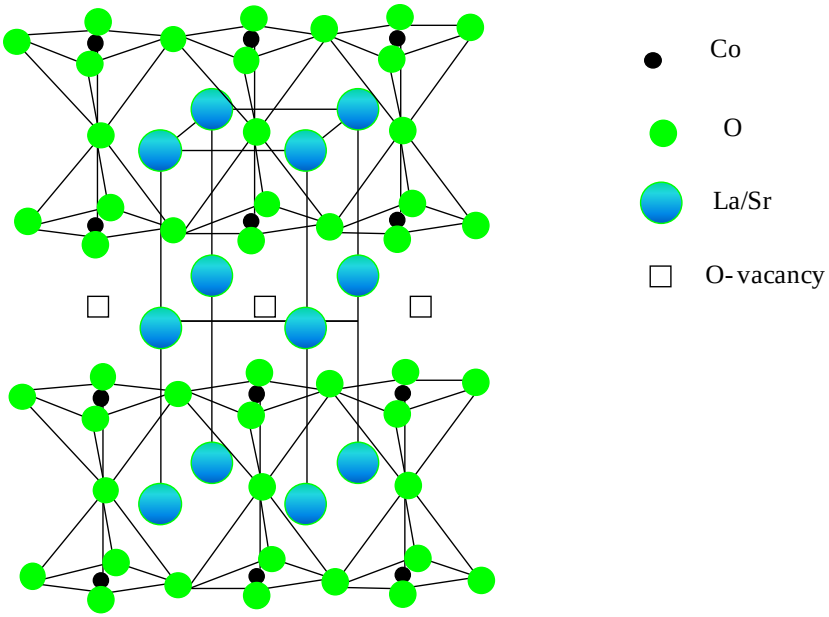

Figure 2.2 Hypothesized structure for $La_{1-x}Sr_xCoO_{3-\delta}$ ($\boldsymbol{x = 0.5}$ and $\boldsymbol{x = 0.7}$) **[10]**

In addition, Bouwmeester and Burggraf determined that the charge compensation during oxygen permeation occurs either by an increase of the transition metal ion valence at the B site or by the formation of ionized oxygen vacancies **[10]**.

A-site deficient $La_{0.6}Sr_{0.4}Co_{0.2}Fe_{0.8}O_{3-\delta}$ based oxides of compositions $La_{0.6-z}Sr_{0.4}Co_{0.2}Fe_{0.8}O_{3-\delta}$, $La_{0.6}Sr_{0.4-z}Co_{0.2}Fe_{0.8}O_{3-\delta}$ and $(La_{0.6}Sr_{0.4})_{1-z}Co_{0.2}Fe_{0.8}O_{3-\delta}$ ($\mathbf{0 \leq z \leq 0.2}$) showed that the charge compensation mechanism in these A- site deficient perovskite is due to the formation of oxygen vacancies rather than the oxidation $B^{+3} \rightarrow B^{+4}$, (**figure 2.3**) **[15]**.

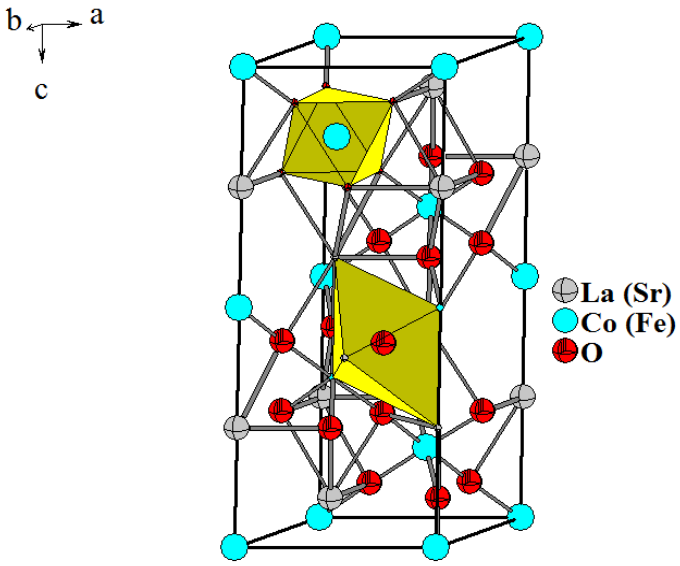

Figure 2.3 Structure of $La_{0.6}Sr_{0.4}Co_{0.2}Fe_{0.8}O_{3-\delta}$ (LSCF6428) **[15, 16]**

The LSCF6428 perovskite system exhibits the following characteristics: (1) high oxygen and electronic conductivity, (2) high temperature stability, (3) low thermal expansion coefficient at operating temperatures, and (4) high point defect (oxygen vacancy) in the structure, which improves its catalytic properties. These advantages of this material make it attractive for oxygen separation membranes and for methane conversion reactors **[15]**.

According to the above mentioned literature, it can be concluded that $La_{06}Sr_{0.4}Co_{0.2}Fe_{0.8}O_{3-\delta}$ is an excellent material and a good candidate for membrane technology because of its high ionic and electronic conductivity and therefore a high oxygen flux. Indeed, the breakthrough of the organic polymer membranes in treatment of refinery gas streams and natural gas treatment became possible through the availability of hollow fibre membranes **[16]**, and thereby increasing the feed flow rate and reducing the membrane

thickness, or by depositing a catalyst that would improve their electronic and ionic conductivity properties **[17]**. Furthermore, the perovskite hollow fibre membrane combines both the feed of molecular oxygen with permeated oxygen from air in a single unit and thereby simplifying the process of oxygen enrichment and potentially decreasing operational and capital costs **[8, 18]**. In addition, in high-temperature processes the perovskite membranes may be more stable than the organic polymeric membranes.

2.2. Notation for point defects.

The defect chemical reactions under consideration here have been described by Kröger and Vink notation **[19]**.

Table 2.1 Kröger-Vink notation for point defects in crystals. Divalent ions are chosen as example with MX as a compound formula with M^{2+} , X^{2-} as cation and anion, respectively.

Symbol	Type of Defect
V_M''	Metal ion vacancy: vacant metal site with effective charge -2 (with respect to the ideal lattice)
$V_X^{\bullet\bullet}$	X ion vacancy: vacant X site with effective charge +2 (with respect to the ideal lattice)
M_M^X, X_X^X	Metal, respectively, X ion on their normal lattice position (neutral)
L_M'	L^+ dopant ion on metal site with effective charge -1 (with respect to the ideal lattice)
$N_M^{\bullet}$	N^{3+} dopant ion on metal site with effective charge +1 (with respect to the ideal lattice)
e'	(Quasi)-free electron in conduction band
$h^{\bullet}$	(Quasi)-free electron hole in valence band
$M_i^{\bullet\bullet}$	Interstitial metal ion metal with effective charge +2 (with respect to the ideal lattice)
X_i''	Interstitial X ion with effective charge -2 (with respect to the ideal lattice)
M'_M	Monovalent metal ion on M^{2+}-position (localised electron, only possible if the metal M has multiple valencies)
$M_M^{\bullet}$	Trivalent metal ion on M^{2+} -position (localised electron hole, only possible if the metal M has multiple valencies)

2.3. Principle of the operation of the oxygen permeation through MIEC perovskite membrane.

Oxygen permeation through MIEC perovskite membrane is a complex process that involves a series of steps. These are schematically shown in **figure 2.4**. The oxygen permeation through a membrane is driven by the oxygen partial pressure difference across it and this process has different steps, which are described below.

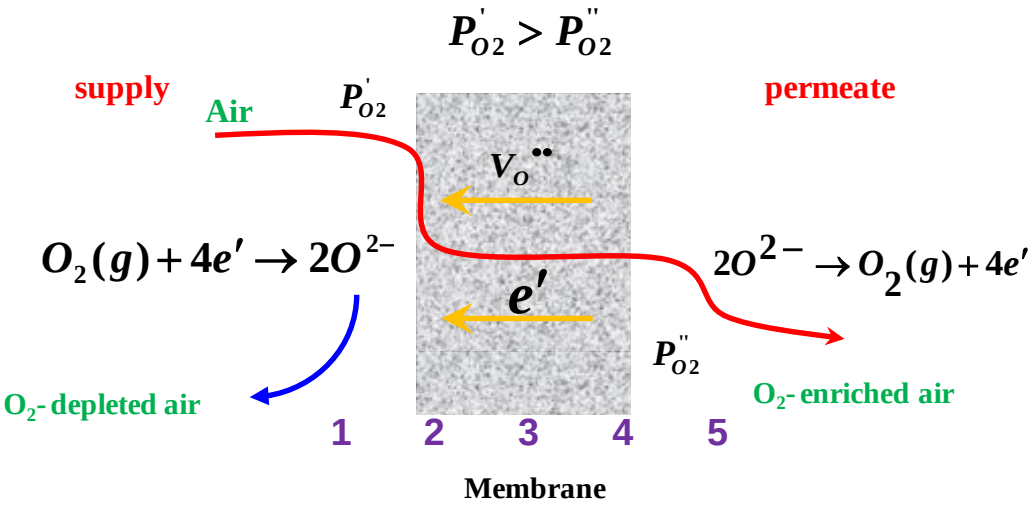

Figure 2.4 Diagram of oxygen permeation process through the MIEC perovskite membranes **[10]**

(1) Initially, mass transfer of gaseous oxygen from the gas stream to the membrane surface (high pressure side). The oxygen is adsorbed on the membrane surface of the high oxygen pressure side **[20]**.

(2) Reaction between the molecular oxygen O_2 and oxygen vacancies $V_O^{\bullet\bullet}$ at the membrane surface high-pressure side P'_{O_2}. The adsorbed oxygen is dissociated into oxygen ions O^{2-} and electron hole $h^{\bullet}$. Different oxygen species are produced upon the reduction of molecular oxygen **[20- 23]**.

$$O_2(g) \longleftrightarrow O_2(ads) \xleftrightarrow{+e'} O_2^- + h^{\bullet} \xleftrightarrow{+e'} O_2^{2-} + h^{\bullet} \longleftrightarrow 2O^- \xleftrightarrow{+e'} 2O_{lattice}^{2-} + h^{\bullet} \quad (2.2)$$

(3) The oxygen species diffuse from the side of high pressure to the side of low pressure of membranes through the combination of mobile oxygen vacancies and electronic defects (holes) while simultaneously electrons are transported in the opposite direction to maintain electrical neutrality **[20-30].**

$$\frac{1}{2}O_2 + V_O^{\bullet\bullet} \leftrightarrow O^{2-} + 2h^{\bullet} \qquad (2.3)$$

(4) Reaction between the lattice and electron hole at the membrane surface (low-pressure side P''_{O_2} . Therefore, on the permeate side, molecular oxygen is formed at the membrane surface **[20, 23]**.

$$O^{2-} + 2h^{\bullet} \rightarrow \frac{1}{2}O_2 + V_O^{\bullet\bullet} \qquad (2.4)$$

(5) Finally, the mass transfer of oxygen from the membrane surface to the gas stream (low pressure side (P''_{O_2}) **[20, 21, 30, 31]**.

The main advantage of MIEC perovskite membranes is that they are 100% selectively permeable to oxygen at high temperature **[10]**.

In general the oxygen permeation rate through MIEC membranes is controlled either by ***bulk diffusion or the transport of electronic charge carriers through the membrane or by surface reactions or surface oxygen exchange.***

Each case is illustrated in **figure 2.5**.

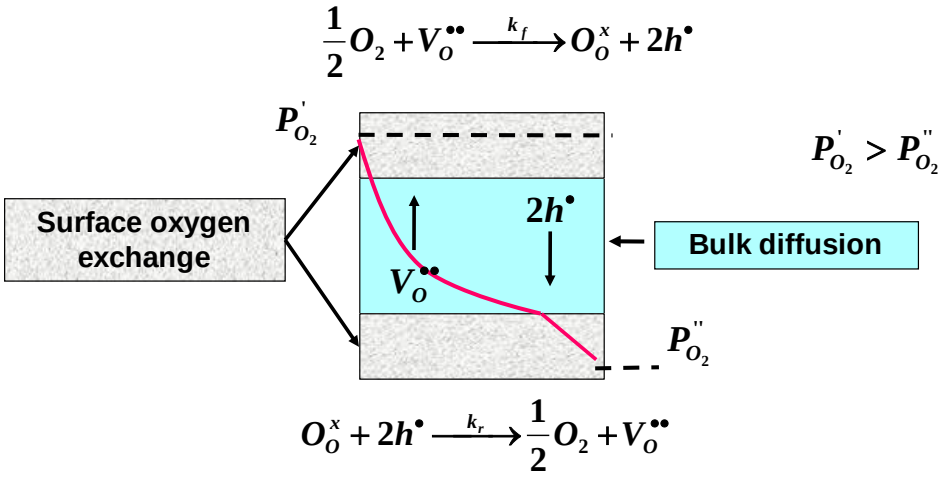

Figure 2.5 Process that controls oxygen permeation through the MIEC perovskite membranes **[10]**.

2.4. Wagner equation

The Wagner equation is the form used for mathematical treatment of the oxygen flux across an ion conducting membrane. It assumes that the oxygen permeation is controlled by ***bulk diffusion or the transport of electronic charge carriers through the membrane.***

The oxygen is selectively transported through the membrane in the form of oxygen ions, driven by an oxygen partial pressure gradient across it (see **figure 2.5**). The flux of oxygen ions is charge compensated by a simultaneous flux of electrons or electron holes **[10]**.

The interaction between the gaseous oxygen with the lattice oxygen is given in eqn. (2.5) using the Kröger-Vink notation [**19**].

$$\frac{1}{2}O_2 + V_O^{\bullet\bullet} + 2e' \leftrightarrow O_O^x \qquad (2.5)$$

It is implicitly assumed that the oxygen vacancies are fully ionized. The interaction between electron and electron holes can be expressed by

$$nil \leftrightarrow e^{'} + h^{\bullet} \qquad (2.6)$$

Considering that eqns (2.5) and (2.6) are in equilibrium, the chemical potential of the different species can be represented by the following relations

$$\frac{1}{2}\nabla\mu_{O_2} + \nabla\mu_{V_O^{\bullet\bullet}} + 2\nabla\mu_{e'} = 0 \tag{2.7}$$

$$\nabla\mu_{e'} + \nabla\mu_{h^{\bullet}} = 0 \tag{2.8}$$

Where, μ_k denotes the chemical potential of the charge carrier k.

The permeation of oxygen ions is charge compensated by a flux of electrons in the reverse direction and only ionized oxygen can move across them. When an oxygen vacancy moves to the site occupied by an oxygen ion, the oxygen ion is relocated to the site released by the oxygen vacancy. The transport of charged defects at steady state under an electrochemical potential gradient is described by the Nernst-Planck equation, (2.9)

$$J_k = -\frac{\sigma_k}{z_k^2 F^2}\nabla\eta_k \tag{2.9}$$

Where, σ_k is the conductivity of the charge carriers k, z_k is charge number, F is the Faraday constant and $\nabla\eta_k$ is the gradient of electrochemical potential of the charge carrier k. The gradient of electrochemical potential can be expressed as function of the gradient in chemical potential $\nabla\mu_k$ and $\nabla\phi$, which is a gradient in electrical potential for each individual charge carrier k

$$\nabla\eta_k = \nabla\mu_k + z_k F\nabla\phi \tag{2.10}$$

At steady state, no charge accumulation occurs and the fluxes of ionic and electronic defects can be expressed by the charge balance, as is expressed in eqn. (2.11).

$$2J_{v_O^{\bullet\bullet}} + J_{h^{\bullet}} = J_{e'} \tag{2.11}$$

Where $J_{v_O^{\bullet\bullet}}$ is the flux of oxygen vacancies is, $J_{h^{\bullet}}$ is the flux of electron holes and $J_{e'}$ corresponds to the flux of free electrons.

Combining eqn. (2.7) with eqn. (2.11) and taking into account eqn. (2.12),

$$J_{O_2} = -\frac{1}{2} J_{V_O^{\bullet\bullet}} \tag{2.12}$$

where, J_{O_2} denotes the flux of oxygen and $J_{V_O^{\bullet\bullet}}$ the flux of oxygen vacancies. One can obtain the flux of oxygen through the membrane represented by eqn. (2.13).

$$J_{O_2} = -\frac{1}{4^2 F^2}\left[\frac{\left(\sigma_{e'} + \sigma_h^{\bullet}\right)\sigma_{V_O^{\bullet\bullet}}}{\left(\sigma_{e'} + \sigma_h^{\bullet}\right) + \sigma_{V_O^{\bullet\bullet}}}\right]\nabla\mu_{O_2} \tag{2.13}$$

Where, $\sigma_{e'}$ denotes partial conductivity of electrons, σ_h partial conductivity of electron holes and $\sigma_{V_o^{\bullet\bullet}}$ partial conductivity of oxygen vacancies. Considering that electronic conductivity is $\sigma_{el} = \sigma_{e'} + \sigma_h^{\bullet}$ and ionic conductivity is $\sigma_{ion} = \sigma_{V_o^{\bullet\bullet}}$. The oxygen flux J_{O_2} through the membrane can also be given by eqn. (2.14)

$$J_{O_2} = -\frac{1}{4^2 F^2}\frac{\sigma_{el}\sigma_{ion}}{\sigma_{el} + \sigma_{ion}}\nabla\mu_{O_2} \tag{2.14}$$

Integrating eqn. (2.14) with respect to the membrane thickness L can be done using the following relation $\nabla\mu_{O_2} = \frac{\partial \mathrm{RT}\ln \mathrm{P}_{O_2}}{\partial \mathrm{x}}$, where x is distance coordinate, R is the gas constant, T is the temperature and P_{O_2} is the oxygen partial pressure.

The final equation (2.15) is the ***Wagner equation***, which has validity for mixed conductors **[10].**

$$Jo_2 = \frac{RT}{16 F^2 L}\int_{\ln P_{O_2}'}^{\ln P_{O_2}''}\frac{\sigma_{el}\sigma_{ion}}{\sigma_{el} + \sigma_{ion}}\partial \ln P_{O_2} \tag{2.15}$$

Kim *et al*. **[32, 33]** developed a surface exchange flux model in order to understand the role of the surface exchange and bulk diffusion during the oxygen transport through the MIEC membrane.

The exchange fluxes i_i at the perovskite membrane – gas interfaces at the inlet and outlet side of the membrane are given by eqn. (2.16)

$$i_i = C_i . k_{i0} \left(e^{n\mu_g / RT} - e^{2n\mu / RT}\right) \qquad (2.16)$$

Where k_{i0} is the surface exchange coefficient, C_i is the density of oxygen ions, n is the reaction order at the interfaces, μ is the chemical potentials of the oxygen ions at the two interfaces and μ_g is the chemical potential of the gas.

$$\mu_g = RT \ln(p / p_0) \qquad (2.17)$$

Where p is the gas pressure and p_0 indicates the standard pressure at 1 atm.

At the interfaces, the following reaction occurs, see **figure 2.6**:

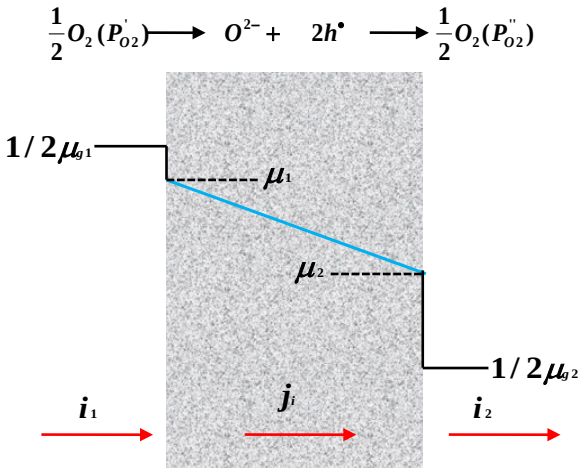

Figure 2.6 Schematic representation of the chemical potential μ distribution and oxygen fluxes i in MIEC membrane **[33]**.

According to surface reaction, see **figure 2.6**, the reaction order at the interfaces is $n = ½$. The exchange oxygen fluxes i_1 and i_2 at the membrane-gas interfaces at the inlet and outlet sides are given by

$$i_1 = C_i \,.\, k_{i0}\ (e^{\mu_{1g}/2RT} - e^{\mu_1/RT}) \tag{2.18}$$

$$i_2 = C_i \,.\, k_{i0}\ (e^{\mu_2/RT} - e^{\mu_{2g}/2RT}) \tag{2.19}$$

The radial oxygen ion diffusion flux j_{O_2} in the tube is given by eqn. (2.20)

$$j_{O_2} = -\frac{C_i\ D_a}{RT}\ \frac{d\mu}{dr} \tag{2.20}$$

Where, r is the radial coordinate of the tube and D_a is the ambipolar oxygen ion-electron hole diffusion coefficient:

$$D_a = D_i \frac{\sigma_e}{\sigma_e + \sigma_i} \tag{2.21}$$

D_i is the ionic diffusion coefficient, σ_e and σ_i are the electronic and ionic conductivities, respectively.

The normalized oxygen permeation flux j_{O_2} can be expressed as:

$$j_{O_2} = -\frac{F}{\pi r l} \tag{2.22}$$

The length of the tube is given by l. Combining the eqns. (2.20) and (2.22) the eqn. (2.23) is obtained

$$-\frac{C_i\ D_a}{RT}\frac{d\mu}{dr}=-\frac{F}{\pi r l} \tag{2.23}$$

Continuity of ion flux requires that the surface exchange fluxes and oxygen permeation flux j_{O_2} at two interfaces match:

$$\frac{F}{\pi r_0 l}=C_i\ k_{i0}\left(e^{\mu_{g1}/2RT}-e^{\mu_1/RT}\right) \tag{2.24}$$

$$\frac{F}{\pi r_{in} l}=C_i\ k_{i0}\left(e^{\mu_2/RT}-e^{\mu_{g2}/2RT}\right) \tag{2.25}$$

Where r_0 and r_{in} are the outer and inner tube diameters.

Integrating the eqn. (2.23) can be obtained (2.26). The eqn. (2.27) is obtained after evaluating the integration limits:

$$\int_{\mu_2}^{\mu_1} d\mu=\frac{RTF}{\pi C_i\ D_a\ L}\int_{r_{in}}^{r_0}\frac{dr}{r} \tag{2.26}$$

$$\mu_1-\mu_2=\frac{R\ T\ F}{\pi\ C_i\ D_a\ l}\ln\left(\frac{r_0}{r_{in}}\right) \tag{2.27}$$

Finding μ_1 and μ_2 from eqns. (2.24) and (2.25), respectively, it can be obtained:

$$\mu_1=RT\ln\left(e^{\mu g_1/2RT}-\frac{F}{C_i\ k_{i0}\ \pi\ r_0\ l}\right) \tag{2.28}$$

$$\mu_2=RT\ln\left(e^{\mu g_2/2RT}-\frac{F}{C_i\ k_{i0}\ \pi\ r_{in}\ l}\right) \tag{2.29}$$

Eliminating μ_1 and μ_2 in eqns. (2.24)-(2.27), the relation below can be obtained

$$\ln\left(\frac{\left(\frac{p'_{O_2}}{p_0}\right)^{1/2}-\frac{F}{C_i\ k_{i0}\ \pi\ r_0\ l}}{\left(\frac{p''_{O_2}}{p_0}\right)^{1/2}+\frac{F}{C_i\ k_{i0}\ \pi\ r_{in}\ l}}\right)=\frac{F}{\pi\ C_i\ D_a\ l}\ln\left(\frac{r_0}{r_{in}}\right) \tag{2.30}$$

When the oxygen transport is ***limited by surface exchange,*** the oxygen chemical potential gradient drop across the thickness of the membrane because μ_1 became close to μ_2 $(\mu_1 \to \mu_2)$. Therefore, the oxygen permeation rate is controlled by the oxygen exchange reaction of the gas-MIEC interface. Under this condition the eqn. (2.30) is reduced to eqn. (2.31).

$$F=\frac{r_{in}\ r_0\ C_i\ k_{i0}\ \pi\ l}{r_0+r_{in}}\left[\left(\frac{p'_{O_2}}{p_0}\right)^{1/2}-\left(\frac{p''_{O_2}}{p_0}\right)^{1/2}\right] \tag{2.31}$$

On the other hand, if the oxygen transport is ***limited by the bulk diffusion*** (i.e. $\mu_1 \to \mu_{g1}/2$ and $\mu_2 \to \mu_{g2}/2$), the oxygen exchange flux from the gas to solid i_{in}, and from solid to the gas, i_{out} are equal to the thermal equilibrium exchange flux i_{ex}

$$I_{in} = I_{out} = I_{ex} \tag{2.32}$$

Furthermore, the chemical potential of the oxygen ion-electron pairs at the two interfaces $(\mu_1$ ***and*** $\mu_2)$ are equal to the chemical potentials of the oxygen gas at the inlet $(\mu_{g1}/2)$ and outlet $(\mu_{g2}/2)$ of the membrane (eqn. 2.33)

$$\mu_g/2=\mu \tag{2.33}$$

So the eqn. (2.30) is changed to

$$F = \frac{\pi\, C_i\, D_a\, l}{2\ln(r_0/r_{in})} \ln\left(\frac{p'_{O_2}}{p''_{O_2}}\right) \tag{2.34}$$

The total oxygen flux can be expressed by the eqn. (2.35).

$$F = j_{O_2} * S_A \tag{2.35}$$

Where, j_{O_2} is the oxygen permeation flux and S_A is the effective area of the membrane tube.

Substituting the eqn. (2.31) into eqn. (2.35) it can be obtained the eqn. (2.36) for the oxygen permeation when the ***surface exchange is the limiting step of the oxygen transport.***

$$j_{O_2} = \frac{r_{in}\, r_0\, C_i\, k_{i0}\, \pi\, l}{S_A(r_0 + r_{in})}\left[\left(\frac{p'_{O_2}}{p_0}\right)^{1/2} - \left(\frac{p''_{O_2}}{p_0}\right)^{1/2}\right] \tag{2.36}$$

Note that the eqn. (2.36) predicts that the oxygen permeation through the membrane is proportional to the pressure term $\left[\left(\frac{p'_{O_2}}{p_0}\right)^{1/2} - \left(\frac{p''_{O_2}}{p_0}\right)^{1/2}\right]$ since the oxygen transport rate is controlled by the surface exchange reaction.

On the other hand, substituting the eqn. (2.34) into eqn. (2.35) one can obtain the oxygen permeation ***limited by the bulk diffusion*** through the membrane, eqn. (2.37).

$$j_{O_2} = \frac{\pi\, C_i\, D_a\, l}{2 S_A \ln(r_1/r_2)} \ln\left(\frac{p'_{O_2}}{p''_{O_2}}\right) \tag{2.37}$$

In this case the oxygen permeation is proportional to $\ln\left(\frac{p'_{O_2}}{p''_{O_2}}\right)$ when the limiting step is the bulk diffusion.

2.5. The oxygen permeation through $La_{0.6}Sr_{0.4}Co_{0.2}Fe_{0.8}O_{3-\delta}$ hollow fibre membrane

Case 1: When oxygen permeation is controlled by bulk diffusion

Tan and Li researched the oxygen flux for a mixed conducting membrane at steady state under the electrochemical potential gradient, when it is controlled by ***bulk diffusion*** **[34]**.

The Nernst –Plank equation, gives a general expression for the flux of charged species.

$$J_i = -\frac{\sigma_i}{z_i^2 F^2}\nabla\mu_i + C_i\upsilon \qquad (2.38)$$

Where, υ and μ_i are the local velocity of the inert marker and electrochemical potential of charged species, respectively.

The electrochemical potential for each charged species is given by eqn. (2.39)

$$\mu_i = \mu_i^0 + RT\ln a_i + z_i F\phi \qquad (2.39)$$

Where μ_i^0, a_i and ϕ are the standard chemical potential, activity and the galvanic internal potential.

The conductivity of charge species σ_i can be correlated to the concentration and diffusivity of charged species i through the Nernst-Einstein equation:

$$\sigma_i = \frac{z_i^2 F^2}{RT} C_i D_i \qquad (2.40)$$

Assuming the following conditions:

(a) The local velocity of the inert market is negligible; (b) the ideal state is applied (activity coefficient is unit); (c) no external current is imposed and (d) one dimensional model is applied **[34]**. Substituting the eqns. (2.40) and (2.39) into eqn. (2.38) can be obtained the transport flux of charged defects at steady state, eqn. (2.41).

$$J_i(x) = -D_i C_i \left[\frac{1 - t_i}{C_i} \cdot \frac{dC_i}{dx} - \sum_{j \neq i} \frac{z_i}{z_j} \cdot \frac{t_j}{C_j} \cdot \frac{dC_j}{dx} \right] \tag{2.41}$$

Where $J_i(x)$ is the flux of species i at distance x from the surface, D_i is the diffusion coefficient (cm^2/s), $dC_i(x)/dx$ is the concentration gradient of species i at distance x, $dC_j(x)/dx$ is the concentration gradient of species j at distance x, z and t are the charge number and transport number of species i and j, respectively. C Is the concentration of species i and j, respectively.

According the step (3) in **figure 2.4** the oxygen vacancy $V_o^{\bullet\bullet}$ and electron hole h, are the only mobile charge carriers in the mixed conducting membrane **[31]**, therefore eqn. (2.41) can be reduced to eqn. (2.42).

$$J_V = -\frac{(C_h + 4C_V) D_V D_h}{C_h D_h + 4C_V D_V} \cdot \frac{dC_V}{dx} \tag{2.42}$$

When the ionic transference number closes to zero in the perovskite ceramic membrane **[35, 36]**, then $C_h D_h >> C_V D_V$ and $C_h >> C_V$, therefore eqn. (2.42) is simplified to

$$J_V = -D_V \cdot \frac{dC_V}{dx} \tag{2.43}$$

The oxygen permeation can be written based on the stoichiometric relations of oxygen and the oxygen vacancy as eqn. (2.12) or

$$J_{O_2} = \frac{D_V}{2} \cdot \frac{dC_V}{dx} \tag{2.44}$$

The diffusion coefficient of oxygen vacancies D_V depends on the temperature and the oxygen defect lattice structure **[37]**. Once the steady-state under the electrochemical potential gradient is established at certain temperature, D_V can then be considered a constant **[31, 34]**.

$$D_V = D_V^0 \exp\left(-\frac{E_D}{RT}\right) \tag{2.45}$$

The oxygen flux or molar flow rate for a hollow fibre membrane can be expressed as

$$J_{O_2} = \frac{1}{2\pi r}\frac{dn'_{O_2}}{dl} = \frac{D_V}{2}\frac{dC_V}{dr} \tag{2.46a}$$

Or

$$dn'_{O_2} = \pi . D_V \frac{\int_{C_V'}^{C_V''} dC_V}{\int_{r_i}^{r_0} \frac{dr}{r}} dl = \pi . D_V \frac{C_V'' - C_V'}{\ln \frac{r_0}{r_{in}}} dl \tag{2.46b}$$

Where, r denote radius variable of the hollow fibre, l is a length of the hollow fibre membrane and r_0 and r_i are the outer and inner radius of the hollow fibre, respectively. The prime and double prime represent the high and low oxygen pressure sides of the membrane **[34]**.

Case 2: When oxygen permeation is controlled by surface reaction

When the oxygen permeation flux is determined by ***surface reaction,*** the following reversible reactions take place at the high and low pressure sides **[34]**.

$$\frac{1}{2}O_2 + V_O^{\bullet\bullet} \xleftrightarrow{K_f / K_r} O_O^x + 2h^{\bullet} \quad (2.47a)$$

$$O_o^x + 2h^{\bullet} \xleftrightarrow{K_f / K_r} \frac{1}{2}O_2 + V_O^{\bullet\bullet} \quad (2.47b)$$

It may involve step 2 in **figure 2.4**, when oxygen adsorption occurs, dissociation, recombination and charge transfer **[38]**. It should be noticed that because of the high electronic conductivity, the electron holes are essentially constant at both surfaces of the membrane, and thus the forward k_f (2.47a) and reverse k_r (2.47b) reaction rates of the surface reactions are pseudo zero-order at steady state under isothermal conditions **[31]**. Therefore, the local rate of oxygen consumed (step 2) or formed (step 4) in the hollow fibre can be, respectively, writing the following equations **[34]**

$$dn_{o2}^{'} = 2\pi\, r_0 \left[K_f (p_{O_2}^{'})^{0.5} C_V^{'} - k_r \right] dl \quad (2.48a)$$

$$dn_{O_2}^{'} = 2\pi\, r_{in} \left[k_r - k_f (p_{O_2}^{''})^{0.5} C_V^{''} \right] dl \quad (2.48b)$$

Substituting eqn. (2.46) in eqn. (2.44) the local oxygen permeation rate in a hollow fibre can be correlated to the partial oxygen pressure

$$dn_{O_2}^{'} = \frac{k_r \left[\left(p_{O_2}^{'}\right)^{0.5} - \left(p_{O_2}^{''}\right)^{0.5} \right]}{\frac{k_f \ln\left(r_o / r_{in}\right)\left(p_{O_2}^{'}\right)^{0.5}\left(p_{O_2}^{''}\right)^{0.5}}{\pi\, D_v} + \frac{\left(p_{O_2}^{'}\right)^{0.5}}{2\pi r_{in}} + \frac{\left(p_{O_2}^{''}\right)^{0.5}}{2\pi r_o}} dl \quad (2.49)$$

Correlation between the Chemical diffusion coefficient ($\tilde{D}$) and the diffusion coefficient of oxygen vacancies (D_V)

Equation (2.7) can be written as a function of neutral oxygen atoms flux

$$J_O = -\frac{1}{4^2 F^2} \frac{\sigma_{el}\sigma_{ion}}{\sigma_{el} + \sigma_{ion}} \nabla \mu_{O_2} + Z_{O_2} F \nabla \phi \quad (2.50)$$

Assuming that the fast movement of electron- holes inside the membrane do not reach a steady state electric field gradient, hence

$$\nabla \phi = 0 \tag{2.51}$$

Then, the neutral oxygen flux through the membrane is

$$J_O = -\frac{1}{4^2 F^2}\frac{\sigma_{el}\sigma_{ion}}{\sigma_{el}+\sigma_{ion}}\nabla \mu_{O_2} \tag{2.52}$$

Where the chemical potential gradient $\nabla \mu_{O_2}$ can also be expressed in terms of a chemical potential driving force $d\mu_{O_2}/dx$

$$\nabla \mu_{O_2} = \frac{d\mu_{O_2}}{dx} \tag{2.53}$$

Remember that the chemical potential is also given by

$$\mu = \mu^{\circ} + RT \ln a \tag{2.54}$$

The neutral oxygen flux can be rewritten as

$$J_O = -\frac{1}{4^2 F^2}\frac{\sigma_{el}\sigma_{ion}}{\sigma_{el}+\sigma_{ion}}\frac{RTd\ln a}{dx} = -\frac{1}{4^2 F^2}\frac{\sigma_{el}\sigma_{ion}}{\sigma_{el}+\sigma_{ion}}RT\frac{d\ln a}{d\ln C_O}\frac{\partial C_O}{\partial x} \tag{2.55}$$

Therefore,

$$J_O = -\frac{1}{4^2 F^2}\frac{\sigma_{el}\sigma_{ion}}{\sigma_{el}+\sigma_{ion}}\frac{d\mu_{O_2}}{dC_O}\frac{dC_O}{dx} \tag{2.56}$$

The chemical diffusion coefficient $\tilde{D}$ is given by

$$\tilde{D} = \frac{1}{16F^2}\frac{\sigma_{el}\sigma_{ion}}{\sigma_{el}+\sigma_{ion}}\frac{\partial \mu_{O2}}{\partial C_o} \tag{2.57}$$

Then, the effective transport of neutral oxygen atoms can be expressed in terms of a chemical diffusion process, considering Fick's first law **[10]**.

$$J_O = -\tilde{D}\frac{dC_O}{dx} \tag{2.58}$$

Where the driving force for diffusion is the gradient in neutral oxygen dC_O/dx and the diffusion is dominated by neutral vacancies.

Therefore

$$J_{O_2} = \frac{1}{2}J_O \tag{2.59}$$

Because $\frac{dC_O}{dx} = -\frac{dC_V}{dx}$ (2.60)

Substituting eqn. (2.58) into (2.59) and considering eqn. (2.60), it can be obtained that

$$J_{O_2} = \frac{1}{2}\tilde{D}\frac{dC_V}{dx} \tag{2.61}$$

Equalizing eqn. (2.58) and (2.61), it can be found that

$$\tilde{D} = D_v \tag{2.62}$$

Note that the chemical diffusion is equal to the vacancy diffusion coefficient.

2.6. Partial oxidation of methane to syngas through MIEC membrane.

The MIEC perovskite membrane reactor has received increasing attention because this improves the performance of methane conversion processes due to simultaneous production of pure oxygen and syngas by combining oxygen separation and high temperature catalytic partial oxidation into a single unit, simplifying the process and reducing the capital costs **[1, 15, 20, 39 - 43]**. **Figure 2.7** presents the simultaneous production of pure oxygen and syngas

in MIEC membrane.

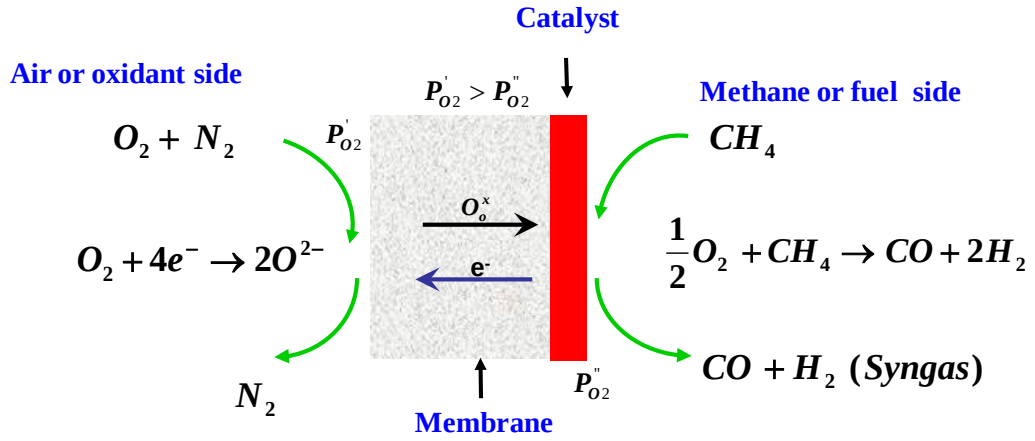

Figure 2.7 Reaction mechanisms for partial oxidation of methane through MIEC membrane **[42-44]**.

At high temperature (800 to 1000) °C, in **air or oxidant side**, gaseous oxygen is adsorbed, dissociated and reduced to lattice oxygen (O^{-2}) on the membrane surface and diffuse through the combination of mobile oxygen vacancies and electronic defects (holes) since the oxygen partial pressure on the air side is lower than that on the methane side. The driving for is the oxygen partial pressure difference across the membrane. On the fuel or methane side, the permeated oxygen is consumed by methane (CH_4) for their partial oxidation to syngas $(CO$ and $H_2)$ or complete oxidation to carbon dioxide and water. The MIEC membrane allow separation of oxygen from air supply at elevated temperature (>700 °C). By combining air separation and catalytic partial oxidation of methane to syngas into membrane reactor, it is expected that this technology reduces the capital costs of natural gas to liquid (GTL) **[43]** and improves selectivity and yields of the products **[45]**.

2.7. Mechanism for partial oxidation of methane to syngas through MIEC membrane.

Sierra *et al.* [46] proposed a mechanism for the partial oxidation of methane over $LaNiO_{3-\delta}$

perovskite through pulse studies. They concluded that the product distribution of the POM reaction is dependent upon the concentration of surface oxygen species. Initially, the O_2 is incorporated into the lattice through different intermediate oxygen species, which are represented in eqns (2.63) **[20-23]**.

$$O_2(g) \longleftrightarrow O_2(ads) \xleftrightarrow{+e} O_2^- + h^\bullet \xleftrightarrow{+e} O_2^{2-} + h^\bullet \longleftrightarrow 2O^- \xleftrightarrow{+e} 2O_{lattice}^{2-} + h^\bullet \qquad (2.63)$$

They did not distinguish the different surface oxygen species and used the Kröger-Vink notation O^* to represent the oxygen species, O_O^x a regular lattice oxygen ion, e' is an electron and $V_O^{\bullet\bullet}$ denotes an oxygen vacancy.

At ***high concentration of reactive lattice oxygen***, CH_4 is completely oxidized to form CO_2 and H_2O.

$$CH_4 + 4O_o^x \rightarrow CO_2 + 2H_2O + 4\,V_O^{\bullet\bullet} \qquad (2.64)$$

Or

$$CH_4 + 4O^* \rightarrow CO_2 + 2H_2O \qquad (2.65)$$

At ***low concentration of lattice oxygen***, on the other hand, it is favoured the partial oxidation of methane as can be observed in the below reaction mechanism. Note that the subscripts s and b refer to surface and bulk, respectively.

$$CH_4 \rightarrow CH_{4-x} + xH_S \qquad (2.66)$$

$$CH_{4-x} \rightarrow C_S + (4-x)H_S \qquad (2.67)$$

$$H_S + H_S \rightarrow H_2 \rightarrow H_{2,g} \qquad (2.68)$$

$$C_S + O^* \rightarrow CO_S \qquad (2.69)$$

$$CO_S \rightarrow CO_g \qquad (2.70)$$

$$CO + O^{*} \rightarrow CO_{2,\,S} \tag{2.71}$$

$$CO_{2,S} \rightarrow CO_{2,g} \tag{2.72}$$

$$2H_S + O^{*} \rightarrow H_2O_s \tag{2.73}$$

$$H_2O_S \rightarrow H_2O_g \tag{2.74}$$

The CH_4 can be also be dissociated by the O^{*} according to the following equation [46]:

$$CH_{4,S} + O^{*} \rightarrow CH_{3,S} + OH_S \tag{2.75}$$

$$CH_{3,S} + 3O^{*} \rightarrow C_S + 3OH_S \tag{2.76}$$

In this step, the absorbed H atom may combine to form hydrogen which easily desorbs. The chemisorbed carbon species are either oxidized to CO or CO_2 by lattice oxygen.

Finally, the re-oxidation process can be written as function of an incorporation and migration process:

$$O^{-} + V_{O,S}^{\bullet\bullet} + e^{'} \leftrightarrow O_{O,s}^{x} \qquad \text{(Incorporation)} \tag{2.77}$$

$$O_{O,S}^{x} + V_{O,b}^{\bullet\bullet} \leftrightarrow O_{O,b}^{x} + V_{O,S}^{\bullet\bullet} \qquad \text{(Migration)} \tag{2.78}$$

Wang *et al.* **[47]** proposed a mechanism for oxidative coupling of methane to C_2 hydrocarbons (ethylene and ethane) using different catalysts on MIEC perovskite membrane at 700-900°C (**Figure 2.8**).

First the reaction of methane with the lattice oxygen and electron holes produces $\bullet CH_3$ radical, water and an oxygen vacancy:

$$CH_4 + O_O^{x} + 2h^{\bullet} \leftrightarrow 2(\bullet CH_3)_{ads} + H_2O + V_O^{\bullet\bullet} \tag{2.79}$$

Two $\bullet CH_3$ radicals form ethane which can react again with lattice oxygen and electron holes giving, ethylene, water and oxygen vacancy.

$$2(\bullet CH_3)_{ads} \rightarrow C_2H_6 \tag{2.80}$$

$$C_2H_6 + O_O^x + 2h^\bullet \rightarrow C_2H_4 + H_2O + V_O^{\bullet\bullet} \quad (2.81)$$

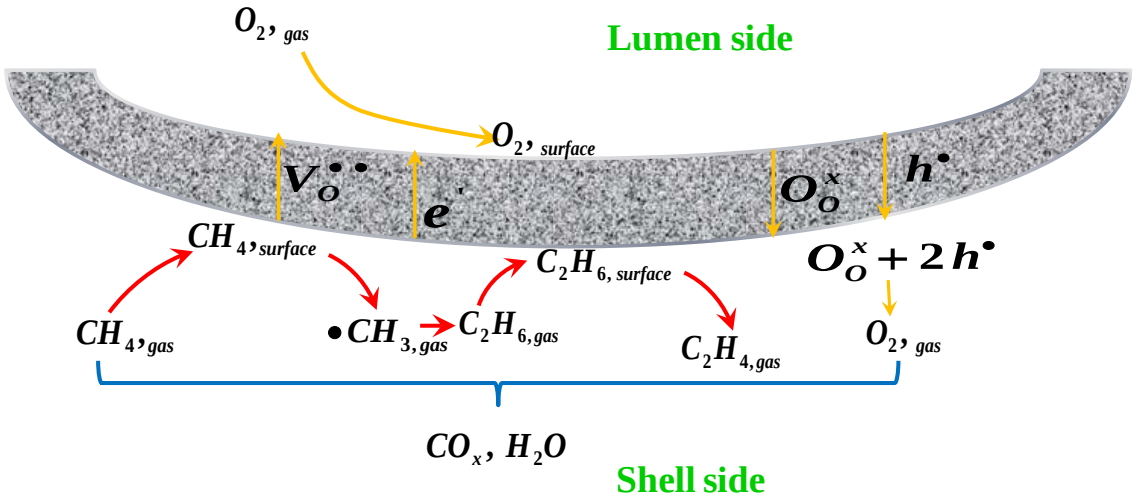

Figure 2.8 Scheme of surface mechanism for methane conversion through MIEC membrane **[47, 49].**

Deeper oxidation of C_1 and C_2 to CO_x can be achieved when the lattice oxygen is not completely consumed:

$$2O_O^x + 4h^\bullet \rightarrow O_{s,\,g} + 2V_O^{\bullet\bullet} \quad (2.82)$$

Therefore the methane conversion is increased but the C_2 selectivity decreases when the oxygen transported across the membrane is too high.

2.8. A brief overview of the geometry of the $La_{0.6}Sr_{0.4}Co_{0.2}Fe_{0.8}O_{3-\delta}$ based membrane.

Below, is given literature relevant to the oxygen permeation studies and the methane oxidation reaction using both unmodified and modified $La_{0.6}Sr_{0.4}Co_{0.2}Fe_{0.8}O_{3-\delta}$ hollow fibre membranes.

Tan *et al.* **[20]** reported the preparation of mixed conducting $La_{0-6}Sr_{0.4}Co_{0.2}Fe_{0.8}O_{3-\delta}$ by phase-inversion spinning. The performances of the modules for air separation under various

operating modes, different temperatures and feed flow rates were studied both experimentally and theoretically. The results revealed that the surface exchange reaction at the lumen side is much more important than that at the shell side, especially for lower operating temperatures. The porous inner surface of membrane favours the oxygen permeation when air is fed in the shell side of the membrane module. At high operating temperature, oxygen permeation can be enhanced by counter current flow operation.

The performance of perovskite (LSFC) hollow fibre membrane reactor (HFMR) in the oxidative coupling of methane was also studied by Tan *et al.* **[3]**. The experimental results indicated that LSFC hollow fibre membranes exhibit good oxygen permeation rate, methane conversion and C_2 yield compared to conventional disk-shaped membrane. The C_2 yield of 15.3 % with a corresponding selectivity of 43.8% were achieved in the HFMR at 950 °C with feed flow rates of CH_4-Ar mixture and air of 17.2 and 32.9 ml (STP)/min, respectively. Higher temperature favoured the formation of ethylene. After 4 week of OCM operation time, the LSCF membrane remained intact in its perovskite structure, mechanical and OCM performances.

Thursfield and Metcalfe **[50]** applied the oxygen-ion conducting MIEC for the production of chemicals. They found out that this membrane promises advantages for oxidation processes when air is used as an oxidant. In additional study, these authors **[44]** evaluated the stability and oxygen permeation of MIEC perovskite $La_{0\text{-}6}Sr_{0.4}Co_{0.2}Fe_{0.8}O_{3\text{-}\delta}$ hollow fibre membrane reactor during the methane oxidation at different temperatures (540-960 $^{\circ}$C). It was found that the mass transfer limited the oxygen flux at high temperatures. On the other hand, the selectivity to CO and H_2 was favoured at low fluxes, whereas the selectivity to CO_2 and H_2O were favoured at high oxygen permeation.

Metcalfe *et al.* **[39]** compared the Pt-modified and unmodified hollow fibre membrane of LSCF6428 for air separation process. They obtained an oxygen permeation of 0.56 μmol.cm^{-}

$^{2}.s^{-1}$ limited by mass transfer at 1000°C whilst at 800 °C a non-mass transfer limited oxygen permeation of 0.14 μmol.cm^{-2}.s^{-1} was reported. The platinum deposited on the membrane shell side improved the oxygen permeation rate compared with the unmodified membrane as the oxygen reduction on the shell side was the rate determining step.

Balachandran *et al.* **[25, 26]** investigated partial oxidation of methane to syngas in $SrFe_{0.2}Co_{0.8}O_{3-\delta}$ (SCF-1) and $La_{0.2}Sr_{0.8}Fe_{0.6}Co_{0.4}O_{3-\delta}$ (SCF-2) tubular membranes at 850 °C. They reported that the system La-Sr-Fe-Co-O permeated larger amounts of oxygen, which was reflected on higher methane conversion (99 %) and CO selectivity (90 %). They also observed the membrane failure after a few minutes of operation as a consequence of oxygen gradients produced after the methane was introduced to the core side of the membrane at 850 °C. A subsequent study of methane oxidation in $SrFe_{0.2}Co_{0.8}O_{x}$ membrane showed high oxygen flux under air/He gradient. Two types of structural failure were also observed when membranes reactors were used in syngas production **[51]**. The first type of failure occurred after a short time of operation by the lattice expansion mismatch of opposite sides of the membrane. The second type of fracture occurred after several days of operation and was a consequence of chemical decomposition of the membrane to produce $SrCO_3$ and elemental Co and Fe.

Ten Elshof *et al.* **[52, 4]** reported that disk-shaped $La_{0.6}Sr_{0.4}Co_{0.8}Fe_{0.2}O_3$ for oxidative coupling of methane (OCM) to ethane and ethylene at 800-900 °C shows C_2 selectivity up to 70% at a very low methane conversion (1 - 3%). Xu and Thomson **[52]** also reported the OCM reaction on several perovskite-type structures, including $La_{0.6}Sr_{0.4}Co_{0.8}Fe_{0.2}O_3$ disk membrane. It obtained a C_2 selectivity around 10-50% and methane conversion close to 3%.

Lane *et al*. [54] reported oxygen permeation and oxygen surface reaction measurements in LSCF 6428 using disc membranes of 25 mm diameter and 0.96-mm thickness under conductivity relaxation technique. An oxygen flux of 0.13 μmol cm^{-2} s^{-1} was obtained under

helium and air at either side of the membrane at 800 ºC. They also demonstrated that oxygen stoichiometry of LSCF6428 perovskite changed with temperature and oxygen partial pressure.

Zeng *et al.* **[55]** reported that the oxygen permeation flux for $La_{0.8}Sr_{0.2}Co_{0.6}Fe_{0.4}O_{3-\delta}$ increases at around 825°C due to an order-disorder transition of the oxygen vacancies in the membrane. Also, the reaction of oxidative coupling of methane (OCM) was performed in LSCF membrane reactor under Air/CH_4 gradient. They obtained high C_2 selectivity (70-90%) and yield (10-18%) at temperature above 850°C when He/CH_4 feed ratio was between 40 and 90. When the He/CH_4 ratio decreased to 20, the C_2 selectivity dropped to less than 40%. The surface catalytic properties for OCM of LSCF membrane was strongly dependent on the oxygen activity of the membrane surface exposed to the methane stream.

Jin *et al.* **[1]** studied the partial oxidation of methane to syngas on $La_{0.6}Sr_{0.4}Co_{0.2}Fe_{0.8}O_{3-\delta}$ tubular membrane reactor packed with NiO/Al_2O_3 catalyst. They found that the conversion of methane was nearly 100% and the CO selectivity was below 70%, owing to the partially oxidized state of the catalyst. Under a reducing atmosphere of CO and H_2, the CO selectivity increased up to 100 %, whereas the methane conversion decreased to 84 %.

2.9. Investigation of other perovskite and non-perovskite membranes for either oxygen permeation or methane oxidation

Caro *et al.* **[40, 15]** studied the perovskite materials $BaCo_xFe_yZr_{1-x-y}O_{3-\delta}$ as hollow fibres for the production of oxygen-enriched air and partial oxidation of methane. They found that the oxygen permeation at high temperature favours O_2 enrichment, reaching an oxygen concentration close to 35 vol. % with a production rate of 7.33 μmol cm^{-2} s^{-1} of O_2-enriched air at 875 °C under a pressure difference of 1.5 bars. The concentration and the rate of

production can be controlled by the temperature, air pressure and gas flow rates. The partial oxidation of methane was also studied at different air flow rates and different methane flows. The CH_4 conversion was 82% and CO-selectivity was 83% whereas the oxygen permeation flux was (4.88-6.88) μmol cm^{-2} s^{-1} at 865 °C. The BCFZ hollow fibres showed a good chemical stability under POM and a lower stability under POM plus steam conditions.

A number of groups have investigated other perovskite and non-perovskite membranes for either oxygen permeation or methane oxidation, see **table 2.2**.

Table 2.2 Research based on perovskite and non-perovskite membranes for either oxygen permeation or methane oxidation.

Membrane material	Membrane form	Thickness (mm)	Reference
$La_{0.6}Sr_{0.4}Fe_{0.9}Ga_{0.1}O_{3-\delta}$	Disc	1	[**56**]
$Sr_{0.77}Fe_{0.54}Al_{0.46}O_{2.54-\delta}$	Disc	0.6	[**57**]
$Ba_{0.5}Sr_{0.5}Co_{0.8}Fe_{0.2}O_{3-\delta}$	Disc	1.5	[**21, 24**].
$SrCo_{0.5}FeO_x$	Tubular	0.25-1.20	[**25**]
$SrFe_{0.2}Co_{0.8}O_{3-\delta}$	Tubular	0.25-1.20	[**26**]
$BaZr_xCoFe_zO_{3-\delta}$	Tubular	0.18	[**40, 15, 58**]
$(La_{0-6}Sr_{0.4})_{0.99}FeO_{3-\delta}$	Disc	1.34	[**27**].

2.10. Stability of mixed ionic electronic conductor membranes

Below, is reviewed the literature related to the stability of the $La_{0.6}Sr_{0.4}Co_{0.2}Fe_{0.8}O_{3-\delta}$ membrane and other perovskite membranes.

Lee *et al.* [**59**] studied the mechanical properties and structural stability of mixed ionic electronic conductor membrane. They considered the mechanical properties as relevant factors for applications of ion conducting oxides since stresses chemically induced can produce component degradation. The reduction of the membrane thickness can also improve

the oxygen permeation performance. The mechanical properties such as fracture strength and toughness of the membrane could be explained with micro structural features and relative density. The membrane failures during the permeation experiment were attributed to stresses induced by reactor configuration and phase separation due to the instability of the perovskite structure in a severe reducing environment for long operation time.

Doorn *et al.* [**60**] studied the stability of oxygen permeable disc membranes of perovskite $La_{0.3}Sr_{0.7}CoO_{3-\delta}$ under oxygen pressure gradient at 900°C for 120 hours. They observed phase separation into strontium oxide (SrO) in the oxygen lean side. When the disc membrane was evaluated over more than 500 h at temperature between 900 and 1100°C, the oxygen lean side was severely degraded. The phase separation was attributed to the kinetic decomposition of the membrane material as a consequence of the cation mobility at the operation temperature.

Xu and Thomson [**61**] investigated the chemical stability of the LSCF6428 membrane in connection with its potential use as a catalytic membrane for the oxidative coupling of methane (OCM). They reported that the module reached steady state oxygen-defect gradient in (15-20 hours) and high stability under air/nitrogen gradients at temperatures up to 960 °C. Also, they found that the apparent activation energy for oxygen permeation determined between 701°C and 963°C was 159 kJ mol^{-1}**.** However, they observed that severe near-surface etching occurs when one side of the membrane is exposed to 100% CH_4 at 850°C under atmospheric pressure, which was reflected on an increase of 5 fold in oxygen flux and OCM reaction rate, while the selectivity of C_{2+} hydrocarbons was cut down from 40 to 10%.

Lein *et al.* [**62**] reported that oxygen permeation through $La_{0.5}Sr_{0.5}Fe_{1-x}Co_xO_{3-\delta}$ (x= 0, 0.5 and 1) membranes under oxygen partial pressure gradients, temperature and time. They have found that at low pO_2 gradients the flux were controlled by diffusion, while at larger pO_2 gradients the flux was controlled by a surface exchange, while the activation energy for

oxygen flux varied in the range 67–105 kJ mol^{-1}. The membranes after about 720 hours at 1150°C under O_2 / N_2 gradient exhibited only the original perovskite phase on the reducing side, while on the oxidizing side various secondary crystalline phases were observed dependent on the composition at the Fe/Co-site and the (Sr + La)/(Fe + Co) ratio of the materials. Moreover, kinetic demixing of the main perovskite phase was also observed, particularly near the surfaces, due to the high temperature and long operation time.

Wang *et al.* [**63**] investigated the effects of kinetic demixing/decomposition and impurity segregation on stabilities of the LSCF6428 hollow fibre membranes under oxygen separation conditions. The membranes were operated under 0.21/0.008 oxygen partial pressure (bar) difference at 950°C for 1128 hours. They found that cobalt oxide grains were separated on the air side of the membrane surface after long-term operation, whilst Sr and Fe enriched the surface layer of air side at 50 nm of depth. The oxygen permeation performance was stable after operating 1128 h, indicating that the demixing/decomposition and impurity segregation would not affect the LSCF6428 HF membranes at the operating conditions applied.

Markus *et al.* [**64**] reported a stable permeation flux of 0.02 μmol $cm^{-2}sec^{-1}$ oxygen during the long-term operation of a $La_{0.58}Sr_{0.4}Co_{0.2}Fe_{0.8}O_{3-\delta}$ membrane at 800°C for nearly 3000 hours. They found degradation of the membrane surfaces due to kinetic demixing of mobile cations and different oxide layers on the feed and the permeate sides of the membrane.

Wang *et al.* **[65]** studied oxygen-separation on three LSCF6428HFM modules under a 0.21/0.009bar oxygen partial pressure difference at 950°C for 1128, 3672 and 5512 hours, respectively. They reported that the microstructure of the membranes exhibited kinetic demixing and decomposition as was determined through different techniques of characterization (i.e., Secondary Ion Mass Spectrometry, SEM, EDXS and XRD). Also, they found secondary crystalline phase grains on the air side surface of the membranes after the long-term operation. In addition, they also observed that Co and Fe enrichment as well as La

depletion on the surface and in the bulk at the air side. The order of cation diffusivities was Co>Fe>Sr>La. Kinetic demixing and decomposition rates of the membranes at the air side were self-accelerating with time, which was attributed to the A-site (i.e., La and Sr) deficient in the perovskite lattice since the B-site cations (i.e., Co and Fe) move faster than the A-site cations, leading to A-site deficiency in the newly generated layers. The oxygen permeation of the LSCF6428HFM modules was not affected by the kinetic demixing and decomposition during long-term operation (up to 5512 hours). However, they supposed that permeability of oxygen may to be affected by secondary phase formation on the air-side surface at even longer operation times.

2.11. Sulphur contamination of mixed ionic electronic conductor membrane

Below is reviewed the literature of the sulphur contamination on perovskite membranes.

Li *et al.* **[66]** measured the oxygen permeation through tubular $La_{0.6}Sr_{0.4}Co_{0.2}Fe_{0.8}O_{3-\delta}$ membranes which were prepared by isostatic pressing. The oxygen permeation fluxes were studies at various downstream oxygen partial pressures and temperatures. The oxygen permeation obtained was about 0.07 μmol cm^{-2} sec^{-1}(STP) at 900°C, when the oxygen partial pressure on the feed and permeate sides are 0.21 and 0.001 atm, respectively. New crystalline phases such as $SrSO_4$, $CoSO_4$, SrO, Co_2O_3, and La_2O_3 were identified by XRD and EDXS. The formation of sulphur-containing phases was attributed to the interaction of the SO_2 trace presence in the air and helium flows with cations segregated at the membrane surface.

Xu *et al*. [67] prepared tubular LSCF6428 membranes and developed a mathematical model for simulating the oxygen permeation performance. They reported that the experimental oxygen permeation increased with decreasing downstream oxygen partial pressure and increasing helium flow rate, which coincided with the results of the oxygen permeation modelling study. Also, they have found that oxygen permeation slightly decreased after

long-term operation (i.e., 110 hours). Furthermore, new crystalline phase such as $SrSO_4$, $CoSO_4$, SrO, Co_2O_3, and La_2O_3 were observed on the surfaces of the tubular membrane, sulphur phases are also associated with the interaction between SO_2 trace present in air and helium.

Tan *et al***. [68]** investigated the catalytic combustion of methane and the effects of operating methane and air feed flow rates on the performance of the LSCF6428HFMR. Also, they developed a mathematical model to predict the performance of the membrane reactor for methane combustion, which combines the local oxygen permeation rate with approximate catalytic reaction kinetics. They have reported that both the methane conversion and oxygen permeation rate can be improved by coating platinum on the air side of the hollow fibre membranes. Also, they found that the membranes change in the metal cation stoichiometry and microstructure together with contamination with sulphur might have their origins in the CH_4 gas supply and SO_2 in the atmosphere. According to the authors, the LSCF6428-catalyst system developed a second phase in lumen side, which did not adversely affect the methane combustion process and performance.

Subsequently, Thursfield and Metcalfe [**39**] studied the oxygen permeation through unmodified LSCF6428 HFM and Pt-modified LSCF6428 HFM under air/helium gradient at 650–1000°C. They reported the absence of mass transfer limitations at lower temperatures and also that the rate-determining step for oxygen permeation is significantly enhanced by deposition of a porous platinum catalyst film onto the air-side of the membranes. It was also found that oxygen permeation (i.e., 0.56 μmol $cm^{-2}s^{-1}$) was limited by mass transfer at 1000°C whilst the non-mass transfer limited permeation at 800 °C was 0.14 μmol cm^{-2} s^{-1}. The module was operated during 500 hours before the onset of significant leakage. The characterization of the post operation membranes by XRD, SEM and EDS revealed localised changes in the stoichiometry of the membranes and the presence of sulphur in the form of

sulphates of strontium, cobalt and calcium. Furthermore, changes of surface microstructure for both shell side and lumen sides of the membrane surfaces were also observed. They associated the sulphur contaminations to the glass-ceramic sealing material employed and sulphur dioxide present in the helium sweep gas and atmosphere.

Franca *et al*. [**69**] studied the oxygen permeation and hydrogen production by steam methane reforming at 900°C over LSCF6428 micro tubular membranes. The characterization of the post operation membrane revealed the presence of a strontium enriched dense layer on the water exposed membrane surface and crystallites enriched with cobalt and sulphur on the methane feed side surface, implying that the performance of the membrane can be affected by the degradation of the LSCF6428.

Yaremchenko *et al*. [**70]** carried out a comparative study of the oxygen transport mechanism through sulphur-free and -containing $Ba_{0.5}Sr_{0.5}Co_{0.8}Fe_{0.2}O_{3-\delta}$ (BSCF) membranes. They have found that oxygen permeation rate decrease due to the partial blockage of the surface by sulphate phase, whilst the bulk ambipolar conductivity remains essentially unchanged. Also, they observed segregation of $BaSO_4$ at the grain boundaries by analysis of SEM/EDXS. The negative impact of sulphur contamination on oxygen permeation was noticeable at temperatures below 850°C. The authors demonstrated that a surface activation process can increase the oxygen flux through sulphur-containing BSCF membranes to the level of that of sulphur-free membranes.

Liu *et al*. **[71]** have found an important degradation mechanism of BSCF perovskite membranes to the operation-induced surface segregation of trace impurities of sulphur that cause a considerable impact on oxygen permeation at low-temperature. Also, they reported an effective method that enables stabilization of the permeation flux at low-temperature in BSCF perovskite membranes. Slater and co-workers found that the sulphate ions can emerge into the lattice of perovskite oxides [**72-73**], and they occupy the B-site of the perovskite

(ABO_3). However, the detailed structure state of the sulphate ions in the perovskite lattice is still unclear.

According to Liu *et al.* **[71],** for a mixed electronic–ionic conductor, the equilibrium of interest is the following:

$$\mathbf{0.5}\boldsymbol{O}_2 + \mathbf{2}\boldsymbol{e}^- \leftrightarrow \boldsymbol{O}^{2-} \tag{2.83}$$

In the mixed conducting materials, the possible species involved in the charge transfer are electrons, anions and cations, consequently the current balance can be written as:

$$\boldsymbol{I}_e + \boldsymbol{I}_{anions} + \boldsymbol{I}_{cations} = \mathbf{0} \tag{2.84}$$

At low temperatures, the motion of metallic ions is very slow, and can be neglected; moreover, there is no protons transport under the conditions for oxygen permeation. Eqn. (2.84) can be written as:

$$\boldsymbol{I}_e + \boldsymbol{I}_{anions} = \mathbf{0} \tag{2.85}$$

Here, the anions are oxygen and sulphate, so eqn. (2.85) is re-written as:

$$\boldsymbol{I}_e + \boldsymbol{I}_{O^{2-}} + \boldsymbol{I}_{SO_4^{2-}} = \mathbf{0} \tag{2.86}$$

When the membranes were treated in air or helium, there is no oxygen chemical potential difference across the membranes, so the electronic current and ions current in the membrane bulk is zero at a balance state, as shown in **figure 2.9A**.

However, on the membrane interface zone the reaction (2.83) still takes place. The thickness of the interface zone varies with membranes and operation conditions [**74**]. Once the sulphate anion transport from the interface zone to the outside surface, they react with barium ions to produce $BaSO_4$, in which sulphate anions have lower chemical potential than occupying B-site of the perovskite. As a result, there is $BaSO_4$ grains found on the membrane surfaces. Only the interface zones are involved in this process, so there are few $BaSO_4$ grains formed. When the membranes were operated for oxygen permeation, there is an oxygen chemical potential difference across the membranes, so the electronic current and

ions current in the membrane bulk zone is not equal to zero at a steady state, as shown in **figure 2.9B**. Under this condition, both interface zones and bulk zone of the membrane are involved in the transport process. After a long time, the sulphate anions in the interface zone of the permeation side and bulk zone transport to the outside surface and react with barium ions to produce $BaSO_4$; and the sulphate anions in the interface zone of the feed side partially transport to the outside surface and react with barium ions to produce $BaSO_4$.

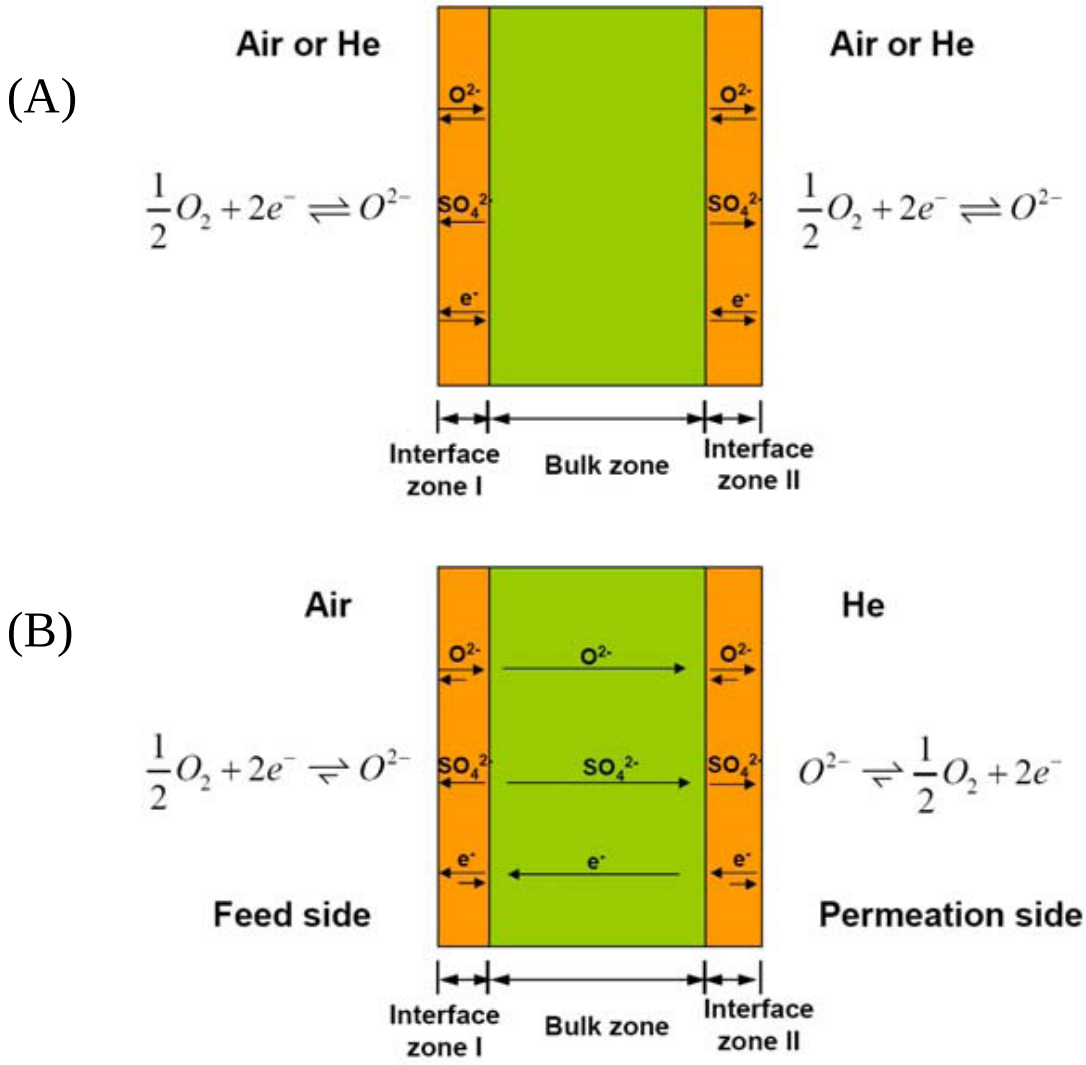

Figure 2.9 Diagram of the transport of electrons and ions when the membrane are (A) treated by air or helium, and (B) operated for oxygen separation [**71**].

2.12. References

[1] W. Jin, S. Li, P. Huang, N. Xu, J. Shi and Y. S. Lin, J. Membr. Sci, 166**, 2000**, 13.

[2] J.T. Ritchie, J.T. Richardson and D. Luss, AIChe journal, 47, **2001,** 9, 2092.

[3] X. Tan and K. Li Ind. Eng. Res.**45, 2006**, 142.

[4] J. E. Ten Elshof, H. J. M. Bowmeester, H. Verweij, Appl. Catal. A: Gen.**,** 130, **1995**, 195.

[5] F.T. Akin, Y.S. Lin, J. Membr. Sci. 209, **2002**, 457.

[6] S. Liu, X. Tan, K. Li, R. Hughes, Catal. Rev. 43 (1–2), **2001**,147.

[7] D. Kang, S. Srinivasan, R. Rhorogood and E.Foster, **1996**, US Patent 5 516359.

[8] B. Steele, C. R. Acad. Sci. Paris, t. 1, Srie II c**., 1998**, 533.

[9] H. Tanaka, M. Misono. Solid State and Materials Science 5, **2001**,381.

[10] H. J. M. Bouwmeester and A. Burggraf, "The CRC Handbook of Solid State Electrochemistry", P. J. Gellings, H. J. M. Bouwmeester Eds. **1997**, 481.

[11] Y. Teraoka, H. M. Zhang, S. Furukawa, N. Yamazoe, Chemistry Letters **1985**, 1743.

[12] Y. Teraoka, T. Nobunaga and N. Yamazoe, Chemistry Letters, **1998**, 503.

[13] H.U. Anderson. Solid State Ionic, 52, **1992**, 33.

[14] J. Mizusaki Solid State Ionic, 52, **1992**, 79.

[15] J. Caro, H. H. Wang, C. Tablet, A. Kleinert, A. Feldhoff, T. Schiestel, M. Kilgus, P. Kölsch and S. Werth. Catal Today 118, **2006**, 128

[16] G. Ch. Kostogloudis and Ch. Ftikos, Solid state Ionics 126, **1999**,143.

[17] S.M. Murphy, D. A. Slade, K.J.Nordheden, S.M. Stagg-Williams, J. Membr. Sci. 277, **2006,** 94.

[18] H. Wang, S. Werth, T. Schiestel and J. Caro, Angew. Chem., 117, **2005**, 7066.

[19] F.A. Kröger and H.J. Vink, Relations between the concentrations of imperfections in crystalline solids, Solid State Physics, Vol. 3, F. Seitz and D. Turnbull, Eds., Academic Press, New York, **1956**, 307.

[20] X. Tan, Y. Liu and K. Li, AIChE Journal, 51, **2005,** 1991.

[21] Z. Shao, G. Xiong, H. Dong, W. Yang L. Lin, Separ., Purif. Technol, 25, **2001**, 97.

[22] P. J. Gellings and H. J. M. Bouwmeester, Catalysis Today, **58**, **2000,** 1.

[23] B. Van Hassel, A. Kawada, T. Sakai, N. Yokokawa, H. Dokiya and H.J.M. Bouwmeester, Solid state Ionics, 66, **1993**, 295.

[24] S. Liu and G. Gavalas; J. Membr. Sci. 246, **2005**, 103.

[25] U. Balachandran, J. Dusek, R. Mieville, R. Poeppel, M. Kleefish, S. Pei, T. Kobylinski, C. Udovich, A. Bose, Appl. Catal., A: G, 133, **1995**, 19.

[26] U. Balachandran, J. Dusek, R. Maiya, R. Mieville, M. Kleefish, C. Udovich, Catal Today, 36, **1997**, 265.

[27] M. Sogaard, P. Vang, M. Mogensen, J. Solid State Chem., 180, **2007**, 1489.

[28] K. Li, X. Tan and Y. Liu, J. Membr. Sci. 272, **2006**, 1.

[29] X. Tan, Y. Liu and K. Li, Eng. Chem. Res. 44, **2005**, 61.

[30] W. Zhang, J. Smit, van Sint Annaland, J. Kuipers, J. Membr. Sci. 291, **2007**, 19.

[31] S. Xu, W. J. Thomson, Ind. Eng. Res. 37, **1998,** 1290.

[32] S. Kim, Y. L. Yang, A. J. Jacobson, B. Abeles, Solid State Ionics, 106, **1998**, 189.

[33] S. Kim, Y. L. Yang, A. J. Jacobson, B. Abeles, Solid State Ionics, 121, **1999**, 31

[34] X. Tan and K. Li, AlChE J., 48, 7, **2002**, 1469.

[35] V. Karton, E. N. Naumivich and A. V. Nikolaev, J. Memb. Sci, 111, **1996**, 149.

[36] L. Qiu, T. H. Lee, L. M. Liu, Y. L. Yang and A. J. Jacobson, Solid State Ionics, 76, **1995**, 321.

[37] K. Huang and J. Goodenough, J. Electrochem. Soc., 148 (5) **2001,** E203.

[38] B. Van Hassel, A. Kawada, T. Sakai, N. Yokokawa, H. Dokiya and H.J.M. Bouwmeester, Solid State Ionics, 66, **1993**, 295.

[39] A. Thursfield and I. Metcalfe, J. Membr. Sci. 288, **2007,** 175.

[40] T. Schiestel, M. Kilgus, S.Peter, K. Caspary, H. Wang and J. Caro, J. Membr. Sci. 258, 1-2, **2005**, 1.

[41] H. Lui, Z. Pang, X. Tan, Z. Shao, J. Sunarso, R. Ding and S. Liu. Ceramic International, Ceramics International, *35*, 8, **2008**, 3201.

[42] S. Hamakawa, K. Sato, T. Inoue, m. Nishioka, K. Kobayashi and F. Mizukami, Catal. Today, 117, **2006**, 297.

[43] H. J. M. Bouwmeester, Catal. Today, 82, **2003**, 141.

[44] A. Thursfield and I. S. Metcalfe, J. Solid State Electrochem. 10, **2006**, 604.

[45] C.T. Au and H.Y. Wang. J. Catal 167, **1997**, 337.

[46] G. Sierra Gallego, C. Batiot-Dupeyrat and F. Mondragon, Dyna, 163, **2010**, 141.

[47] H. H. Wang, Y. Cong, Y. Zhu, W. Yang, React Kinet. Catal. Lett., **79, 2003**, 351.

[48] J. Caro, Chinese J. of Catal., 29, **2008**, 1169.

[49] R. Dittmeyer, J. Caro, Handbook of Heterogeneous Catalysis, Eds. G. Ertl, H. Knozinger, J. Weitkamp, **2006**.

[50] A. Thursfield, I. Metcalfe, J. Mater. Chem., 14, **2004,** 2475.

[51] S. Pei, M. S. Kleefish, T. P. Kobylinski, J. Faber, C. A. Udovich, V. Zhang-McCoy, B. Dabrowski, U. Balachandran, R. L. Mievielle, R. B. Poeppel, Catal. Lett. 30, **1995**, 201.

[52] J. E. Ten Elshof, B. A. Van Hassel, H. J. M. Bouwmeester, Catal. Today, 25, **1995**, 397.

[53] S. J. Xu, W.J. Thomson, AlChE J. 43, **1997**, 2731.

[54] J. A. Lane; S. J. Benson,D. Waller,J. A. Kilner. **Solid State Ionics**, 121, **1999**, 201.

[55] Y. Zeng, Y. S. Lin and S. L. Swartz, J. Membr. Sci. 150, **1998**, 87.

[56] G. Etchegoyen, T. Chartier, A. Julian, P. Del Gallo; J. Membr. Sci. 168, **2006**, 86.

[57] A. Kovalevsky, V. Kharton, A. Shaula, J. Frade, J. Membr. Sci. 278, **2006**, 12.

[58] A. Kleinert, A. Feldhoff, T. Schiestel, J. Caro, Catal. today, 118, **2006**, 44.

[59] S. Lee, S. K. Woo, K. S. Lee, D. K. Kim, Desalination 193, **2006**, 236.

[60] R.H.E. van Doorn[1, 1], H.J.M. Bouwmeester, A.J. Burggraaf, Solid State Ionics, 111, 3–4, **1998**, 263.

[61] S. J. Xu, W. J. Thomson. Ind. Eng. Chem. Res., 37, **1998**, 1290.

[62] H. L. Lein, K. Wiik, T. Grande, Solid State Ionics, 177, 19–25, **2006**,1587.

[63] B. Wang, B. Zydorczak, Z.T. Wu and K. Li, J. Membr. Sci. 344, **2009**, 101.

[64] D. Schlehuber; E. Wessel; L. Singheiser; T. Markus, J. Membr. Sci.351, 1-2, **2010**, 16.

[65] B. Wang; B. Zydorczak; D. Poulidi; I. S. Metcalfe; K. Li. J. Membr. Sci., 369, 1-2, **2011**, 526.

[66] S. Li, W. Jin, P. Huang, N. Xu;J. Shi, Y. S. Lin, Membr. Science 166, **2000**, 51.

[67] N. Xu, S. Li, W. Jin, J. Shi, Y. S. Lin, AlChE J. 45, 12, **1999**, 2519.

[68] X. Tan, K. Li, A. Thursfield, I. S. Metcalfe, Catal. Today 131, **2008**, 292.

[69] R. V. Franca, A. Thursfield, I. S. Metcalfe, J. Membr. Sci., 389, **2012**, 173.

[70] A. A. Yaremchenko, C. Buysse, V. Middelkoop, F. Snijkers, A. Buekenhoudt, J.R. Frade, A. V. Kovalevsky, J. Membr. Sci. 428, **2013**, 123.

[71] Y. Liu, X. Zhu, M. Li, H. Liu, Y. Cong, W. Yang, Angew. Chem. Int. Ed., 52, 11, **2013**, 3232.

[72] J.F. Shin, A. Orera, D.C. Apperley, P.R. Slater, *J. Mater. Chem.*, *21*, **2011,** 874.

[73] J.M. Porras-Vazquez, P.R. Slater, *J. Power Sources*, *209*, **2012,** 180.

[74] X.F. Zhu, H.Y. Liu, Y. Cong, W.S. Yang, *AIChE J*, *58*, **2012,** 1744.

Chapter 3.

Experimental details

3. Experimental details

This chapter describes the fundamentals of the catalyst preparation methods, module assembly, catalytic surface modification, catalytic reaction conditions and finally, the instrumental and principal fundamental of various techniques used to determine the structure, morphology and texture of the membrane.

3.1. Preparation of LSCF 6428 hollow fibre membranes

The preparation of $La_{0.6}Sr_{0.4}Co_{0.2}Fe_{0.8}O_{3-\delta}$ (LSCF6428) hollow fibre membranes is described in **appendix I; figure I.1**, according to the phase-inversion/sintering technique used by Prof. K. Li, Imperial College **[1-3]**. Briefly, the LSCF6428 powder was added carefully to a polymer solution and stirred for 48 hours. This mixture was degassed at room temperature for 30 min and then transferred to a stainless steel reservoir to make the hollow fibre precursors using a spinneret. The hollow fibre precursors were then immersed in a water bath for improving the solidification process. Finally, they were thermally treated up to 1100-1280 °C.

3.2. Description of typical oxygen permeation experiment.

Figure 3.1 is schematically represents the oxygen permeation experiments carried out in this work using LSCF6428 hollow fibre membrane reactor.

The hollow fibre membrane reactors for oxygen permeation measurements were assembled with four gas-tight LSCF hollow fibre membranes, further details can be seen in section 3.5. The membrane reactor was placed inside a tubular furnace and the temperature at the centre of the reactor was monitored. The chromatographs A and B were calibrated using Air and a single gas standard mixture consisting of 2% oxygen and 2% nitrogen balance gas helium. The air flow was connected into the shell side while the helium gas flow sweeps into the

lumen side of the reactor. The gas flow rates were controlled using digitals flow meters. The gas flow rates were independently monitored at the lumen and shell side outlets with a digital flow meter at the GC gas sampling valve outlet.

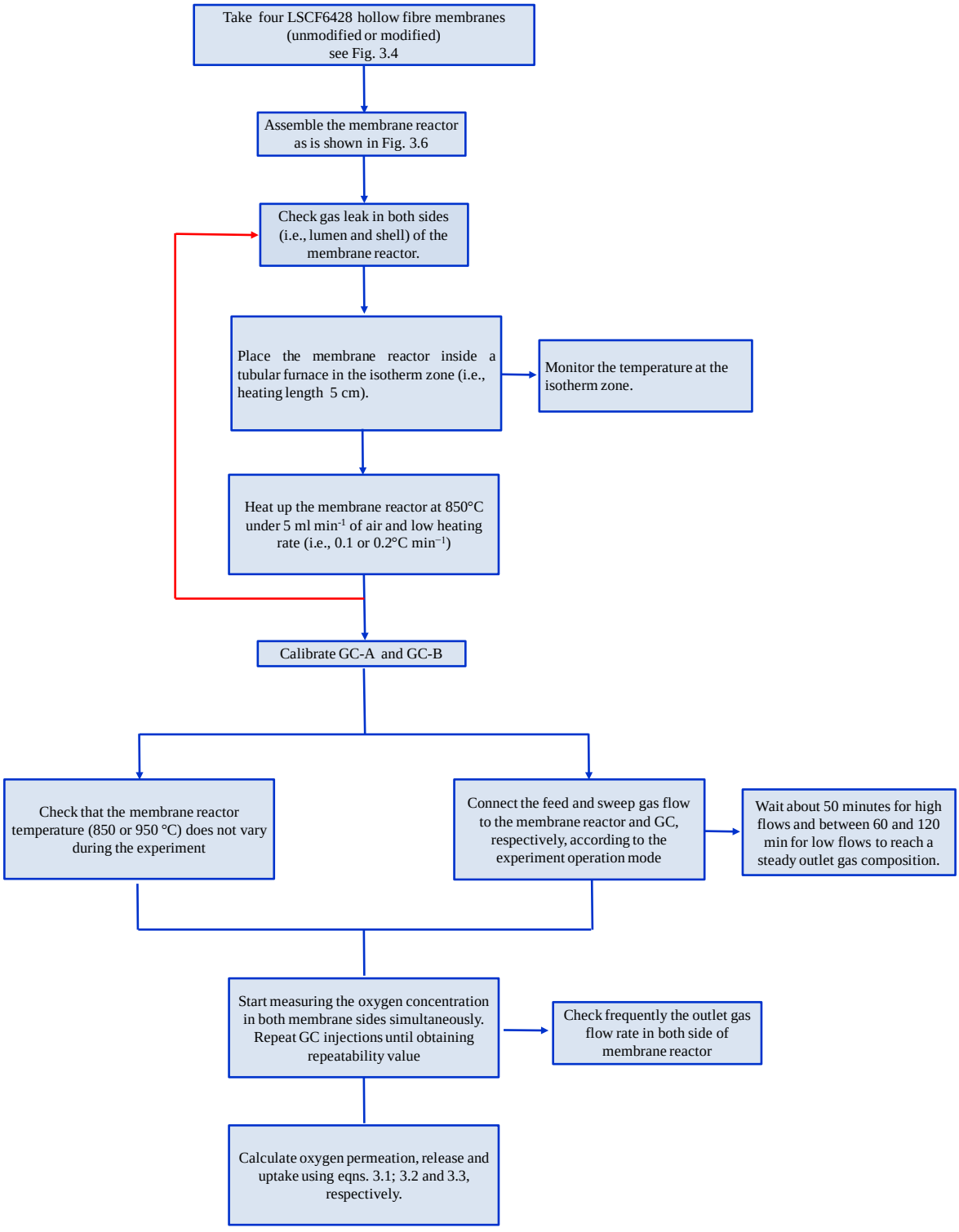

Figure 3.1 Schematic representation of the steps carried out during the oxygen permeation experiments

The integrity of the module seals and membranes was continually monitored following the nitrogen content in the product stream from the lumen outlet. The total GC analysis time was 5 minutes. The measurements of outlet gas compositions during oxygen permeation experiments were made for period between 50 and 120 min, after so, a temperature change or gas supply rate change was produced. At least six analyses were performed for each experimental condition.

3.3. Catalyst preparation

3.3.1. Cobalt oxide catalyst

1 g of cobalt oxide 99.7% (Alfa Aesar) was mixed in 20 ml of 98% ethylene glycol. This paste was maintained at 75°C and stirred continuously until homogeneous. The average surface loading of the catalytically modified for hollow fibres was approximately 10 mg cm^{-2}, see **appendix I, section I.4,** and a layer thickness of 29 μm ± 2, (**figure 3.2**).

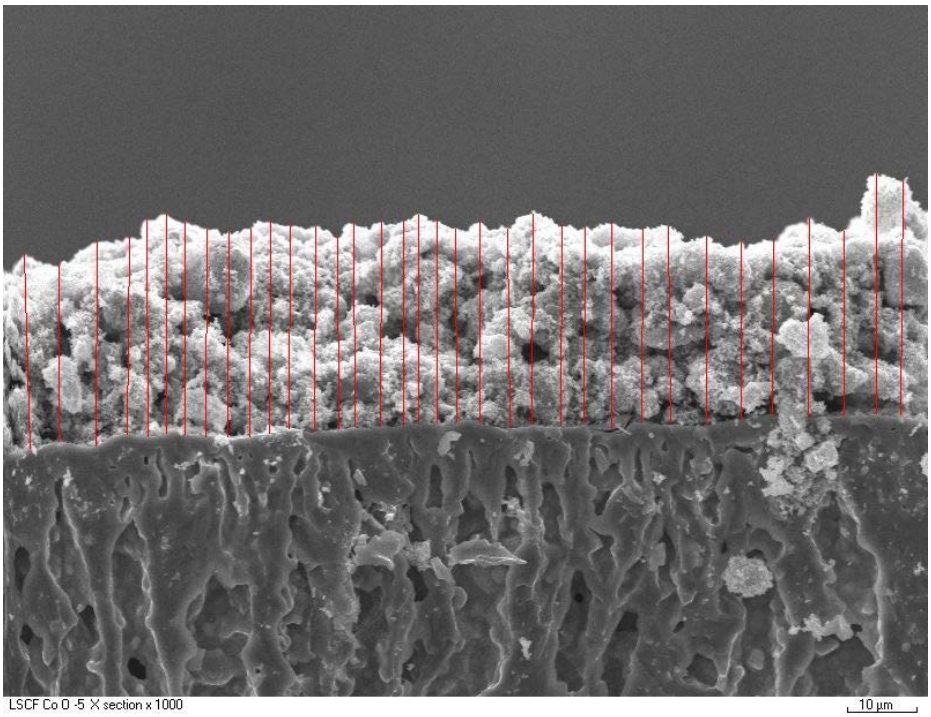

Figure 3.2 SEM images of the thickness of cobalt oxide catalyst before reaction

3.3.2. 5 wt % Nickel nanopowder supported on LSCF6428

Nickel nanopowder of average particle size 90 nm (Sigma-Aldrich) was used. The nanopowder was weighed out (0.05 g) and mixed with a 0.95 g of LSCF6428 powder to obtain 5 wt% Ni dispersed on LSCF6428. The mixture was stirred in ethylene glycol for 24 hours to obtain an even paste, the liquid has evaporated and the resultant powder was ground. The average surface loading of the catalytically modified hollow fibres was approximately 57 mg cm^{-2}, see **appendix I, section I.4** and the layer thickness was 26 μm ± 2, (**figure 3.3**).

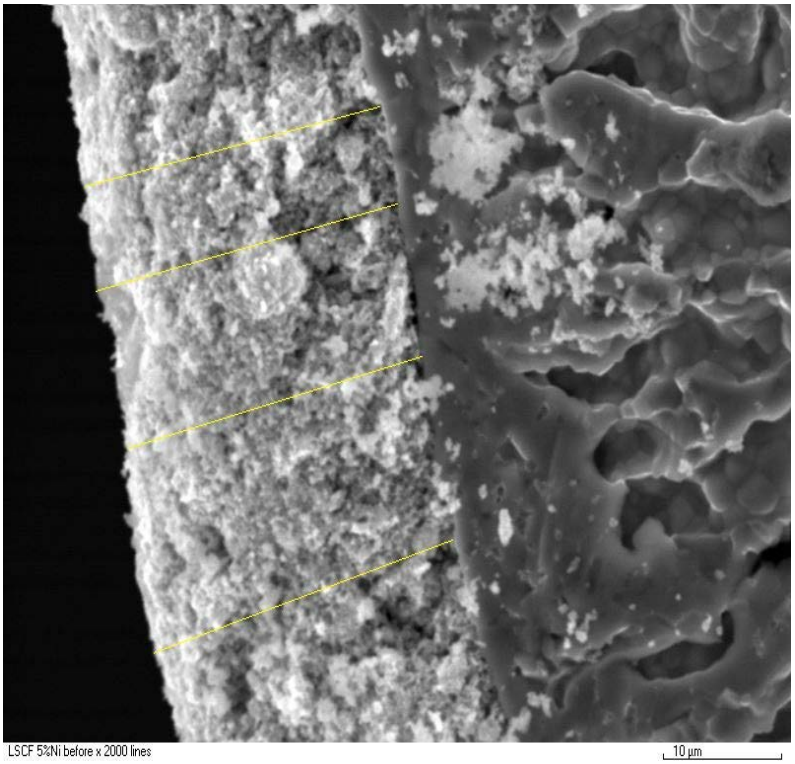

Figure 3.3 SEM images of the thickness of 5 wt % Ni-LSCF6428 catalyst before reaction.

3.4. Catalytic modification of the membrane external surface

Four hollow fibres were coated on the shell side surface with each catalyst in slurry form in ethylene glycol. This was applied to the shell-side surface of the central 5 cm of each hollow fibre using a small fine brush as shown in **figure 3.4**. The membranes were thermally

treated to remove the organic resin using a programmed temperature ramp of 1 °C min^{-1} from room temperature up to 400°C and held for 1 hour. Then the temperature was increased up to 850°C at 1°C min^{-1} and held for 1 hour. Subsequently, the membrane reactor was cooled down to 25°C at 1°C min^{-1}.

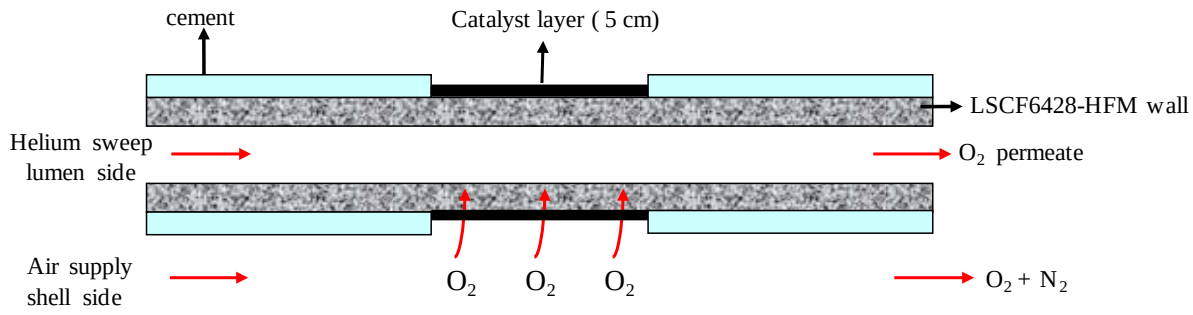

Figure 3.4 Schematic representation of a single LSCF6428 hollow fibre membrane showing the catalyst-coated zone.

3.5. Oxygen permeation module assembly

The reactor was assembled using four parallel hollow fibre membranes (HFM) for increasing the mechanical resistance and the surface area to small volume ratio, which gives more separation area per unit volume of membrane element [**4**] and separation efficiency. However, the membranes operate at high temperatures (800–900 °C) and a large energy penalty is associated with heating a high air volume.

These HFM are engineered into a pair MACOR tubes in order to create a hollow fibre (HF) bundle. Both ends of the bundle were attached to the gas inlet and outlet by a length of flexible silicone tubing in order to accommodate the thermal expansion of the membranes, see **figure 3.5.**

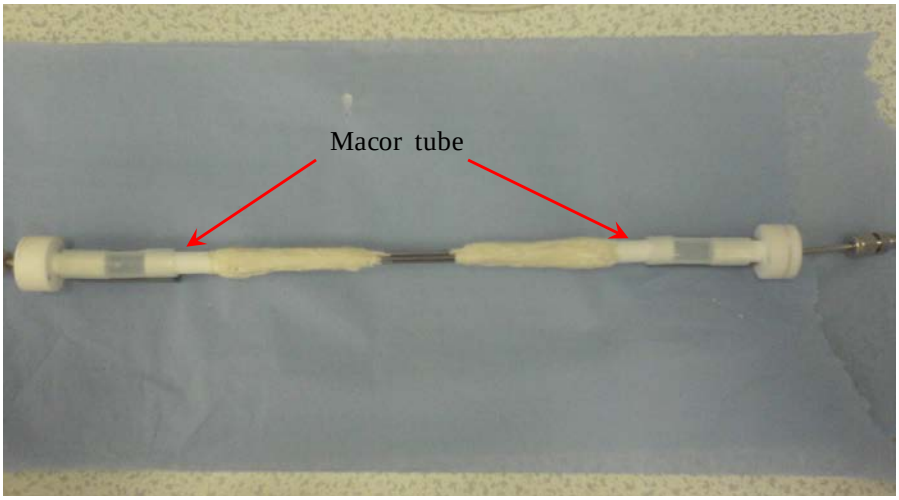

Figure 3.5 Photo of a four LSCF6428 hollow fibre membrane after assembly.

The temperature was controlled by a furnace (Vecstar Furnaces, UK) of total length 15 cm equipped with an eight-segment Eurothermcontroller. The heated zone (13 cm in length) had a central linear heating zone of 5 cm. The sealant used was a commercial high temperature water-based glass-ceramic ((i.e., Li_2O x Al_2O_3 x $nSiO_2$ or LAS-System) for alkaline silicate glass solid solution, Heavy Grade Fortafix, UK [**5**].

The same sealant was also used to partially cover the four hollow fibre membranes so that only the centre zone (5 cm) was uncovered, as shown in **figure 3.6**, which coincided with the isothermal zone of the furnace. A heating or cooling rate of 0.2°C min^{-1} was used throughout this investigation to avoid that the membranes undergo fracture due to thermal expansion.

The HF bundle was housed inside using a quartz tube with 99.995 % of SiO_2 [**5**], which have internal and external diameters of 2.8 and 3.0 cm, respectively. All experiments were carried out under atmospheric pressure on both sides of the membrane at 850˚C and 900˚C. All gas flows are quoted at standard temperature and pressure (STP). The internal volume of the fibres is referred to as the lumen side (helium sweep-side), and the outside of the hollow fibres is referred to as the shell side (air supply-side). A schematic representation of the hollow fibre membrane reactor is given in **figure 3.6**.

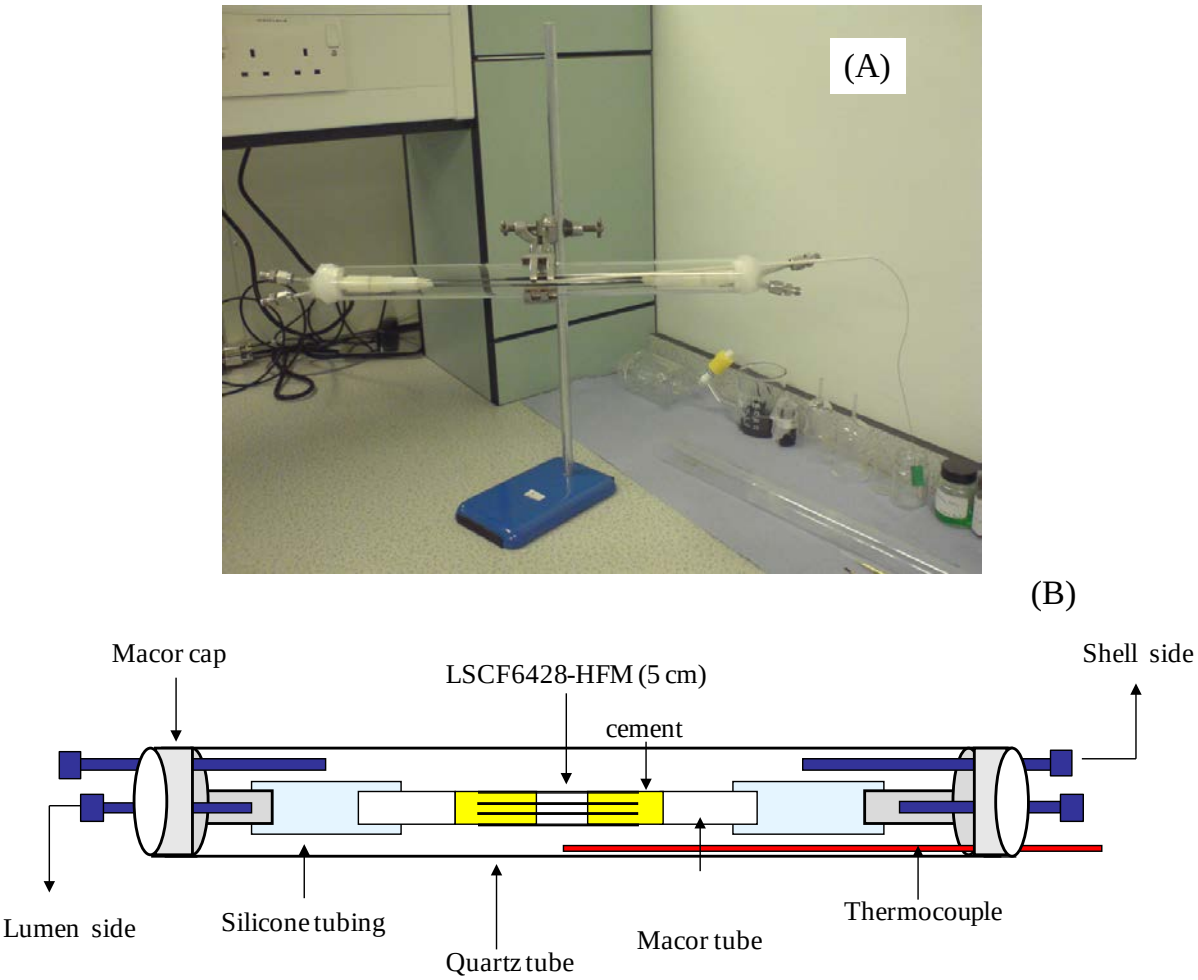

Figure 3.6 Photo and diagram of the LSCF6428 hollow fibre membrane reactor module

3.6. Apparatus and reactor module assembly

The system consisted of a gas supply, gas flow controller, hollow fibre membrane reactor module, furnace and gas chromatographs (**figure 3.7**). All experiments were carried out at standard pressure (i.e. 1 atm) on both sides of the membrane. The gas supplies to the reactor module in all experiments were controlled by Chell Hasting mass flow controllers.

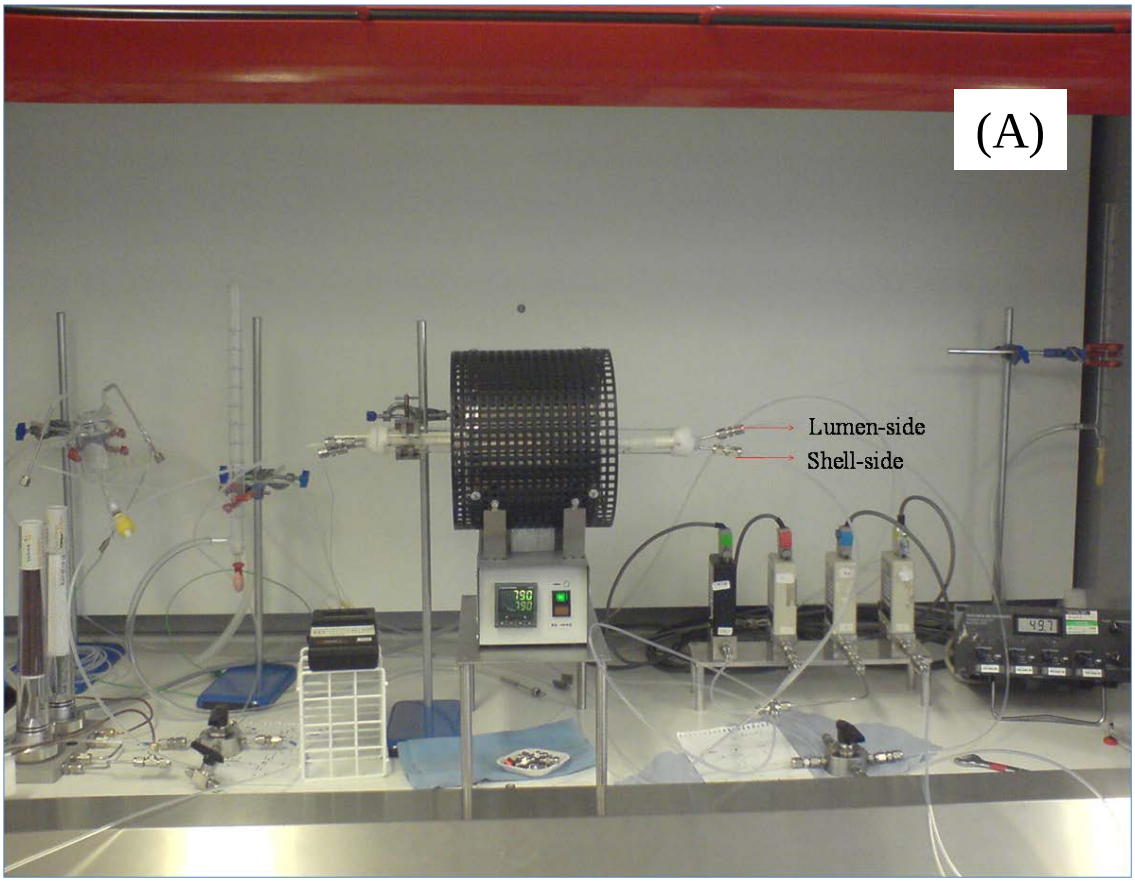

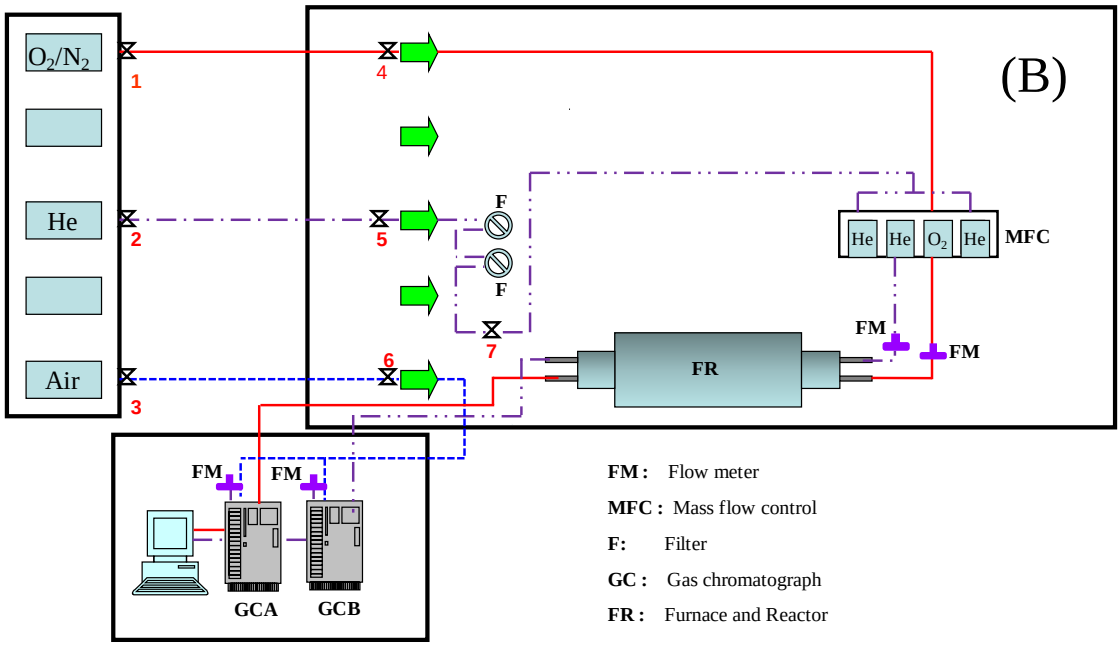

Figure 3.7 Photo and diagram of the rig of oxygen permeation and catalytic studies

3.7. Gas Chromatography calibration

Two Varian 3900 chromatographs were used (denoted GCA and GCB) each equipped with a thermal conductivity detector (TCD) and Molecular sieve 5A column. Helium was used as carrier gas at 20 ml min^{-1}, see **appendix I, figure I.2**.

The GCB calibration was performed using a gas mixture containing 2% oxygen and 2% nitrogen balance gas helium. Calibration of GCA was carried out using air. All calibrations were carried out at least six times to test reproducibility and the maximum relative error was below 5%, see **appendix I, figure I.3**

3.8. Furnace

The furnace (Vecstar Furnaces, UK) equipped with an eight-segment Eurotherm controller had a total length of 15 cm. The heated zone (13 cm in length) had a central linear heated zone of 5 cm, which showed a drop of 30°C from its centre point over the operating temperature range of concern. The temperature profile of the reactor module was determined by repositioning the internal thermocouple in 0.5 cm steps and leaving for 15 min at each position to ensure that ensure thermal equilibrium was reached and the reading was accurate.

3.8.1 Temperature profiles of the hollow fibre reactor

The internal temperature profile of the reactor module is given in **figure 3.8**., for set point temperatures of 850°C. Both temperature profiles showed similar behaviour or good repeatability of the results. It can be observed that a maximum temperature of 850˚C is reached at the centre of the hollow fibre reactor. This value was fairly constant over the central 5 cm. Further away from this zone the temperature rapidly decreases. A similar behaviour was observed on the opposite side of the membrane. It is clearly noted that the central region of length 5 - 6 cm presents a fairly constant temperature of 850˚C (the

isothermal zone). Hence, this temperature zone was selected for depositing a layer of catalyst over four parallel hollow fibre membranes to perform the oxygen permeation studies **[2, 7]**.

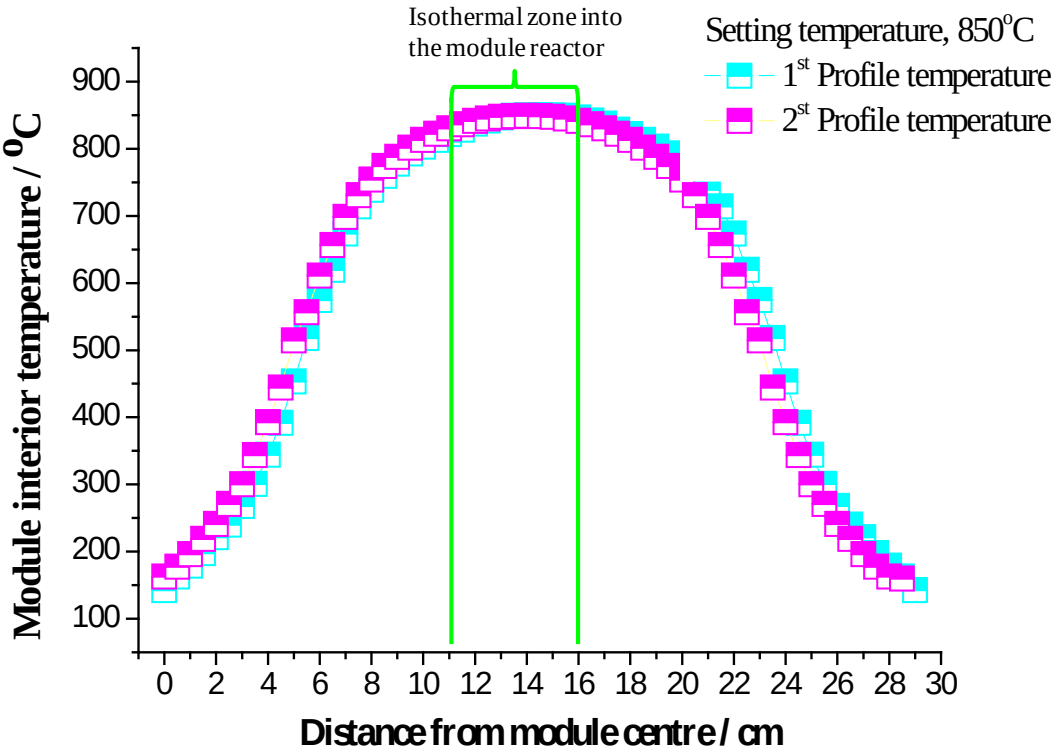

Figure 3.8 Internal temperature profiles of the membrane module reactor for set point temperatures of 850°C.

3.9. Models for oxygen flux measurements in a hollow fibre membrane reactor

The measurements were carried out using three modes of operation which are illustrated below in **figure 3.9**.

Mode 1: In this operating mode the air feed is on the lumen side of the hollow fibre membrane, while helium is co-current sweep into the shell side of the module (denoted by ALHS–air-lumen, helium-shell).

Mode 2: This operating mode the air is introduced into the shell side of the hollow fibre membrane reactor, whereas helium flows is co-current in lumen side of the hollow fibre membrane reactor (denoted by ASHL–air-shell, helium-lumen).

Mode 3: In this operating mode the air feed on the shell side of the module, while helium is fed into the lumen side membrane in opposite direction of the feed air inlet.

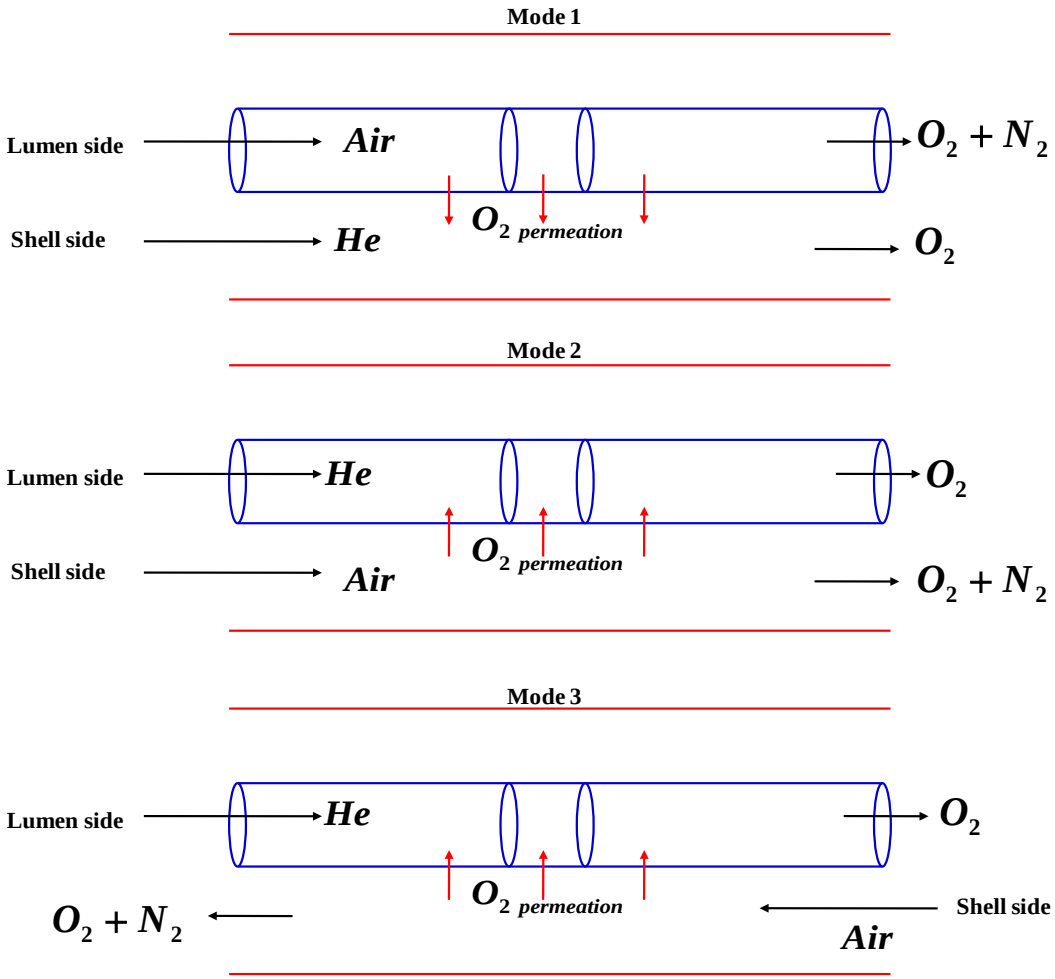

Figure 3.9 Operating modes of the hollow fibre membrane reactor for oxygen permeation

The system was operated at 850°C and 900°C and on-line gas analysis was simultaneously carried out on the exit gases from both sides of the membrane. Synthetic air containing ca 20% oxygen (balance nitrogen) was used and the flow rate was varied from 5 to 150 ml (STP) min^{-1}. High purity helium flow (99.999 % BOC) was fed at the inlet from 10 to 200

ml (STP) min^{-1}. A delay time of 50 minutes for high flows and 1 to 2 hours for low flows was required for the system to reach a steady outlet composition (defined as less than a 5% change in oxygen partial pressure on both sides over thirty minutes).

An experiment was carried out in order to calculate the oxygen incorporation **($\Delta\delta$)** in the membranes using mode 2 (ASHL) with simultaneous analysis of both sides. The air flow rate used was 75 ml min^{-1} and helium flow was 50 ml min^{-1}. The GC analysis was carried out every four hours. Prior to the experiments the membranes were annealed for approximately 500 hours under air flow (5 ml min^{-1}) on both sides at 850 °C. The difference between the oxygen release obtained in lumen side and oxygen uptake measurement in shell side during the experiment gives the oxygen incorporated into LSCF6428 structure and the steady state was reach when both measurements (i.e. oxygen release and oxygen uptake) converged.

3.10. Determination of the oxygen permeation, oxygen release and oxygen uptake, when operated in mode 2

Oxygen permeation, oxygen release, oxygen uptake were calculated using mode 2 is shown in **figure 3.10** and eqns. are (3.1), (3.2) and (3.3) respectively.

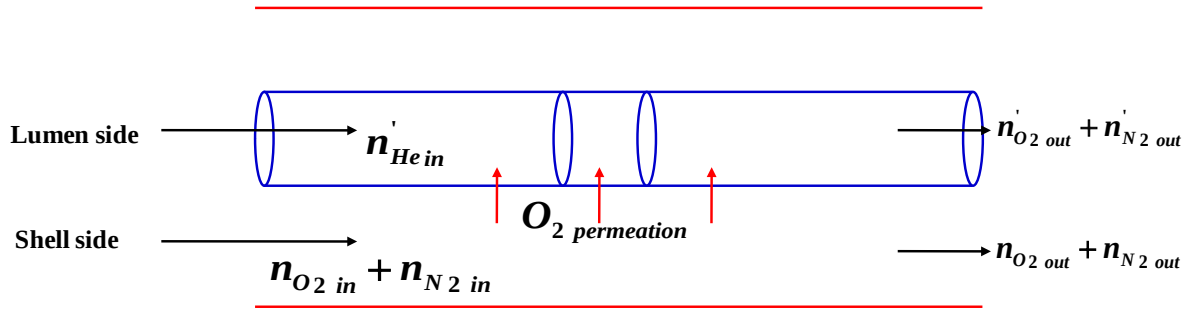

Figure 3.10 Membrane reactor with nomenclature and showing the elements (i.e. oxygen, nitrogen and helium) used in the equations for calculate oxygen permeation, oxygen release, oxygen uptake.

$$O_{2\ permeation} = \left(n'_{O_2\ out} - \frac{n'_{N_2\ out}}{4} \right) \left(\frac{n'_{He\ in}}{S_A} \right) \quad (3.1)$$

$$O_{2\ release} = n'_{He\ in} \left(n'_{O_2\ out} - \frac{n'_{N_2\ out}}{4} \right) \quad (3.2)$$

$$O_{2\ uptake} = n_{O_2\ in} - \left(n_{O_2\ out} + \frac{n'_{N_2\ out}}{4} \right) \quad (3.3)$$

Where $O_{2\ permeation}$ is the oxygen permeation into the lumen side (µmol cm^{-2} s^{-1}), $O_{2\ uptake}$ is the oxygen uptake from the shell side (µmol s^{-1}), $O_{2\ release}$ is the oxygen release into the lumen side (µmol s^{-1}), $n_{O_2\ in}$ is the molar flow of the oxygen at the inlet in the shell side (µmol s^{-1}), $n_{O_2\ out}$ is the molar flow of oxygen outlet in the shell side (µmol s^{-1}), $n'_{O_2\ out}$ is the molar flow of the oxygen outlet in the lumen side (µmol s^{-1}). The nitrogen can be also found in the effluents or permeated side due to pores, pinholes or cracks. The molar flow of the nitrogen outlet in the lumen side (µmol s^{-1}) is $n'_{N_2\ out}$. The correction term for gas phase oxygen transport through pores, pinholes or cracks of the membrane is $n'_{N_2\ out} / 4$ considering that the composition of air is approximately 20 % of oxygen and 80% nitrogen.

The term $n'_{He\ in}$ is the molar flow of the helium inlet (µmol s^{-1}), the factor to convert ml to molar volume is 1/22400 (1 mole is equivalent to 22400 ml at STP), 1/60 is a factor to convert the rate from minutes to seconds and S_A is the superficial active membrane area for oxygen permeation which can be approximated by

$$S_A = \frac{2\pi(r_0 - r_{in})}{\ln(r_o / r_{in})} nl \quad (3.4)$$

Where r_0 and r_i are the outer and inner radius of a typical hollow fibre, n is the number of hollow fibres and l is the active working length. The radius r_0 and r_{in} were typically 0.07

and 0.05 cm, respectively. Assuming that only the central linear heating zone of the furnace is used (l = 5 cm) an active membrane area of ca 7.6 cm^2 provided by the four hollow fibres is obtained.

3.10.1. Rate of oxygen incorporation ($\Delta\delta$)

The rate of incorporated oxygen is determined using the following equation:

$$\Delta\delta = \frac{2\left(O_{2\ uptake} - O_{2\ release}\right)}{n_{LSCF_{6428}}} \tag{3.5}$$

Where $\Delta\delta$ is the rate of oxygen incorporated into the membrane per unit time measured in h^{-1} and is the subtraction of the oxygen uptake $(O_{2\ uptake})$ from equation (1) and oxygen release $(O_{2\ release})$ from equation (2), divided by the molecular weight of LSCF6428 $(n_{LSCF_{6428}})$.

3.11. Calculation of the oxygen permeation rate constant (k)

In order to get insight into the oxygen permeation mechanism and also determine the overall apparent rate constant of the oxygen flux a mathematical model was development based on material flow balance. Wagner equation assumes that oxygen bulk diffusion is the rate limiting of oxygen flux across an ionic-conducting membrane [**8**]. However, Bouwmeester *et al*. **[9, 10**] and Dou *et al*. [**11**] reported that oxygen ion surface exchange kinetics may exert partial or dominant control on oxygen permeation under certain experimental conditions. Also, Lin *et al*. [**12**], Bouwmeester *et al*. [**9**] and Ling *et al*. [**13**] have correlated the oxygen permeation rate to directly measurable variables such as the membrane thickness and the oxygen partial pressure at both sides. Xu and Thompson [**14**], on the other hand, developed a model based on the distribution of total oxygen permeation resistances; which allow them to distinguish the various steps in the oxygen permeation mechanism. Thus, there is a high

motivation to simplify the overall oxygen permeation rate constant model over LSCF6428 membrane based on material flow balance and considering mass transfer of gaseous oxygen from the gas stream to the membrane surface (high pressure side) and the mass transfer of oxygen from the membrane surface to the gas stream (low pressure side).

3.11.1. Co-current flow operation

The model used to calculate the rate constant **(k)** for oxygen permeation using Mode 2 is shown schematically in **figure 3.11**.

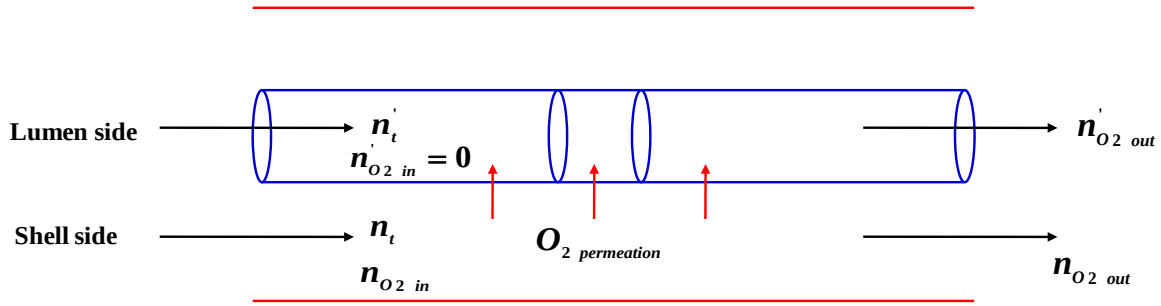

Figure 3.11 Membrane reactor with nomenclature and showing an element used in the formulation of the material balance in Mode 2 operation.

In this model, a plug flow is assumed on both sides of membrane (i.e. lumen and shell side). The reactants are fed into the reactor at the inlet, the reaction takes place within the reactor as the reacting perfect mixing across section and the products are removed from the reactor at the outlet, see **figure 3.12**.

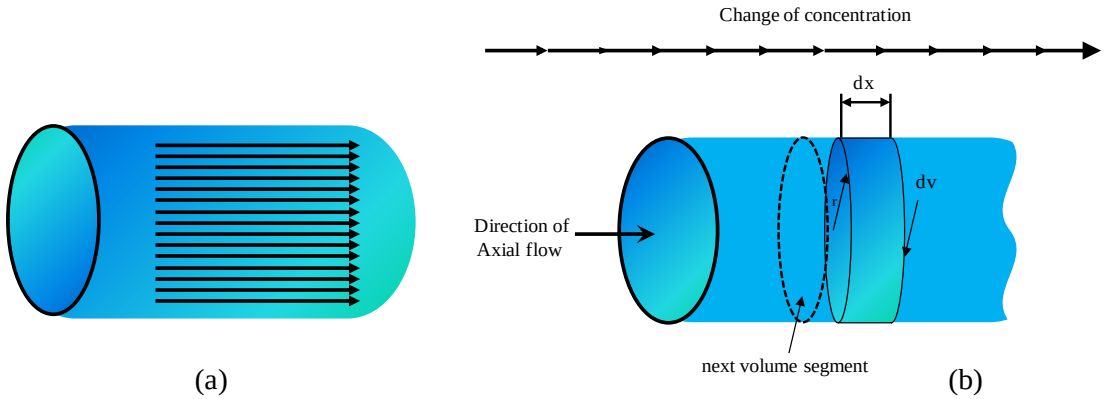

Figure 3.12 Schematic representation of plug flow reactor (a) and differential elements (b) **[6].**

In an ideal plug flow reactor, the flow rates are uniform over cross-section and the axial mixing is negligible due to either diffusion or convection. The plug flow is obtained when there is a good radial mixing, which is achieved at high flow rates (turbulent flow, $R_e > 10^4$) and when axial mixing may be neglected (i.e., $\mathbf{Reactor\ lenght} / \mathbf{Reactor\ diameter} \geq \mathbf{50}$) [**15**]. In this model the oxygen flux is related to molar flows if plug flow is assumed

Lumen side:

Input= output - loss through of membrane

$$n'_{O2} = n'_{O_2} + \partial n'_{O_2} - j'_{O_2}\partial A \tag{3.6}$$

$$j'_{O_2} = \frac{\partial n'_{O_2}}{\partial A} \tag{3.7}$$

Shell side:

Input= output + loss through of membrane

$$n_{O_{2\ in}} = n_{O_2} + \partial n_{O_2} + j_{O_2}\partial A \tag{3.8}$$

If $n_{O_{2\ in}} = n_{O_2}$ then

$$jo_2 = -\frac{\partial n_{O2}}{\partial A} \tag{3.9}$$

Oxygen permeation is also given by

$$jo_2 = k\left(P_{O_2} - P'_{O_2}\right) \tag{3.10}$$

The steady oxygen flux is assumed to be directly related to the partial pressure of oxygen difference across the membrane. P_{O_2} and P'_{O_2} are the partial pressure of oxygen in the shell and lumen sides, respectively.

$$j_{O_2} = j'_{O_2} = k\left(P_{O_2} - P'_{O_2}\right) \tag{3.11}$$

For gas, the partial pressure is $P_{O_2} = x_0 P$ (3.12)

And molar fraction is $x_0 = \frac{n_{O_2}}{n_t}$ (3.13)

Substituting in eqn. (3.11), the eqn. (3.13), it is obtained

$$j_{O_2} = j'_{O_2} = k\left(\frac{n_{O_2}}{n_t} P - \frac{n'_{O_2}}{n'_t} P'\right) \tag{3.14}$$

$P = P'$, then P is constant

Eqn. (3.14) can be rewritten as:

$$j_{O_2} = j'_{O_2} = kP\left(\frac{n_{O_2}}{n_t} - \frac{n'_{O_2}}{n'_t}\right) \tag{3.15}$$

Remember the eqn. (3.9) and replaced in the eqn. (3.15)

$$-\frac{\partial n_{O_2}}{\partial A} = \frac{\partial n'_{O_2}}{\partial A} = k\,P\left(\frac{n_{O_2}}{n_t} - \frac{n'_{O_2}}{n'_t}\right) \tag{3.16}$$

Where n_t is the total molar flow rate in the shell side, n'_t is the total molar flow rate in the lumen-side and A is the area of the membrane (cm^2).

The overall oxygen balance is:

$$n_{O_2} + n'_{O_2} = n_{O_2\,in} + n'_{O_2\,in} \tag{3.17}$$

If $n'_{O_2 in} = 0$, therefore the eqn.(3.17) reduces to

$$n_{O_2} + n'_{O_2} = n_{O_2\,in} \tag{3.18}$$

Dividing by n'_t eqn. (3.18) gives eqn. (3.19)

$$\frac{n'_{O_2}}{n'_t} = \frac{n_{O_2\,in}}{n'_t} - \frac{n_{O_2}}{n'_t} \tag{3.19}$$

Substituting eqn. (3.19) in eqn. (3.16), it is obtained

$$-\frac{\partial n_{O_2}}{\partial A} = kP\left(\frac{n_{O_2}}{n_t} - \frac{n_{O_2 in} - n_{O_2}}{n'_t}\right) \tag{3.20}$$

$$-\frac{\partial n_{O_2}}{\partial A} = kP\left(-\frac{n_{O_2 in}}{n'_t} + \frac{n'_t n_{O_2} + n_t n_{O_2}}{n_t n'_t}\right) \tag{3.21}$$

Integrating eqn. (3.21)

$$\int \frac{dn_{O_2}}{-\frac{n_{O_2 in}}{n'_t} + \frac{n'_t n_{O_2} + n_t n_{O_2}}{n_t n'_t}} = -kP\int dA \tag{3.22}$$

Resolving the integral,

$$\frac{n_t\, n'_t}{n'_t + n_t} \ln\left[\frac{n_{O_2 out}}{n_{O_2\,in}}\left(1 + \frac{n_t}{n'_t}\right) - \frac{n_t}{n'_t}\right] = -\,k\,P\,A \tag{3.23}$$

The rate constant (k) was determined by plotting

$$\frac{n'_t}{n'_t + n_t} \ln\left[\frac{n_{O_2\,out}}{n_{O_2 in}}\left(1 + \frac{n_t}{n'_t}\right) - \frac{n_t}{n'_t}\right] \quad vs. \quad \frac{1}{n_t} \tag{3.24}$$

A straight line was obtained; with slope (m) is given by

$$m = k\ P\ A \tag{3.25}$$

From eqn. (3.25), the rate constant was obtained

$$k = \frac{m\ (mol * \sec^{-1})}{P\ A} \tag{3.26}$$

3.11.2. Counter current flow operation

The model used to calculate the rate constant (k) using mode 3 is indicated in the **figure 3.13**.

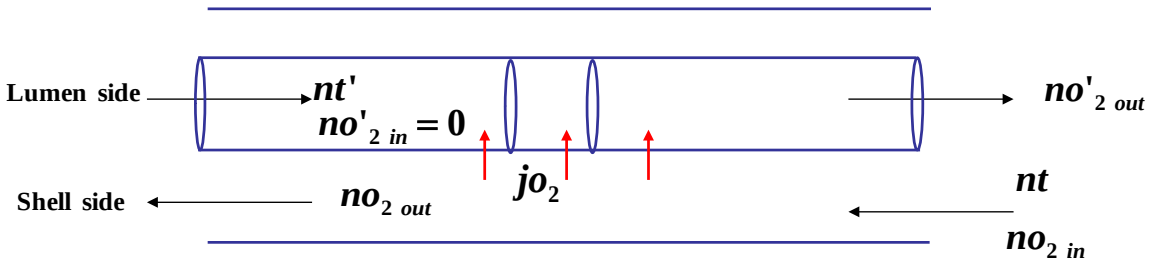

Figure 3.13 Membrane reactor with nomenclature and showing an element used in the formulation of the material balance in mode 3 operation

Oxygen permeation is related to molar flows if plug flow is assumed by

Lumen side:

$$j'_{O_2} = \frac{\partial n'_{O_2}}{\partial A} \tag{3.27}$$

Shell side:

$$j_{O_2} = -\frac{\partial n_{O_2}}{\partial A} \tag{3.28}$$

The steady state oxygen permeation is directly related to the oxygen partial pressure difference across the membrane. P_{O_2} and P'_{O_2} are the partial pressure of oxygen in the shell and lumen sides respectively

$$j_{O_2} = j'_{O_2} = k\left(P_{O_2} - P'_{O_2}\right) \tag{3.29}$$

Therefore

$$\frac{\partial n_{O_2}}{\partial A} = \frac{\partial n'_{O_2}}{\partial A} = k\,P\left(\frac{n_{O_2}}{n_t} - \frac{n'_{O_2}}{n'_t}\right) \tag{3.30}$$

Overall oxygen balance is:

$$n'_{O_2 in} + n_{O_2} = n_{O_2 out} + n'_{O_2} \tag{3.31}$$

If $no'_{2in} = 0$ and dividing by n_t therefore the eqn. (3.31) reduces to

$$\frac{n_{O_2}}{n_t} = \frac{n_{O_2 out}}{n_t} + \frac{n'_{O_2}}{n_t} \tag{3.32}$$

Substituting the eqn. (3.32) in eqn. (3.30) it can be obtained

$$\frac{\partial n'_{O_2}}{\partial A} = k\ P\left[\left(\frac{n_{O_2 out}}{n_t} + \frac{n'_{O_2}}{n_t}\right) - \frac{n'_{O_2}}{n'_t}\right] \tag{3.33}$$

Integrating eqn. (3.33)

$$\int \frac{dn'_{O_2}}{\frac{n_{O_2 out}}{n_t} + \left(\frac{n'_t - n_t}{n_t n'_t}\right) n'_{O_2}} = k\ P \int dA \tag{3.34}$$

Resolving the integral (3.34)

$$\frac{n_t n'_t}{n'_t - n_t} \ln\left[1 + \frac{n'_{O_2 out}}{n_{O_2 out}}\left(1 - \frac{n_t}{n'_t}\right)\right] = k\ P\ A \tag{3.35}$$

The rate constant (k) was found by plotting

$$\frac{n'_t}{n'_t - n_t} \ln\left[1 + \frac{n'_{O_2\ out}}{n_{O_2\ out}}\left(1 - \frac{n_t}{n'_t}\right)\right] vs.\ \ \frac{1}{n_t} \tag{3.34}$$

The slope of the resulting line corresponds to:

$$m = k\ P\ A \tag{3.35}$$

From eqn. (3.35), it the rate constant was obtained

$$k = \frac{m\ (mol * \sec^{-1})}{P\ A} \qquad (3.36)$$

3.12. Partial oxidation of methane (POM) in catalytic hollow fibre membrane reactor

The catalytic hollow fibre membrane reactors for the POM experiments were assembled in the same way as that for the oxygen permeation experiments as described above in section 3.5 (**figure 3.6**). The experimental setup for the POM experiments is shown in **figure 3.14** with the lumen side helium sweep replaced with air and shell side methane supply.

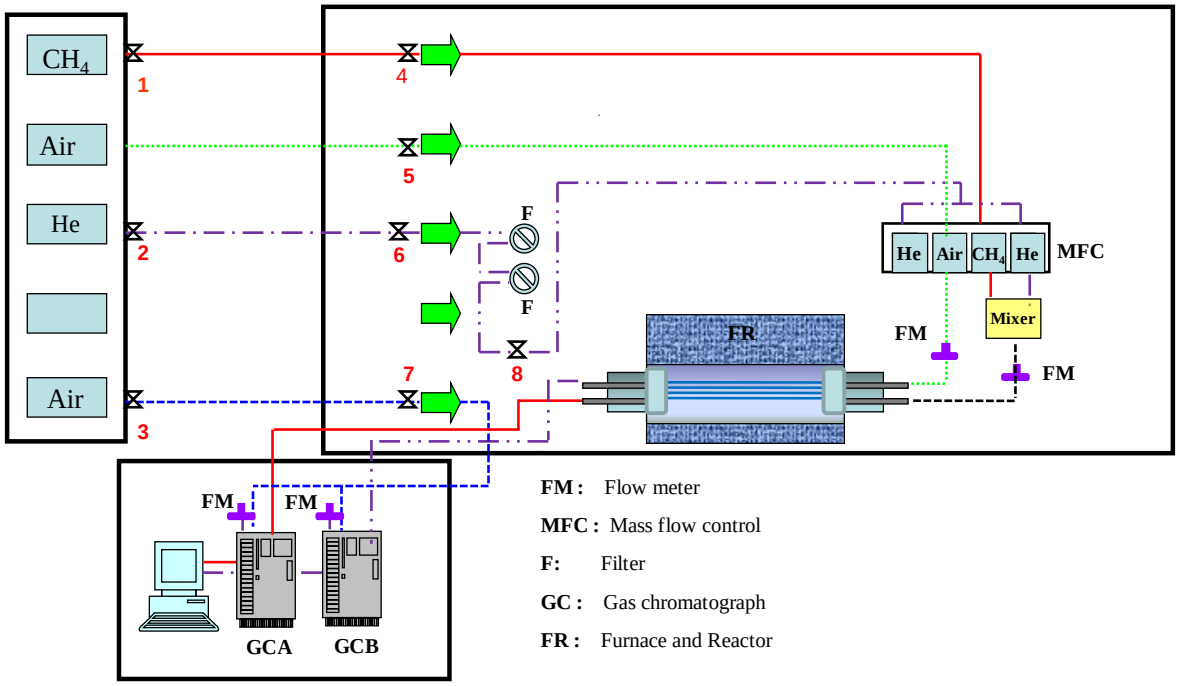

Figure 3.14 Schematic diagrams of the apparatus for partial methane oxidation and catalytic studies

10% Methane in helium was diluted with 99.99 % helium to obtain a composition of 4 % methane. This mixture was fed at 25 ml (STP) min^{-1} to the shell side of the reactor, while air or 2% O_2/He with a flow rate 25 ml (STP) min^{-1} supply were introduced co-currently into the lumen side. The reaction temperature was 850 °C. The products were analysed on-line with two Varian 3900 chromatographs (GCA and GCB), which are equipped with a thermal

conductivity detector (TCD) and Shin Carbon ST Micropaked column for GCB and Molecular sieve 5A column for GCA. Helium was used as carrier gas and set to 20 ml min^{-1}. GCB calibration was performed using a gas mixture containing 2% hydrogen, 0.5% oxygen, 2% nitrogen, 2% carbon monoxide, 2% methane, 2% carbon dioxide, 2% ethylene and 2% ethane, balance helium **(appendix I, figure I.4**). The temperature-programmed condition for the Shin carbon ST Micropaked column is given in **figure 3.15**. A pre-conditioned time of 10 min to stabilize the column was used. GCA calibration was performed using synthetic air containing ca. 20 % oxygen (balance nitrogen).

All calibrations were carried out at least eight times to test repeatability and the maximum relative error was below 5% in all cases. Concentrations of these species were determined by calibrating against the standard gases of all the product species. Both chromatographs were calibrated at least once over a 14 day period.

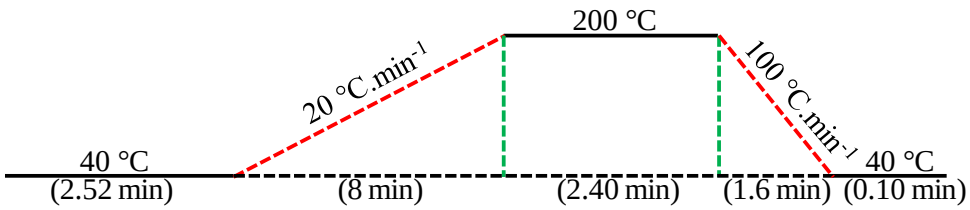

Figure 3.15 Temperature programme required for the Shin carbon ST Micropaked column of the GCB.

The oxygen permeation flux $(O_{2\ permeation})$ was calculated from oxygen atoms of all the oxygen containing products (eqn.3.28), except the water, which was calculated from a hydrogen balance on the shell side, assuming that hydrogen was not accumulated in the membrane reactor. The conversion of methane (X_{CH_4}) was determined from eqn. (3.39)

$$O_{2\ permeation} = (n_{O_{2\ out}} + \frac{1}{2} n_{CO\ out} + n_{CO_2\ out} + \frac{1}{2} n_{H_2O}) \times 1/S_A \qquad (3.37)$$

$$H_2O = 2(n_{CH_4\ inlet} - n_{CH_4\ out}) - (2(n_{C_2H_4\ out}) + 3(n_{C_2H_6\ out})) \quad (3.38)$$

$$X_{CH_4} = \frac{n_{CH_4\ inlet} - n_{CH_4\ outlet}}{n_{CH_4\ inlet}} \times 100 \quad (3.39)$$

Selectivity of each product was calculated using the following equations:

$$S_{CO} = \frac{n_{CO\ out}}{n_{CO} + n_{H_2} + n_{CO_2} + 2(n_{C_2H_4}) + 2(n_{C_2H_6})} \times 100 \quad (3.40)$$

$$S_{CO_2} = \frac{n_{CO_2\ out}}{n_{CO} + n_{H_2} + n_{CO_2} + 2(n_{C_2H_4}) + 2(n_{C_2H_6})} \times 100 \quad (3.41)$$

$$S_{C_2H_4} = \frac{2(n_{C_2H_4 out})}{n_{CO} + n_{H_2} + n_{CO_2} + 2(n_{C_2H_4}) + 2(n_{C_2H_6})} \times 100 \quad (3.42)$$

$$S_{C_2H_6} = \frac{2(n_{C_2H_6\ out})}{n_{CO} + n_{H_2} + n_{CO_2} + 2(n_{C_2H_4}) + 2(n_{C_2H_6})} \times 100 \quad (3.43)$$

$$S_{H_2} = \frac{1}{2} \times \frac{n_{H_2\ out}}{n_{CO} + n_{H_2} + n_{CO_2} + 2(n_{C_2H_4}) + 3(n_{C_2H_6})} \times 100 \quad (3.44)$$

The carbon balance was calculated from the following relation:

$$Carbon\ balance = \frac{n_{CO} + n_{CO_2} + 2(n_{C_2H_4}) + 2(n_{C_2H_6})}{n_{CH_4\ inlet} - n_{CH_4\ outlet}} \times 100 \quad (3.45)$$

3.13. Characterisation of catalyst and LSCF6428 hollow fibre membrane

The catalytic properties (i.e., activity, selectivity and stability) of a catalyst and LSCF6428 hollow fibre membrane reactor are determined by its composition, structure, morphology, texture and mechanical properties.

Characterisation of the unmodified and modified LSCF6428HFM before reaction is paramount to obtain the signature characteristics of the hollow fibre membrane (i.e. $La_{0.6}Sr_{0.4}Co_{0.8}Fe_{0.2}O_{3-\delta}$) and catalyst (i.e. 5%Ni/LSCF6428). In addition, the characterisation of post-reaction of the unmodified and modified LSCF6428HFM reactor together with the oxygen permeation and catalytic studies enables to assess the effect of the reaction operation conditions on the reactor performance. In these studies, several characterisation techniques have been employed to determine the elemental composition, structure, morphology, texture and stability of the catalyst/LSCF6428HFM reactor and correlated with the catalytic properties. A brief description of the characterisation techniques are discussed in the following sections.

In the **figure 3.16** shows the different zone of the membrane, where was take the sample for different analysis.

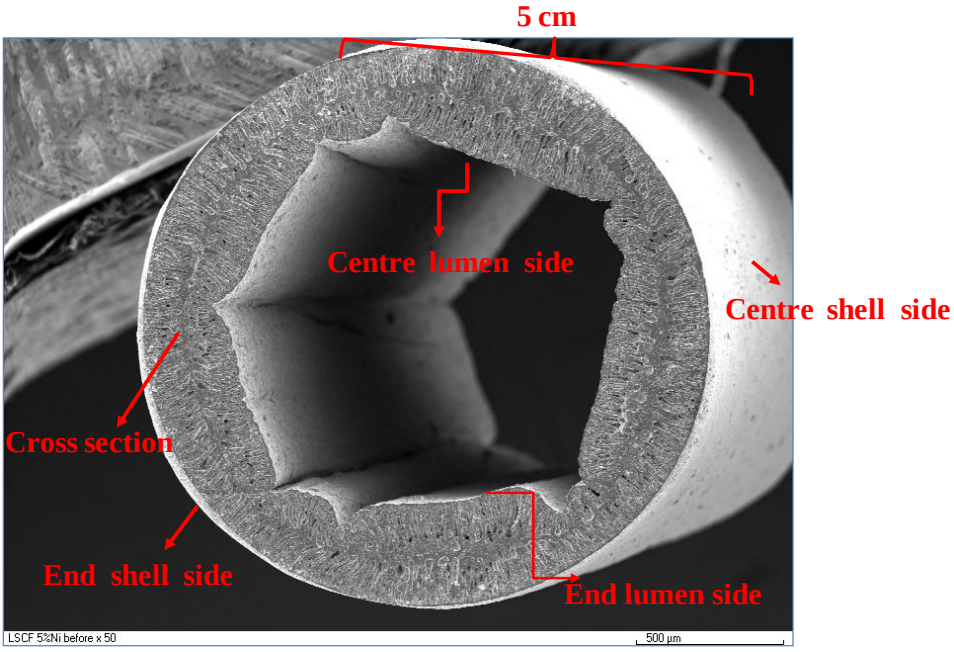

Figure 3.16 Schematic of the zones of hollow fibre membrane for XRD, SEM and EDX analysis

3.13.1. X-ray diffraction (XRD)

This technique consists of striking a crystalline sample (i.e., single crystal or polycrystalline powder) with a monochromatic beam of X-rays at some angle θ, where a portion is scattered by the layer of atoms at the surface. The unscattered portion of the beam penetrates to the second layer of atoms where again a fraction is scattered and the remainder passes on to the third layer **[16]**, **figure 3.17**.

Diffraction is the cumulative effect of this scattering from the regularly spaced centres of the crystal. X-ray diffraction requires the following conditions: (a) the spacing between the layers must be roughly the same as the wavelength of the radiation and (b) the scattering centres must be spatially distributed in a highly regular way **[17]**.

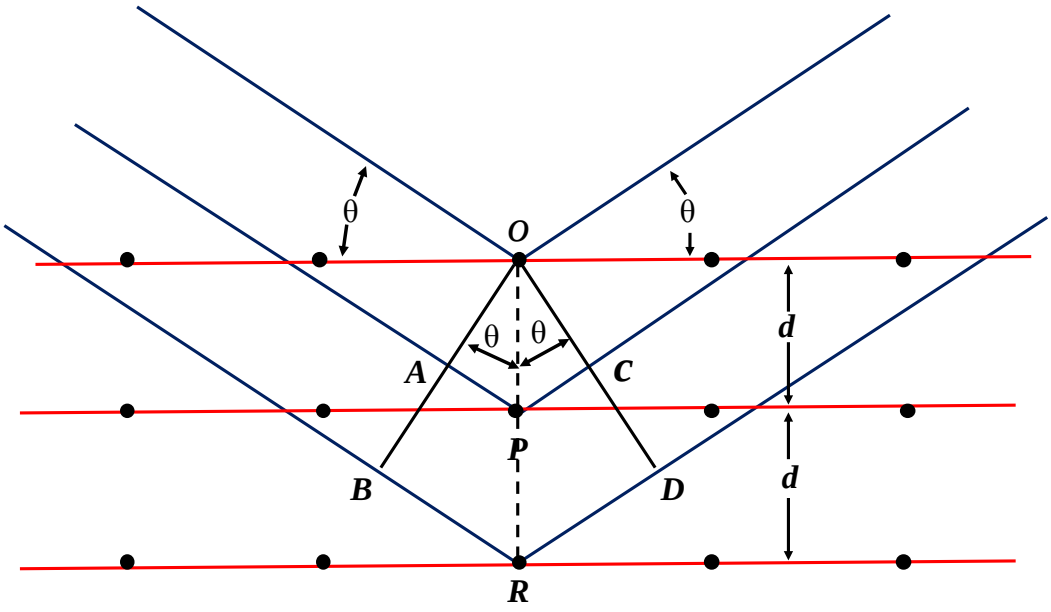

Figure 3.17 Diffraction of X-rays by the (hkl) planes of a crystal **[16, 17]**.

W.L. Bragg considered that the diffraction of X-rays by crystals occurs when a monochromatic radiation strikes the crystal at angle θ; scattering takes place as a consequence of interaction of the radiation with atoms located at O, P, and R positions (**figure 3.17**). If the distance:

$$AP + PC = n\lambda \tag{3.46}$$

Where, n is an integer (the order of reflection or diffraction), the scattered radiation will be in phase at OCD and the crystal will appear to reflect the X-radiation. Since

$$AP = PC = d_{hkl}\sin\theta \tag{3.47}$$

Where, d_{hkl} is the interplanar spacing of the crystal planes of indices (hkl). Thus, the conditions for the constructive interference of the beam at angle θ are:

$$n\lambda = 2d_{hkl}\sin\theta \tag{3.48}$$

Eqn. (3.48) is known as the **Bragg equation** and establishes that X-ray is reflected from the crystal structure only if the angle of incidence satisfies the condition that:

$$\sin\theta = \frac{n\lambda}{2d_{hkl}} \tag{3.49}$$

At all other angles, destructive interference occurs (Bragg's Law). Powder XRD is a very important technique for the qualitative and even quantitative characterization of catalytic materials **[18]**. The diffraction pattern (i.e., peak positions and relative peak intensities) serves as a fingerprint from which the phase (or phases) can be identified by comparison with the data bank (i.e., X-ray Powder Diffraction File administrated by the Joint Committee for Powder Diffraction Standards, JCPDS) **[19]**. In addition, information can be obtained on the degree of crystalline, unit cell parameters and crystal size.

Bragg's law is only valid for perfect crystals and monochromatic radiation $(K\alpha_1)$, in practice deviations from the ideal case are frequently observed, especially in polycrystalline specimens because of the presence of imperfections (particularly sub-grain boundaries), and lattice strains. Several variables contribute to the broadening of the X-ray peaks: structural defects, instrumental factors and crystal size. Nevertheless, it is generally assumed that the

main contribution comes from the particle size since the instrumental factors can be subtracted from the observed peak breadth whereas the contribution of the structural defects could be less important, especially for supported catalysts **[20]**.

The characterisation of the samples by X-ray diffraction was carried out using a PANalytical XPert- Pro diffractometer fitted with a X' Celerator and equipped with an X-ray tube (CuK_α radiation λ = 1.54060 Å; 40 kV, 30 mA). The specimens were prepared by grinding a small amount of each sample (ca. 100-150 mg) using an agate mortar and pestle and then loading into a flat sample holder. In studies on membrane the sample was cut into sections approximately 1 cm in length and 0.2 cm wide and arrayed on the amorphous plasticene attached to the sample holder. The data were collected at room temperature in **θ/2θ** reflection mode, from 3° to 100° 2θ, using steps of 0.033°, with time per step of 100s in continuous mode. The instrument was interfaced with a computer for collected data.

3.13.1.1. X-ray diffraction line broadening. Crystallite size determination

XRD methods for crystallite size determination are applicable to crystallites in the range of 2-100 nm. The diffraction peaks are very broad for crystallites below 2-3 nm, while for particles with size above 100 nm the peak broadening is too small. When the analyzed crystals are free from micro strains and defects, peak broadening depends only upon the crystallite size and diffractometer characteristics. The ***Scherrer equation*** (eqn. 3.50) is normally used for crystallite size determination:

$$\beta = K\,\lambda / L\,\cos(\theta) \qquad (3.50)$$

where β is the crystallite size, λ is the X-ray wavelength, L is the width of the peak (i.e., full width at half maximum, FWHM, peak intensity or integral breadth, see **figure. 3.18**) after correcting it for instrumental peak broadening (L expressed in radians), θ is the Bragg

angle and K is the constant of proportionality (the Scherrer constant). This constant depends upon the way to find out the value of L, the shape of the crystal and the size distribution. The value used in this work was 0.9, considering FWHM [**21**].

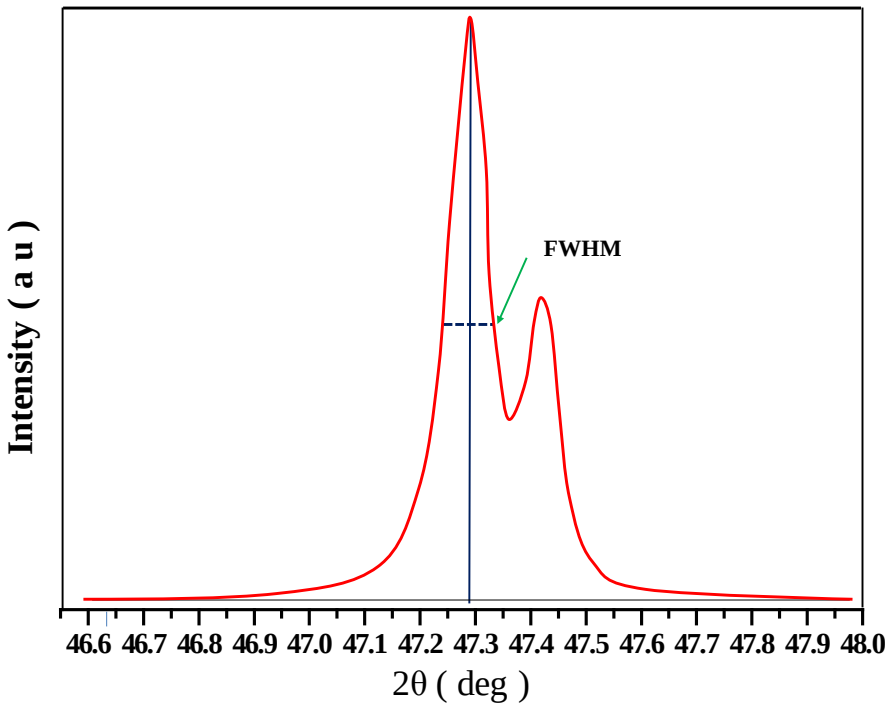

Figure 3.18 The full width of the diffraction peak at a height half-way of the peak maximum, in radians, **[16, 20]**.

3.13.2. Scanning electron microscopy (SEM)

In a scanning electron microscopy (SEM), the surface of a solid sample is scanned with a beam of high energy electrons, when the electron beam interacts with the specimen; this energy is dissipated as a variety of signals produced by electrons – the sample interacts because the incident electrons are decelerated in the solid sample (**figure 3.19**). All of these signals have been used for surface studies, because they reveal surface-sensitive information such as: external morphology (texture), chemical composition, crystalline structure and orientations of materials **[22-23]**.

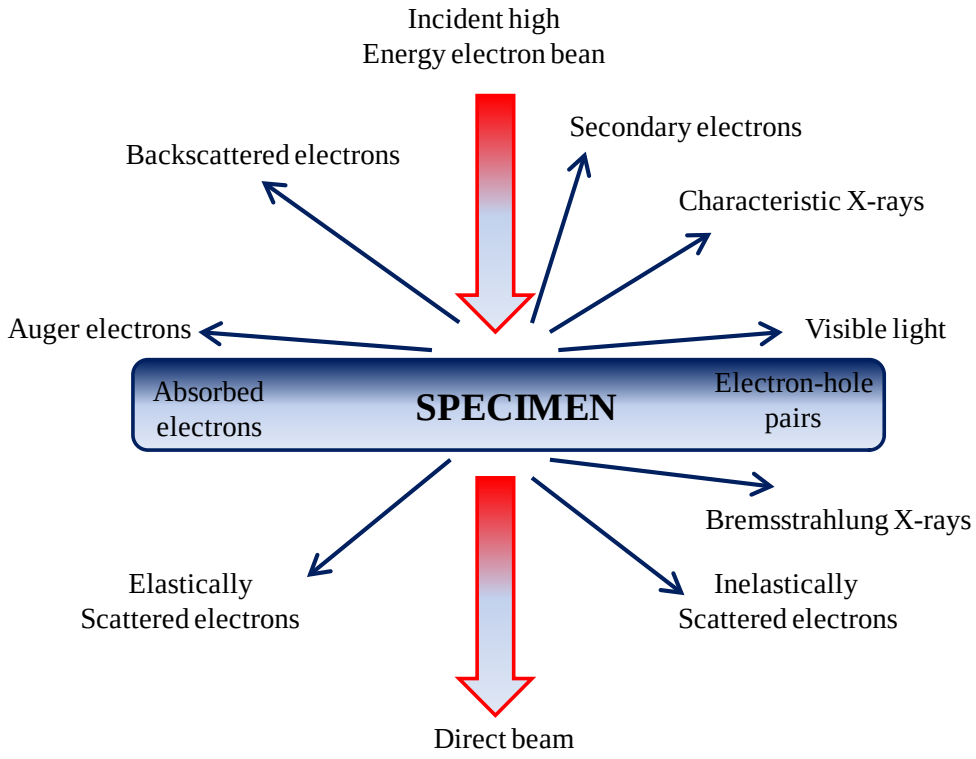

Figure 3.19 Signals generated from the interaction of the electron beam with a thin specimen. The arrows do not correspond necessarily with the signal's physical direction **[22, 23]**.

The principle of operation of an SEM instrument is schematically illustrated in **figure 3.20**. At the top of the microscope's column a narrow beam of electrons is produced by heating the Tungsten filament. The electrons are focused by one or more magnetic condenser lens and objective lens system which control the size and angular spread of the beam. Then, the electron beam passes through pairs of scanning coils or pairs of deflector plates in the electron column, which is the final lens. This electron beam is deflected in the x and y axes to scan over a rectangular area of the sample surface. When the primary electron beam interacts with the sample the electrons lose energy by repeated random scattering and absorption within a teardrop-shaped volume of the specimen. The beam current absorbed by the specimen can also be detected and used to create images of the distribution of specimen current.

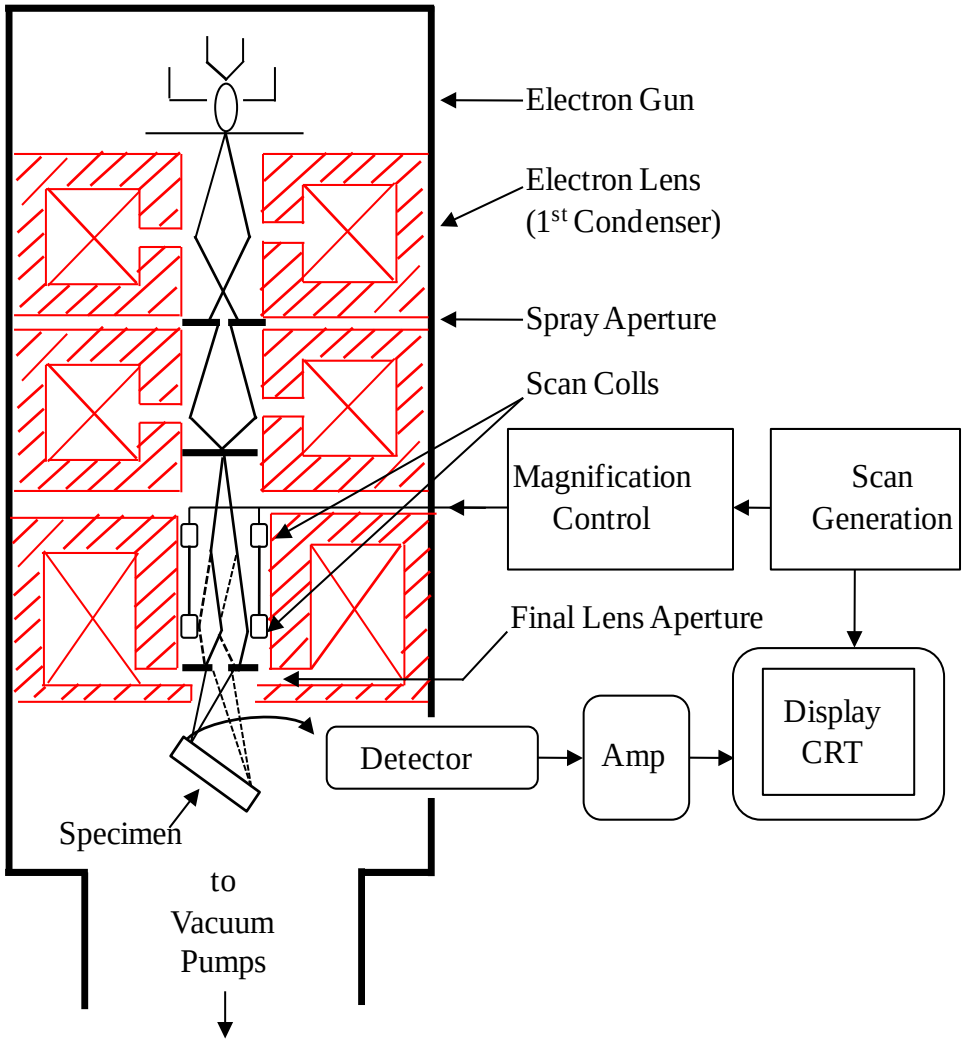

Figure 3.20 Schematic of the Scanning Electron Microscopy (SEM) **[22]**

Electronic amplifiers are used to amplify the signals which are displayed as variations in brightness on a cathode ray tube (CRT). The raster scanning of the CRT display is synchronised with that of the beam on the specimen in the microscope, and the resulting image is therefore a distribution map of the intensity of the signal being emitted from the scanned area of the specimen. The image may be captured by photography from a high resolution cathode ray tube or is digitally captured and displayed on a computer **[17, 22]**.

The SEM images were simulated using the software Scanning Probe Image Processor (SPIP 6.0.9) in order to determine the diameter of grain boundary and pore areas.

3.13.3. Energy-dispersive x-rays spectroscopy (EDXS)

Energy dispersive x-rays spectroscopy (EDXS) is a semi-quantitative analysis technique widely used to determine the presence, amount and distribution of elements in a sample. The advantages of EDXS analysis are the following: (1) it does not destroy the sample and (2) EDXS analysis is done on a spatial basis (i.e. the composition of one part of a sample may be compared with an adjacent part of the sample). X-rays result from an inelastic scattering in which a vacancy in an inner orbital shell is produced and immediately filled by an electron from a shell of higher energy. The energy difference between the shells may be emitted in the form of X-ray radiation. The energy and the wavelength of the X-ray produced are characteristic of the element and are related by the equation, $\lambda = 1.24/E$, where λ is the wavelength in nm and E is the energy in keV. Each X-ray produced has a name based on the name of the electron shell (K, L, M, N) in which the vacancy was created and on the number of orbital shell jumps made by the electron that filled the vacancy. Hence, a one-shell jump is denoted by a subscript α, a two shell jump by subscript β, and so on. For example, a vacancy in the K shell filled by an electron from the L shell would create a K_α X-ray **[22]**.

Semi-quantitative elemental compositions were verified by energy-dispersive X-rays spectroscopy using an Emission Scanning Electron Microscope Röntec Quanta 1, 200 30XL FEI which was equipped with a light-element energy-dispersive X-ray spectrometer (EDXS). To investigate structural changes at the membrane surfaces, membrane specimens were prepared by carefully breaking the hollow fibre membrane into sections of length 1 cm and 0.2 cm wide. The instrument was interfaced with a computer for collected data.

3.14. Reference

[1] S. P. Deshmukh and K. Li, J. Membr. Sci. 150 (1), **1998**, 75.

[2] X. Y. Tan, Y. T. Liu, K. Li, AlChE J. 51 (7), **2005**, 1991.

[3] X. Tan., Y. Liu and K. Li, Ind. Eng. Chem. Res. 44 , **2005**, 61.

[4] K. Li, Ceramic membrane for separation and reaction. John Wiley & Sons, Ltd. England**, 2007**, 1-20.

[5] Fortafix, High Temperature Sealants and Adhesives. Fire Resistant Sealants. Heat Resistant Cements, http://www.fortafix.com.

[6] Robson Scientific, Industrial Quartz and Borosilicate Glass Blowing, http://www.robsonscientific.co.uk.

[7] A. Thursfield and I. Metcalfe, J. Mater. Chem. 14, **2004,** 2475.

[8] C. Wagner, Diffusion and high temperature oxidation of metals. Atom movements, Clevelands: ASM., **1951**, 153.

[9] H.J. M. Bowmeester, H. Kruidhof & A. J. Burggraf, Solid State Ionics, 72, **1994**, 185.

[10] H.J. M. Bowmeester, H. Kruidhof, A. J. Burggraf & P. J. Gellings Solid State Ionics, 53, **1992**, 460.

[11] S. Dou, C. R.Mason and P. D. Pacey. J. Electrochem. Society, 132, **1991**, 1843.

[12] Y.S. Lin, W. Wang & J. Han, AlChE J. 40, **1994**, 786.

[13] S. Ling, M. P. Anderson and T. A. Ramanarayanan, Solid State Ionics, 59, **1993**, 33.

[14] S.J. Xu and W.J. Thomson, Chem. Eng. Sci. 54, **1999**, 3839.

[15] I. S. Metcalfe, Chemical Reaction Engineering, Oxford University Press Inc. London, **1997**, 8.

[16] C. Hammond, The Basics of Crystallography and Diffraction, 2nd Edn., Oxford University Press, Oxford, **2001**.

[17] D.A. Skoog, F.J. Holler, T.A. Nieman, Principles of Instrumental Analysis, 5th Edn., Thomson Learning, Victoria, **1998.**

[18] G. Perego, Catal. Today, 41, **1998,** 251.

[19] JCPDS, Powder Diffraction Standards File (1989) International Centre for Diffraction Data, Swarthmore, PA.

[20] J.R. Anderson, Structure of Metallic Catalysts, Academic Press, London, **1975.**

[21] J.I. Langford and A.J.C. Wilson, J. Appl. Cryst. 11, **1978**, 102.

[22] J. Goldstein, D.E. Newbury, D. C. Joy, P. Echlin, C. E. Lyman, E. Lifshin, Scanning Electron Microscopy and X-ray Microanalysis, Kluwer Academic / Plenum Publishers, **2003.**

[23] D.V. Williams, C.B. Carter, Transmission Electron Microscopy, Plenum Press, New York, **1996**.

Chapter 4.

Oxygen permeation flux through LSCF6428 hollow fibre membranes

4 Oxygen permeation flux through unmodified LSCF6428 hollow fibres membranes

The oxygen release and uptake of the $La_{0.6}Sr_{0.4}Co_{0.2}Fe_{0.8}O_{3-\delta}$ hollow fibre membranes without catalysts has been studied experimentally under different operations conditions (i.e. mode 1, 2 and 3) at 850°C and 900°C. An extensive analysis was conducted to investigate the oxygen incorporated through unmodified LSCF6428 HFM used mode 2 at 850°C. A model for determining the reaction rate constants for two different modes of operation co-current (mode 2) and counter-current (mode 3) was developed and the results were compared. The stability of the LSCF6428 hollow fibre membrane module under oxygen separation conditions during 1360 hours were studied by different techniques such as XRD, SEM and EDX.

4.1. Oxygen release and oxygen uptake using mode 1 and mode 2 of operation of at 850 °C

Figure 4.1 shows the oxygen release and uptake behaviour of unmodified hollow fibre membranes for two modes of operation (mode 1 and mode 2). The mode 1 corresponds to the air fed on the lumen side of the membranes and the helium sweep on the shell side (ALHS–air-lumen, helium-shell) in co-current flow (**figure 4.1A**). It can be appreciated that both the oxygen release and uptake measurements increases slightly as rising helium flow from 10 to 125 ml min^{-1}. This is possibly due to the fact that the increase of helium flow rate reduces the oxygen partial pressure on the shell side and therefore increasing the oxygen partial pressure difference across the membrane, which is reflected on higher oxygen flux **[1].** However, the oxygen release and uptake trend did not vary linearly with helium flow rate, indicating that the mass-transfer resistance of the membrane is a function of the helium flow rate **[2, 3].** This finding was verified with the proposed model (eqn. 3.15) where it was

obtained the dependence of oxygen flux with helium flow. Reynolds numbers also changed from laminar to turbulent flows; see **appendix II.6, table II.6 and II.7.**

Furthermore, it can be observed that the oxygen release and uptake trends rise when increasing the air flows (10-75) ml min^{-1}. This could be attributed to the fact that the set air flow determines the amount of the oxygen that permeates across the membrane. It is worth remarking that the oxygen uptake was nearly an order of magnitude higher than the oxygen release. This behaviour is tentatively attributed to the following causes:

1. The steady state in the membrane reactor was not achieved during the experiment.

2. Oxygen was incorporated into $La_{0.6}Sr_{0.4}Co_{0.2}Fe_{0.8}O_{3-\delta}$ membrane crystal structure during the experiment. According to the dopant concentration, the theoretical value of δ ($\delta \approx \frac{1}{2}[Sr]$) would be 0.2 [**4**], which is within the analytical capabilities of the equipments used in this work.

3. The membrane stoichiometry was changing during the experiment.

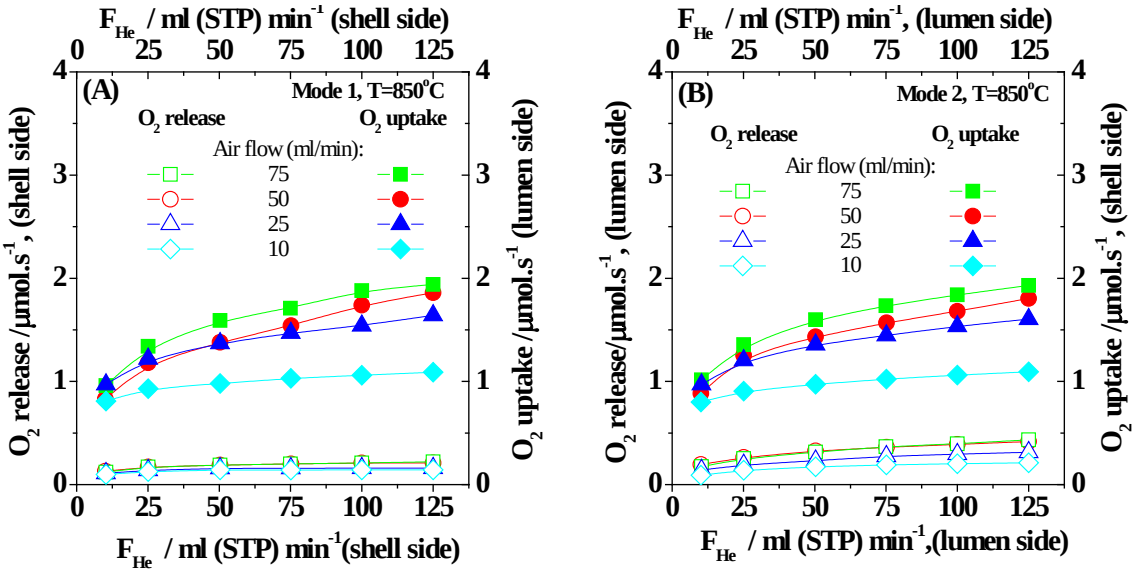

Figure 4.1 Effect of two different modes of operation before the membrane reactor reached the steady state: (A) Air flow feeds on the lumen side of the membranes reactor and the helium flow sweep on the shell side in co-current (mode 1). (B) Air flow feeds on the shell side of the membranes reactor and the helium flow sweep on the lumen side in co-current flow (mode 2).

A similar trend was also observed in mode 2 of operation of the hollow fibre membrane reactor, **figure 4.1B**.

Comparing the results between mode 1 (**figure 4.1A**) and mode 2 (**figure 4.1B**) at 850°C, it can be noted that the oxygen release measurements for mode 1 are similar that the measurements obtained from mode 2 (see **appendix II.1, figure II.1**). This finding can be rationalised considering that the membrane cross section showed a sandwich-like structure, i.e., a central dense block between two finger-like structures of the LSCF6428 hollow fibre membrane (**figure 4.11**). A different trend was reported by Li *et al.*, **[2]** in a previous oxygen permeation study due to the difference between the inner porous surface structure and outer dense surface structure of the LSCF6428-HFM (**figure 1.3**).

4.2. Oxygen release and oxygen uptake using mode 2 of operation on unmodified LSCF6428 HFM at 850°C for long term of operation.

In order to rationalize the difference between the oxygen release and oxygen uptake measurements, an experiment on unmodified LSCF6428 HFM using mode 2 during a long period of operation, was carried out, **figure 4.2**.

In **figure 4.2A** it can be appreciated that the oxygen uptake and the oxygen release increases with time. The measurements of both parameters during the initial period of the experiments showed a similar trend, however oxygen uptake was slightly higher than the oxygen release.

After approximately 325 hours of run time the oxygen release and oxygen uptake started to converge, reaching similar values after nearly 492 hours of operation (**figure 4.2B** and **appendix II.2, figure II.2**). This trend suggests that steady state was achieved after a long operation time, likely due to the partial reduction of the membrane because of long annealing time (i.e. 360 hours) under low air flow (5 ml. min^{-1}) at both membrane sides. It is worth remarking that this long annealing time was due to technical problems with PC, which did not

record the GC analysis data because of a communication problem between the PC and the GC.

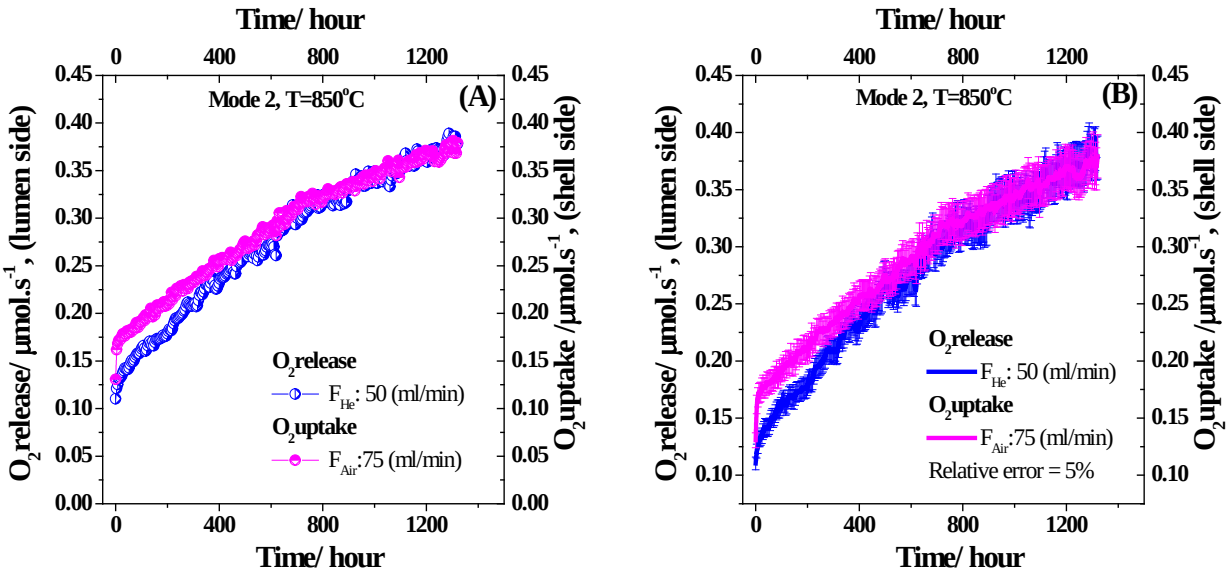

Figure 4.2 (A) Oxygen release and oxygen uptake on mode 2 as a function of time on stream and (B) oxygen release and oxygen uptake measurements on mode 2 with accuracy ± 5% (**appendix II.3**)

In addition, it can be observed that the LSCF6428-HFM reactor exhibited high operational stability during 1320 hours of operation under oxygen chemical potential pressure difference at 850^{o}C. A previous study for oxygen permeation on LSCF6428-HFM reactor did show a comparable operation time **[5]**.

In **figure 4.3A** is illustrated the dependence of the rate of oxygen incorporated into the hollow fibre membranes as a function of run time, calculated according to eqn. (3.5). Indeed, the rate of oxygen incorporated into the hollow fibre membranes slightly decreased and reached a value constant close to zero at time on stream above 490 hours, the error propagation of this measurement was within 5% as is shown in **appendix II.2 and II.3**. The determination of the apparent rate constant for the oxygen incorporation into LSCF6428 hollow fibre membranes, was calculated assuming that the reaction is first order; the results was 5x10^{-6} µmol sec^{-1} bar^{-1} cm^{-2}, see **appendix II.5, figure II. 4.**

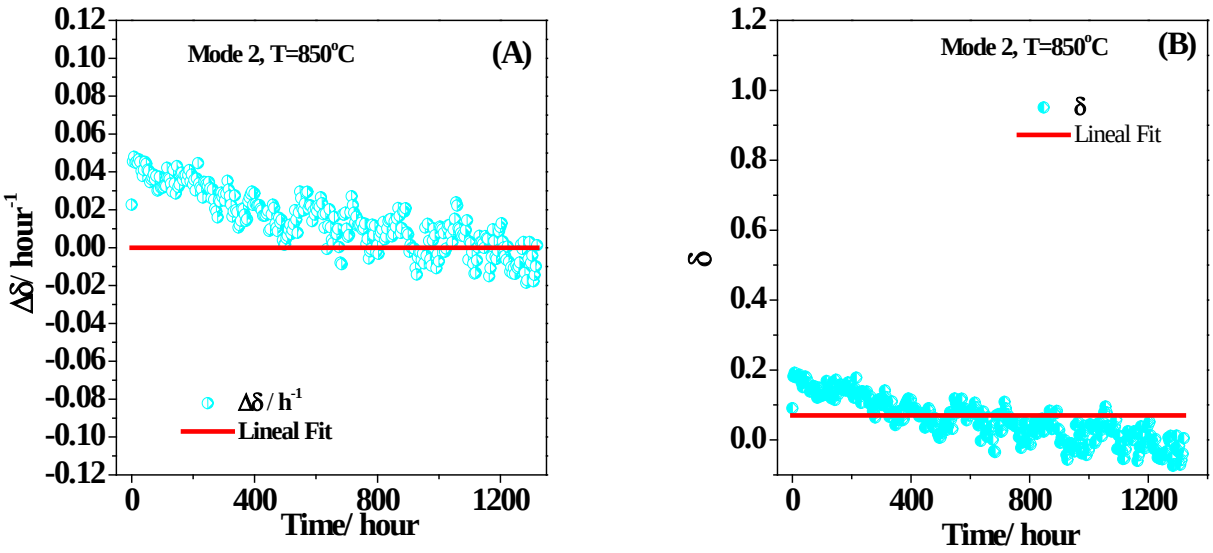

Figure 4.3 Rate of oxygen incorporated into membrane as a function of run time (A) and oxygen incorporated non- dimensional (B) for long term of operation.

Note that the apparent rate constant for the oxygen incorporation into LSCF6428 is significantly lower than that for the oxygen permeation (0.16 µmol sec^{-1} bar^{-1} cm^{-2}), indicating that oxygen is being released faster than that is being incorporated.

When one considers the rate of oxygen incorporated into the membrane structure, calculated according to eqn. (3.5) multiplied by the interval of collection time (4 hours), see **figure 4.3B**. It can be observed that initial oxygen vacancies correspond to the theoretical value (δ = 0.2) based on LSCF6428 membrane stoichiometry [**4**]. Furthermore, a value of δ close to zero was reached at steady state condition owing to similar measurements of oxygen uptake and release.

4.3. Oxygen uptake and oxygen release measurements under mode 2 (co-current) and mode 3 (counter-current) operation at 850°C and 900°C.

The experimental tests were performed using different sweep gas configurations (co-current (mode 2) and counter-current (mode 3) on an unmodified LSCF6428HFM reactor. The effect of the co-current and counter-current mode of operation is presented in **figure 4.4**. In the

mode 2 (co-current) of sweep flow operation, it can be observed that the oxygen release measurements from the lumen side are similar to the oxygen uptake data obtained directly from the shell side considering the accuracy ± 5% (**figure 4.4A**). A similar tendency was obtained in the previous measurements of the oxygen release and oxygen uptake at long operation time (see **figure 4.2A**).

Moreover, it can be emphasized that the oxygen release (ca., 0.32 µmol sec^{-1}) and oxygen uptake (ca., 0.26 µmol sec^{-1}) are slightly lower when compared with oxygen release and oxygen uptake measurements obtained in the long term permeation experiment (ca., 0.38 µmol sec^{-1}). According to Li *et al*., [**5**], this difference could be attributed to mass transfer effects and kinetic demixing of mobile cations of the membrane due to oxygen pressure difference across the membrane during long operation time at high temperature.

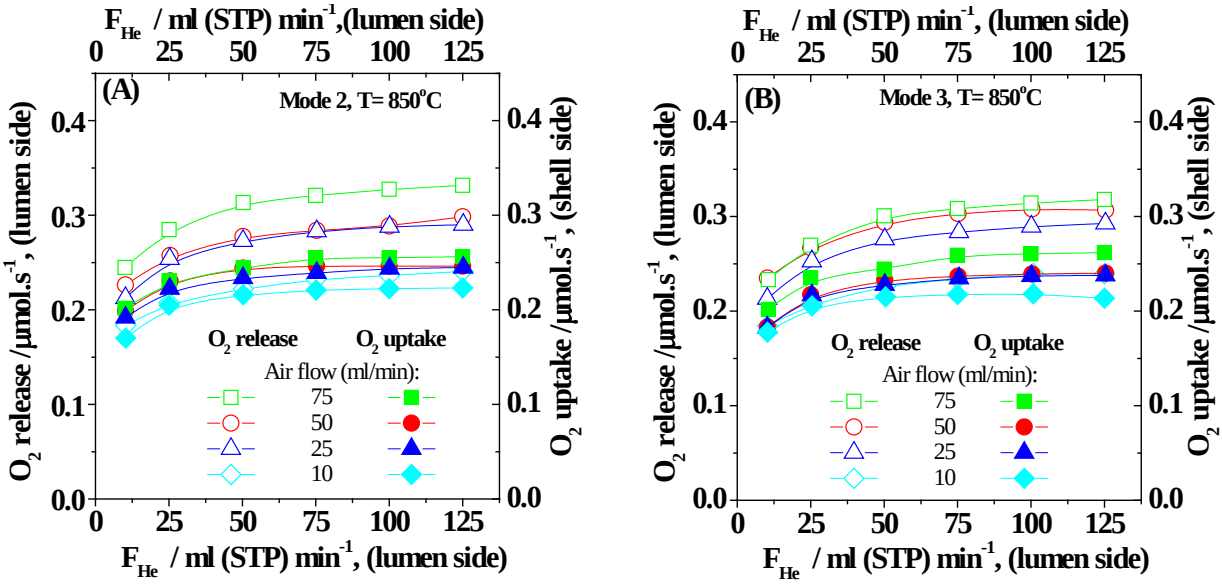

Figure 4.4 Dependence of the oxygen release and oxygen uptake against two configurations of flow operation at 850°C: (A) mode 2 (co-current) and (B) mode 3 (counter-current) after the reactor reached the steady state

Similar results were obtained when the reactor was operated in counter-current (mode 3) as shown in **figure 4.4B**. Comparing the results between mode 2 and mode 3 of flow operation, it can be noted that the experimental data from counter-current are slightly higher than that

obtained from the co-current flow operation, (**figures 4.4A and 4.4B**). This is due to the fact that oxygen partial pressure difference across the membrane in counter-current is larger than co-current flow operation. In **appendix II.6, figure II.7,** is given the profiles of oxygen inlet (nO_2 inlet) and oxygen outlet (nO_2 out) across membrane for mode 2 (co-current) and mode 3 (counter-current). Also, it can be appreciated that both the oxygen release and oxygen uptake increased with rising helium flow rate under mode 2 and 3. This is due to high helium flows rate that reduces oxygen partial pressure on the lumen side, increasing the oxygen partial pressure difference across the membrane. This improves the diffusion of the lattice oxygen from the shell side toward the lumen side [**1**]. Furthermore, the oxygen release did not change significantly at air flow above 50 ml min^{-1}, this indicates that the effects of gas-solid mass transfer (steps 1 and 5), see **figure 2.4**, and are negligible under these operation conditions [**6**].

In **figure 4.5** is illustrated the oxygen release and oxygen uptake against the helium flow at 900˚C for mode 2 and mode 3.

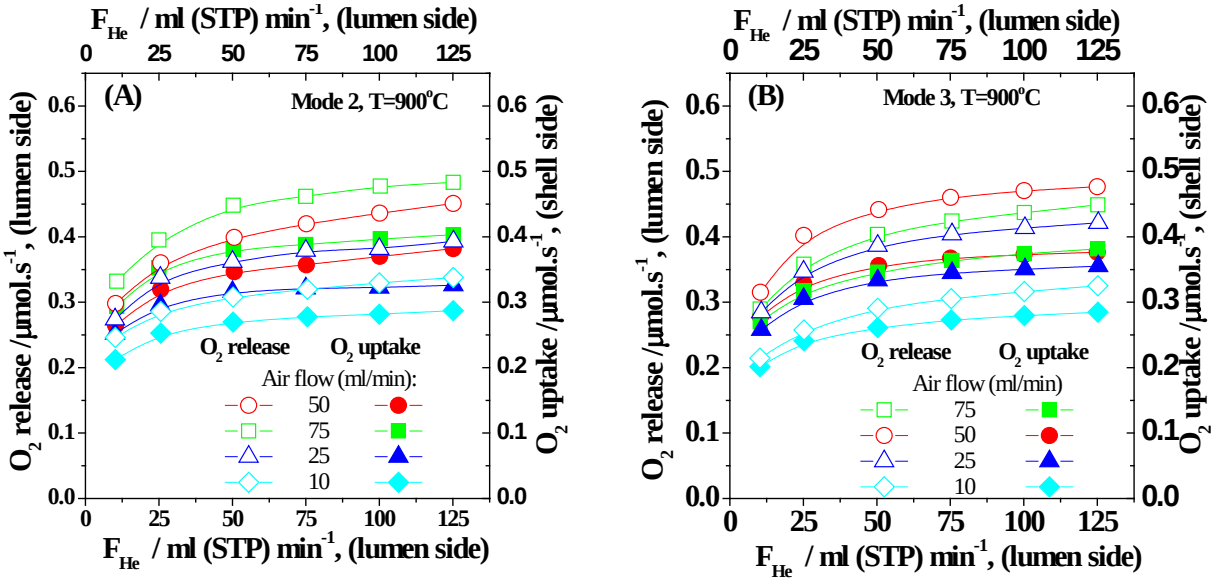

Figure 4.5 Dependence of the oxygen release and oxygen uptake against two configurations of flow operation at 900°C: (A) mode 2 (co-current) and (B) mode 3 (counter-current).

Both modes present a similar tendency than the measurements of the oxygen release and oxygen uptake obtained at 850˚C, but a significant rise in the values was observed because the temperature plays an important role in the bulk oxygen diffusion and the oxygen surface reaction rates **[2, 7].**

4.4. Reaction rate constants for two different modes of operation (i.e. mode 2 (co-current) and mode 3 (counter-current)) at 850°C and 900°C.

The apparent reaction rate constants against helium flow for two different modes of operation (co-current and counter-current) at 850°C and 900°C are shown in **figure 4.6**.

As discussed earlier, the apparent rate constant for co-current operation was calculated from eqn. (3.23) and the apparent rate constant for counter-current operation was obtained from eqn. (3.35) (**figure 4.6A**), where in the model assumes plug flow in the gas phase and a flux expression whereby the flux depends upon an overall rate constant multiplied by the local oxygen partial pressure difference across the membrane.

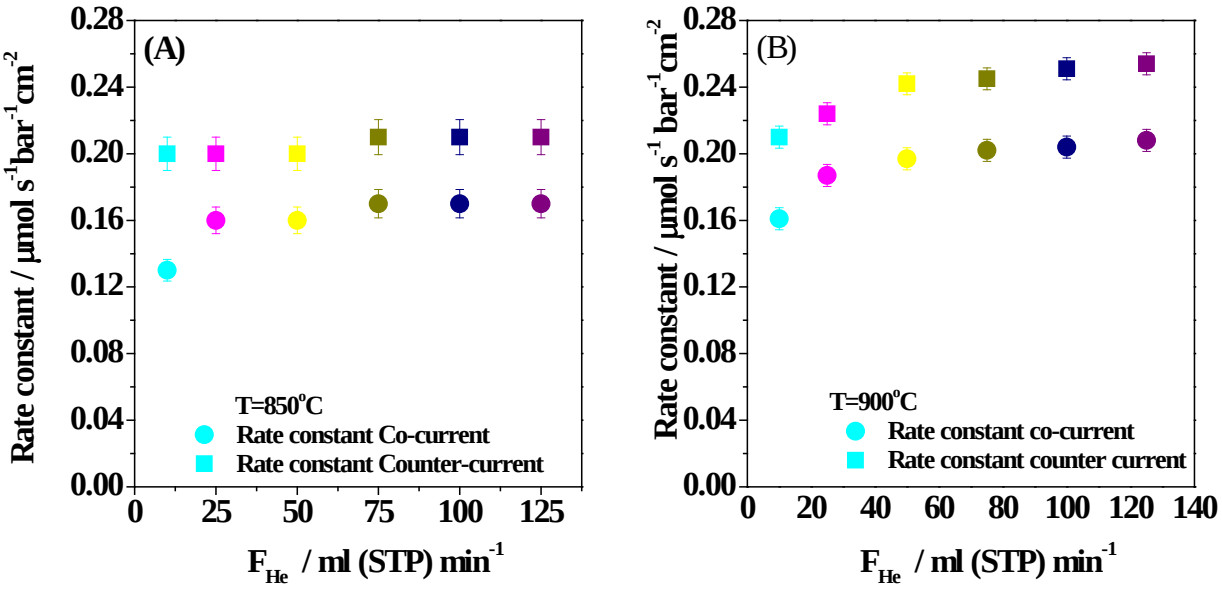

Figure 4.6 Reaction rate constant for different helium flows under two mode of flow operation at 850°C (A) and 900°C (B).

The rates of oxygen uptake and release are assumed to be equal. So, these equations can be only applied when membrane reactor has reached steady state. It can be noted in **figure 4.6A** that for both configurations co-current (mode 2) and counter-current (mode 3) the apparent rate constants reach a constant value for helium flow rates above 50 ml min^{-1}. Any further increase in the helium flow does not produce a higher rate constant. Moreover, the apparent rate constants appear to change at lower flow rates indicating that the model is invalid at such low flows possibly due to gas-solid mass transfer effects and low Reynolds numbers ($\mathbf{Re < 2000}$), see **appendix II.7, tables II.6** and **II.7 [6],** since the model is based on the assumption that the oxygen flux is related to plug flows.

In addition, it can be observed for instance, that for mode 3 at 50 ml min^{-1} helium flows, the apparent reaction rate constant obtained was 0.21 µmol sec^{-1} bar^{-1} cm^{-2}, and the apparent reaction rate constant for mode 2 under similar experimental conditions was 0.16 µmol sec^{-1} bar^{-1} cm^{-2} (**figure 4.6A**). This difference can be attributed to the fact that in counter-current the overall effective driving forces for oxygen migration across the membrane is slightly larger than that in co-current flow operation, because two flows (air and helium) move in opposite directions, causing that the oxygen partial pressure gradient along the length of the membrane is maintained nearly constant **[2, 8].**

A similar experiment was conducted at 900°C, and the data obtained are given in **figure 4.6B**. At 50 ml min^{-1} helium flow rate and mode 3 a reaction rate constant of 0.24 µmol sec^{-1} bar^{-1} cm^{-2} was obtained. On the other hand, for mode 2, the reaction rate constant was 0.20 µmol sec^{-1} $bar^{-1}cm^{-2}$ which presents a fairly small difference compared with that obtained from mode 3. For more details see **appendix II.6 (figures II.5** and **II.6).**

4.5. Calculation and comparison of oxygen permeation resistance*.*

In order to find out the resistance of surface oxygen exchange kinetics and bulk diffusion of oxygen vacancies in the membrane the following equations were used [**6**]**.**

1. The resistance by exchange reaction at the oxygen-rich side (shell side) $R_{ex}^{'}$:

$$R_{ex}^{'} = 1/k_f P_{O_2}^{'\ 0.5} \quad (4.1)$$

2. The resistance by exchange reaction at the oxygen-lean side (lumen side) $R_{ex}^{''}$:

$$R_{ex}^{''} = 1/k_f P_{O_2}^{''\ 0.5} \quad (4.2)$$

3. The resistance by bulk diffusion, R_{diff}:

$$R_{diff} = 2L/D_v \quad (4.3)$$

4. Total permeation resistance R_t

$$R_t = R_{ex}^{'} + R_{ex}^{''} + R_{diff} \quad (4.4)$$

Where, $P_{O_2}^{'}$ and $P_{O_2}^{''}$ are partial pressure of oxygen in the shell and lumen side (atm), respectively. The forward reaction rate constant (k_f) is $1.65\text{x}10^{-4}\ cm\ atm^{-0.5}\ s^{-1}$ and $4.64\text{x}10^{-4}\ cm\ atm^{-0.5}\ s^{-1}$ as the reverse reaction rate constant (k_r) is $1.24\ \text{x}10^{-7}\ mol\ cm^{-2}\ s^{-1}$ and $3.72\ \text{x}10^{-7}\ mol\ cm^{-2}\ s^{-1}$ at 850°C and 900°C, respectively for the below reactions [**6**], see **figure 2.4**.

$$\frac{1}{2}O_2 + V_O^{\bullet\bullet} \xleftrightarrow{k_f/k_r} O_O^x + 2h^{\bullet} \quad \text{(Step 2)} \quad (4.5)$$

$$O_O^x + 2h^{\bullet} \xleftrightarrow{k_r/k_f} \frac{1}{2}O_2 + V_O^{\bullet\bullet} \quad \text{(Step 4)} \quad (4.6)$$

The diffusion coefficient of oxygen vacancies (Dv) is $5.96\text{x}10^{-6}\ cm^2 s^{-1}$ and $8.34\text{x}10^{-6}\ cm^2 s^{-1}$ at 850°C and 900°C, respectively [**8**] and **L** is the membrane thickness (i.e., $0.025\ cm$).

In the **figure 4.7** is shown the distribution of total permeation resistance for 850°C and 900°C.

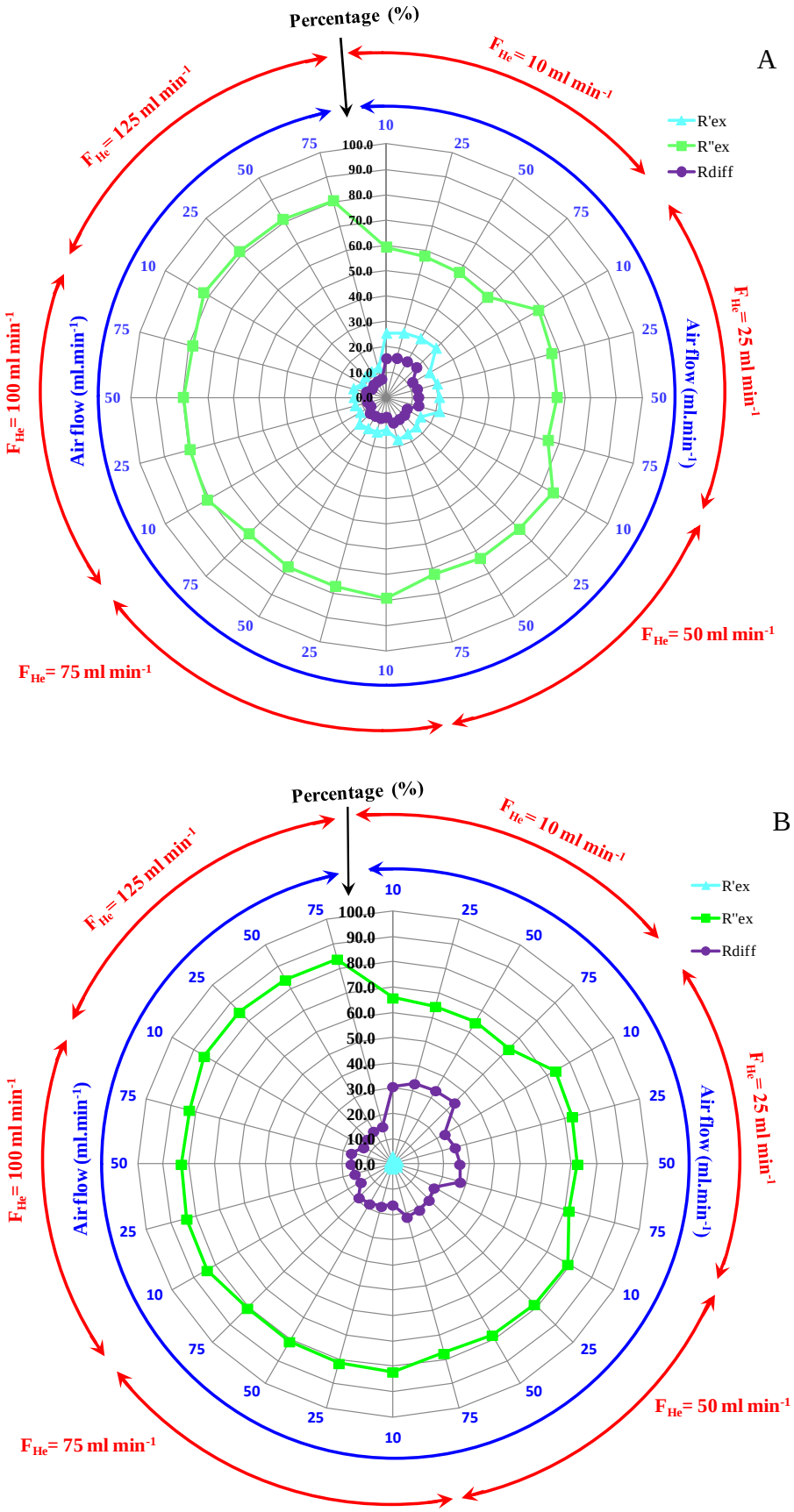

Figure 4.7 Effect of air flow on distribution of total permeation resistance under co - current at 850°C (A) and co - current at 900°C (B).

It can be appreciated that at low helium flow (i.e., 10 ml min^{-1}) the resistance of surface exchange at the oxygen lean side or lumen side ($R_{ex}^{''}$) was between 56 and 59 %, indicating that $R_{ex}^{''}$ controls the oxygen permeation rate since $R_{ex}^{'}$ (25-28 %) and R_{diff} (15-17 %) showed lower contribution to the overall oxygen permeation rate, see **figure 4.7**A and **appendix II.8, figure II.10**

Furthermore, at helium flows between 25 and 75 ml.min^{-1}, $R_{ex}^{''}$ gradually increased up to 80 % and did not vary at higher helium flows (100 and 125 ml min^{-1}). Note that $R_{ex}^{'}$ and R_{diff} decreased at helium flow above 10 ml min^{-1}. This finding indicates that oxygen permeation is rate limited by surface exchange on the oxygen lean side or lumen side ($R_{ex}^{''}$) at 850°C, **figure 4.7A** and **appendix II.8, figure II.11**. Note that the $R_{ex}^{''}$ also limited the oxygen permeation rate at 900°C, **figure. 4.7B**. However, the overall R_{diff} significantly increased (i.e., 34 - 13 %) whilst $R_{ex}^{'}$ decreased (i.e., 3 - 0.6 %) compared to R_{diff} (17 – 7 %) and $R_{ex}^{'}$ (28 – 11 %) obtained at 850°C, **appendix II.8, figure II.10.** This finding suggests that the contribution of bulk diffusion on the oxygen permeation rate increased as rising the temperature (900°C), in agreement with a previous report **[6].**

It is worth remarking that the oxygen flux varies inversely with membrane thickness and that at low membrane thickness the oxygen permeation is controlled by surface exchange reaction [**8, 9**], see **figure 4.8**, which is in total agreement with the above-discussed results. However, the apparent activation energy (Ea) determined with two temperatures (850 and 900°C) was significantly lower (i.e., 43 – 45 kJ mol^{-1}), than that given in the literature (i.e., 115 kJ mol^{-1}) when oxygen permeation rate is controlled by surface exchange kinetics at temperature above 850°C, see **appendix II.10, table II.8** [**6**]. This difference is tentatively attributed to the contribution of R_{diff} at 900°C and also to the use of only two series of oxygen flux

measurements (850°C and 900°C) to find out the Ea, which can generate a large error in the obtained value. However, we cannot rule out the possible aggregation of surface elements or degradation of the membrane occurred after several hours of operation that could also affect the oxygen permeation values.

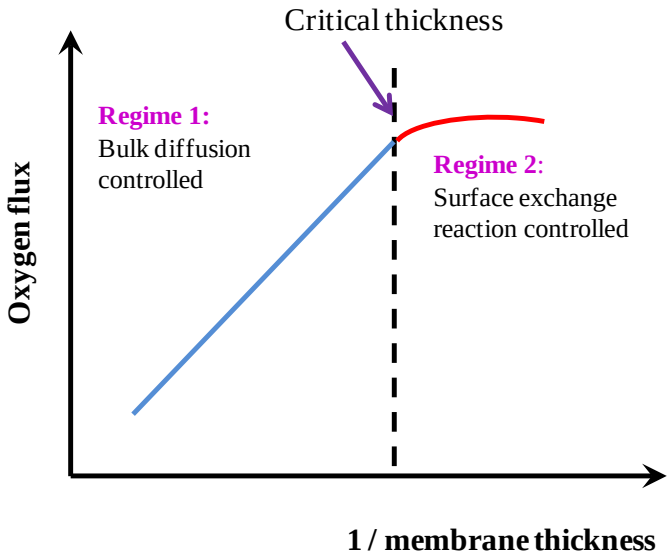

Figure 4.8 Effect of membrane thickness on oxygen permeation [**9**]

Figure 4.9 is given the residence time from shell side against residence time from lumen side. It can be observed that lumen side shows smaller residence times compared with residence times from shell side.

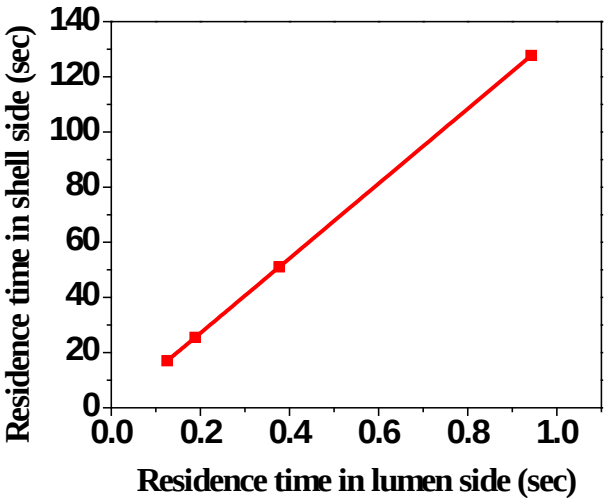

Figure.4.9 Residence time from shell side against residence time from lumen side.

This suggests that the mass transfer of oxygen from the membrane surface to the gas stream in the lumen side was very fast in agreement with results obtained from the distribution of total permeation resistance where it was concluded that oxygen permeation rate is limited by the association of oxygen ion to form oxygen molecules.

4.6. Characterization of the unmodified LSCF6428 HFM before and after oxygen permeation by different techniques.

4.6.1. X ray-diffraction (XRD):

The diffraction profiles for the unmodified LSCF 6428 hollow fibre membrane module before and after 1360 hours oxygen release and uptake experiments are shown in **figure 4.10**. The XRD patterns for lumen side and shell side of unmodified LSCF 6428 hollow fibre membrane before reaction are given in **figure 4.10b** and **4.10c**, respectively. Both XRD profiles display the signature characteristic of the hollow fibre membrane (i.e., $La_{0.6}Sr_{0.4}Co_{0.8}Fe_{0.2}O_{3-\delta}$) as the main crystalline phase **[10]**, whose crystal size for lumen and shell side before reaction was approximately 22 nm (0.022 μm) and 23 nm (0.023 μm), respectively, see **appendix II.11, table II.9.**

In the **figures 4.10B** and **4.10C** are given the diffraction profiles for centre lumen side and centre shell side of the unmodified LSCF6428-HFM after 1360 hours of operation and the crystal size for lumen and shell side post reaction are 25 nm (0.025μm) and 24 nm (0.024μm), respectively**,** see **appendix II.11, table II.9**. It can be clearly noted that the principal crystalline phase is LSCF6428 for both samples. Furthermore, other crystalline phases such as Co_3O_4 (00-042-1467), CoO (00-048-1719), SrO_2 (00-007-0234) and trace amounts of $SrSO_4$ (00-005-5935) were observed in the shell side centre XRD pattern (**figure 4.10C**).

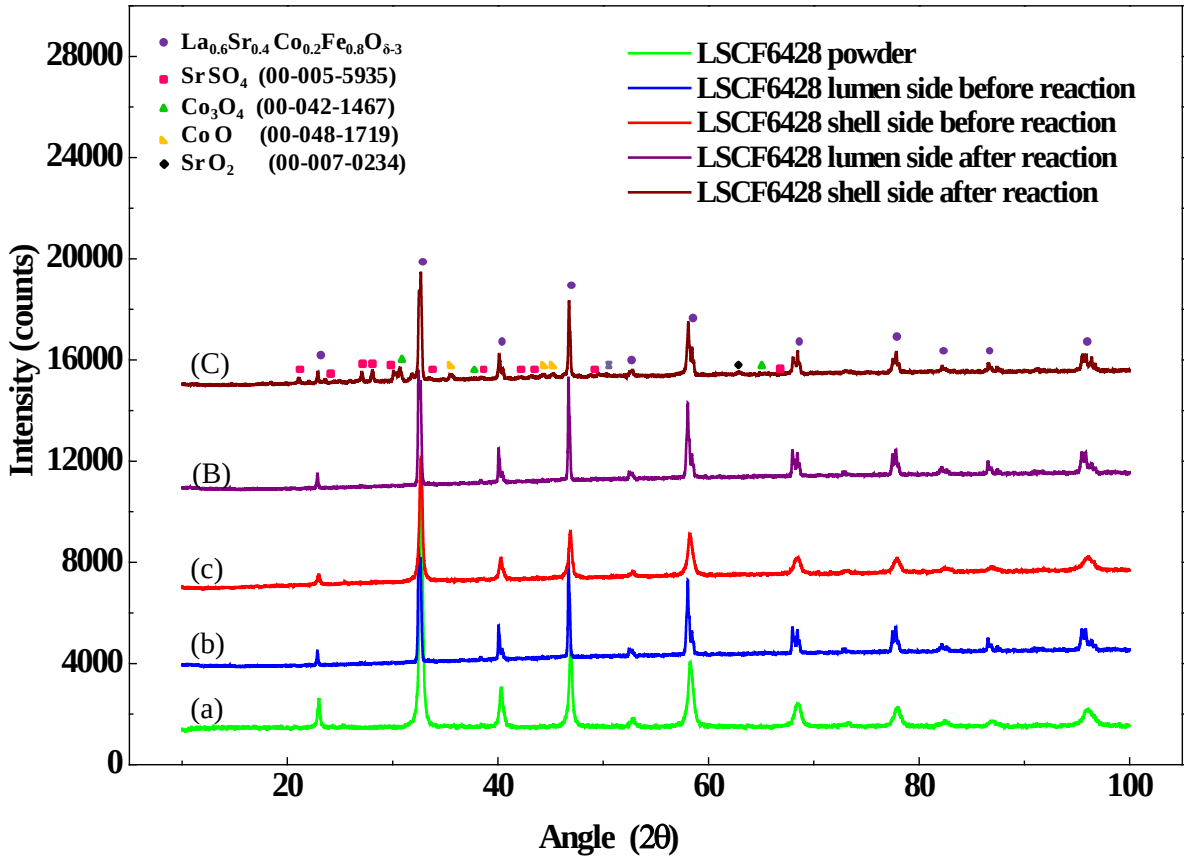

Figure 4.10 XRD patterns of the unmodified $La_{0.6}Sr_{0.4}Co_{0.2}Fe_{0.8}O_{3-\delta}$ hollow fibre membrane. LSCF6428 powder (a), Lumen side (b) and Shell side (c) before the oxygen flux measurements. Centre lumen side (B) and centre shell side (C) after 1360 hours of oxygen permeation experiments carried out under different modes of flow operation (i.e. mode 1: ALHS–air-lumen, helium-shell. Mode 2: ASHL–air-shell, helium-lumen and mode 3: air fed on the shell side of the module, while helium was fed into the lumen side membrane in opposite direction of the feed air inlet).

Considering the above-mentioned results we can infer that after oxygen flux experiments the shell side of membrane was contaminated by sulphur due to the presence of $SrSO_4$. This finding is in line with previous reports **[11-14]**. The formation of sulphur-containing phases is attributed to surface interaction of the tubular membrane with SO_2 trace presence in the air and helium flows, whereas metal oxides are due to phase segregation of the elements at the surface. Sulphur impurity and segregation of strontium and cobalt to form different crystalline oxide phases can reduce the oxygen flux capability of the LSCF6428-HFM, as was previously reported **[11-14]**.

4.6.2. Scanning Electron Microscopy (SEM):

The SEM micrographs of the cross section of the $La_{0.6}Sr_{0.4}Co_{0.2}Fe_{0.8}O_{3-\delta}$ hollow fibre membrane before and after oxygen permeation measurements are given in **figures 4.11a** and **4.11A**, respectively. It is also included the simulated images with software SPIP 6.0.9.

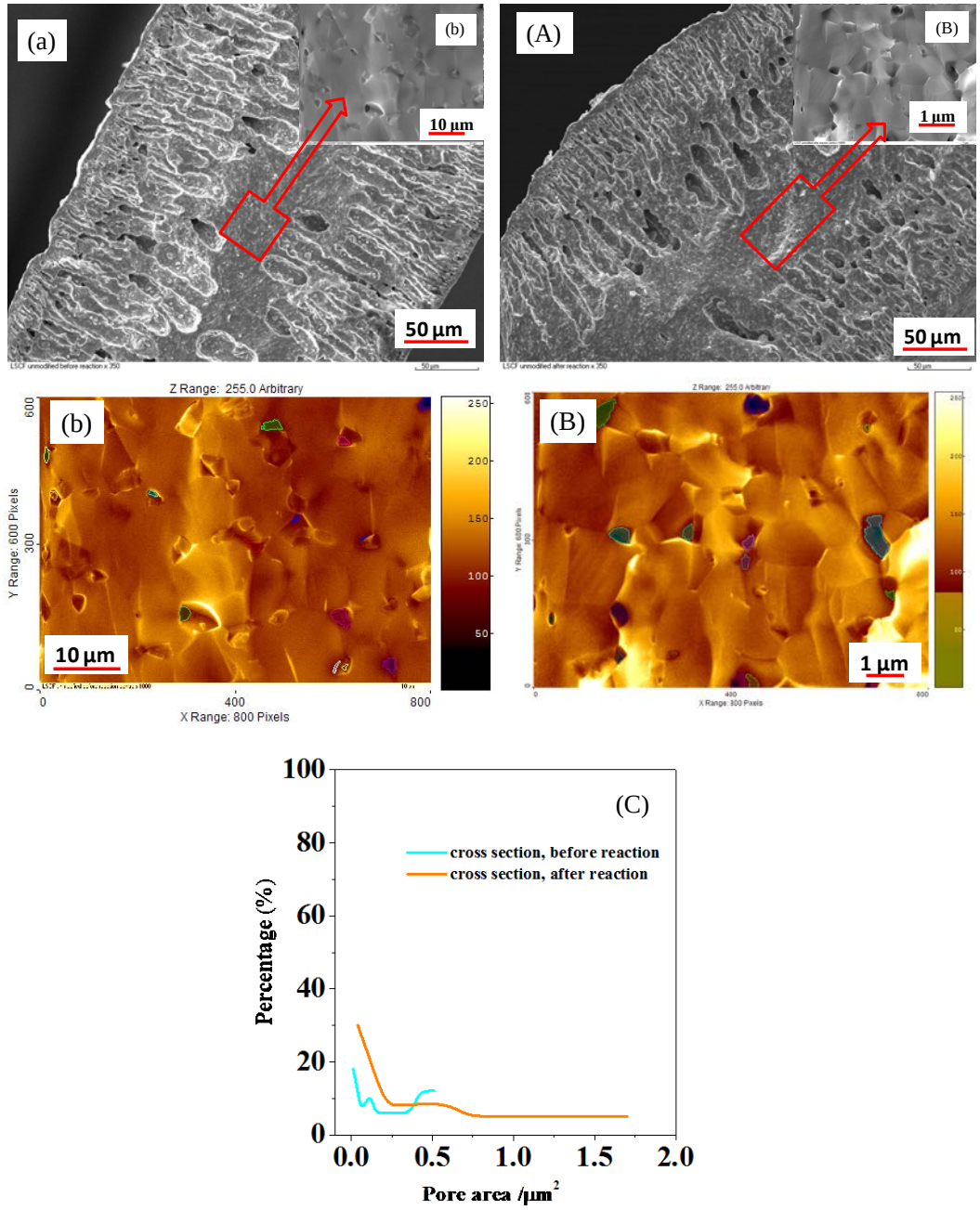

Figure 4.11 SEM images of the cross section before reaction (a) and after reaction (A). Magnification of the central dense layer before reaction (b) and after oxygen fluxes measurements (B). Distribution of the area of pore on cross section of membrane before reaction and post reaction (C)

In both micrographs it can be seen finger-like structures around the outer and inner walls and a dense structure is observed in the centre. **Figure 4.11b** and **4.11B** is the microstructure of the central dense layer of the membrane before and after reaction, respectively. When one compares both images, it can be noted that the dense layer after reaction is similar than that before reaction, in line with a previous report **[15]**. The distribution of pore area determined by simulation of the images using the software scanning probe image processor (SPIP 6.0.9), see **figure 4.11c** and **4.11C**, showed the higher percentages of pore area at values below 0.5 μm^2 for both samples, see **appendix II.12.1, figures II.14** and **II.15**.

The micrographs for centre lumen side of the LSCF6428 hollow fibre membrane before and after reaction are given in **figures 4.12a** and **4.12A**, respectively. Comparison of the panoramic images before and after reaction, clearly show that smaller crystallites decorates the grain boundaries (**figure 4.12A**).

In the magnification image for centre lumen side before and after reaction, **figure 4.12**, the perimeters of the grain boundaries were measured using SPIP 6.0.9 software. Note that the perimeter range between 0.02 and 35 μm represent around 90 % of the total grain boundary analysed for both sample, see **appendix II.12.2, figures II.16** and **II.17**. It is worth remarking that micro-wires on the grain boundary are also observed, but it was not possible to determinate their elemental composition due to resolution limitation of EDX analysis.

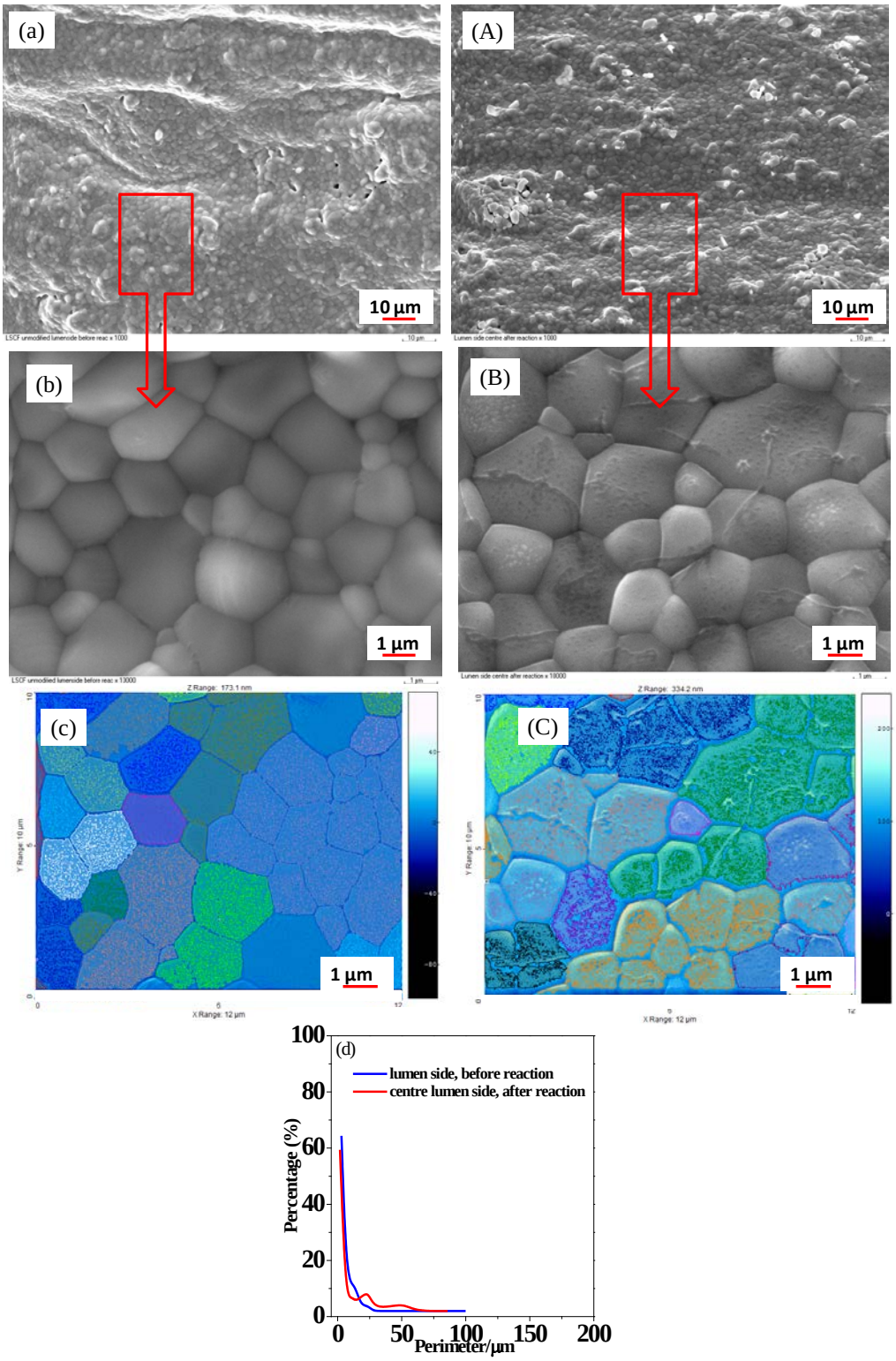

Figure 4.12 SEM micrograph of the centre lumen side before reaction (a) and image magnified (b). SEM images of the centre lumen side after oxygen fluxes measurements (A) and image magnified (B). Simulation SEM images centre lumen side before (c) and after oxygen fluxes measurements (C) and distribution of the grain boundary perimeter of centre lumen side before and after reaction.

The SEM images of the end lumen side for LSCF6428 before and post operation are given in the **figure 4.13**.

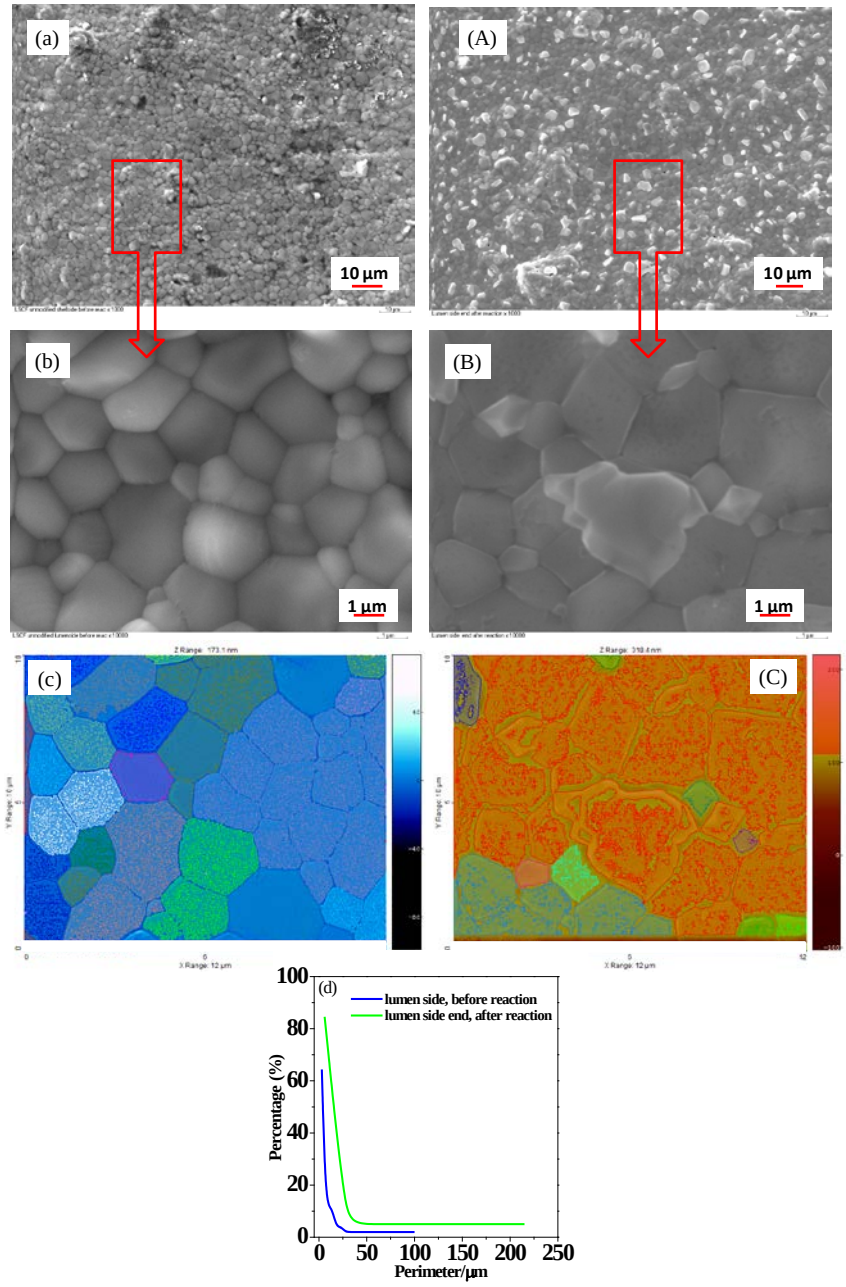

Figure 4.13 SEM images of the end lumen side before reaction (a) and its magnification (b). SEM micrograph end lumen side after oxygen fluxes measurements (A) and magnified image (B). Simulation SEM images of end lumen side before (c) and after oxygen fluxes measurements (C) and distribution of the grain boundaries perimeter of end lumen side both before and after reaction (d).

This membrane section did not show large differences in the particle size after reaction, as was confirmed in the magnified image (**figure 4.13B**). Also, note that small particles decorate the surface of the LSCF membrane.

Indeed, the microstructure of the end lumen side before and after reaction (**figure 4.13b**) showed similar overall grain boundaries perimeter between 0.02 and 25 μm, which represents around 90 % of the total analysed perimeter, see **figs. 4.13c** and **4.13C**, **appendix II.12.2, figures. II. 16** and **II. 18.**

Considering the above mentioned results obtained by SEM micrographs in the centre lumen side and end lumen side, it can be concluded that the membrane surface did not undergo morphological changes after a long operation time at high temperature in agreement with the grain boundary dimension, which did not vary compared to the post operation sample.

In **figure 4.14** is given the SEM photograph of the centre shell side before and after reaction. The magnifications of the centre shell side before reaction are shown in **figures 4.14a** and **4.14b**, it can be noted that the overall grain boundaries perimeter is between 0.002 and 3 μm, representing above 90 % of the total analysed perimeter, see **appendix II.12.3, figure II.19**. On the other hand, the magnifications of the centre shell side after reaction are given in **Figures 4.14A, B** and **C**. Note that small cavities or pores seem to be created at the interface of the grain boundaries after reaction (**figure 4.14B**) as a possible consequence of the degradation of the grain boundaries. In addition, a severe change in the morphology of the membrane can be observed, owing to the segregation of small and large particles dispersed on the membrane surface (**figures. 4.14B** and **4.14C**). A poor contrast between the remaining grain boundaries and the small particles made it difficult to obtain a good simulation of this image for this reason it was not included in the text.

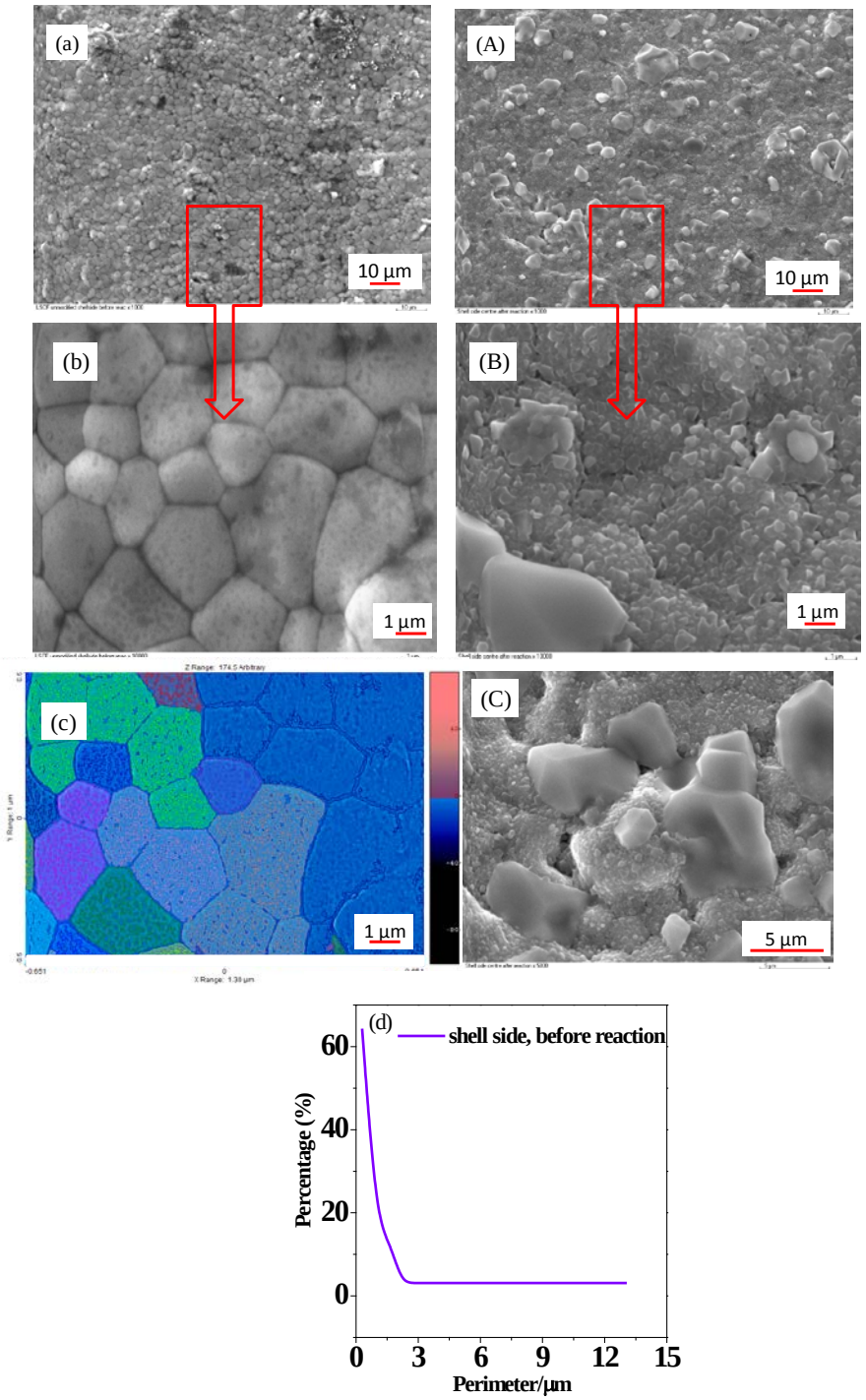

Figure 4.14 SEM micrograph of the centre shell side before reaction (a) and magnification (b), simulation by SPIP 9.0.6 (c) and grain boundaries perimeter of centre shell side before reaction (d). SEM micrograph centre shell side after oxygen fluxes measurements (A). Images magnified (B) and (C). Distribution of the grain boundary perimeter of centre shell side before reaction (d)

The SEM micrographs of the end shell side of the LSCF6428 hollow fibre membrane before and after oxygen permeation measurements are given in **figures. 4.15a** and **4.15A**,

respectively. The microstructures of the end shell side after reaction are shown in the **figures 4.15A, B** and **C**, which shown similar morphology change than that observed in the centre shell side.

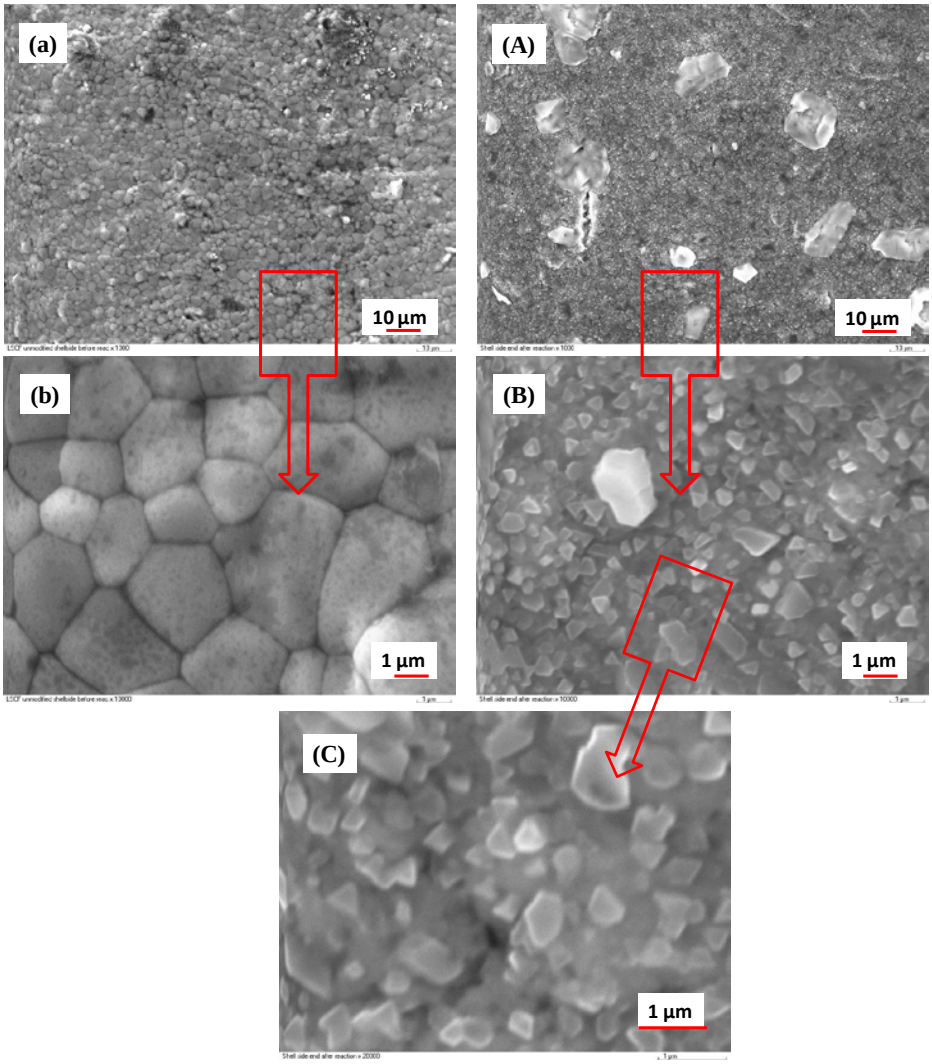

Figure 4.15 SEM micrograph of the end shell side before reaction (a) and image magnification (b). SEM micrograph end shell side after oxygen fluxes measurements (A). Image magnified (B) and (C).

Considering the above mentioned XRD and SEM results from the centre shell side and end shell side of the LSCF6428-HFM after 1360 hours of operation, it can be clearly observed a morphology change on the shell side of the membrane surface. This is attributed to kinetic demixing of mobile cations and decomposition of the membrane due to its high thermal

treatment and long operation time. Moreover, the presence of $SrSO_4$ from the possible interaction of SO_2 traces present in air and helium gases with LSCF6428-HFM at high operation temperatures contaminate the membrane or more likely to the polyethersulfone (PESf) binder used in the manufacture of the membrane, see **figure 4.10C**. In addition, the segregation of secondary crystalline phases (i.e., Co_2O_3, CoO and SrO_2) were observed on the shell side surface of the membranes after the long-term operation (**figure 4.10B**). These crystalline oxide/sulphate phases have been observed by others **[15-25]**.

4.6.3. Energy dispersive x-rays spectroscopy (EDXS)

In **table 4.1** is given the EDXS results of different zones of the LSCF6428 hollow fibre membrane before and after oxygen flux experiments, according to the zones described in **Chapter 3 (figure 3.11**). The values clearly indicated in **table.4.1** are the average atomic %, except for the elements S, Ca and Al. For more detail see **appendix II.13, figure II. 20** to where all the EDXS results are given.

It is clearly noticeable that the elemental compositions of the metals in the centre lumen side after oxygen permeation experiments showed a small change compared with lumen side before the reaction (i.e., La, Co and Fe depletion 5.1%, 1.2% and 6.3% respectively and Sr enrichment 5.9%). However, when one considers the error of the measurement of EDXS analysis the stoichiometry of the membrane bulk did not change (i.e., La0.6:Sr0.4:Co0.2:Fe0.8). Also, the end of the lumen side after reaction showed a similar stoichiometry (i.e., La0.6:Sr0.4:Co0.2:Fe0.8). Note that sulphur content of 0.5 % was detected on this membrane section; see **table 4.1** and **appendix II.13, table II.10**. The presence of Al and Ca in **table 4.1** is attributed to the sample holder of SEM analyzer and water used in the membrane preparation, respectively.

Table 4.1 Summary of EDXS results of different zones of the LSCF6428 hollow fibre membrane before and after oxygen permeation measurements.

Membrane	*Condition*	*Section (side)*	*Absolute atomic %*							*Experimental stoichiometry*
			La	*Sr*	*Co*	*Fe*	*O*	*Ca*	*S*	*Al*	
LSCF6428	**BR**	**Lumen**	**8.0**	**5.6**	**2.3**	**10.3**	**73.8**				**La0.6:Sr0.4:Co0.2:Fe0.8**
LSCF6428	AR	Centre lumen	5.1±0.92	5.9±1.13	1.2±0.50	6.3±1.11	50.4±9.52	0.1	0.5	30.5	La0.6:Sr0.4:Co0.2:Fe0.8
LSCF6428	AR	End lumen	6.3±0.6	4.2±0.63	1.7±0.5	8.8±1.05	73.8±12.9	0.1	0.4	4.9	La0.6:Sr0.4:Co0.2:Fe0.8
LSCF6428	**BR**	**Shell**	**7.2**	**5.6**	**2.2**	**9.8**	**75.4**				**La0.6:Sr0.4:Co0.2:Fe0.8**
LSCF6428	AR	Centre shell	7.2±0.78	7.6±1.06	2.9±0.59	9.1±1.2	64.7±11.6	0.3	2.9	5.3	La0.6:Sr0.4:Co0.2:Fe0.8
LSCF6428	AR	End shell	5.9±0.66	5.5±0.81	2.7±0.55	7.9±1.03	73.1±13.1	0.2	1.8	2.9	La0.6:Sr0.4:Co0.2:Fe0.8

BR before reaction; AR: after reaction

According to EDXS results, the bulk of membrane keeps its stoichiometry, although second crystalline phases were formed on shell side surface membrane during the experiments. This is attributed to the kinetic demixing of mobile cations and decomposition of the membrane over the long operation time. Similar finding were reported by Wang *et al.* and Doorn *et al.* **[5, 20-27]**.

As was discussed above, the SEM images of post-reaction membrane showed particles dispersed on the membrane surface, which were analysed by EDXS. According to this analysis, the particles exhibited a high concentration of strontium and sulphur, suggesting in line with XRD result, that these particles are mainly composed of $SrSO_4$, **appendix II.13, tables II.11, II.13, II.15** and **II.17.**

According to the results obtained from XRD, SEM and EDXS analysis both the lumen side and the shell side of the LSCF6428 hollow fibre membrane reactor after 1360 hours of operation showed an evidence for a kinetic demixing of mobile cations and decomposition of the membrane surface, although the LSCF6428 membrane stoichiometry did not change. This process seems to be more severe on the shell side likely due to the causes given below.

1. The relative high temperature on the shell side could produce hot spots due to heat transfer effect compared to the lumen side. These hot spots might induce diffusion of the metals such as La, Fe, Sr and Co leading to changes in oxidation state, coordination symmetry environment of the La, Sr and Co, Fe cations. This could provoke changes in the surface composition compared to bulk composition of the membrane because of segregation of metal oxides phases.

2. The presence of sulphur from the air and helium flows employed during the experiments. The SEM micrograph showed a severe change in morphology of the membrane, owing to the change of the grain boundary size and large particles dispersed on the membrane

surface. Those particles were analyzed by EDXS and found out that contain high concentrations of Sr, S and O, which is in agreement with the detection of $SrSO_4$ by XRD.

It is worth remarking that the oxygen permeation of the modules was not affected during long-term operation despite the evident kinetic demixing and apparent decomposition of the LSCF6428 HFM reactor.

4.7. Thermodynamic calculation.

Figure 4.17 shows the standard Gibbs free energy for various reactions that involve SO_2 as sulphuring agent and different perovskites, considering single perovskite phases due to absence of thermodynamic data for LSCF6428 perovskite. It can be appreciated that the reactions that require higher stoichiometry amount of SO_2, model molecule for sulphur generation, are thermodynamically favourable because of their lower ΔG. The dependence of ΔG at 850°C with the SO_2/O_2 ratio indicates that $CoSO_4$ and $SrSO_4$ are thermodynamically favourable for SO_2/O_2 ratio around 2.5 for both $LaCoO_3$ and $Sr_2Fe_2O_5$ when are used as model perovskite. These findings are in agreement with experimental results obtained in this work. In **appendix II.15, figures II.25** and **II.26** are given different plots of the dependence of ΔG against temperature for various reactions that involve H_2S and S_2O as sulphuring agents and different perovskite. Also, it is shown the dependence of ΔG at 850°C with the H_2S/O_2 ratio and S_2O/O_2 ratio for different perovskite; see **appendix II.15, figures.II.25** and **II.26**. Note that $CoSO_4$ and $SrSO_4$ are also thermodynamically favourable when H_2S and S_2O are considered as sulphuring agents.

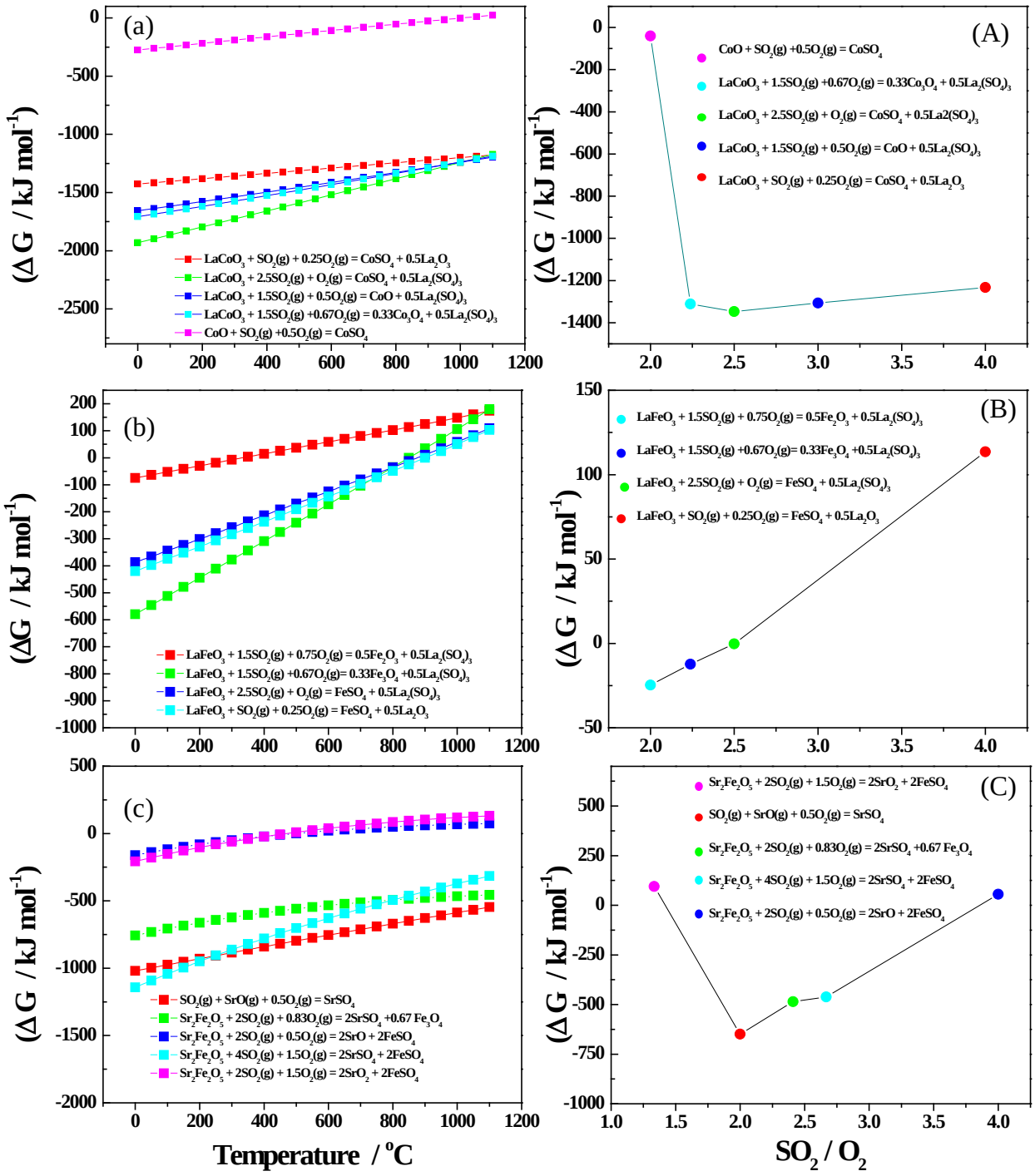

Figure 4.16 Dependence of standard Gibbs free energy with temperature for various sulphurization reactions of different perovskite.

The phase stability diagram of the Sr-O-S and Co-O-S systems is shown in **figure 4.18**. In these diagrams can be appreciated that both $SrSO_4$ and $CoSO_4$ are stable at high temperature and partial pressure of SO_2. However, when the partial pressure of SO_2 decreases the

sulphates species, particularly $CoSO_4$, produce Co and Sr oxides. Note that $SrSO_4$ requires higher temperature and lower partial pressure of SO_2 than $CoSO_4$ to be oxidised.

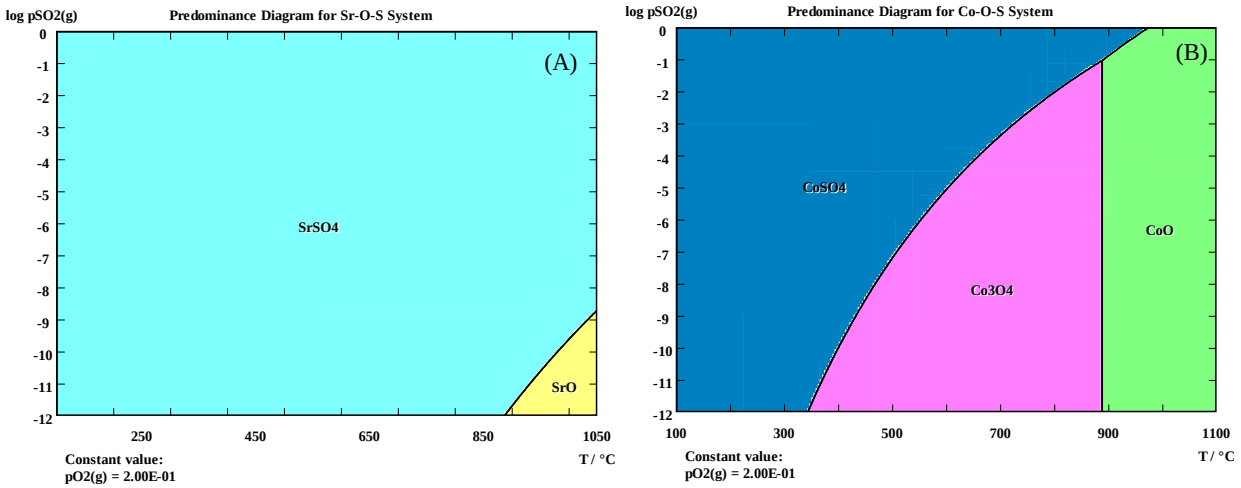

Figure 4.17 Phase stability diagrams for Sr-O-S and Co-O-S systems.

4.8. Conclusions

According our results of oxygen release and uptake experiments performed in a hollow fibre $La_{0.6}Sr_{0.4}Co_{0.2}Fe_{0.8}O_{3-\delta}$ membrane reactor can be concluded that:

1. With increased helium flow rate, an increased driving force for oxygen migration across the membrane is promoted, because the oxygen partial pressure gradient is increased.

2. The mode of flow operation mode 2 (co-current) and mode 3 (counter-current) does not affect the oxygen uptake and oxygen release experimental data.

3. Oxygen flux can be enhanced at high temperatures, because this plays an important role in bulk oxygen diffusion and the oxygen surface reaction rates.

4. The data for calculating the apparent overall rate constant are fairly well fitted at high helium flow rates, but at low helium flows the model is invalid possibly due to mass transfer effects and low Reynolds numbers ($\mathbf{Re < 2000}$).

5. The calculated apparent reaction rate constants for mode 2 (co-current) and mode 3 (counter-current) operation were similar because the oxygen flux depends mainly on the difference of oxygen partial pressure across the membrane. Furthermore, the apparent reaction rate constants were independent of the helium flow rates on the lumen side.

6. The oxygen permeation rate is limited by surface exchange on the oxygen lean side or lumen side ($\boldsymbol{R}_{ex}^{''}$) at 850°C and 900°C and the contribution of bulk diffusion on the oxygen permeation rate increased with a rise in the temperature (900°C), according to distribution of total oxygen permeation residence.

7. The LSCF6428 hollow fibre membrane reactor after 1360 hours of operation presented signs of kinetic demixing of mobile cations and sulphur contamination, according of the results obtained from XRD, SEM and EDXS analysis.

8. Thermodynamic calculation and phase stability diagram showed that $SrSO_4$ and $CoSO_4$ are facilitated under operation conditions in agreement with the experimental results.

4.9. References

[1] C. Tablet, G. Grubert, H. Wang, T. Schiestel, M. Schroeder, B. Langanke, J. Caro. Catal Today, 104, **2005**, 126.

[2] X. Tan, Y. Liu and K. Li, AIChE J. 51, 7, **2005**, 1991.

[3] A. Thursfield and I. Metcalfe, J. Solid Electrochem, 10, **2006**, 604.

[4] M. H. R. Lankhorst and J. E. ten Elshof. J. Solid State Chem. 130, **1997**, 302.

[5] B. Wang, B. Zydorczak, Z.T. Wu and K. Li, J. Membr. Sci., 344, **2009**, 101.

[6] S.J. Xu, W. J. Thomson, Chem. Engineering Science, 54, **1999**, 3839.

[7] J. W. Stevenson, I. Armstrong, R. D. Carneim, L. Pederson, and W. J. Weber, J. Electrochem. Soc., 143, 9, **1996,** 2722.

[8] R.H. Perry, D. W. Green and J. O. Maloney, Perry's Chemical Engineers' Handbook, ed. Seventh, International edition, Section 16, **1997**, 22.

[9] N. Xu, S. Li, W. Jin, J. Shi, Y. Lin, AlChE J. 45, **1999**, 12, 2519.

[10] V. G. Sathe, S. K. Paranjpe, V. Siruguri and A. V. Pimpale. J. Phys. Condens. Matter, 10, **1998**, 4045.

[11] W. Jin, S. Li, P. Huang, N. Xu J. Shi and Y. S. Lin, J. Membr. Sci., 166, **2000**, 13.

[12] A. Thursfield and I. Metcalfe, J. Solid Electrochem. 10**, 2006,** 604.

[13] J. E. ten Elshof, H. J. M. Bowmeester, H. Verweij, Appl. Catal. A: Gen.**,** 130, **1995**, 195.

[14] S. Li, W. Jin, P. Huang, N. Xu, J. Shi, Y. S. Lin, J. Membr. Sci. 166, **2000**, 51

[15] X. Tan, Z. Wang, H. Liu and S. Liu. J. Membr. Sci. 324, **2008**, 128.

[16] C. Y. Tsai, A. G. Dixon, W. R. Moser, Y.H. Ma, AlChE J. 43, **1997**, 2741.

[17] C. Y. Tsai, A. G. Dixon, W. R. Moser, Y.H. Ma, M.R. Pascucci, J. Am. Ceram. Soc., 81, **1998**, 1437.

[18] W. Jin, S. Li, P. Huang, N. Xu, J. Shi and Y.S. Lin; J. Membr. Sci., 166, **2000**, 13.

[19] R.H.E. van Doorn, H.J.M. Bouwmeester, A. J. Burggraf. Solid State Ionics 111, **1998**, 263.

[20] S. Li, W. Jin, P. Huang, N. Xu;J. Shi, Y. S. Lin, . Membr. Science 166, **2000**, 51.

[21] N. Xu, S. Li, W. Jin, J. Shi, Y. S. Lin, AlChE J. 45, 12, **1999**, 2519.

[22] X. Tan, K. Li, A. Thursfield, I. S. Metcalfe Catal., Today 131, **2008**, 292.

[23] R. V. Franca, A. Thursfield, I. S. Metcalfe. J. Membr. Sci., 389, **2012**, 173.

[24] A. A. Yaremchenko, C. Buysse, V. Middelkoop, F. Snijkers, A. Buekenhoudt, J.R. Frade, A. V. Kovalevsky. J. Membr. Sci. 428, **2013**, 123.

[25] Y. Liu, X. Zhu, M. Li, H. Liu, Y. Cong, W. Yang., Angew. Chem. Int. Ed., 52, 11, **2013**, 3232.

[26] D. Schlehuber, E. Wessel, L. Singheiser, T. Markus, J. Membr. Sci., 351, **2010**, 16.

[27] B. Wang, B. Zydorczak, D. Poulidi I.S. Metcalfe, K. Li, J. Membr. Sci., 369, **2011**, 526.

Chapter 5.

Oxygen flux through the LSCF6428 hollow fibre membrane modified with Co_3O_4 and 5%Ni-LSCF6428 catalyst

5. Oxygen permeation through the LSCF6428 hollow fibre membrane modified with a Co_3O_4 and 5%Ni-LSCF6428 catalyst

The oxygen permeation, oxygen release and oxygen uptake of the $La_{0.6}Sr_{0.4}Co_{0.2}Fe_{0.8}O_{3-\delta}$ hollow fibre membrane which has been modified with a Co_3O_4 and 5%Ni-LSCF6428 catalyst has been studied under two operation flow modes (mode 1 and 2) and two temperatures (850°C and 900°C). Also, the apparent rate constant was determined from the model developed in chapter 4 and the results obtained are compared with data from unmodified LSCF6428-HFM. In addition, both reactors (i.e. Co_3O_4/LSCF6428HFM and 5%Ni-LSCF6428/LSCF6428-HFM) have been characterised by techniques such as XRD, SEM and EDX.

5.1. Oxygen permeation through the LSCF6428 hollow fibre membrane modified with cobalt oxide at 850°C and 900 °C

The oxygen permeation behaviour of the LSCF6428 hollow fibre membranes coated with cobalt oxide (Co_3O_4/LSCF6428-HFM) for two modes of operation are shown in **figure 5.1**. mode 1 corresponds to the air fed on the lumen side of the membranes and the helium sweep on the shell side in co-current flow **(figure 5.1A**). It can be observed that the oxygen permeation increases as helium flows rises. However, the oxygen permeation trend followed a non-linear behaviour, indicating that the driving force of oxygen across the membrane is a function of the operating helium flow rate. This may be due to the reduction of the oxygen partial pressure side when increasing the helium flow rate, which promotes an increasing driving force for oxygen permeation. Similar behaviour for the unmodified LSCF6428 hollow fibre membrane at different conditions has been reported previously **[1, 2]**. Note that

oxygen permeation behaviour from 100 to 150 ml min^{-1} of Air flow was very similar, this is probably due to the small and negligible effect of gas–solid mass transfer resistances (steps 1 and 5), **figure 2.4**, on the oxygen permeation rate.

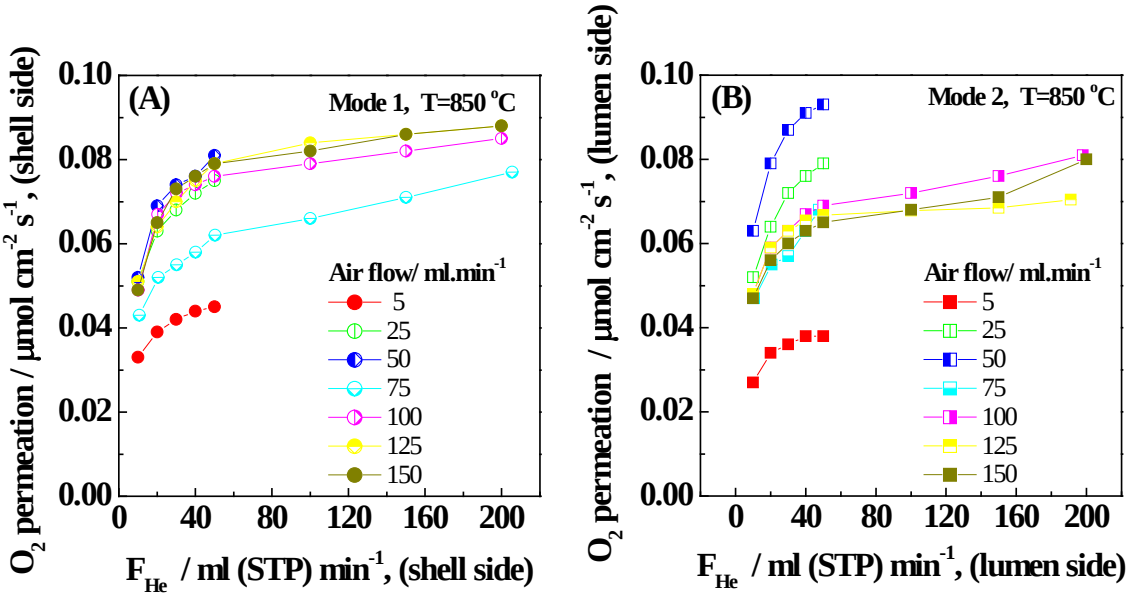

Figure 5.1 Oxygen permeation of the Co_3O_4/LSCF6428-HFM system under two different modes of operation at 850 °C. (A) mode 1, air flow is in lumen side of membrane. (B) mode 2, air flow is in shell side of membrane.

Figure 5.1B corresponds to the second mode of operation where the air is fed on the shell side of the membrane and the helium sweep is on the lumen side in concurrent flow. Comparing the two operation modes (i.e. mode 1 against mode 2), the oxygen permeation for mode 1 is slightly higher than oxygen permeation from mode 2 (**figure 5.1**). Except for the oxygen flux measurements carried out at 50 ml min^{-1} of air flow rate, where an opposite behaviour was observed in **figure 5.1B**. Indeed, this was the first experiment carried out under the second mode of operation. This opposite behaviour is tentatively attributed to either a partial reduction of the cobalt oxide catalyst with the carrier helium flow during the first mode experiments or uncertainty in the experimental data. This finding is likely

associated to the fact that the Co_3O_4 catalyst is not stable at elevated temperatures because of easy oxygen loss from its structure that changes the valence from Co^{3+} to Co^{2+} [**8**].

On the other hand, the larger oxygen flux in mode 1 relative to the mode 2 is attributed to differences in surface areas between shell side and lumen side. It is envisaged that cobalt oxide catalyst coated on the shell side of the membrane could decrease the specific surface area in that membrane side. This would be reflected in a lower oxygen flux compared with the oxygen permeation from mode 1. Tan *et al*. **[1]** reported for unmodified LSCF6428 hollow fibre membrane an opposite behaviour to the trend observed here. This difference may be attributed to the surface area decrease produced by cobalt oxide catalyst coating over the shell side.

The **figure 5.2** shows the oxygen permeation measurements at 900 ˚C for Co_3O_4/LSCF6428-HFM under mode 2.

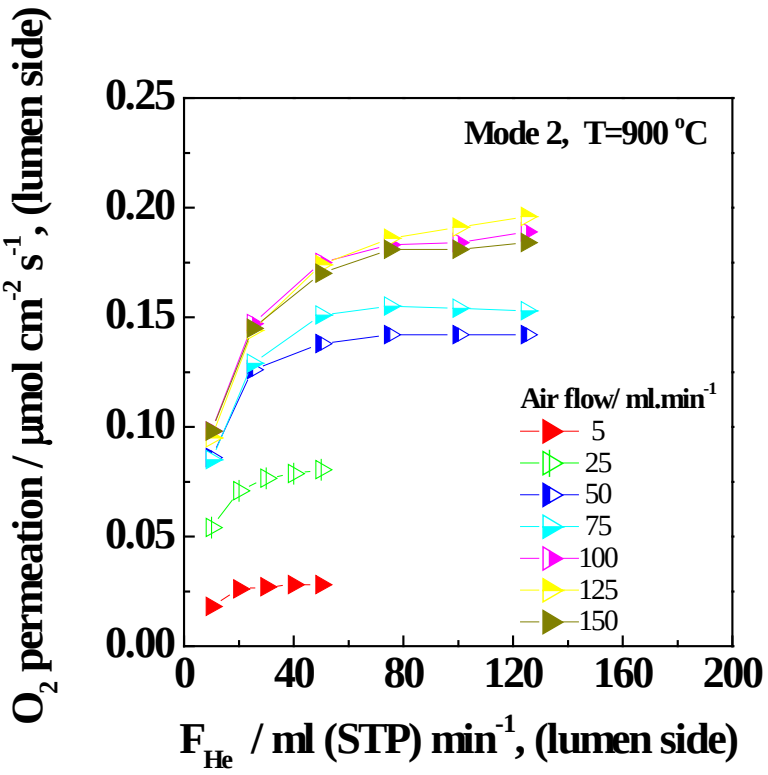

Figure 5.2 Oxygen permeation of the Co_3O_4/LSCF6428-HFM system under mode 2 at 900˚C

The oxygen flux increases with rising helium flows from 5 to 150 ml min^{-1}, this may be due to the diminution of the oxygen partial pressure side when increasing the helium flow rate, which enhances the driving force for oxygen permeation **[1, 2]**. On the other hand, it can be clearly appreciated that oxygen permeation increases as air flow becomes higher. However, at high air flows (100, 125 and 150 ml min^{-1}) the oxygen flux did not vary, indicating that the effect of gas-solid mass transfer resistances is negligible under these conditions [**3-7**].

The oxygen permeation against the air flow at different temperatures is illustrated in **figure 5.3**. This shows that the oxygen flux at 850˚C for mode 1 is slightly higher than the values obtained under mode 2. This trend is attributed to the larger oxygen partial pressure difference between lumen and shell sides as a consequence of the catalyst coated on the shell side.

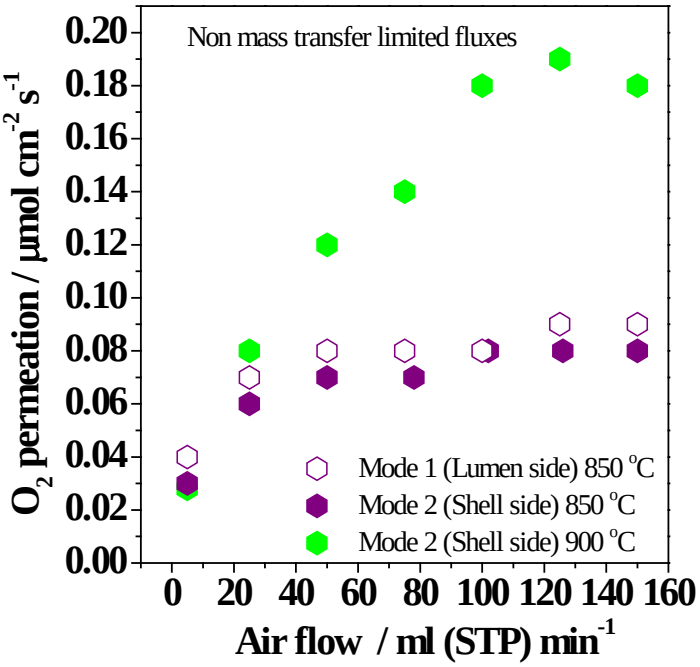

Figure 5.3 Comparison of the oxygen permeation versus air flow for Co_3O_4/LSCF6428-HFM system under two modes of flow operation at 850 °C and 900 °C

In contrast, the oxygen permeation measurements at 900 ˚C were significantly higher than the values obtained at 850 ˚C. Note that the air flow required for obtaining similar oxygen permeation was higher (i.e. 100 ml min^{-1}) at 900˚C than that obtained at 850˚C (i.e. 50 ml

min^{-1}). A similar tendency and similar oxygen permeation values were obtained by Tan *et al.* **[1]** and Thursfield *et al.* **[9]**. This finding suggests that the temperature plays an important role in the oxygen driving force across the membrane reactor and also in the oxygen surface reaction rates and the bulk oxygen diffusion **[1]**.

5.2. Oxygen release and oxygen uptake using mode 2 of operation on Co_4O_3/LSCF6428 HFM.

In order to compare the oxygen release with the oxygen uptake, an experiment on a fresh Co_4O_3/LSCF6428-HFM reactor was carried out, increasing the temperature at 0.2°C.min^{-1} up to 850 °C (72 hours). The experiment was made using the mode 2 of flow operation and the oxygen release (µmol sec^{-1}) and oxygen uptake (µmol sec^{-1}) were calculated from eqn. (3.3) and (3.4), respectively.

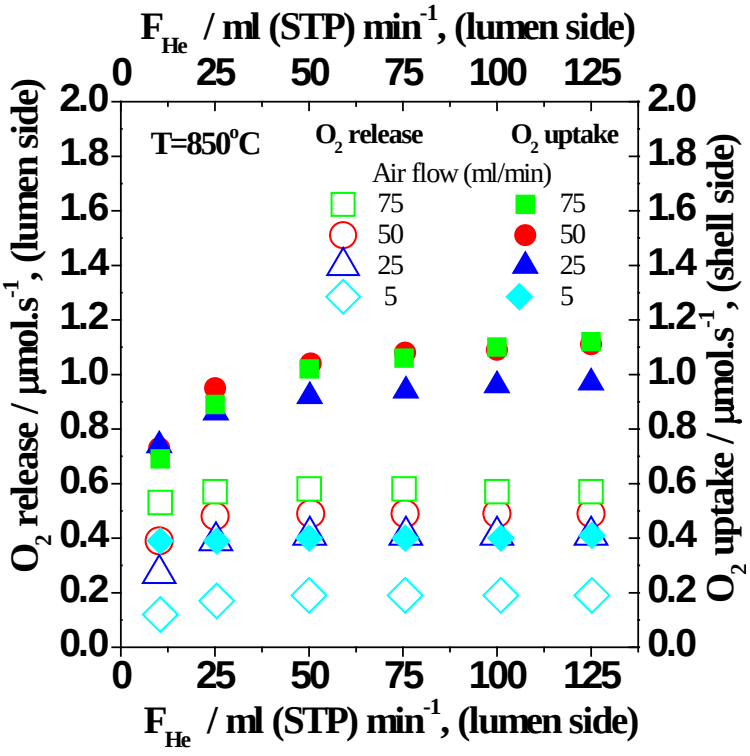

Figure 5.4 Comparison between oxygen uptake and oxygen release against helium flow at 850 ˚C.

The results are compared in **figure 5.4**; it can be observed that oxygen uptake measurements are higher than the oxygen release values. This difference is tentatively attributed to oxygen incorporation to the $Co_3O_4/La_{0.6}Sr_{0.4}Co_{0.2}Fe_{0.8}O_{3-\delta}$ hollow fibre membrane structure, as was previously determined for unmodified LSCF6428-HFM (see **Chapter 4**). To verify these statement further experiments were carried out.

To find out the effect of air dilution (i.e. air was diluted with helium to obtain 15 vol. % O_2) under the mode 2 an experiment was carried out (see **figure 5.5**). It can be noted that the oxygen release and the oxygen uptake present a better agreement, but both measurements did not converge. According to this result, it was decided to measure the oxygen release and the oxygen uptake for a longer period of operation.

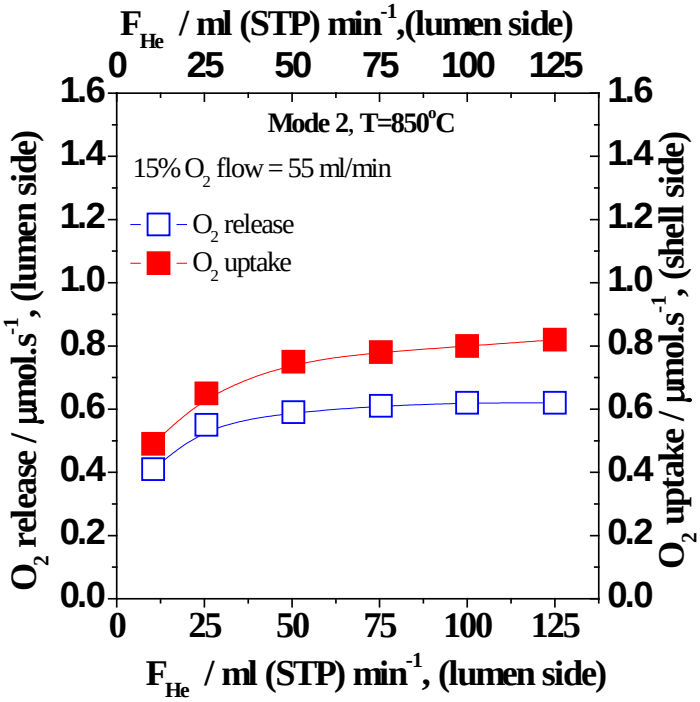

Figure 5.5 Dependence of oxygen uptake and oxygen release versus helium flow at 850 °C using a mixture 15 % O_2

In **figure 5.6** are given the measurements obtained from Co_3O_4/LSCF6428-HFM reactor under mode 2. It can be observed that oxygen release increased while oxygen uptake held

constant upon operation time where the air and helium flow were 50 ml (STP) min^{-1}, **figure 5.6A**.

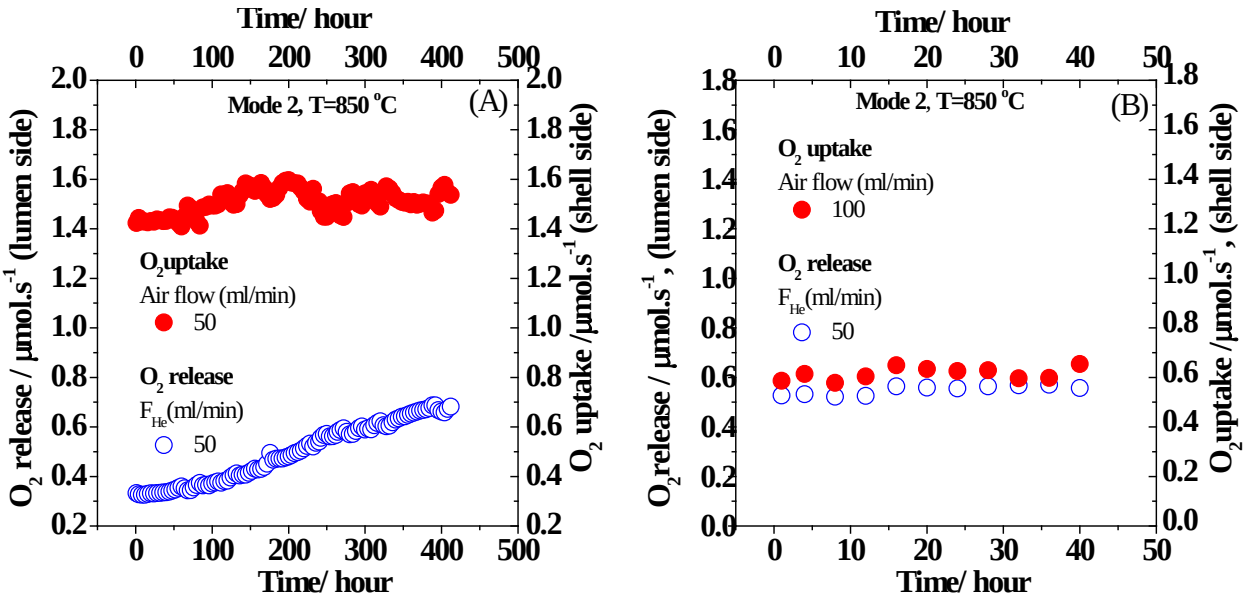

Figure 5.6 Oxygen release and oxygen uptake as a function of time for 50 ml.min^{-1} of air flow (A) and 100 ml.min^{-1} of air flow (B).

On the other hand, when the air flow was increased to 100 ml min^{-1} and helium flow was held at 50 ml min^{-1} under mode 2, both measurements (i.e. oxygen release and oxygen uptake) immediately converged, **figure 5.6B**. This is tentatively attributed to the increase of the amount of oxygen that permeates across the membrane, which rapidly achieves the steady state.

5.3. Calculation and comparison of oxygen permeation resistance.

The distributions of total permeation resistance of Co_3O_4-LSCF6428HFM reactor was determining using the eqns 4.1 to 4.4 at 850°C [**3**] and the data are given in the **figure 5.7.** It can be appreciated that at low helium flow (i.e., 10 ml min^{-1}) the resistance of surface exchange at the oxygen lean side or lumen side ($R_{ex}^{''}$) was between 58 and 44 %, indicating that $R_{ex}^{''}$ controls the oxygen permeation rate. On the other hand, $R_{ex}^{'}$ (27-35 %) and R_{diff}

(15-17 %) showed inferior contribution to the overall oxygen permeation rate in the distribution of total permeation resistance at 850°C, **appendix III.1, figure III.1**.

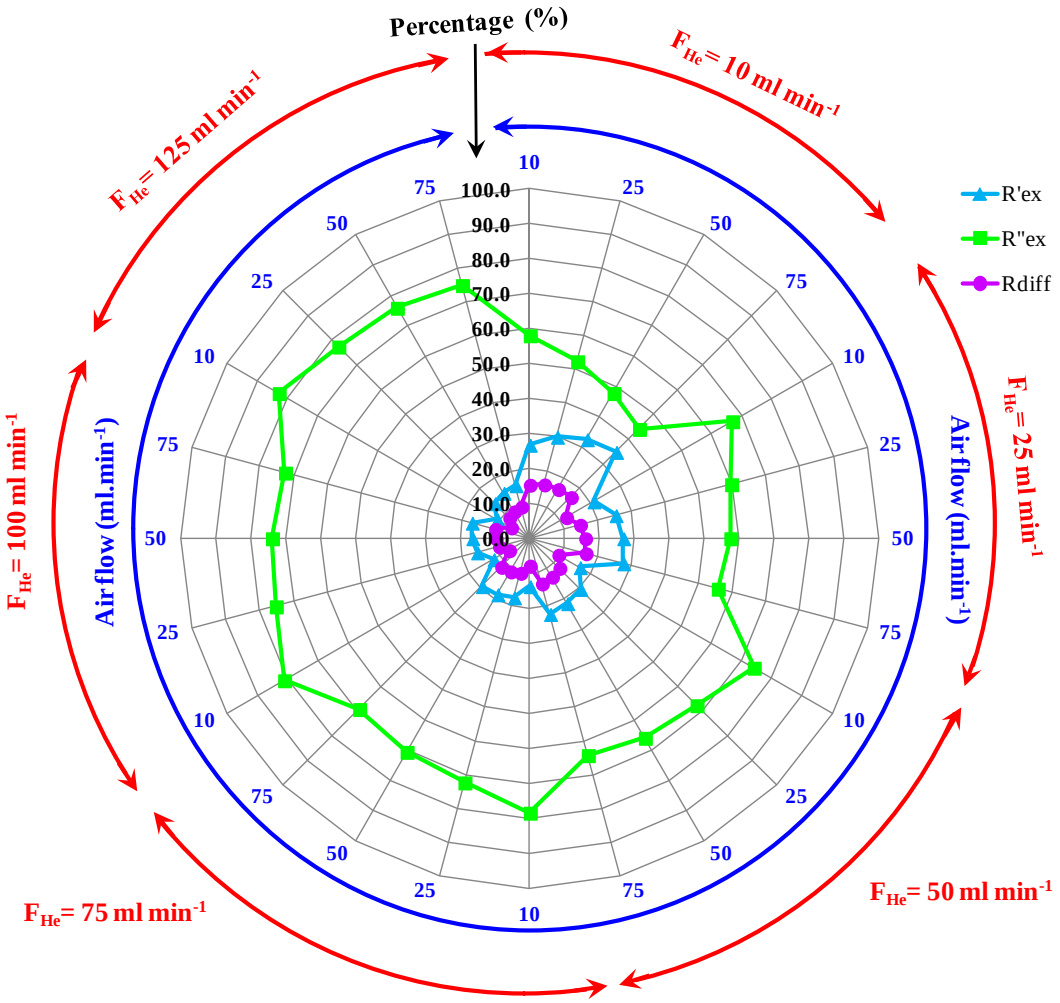

Figure 5.7 Effect of air and helium flows on the distribution of total permeation resistance for Co_3O_4/LSCF6428-HFM at 850°C.

In addition, according to the results shown in **figure 5.7**, it can be observed that $\boldsymbol{R}_{ex}^{''}$ slightly decrease and $\boldsymbol{R}_{ex}^{'}$ increase slightly with increasing air flow rate. Furthermore, at helium flows between 25 and 125 ml min^{-1}, $\boldsymbol{R}_{ex}^{''}$ gradually increased up to 83 % whilst $\boldsymbol{R}_{ex}^{'}$ and $\boldsymbol{R}_{diff}$ decreased at helium flow above 10 ml min^{-1}. This result suggests that oxygen permeation rate is limited by surface exchange on the oxygen lean side or lumen side ($\boldsymbol{R}_{ex}^{''}$) at 850°C, **figure 5.8** and **appendix III.1, figure III.1**.

5.4. Apparent reaction rate constants from Co_3O_4/LSCF6428-HFM under mode 2 of operation flow at 850°C

The dependence of the apparent reaction rate constants calculated from eqn. (3.23) for Co_3O_4/LSCF6428-HFM reactor with He flow is given in **figure 5.8.**

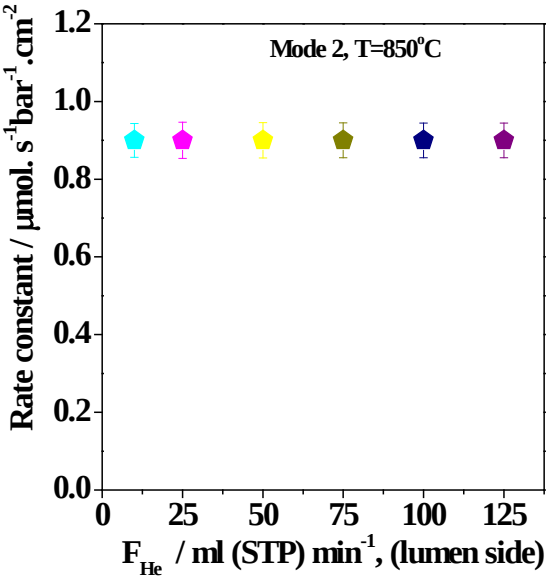

Figure 5.8 Apparent reaction rates constant for different helium flows under second mode of flow operation at 850°C

Note that the apparent rate constant did not change with helium flow, possibly due to the presence of Co_3O_4 in the shell side that catalyses the dissociation of the oxygen molecule [**10**], which is reflected on the apparent rate constant (i.e., 0.9 µmol sec^{-1} $bar^{-1}cm^{-2}$). The apparent activation energy was not calculated due to the absent of apparent rate constant at 900°C, since the mole of oxygen outlet in shell side was not measured during these experiments.

5.5. Characterization of the Co_3O_4/LSCF6428-HFM system before and after reaction by different techniques.

5.5.1. X-ray diffraction (XRD).

The diffraction profiles for the Co_3O_4/LSCF6428-HFM system before and after 672 hours of oxygen permeation measurements are shown in **figure 5.9**.

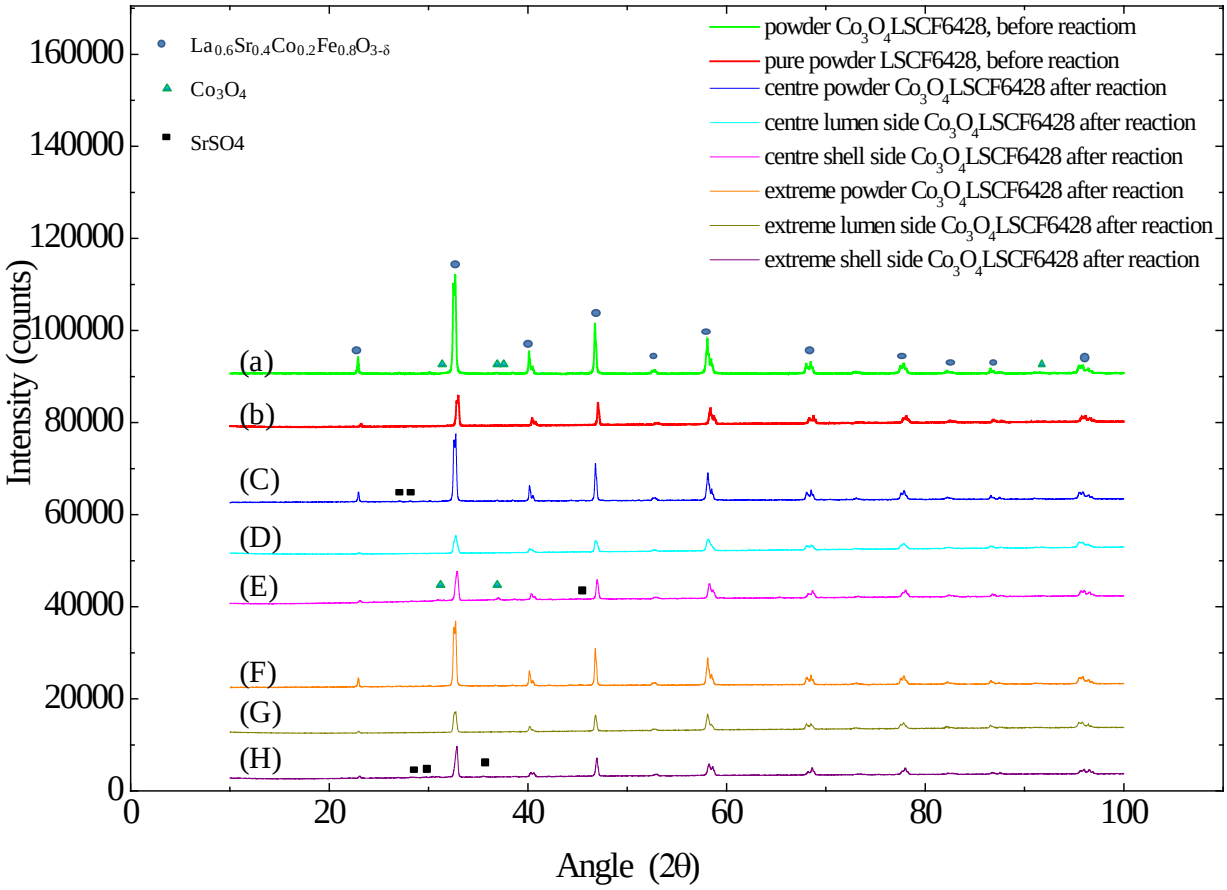

Figure 5.9 XRD patterns of the hollow fibre membrane $La_{0.6}Sr_{0.4}Co_{0.2}Fe_{0.8}O_{3-\delta}$ modified with cobalt oxide catalyst. Unmodified LSCF6428 powder (a), Co_3O_4/LSCF6428 powder (b), before the oxygen permeation measurements. Centre powder (C), centre lumen side (D), centre shell side (E) and powder end HFM (F), end lumen side (G) and end shell side (H) are after 672 hours of oxygen permeation experiments

Both the XRD patterns for unmodified LSCF6428-HF and Co_3O_4/LSCF6428-HFM display the sign characteristic of the perovskite phase presents in the hollow fibre membrane (i.e. $La_{0.6}Sr_{0.4}Co_{0.8}Fe_{0.2}O_{3-\delta}$) **[11]** as the main crystalline phase (**figures 5.9a** and **5.9b**). On the other hand, the XRD pattern for Co_3O_4/LSCF6428-HFM also presented a secondary crystalline phase (i.e., Co_3O_4 (00-042-1467)) because of deposition of the cobalt oxide catalyst on the surface of the hollow fibre membrane (shell side). The crystal size for lumen side and shell side before reaction was around 22 nm (0.022 μm) and 23 nm (0.023 μm), respectively, **appendix III.2, table III.1**.

In **figures 5.9C, 5.9D** and **5.9E** are given the diffraction profiles of the centre powder, centre shell side and lumen side of the Co_3O_4/LSCF6428-HFM after 672 hours of operation, respectively. It can be observed that all XRD profiles exhibit not only the principal crystalline phase of the LSCF6428, but also the cobalt oxide and trace amounts of $SrSO_4$ both in the centre powder **(figure 5.9C**) and centre shell side (**figure 5.9E**). The crystal size of the centre shell side and centre lumen side of Co_3O_4/LSCF6428-HFM reactor after reaction are 26 nm (0.026 μm) and 22 nm (0.022 μm), respectively, see **appendix III.2, table III.1**.

The XRD patterns for powder sample from the end of the HFM, end shell side and end lumen side of the Co_3O_4/LSCF6428-HFM after 672 hours of oxygen permeation measurements are shown in **figures 5.9F, 5.9G** and **5.9H**. It can be clearly noted that the principal crystalline phase is LSCF6428 for all samples whereas trace amounts of $SrSO_4$ were also observed for the end shell side sample. Furthermore, the crystal size for end shell side and end centre lumen side are 26 nm (0.026 μm) and 22 nm (0.022 μm), respectively see **appendix III.2** and **table III.1.**

Considering the above-mentioned results we can infer that after oxygen permeation experiments the shell side of the membrane was contaminated by sulphur (i.e. $SrSO_4$) in line with previous reports **[2, 12-17]**. Indeed, Thursfield and Metcalfe have also found traces of sulphur on the membrane surface (i.e. $SrSO_4$ and $CoSO_4$) **[17]**. They associated the presence of these phases to sulphur impurity both in the air and helium gases employed during the experiments. According to previous reports in the literature **[2, 12-17]**, these contaminants may can decrease the oxygen permeation capability of the LSCF6428-HFM system. It is worth remarking that the crystalline size of shell side and lumen side post operation (672 hours) did not change compared to the crystalline size of both membrane sides before reaction. This finding suggests that the reaction atmosphere did not affect the crystalline size of Co_3O_4/LSCF6428-HFM reactor.

5.5.2. Scanning electron microscopy (SEM).

The SEM micrographs of the cobalt oxide deposited on the LSCF6428-HFM system before oxygen permeation measurements are given in **figure 5.10**.

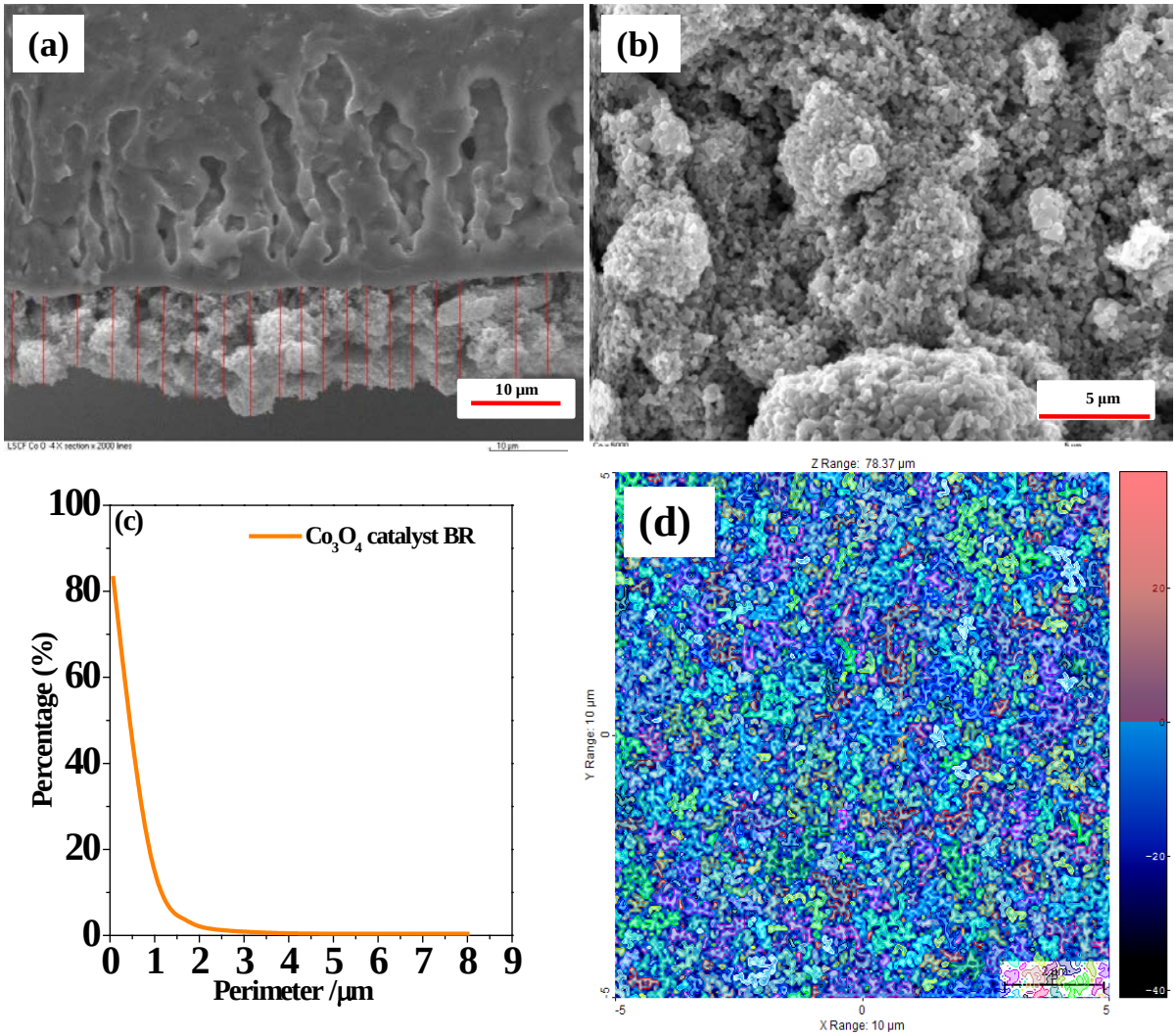

Figure 5.10 SEM images of the cross section of the Co_3O_4/LSCF6428-HFM (a) and Co_3O_4 catalyst in shell side (b), distribution of the catalyst particle perimeter before reaction (c), simulated image of Co_3O_4 catalyst in shell side of LSCF6428-HFM (d).

Figure 5.10a corresponds to cross section of the Co_3O_4/LSCF6428-HFM. It can be observed the dense outer skin in line with previous reports **[1, 2, 16, 17]**. The shell side of the Co_3O_4/LSCF6428-HFM shows well-distributed Co_3O_4 particles with a thickness of 29 µm

(**figures. 5.10b** and **5.10d**). The perimeter of the Co_3O_4 particle with irregular shapes is between 0.07 and 3 µm, see **figures. 5.10c, appendix III.3, figures. III. 4** and **III.5**.

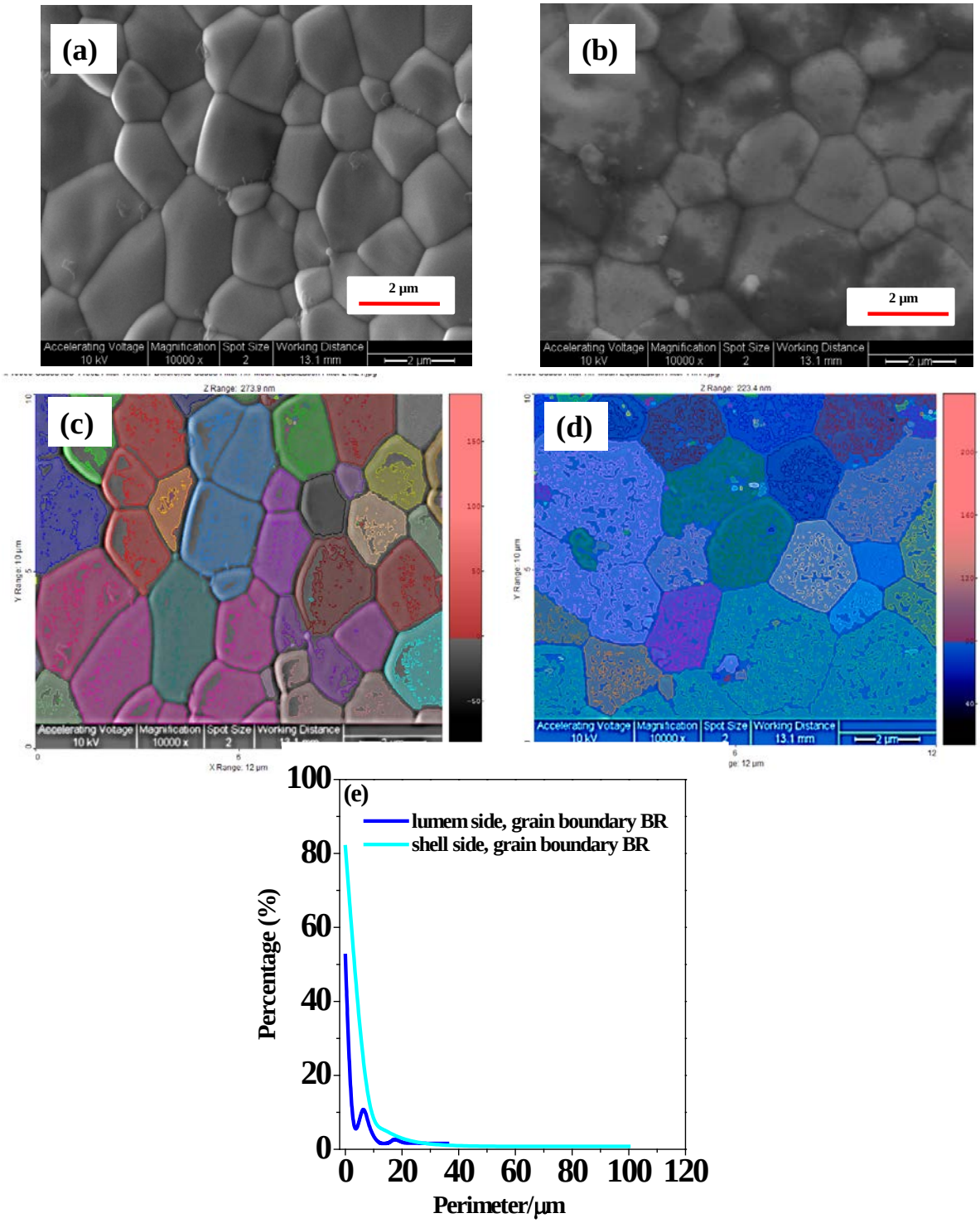

Figure 5.11 SEM micrographs of the lumen side (a) and shell side (b) before oxygen permeation, images simulated of both lumen (c) and shell side (d). Distribution of the grain boundary perimeter of lumen side and shell side before reaction (e).

The microstructure of the shell side and lumen side before reaction are given in **figure 5.11**. In **figures 5.11c, 5.11d** and **5.11e**, it can be observed that 96 % of the grain boundary perimeters are between 0.02 and 20 μm for both sides based on the simulated images by SPIP 6.0.9 software.

The SEM images of the Co_3O_4/LSCF6428-HFM cross section after oxygen permeation are shown in the **figures 5.12A** and **5.12B**. It can be clearly appreciated in both photographs the finger-like layer around the outer and inner walls and the dense layer in the centre. The **figures 5.12C** and **5.12D** images belong to the microstructure of the central dense layer of the membrane after the reaction. Small cavities can be clearly observed, suggesting that some porosity is still present, even in the dense layer.

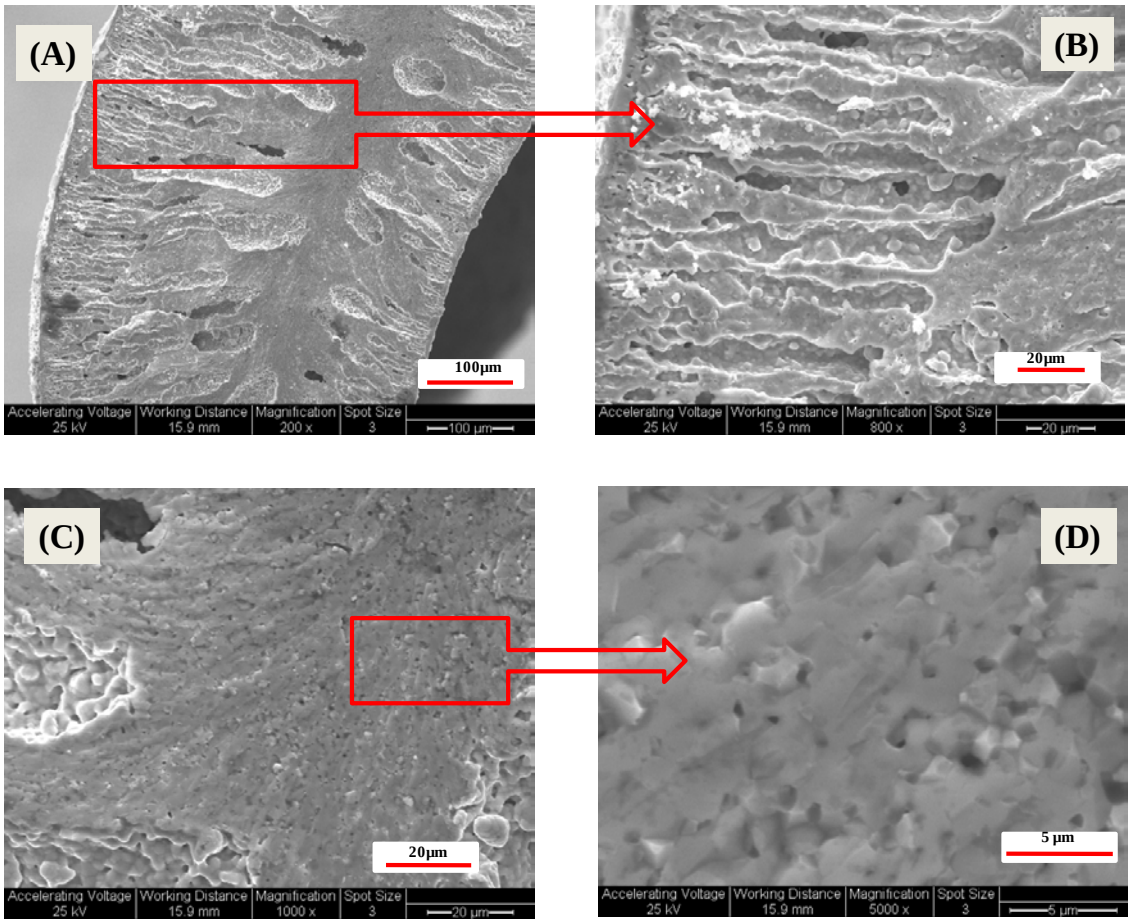

Figure 5.12 SEM micrographs cross section of the Co_3O_4/LSCF6428-HFM after oxygen permeation. Cross section (A), Finger like image magnified (B), central dense layer (C) and image magnified (D).

The SEM micrographs of the centre shell side of the Co_3O_4/LSCF6428-HFM post operation are given in **figure 5.13**. The **figures 5.13A** and **5.13B** correspond to centre shell side and simulated images, respectively. Comparison the **figures 5.10b** (before reaction) and **5.13A** (post reaction) can be observed the agglomeration of the cobalt oxide particle after oxygen permeation experiments, as a consequence of the high operation temperature. Indeed, the distribution of the grain particle perimeter of cobalt oxide catalyst increased from 0.07 to 3 μm (before reaction) up to 0.14 to100 μm for 98 % of the overall grain particle perimeter measured (see **figure 5.13C** and **appendix III.3, figures III.4** and **III.5).**

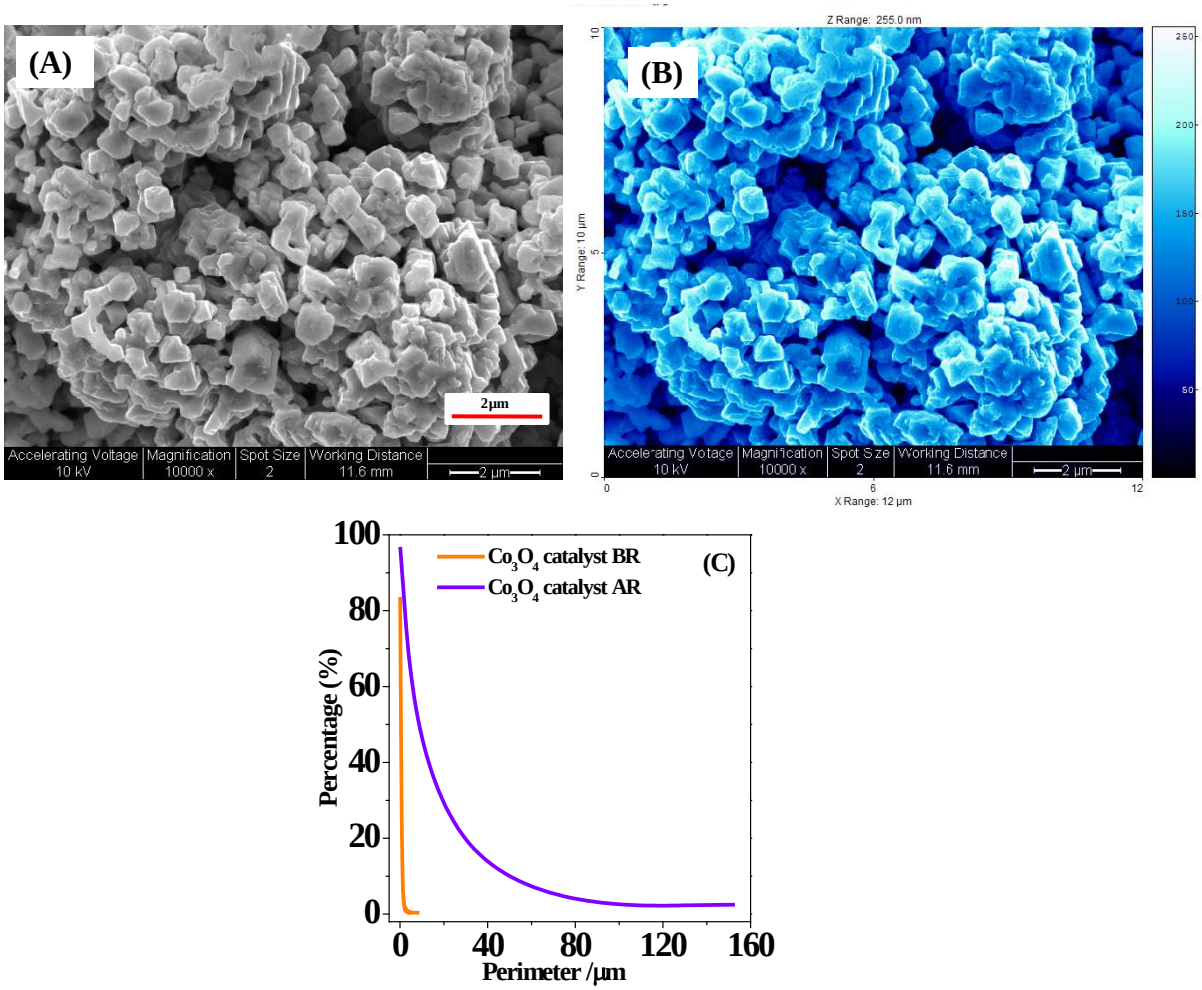

Figure 5.13 SEM image magnified of the centre shell side after oxygen permeation. (A) and simulated image (B). Distribution of the grain particle perimeter of shell side (C)

The SEM micrographs of the centre lumen side after reaction are shown in **figure 5.14**.

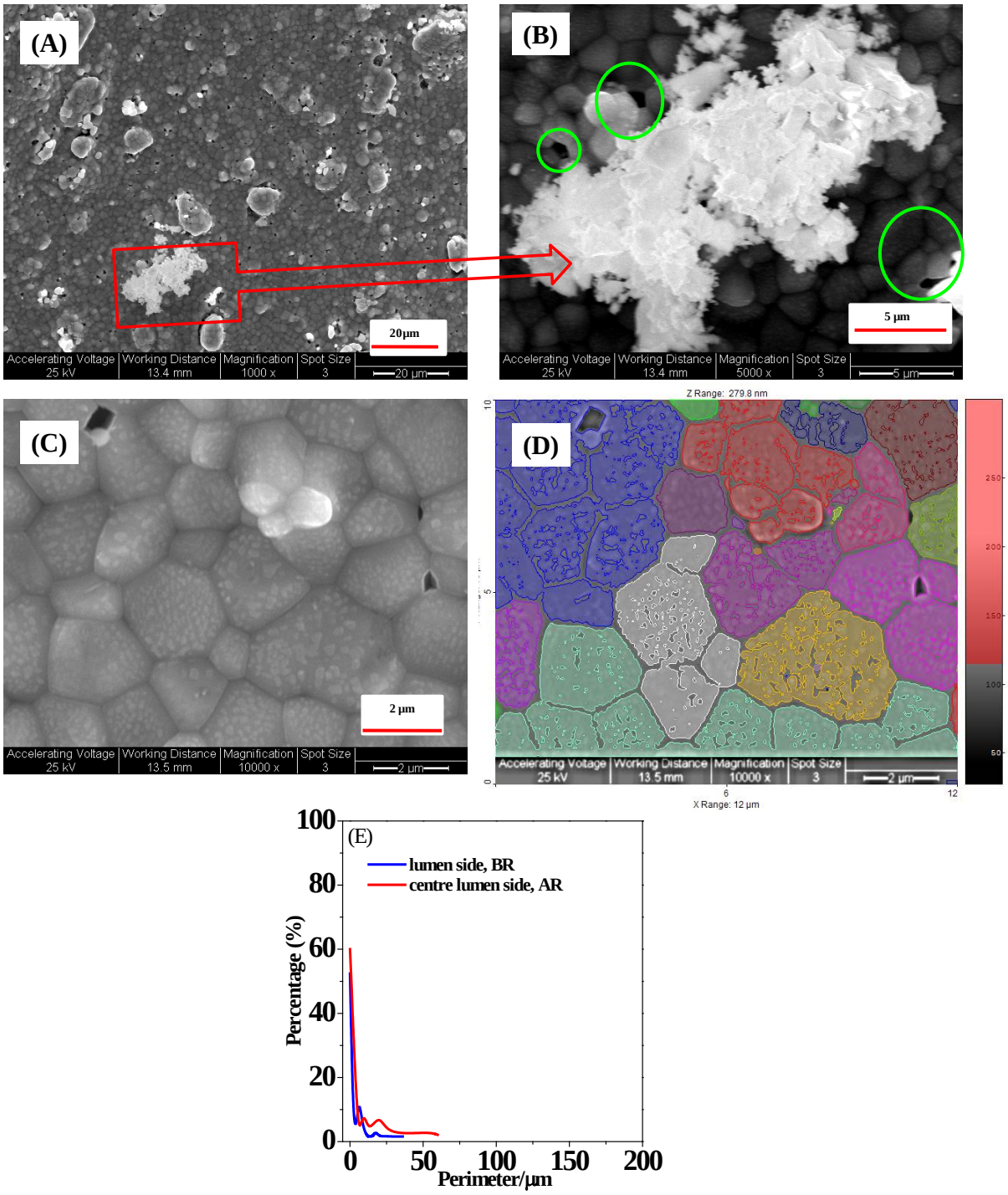

Figure 5.14 Micrograph of the centre lumen side (A), images magnified (B,C) and image simulated by SPIP6.0.9 (F). Distribution of the grain particle perimeter of shell side (G) and grain boundary perimeter of lumen side (H), before and after reaction, respectively

It can be clearly visualized that the range of the grain boundary perimeter (i.e., 0.03 and 25 µm) did not vary with respect to the grain boundary distribution of the lumen side (0.02 and 24 µm) before reaction. These ranges represent between 93 and 99 % for the overall grain particle perimeter measured (**figure 5.14E**). Also note that small cavities are apparently formed at the interface of some grain boundaries, according to the microstructure image for the centre lumen side (**figures 5.14B** and **5.14C).** This region boundary has usually a high oxygen vacancy concentration and therefore permits diffusion of lattice oxygen much faster across the membrane **[18-21].**

The microstructure of the end shell side of the Co_3O_4/LSCF6428-HFM after oxygen permeation is shown in **figure 5.15.**

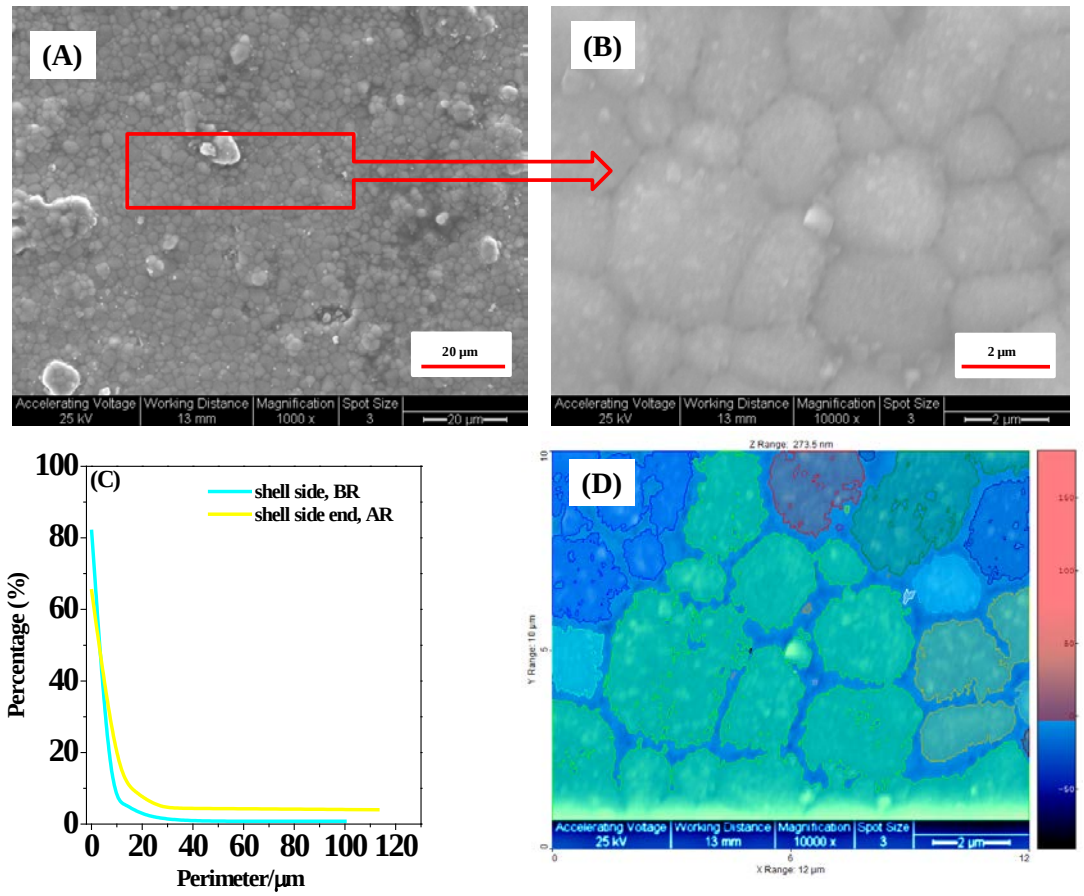

Figure 5.15 SEM images of the end shell side (A), images magnification (B) and images simulate (D). Distribution of the grain boundary perimeter of the end shell side (C)

It can be appreciated that the range of the grain boundaries perimeter for shell side (i.e., 0.03 to 27 μm) did not vary relative to the grain boundary perimeter from the shell side (0.02-20 μm) before reaction, see (**figure 5.15C**). The perimeter ranges represented 93 % and 97%, respectively, of the overall grain boundary perimeter measured.

The microstructures of the end lumen side of the Co_3O_4/LSCF6428-HFM after oxygen flux experiment are given in **figure 5.16**.

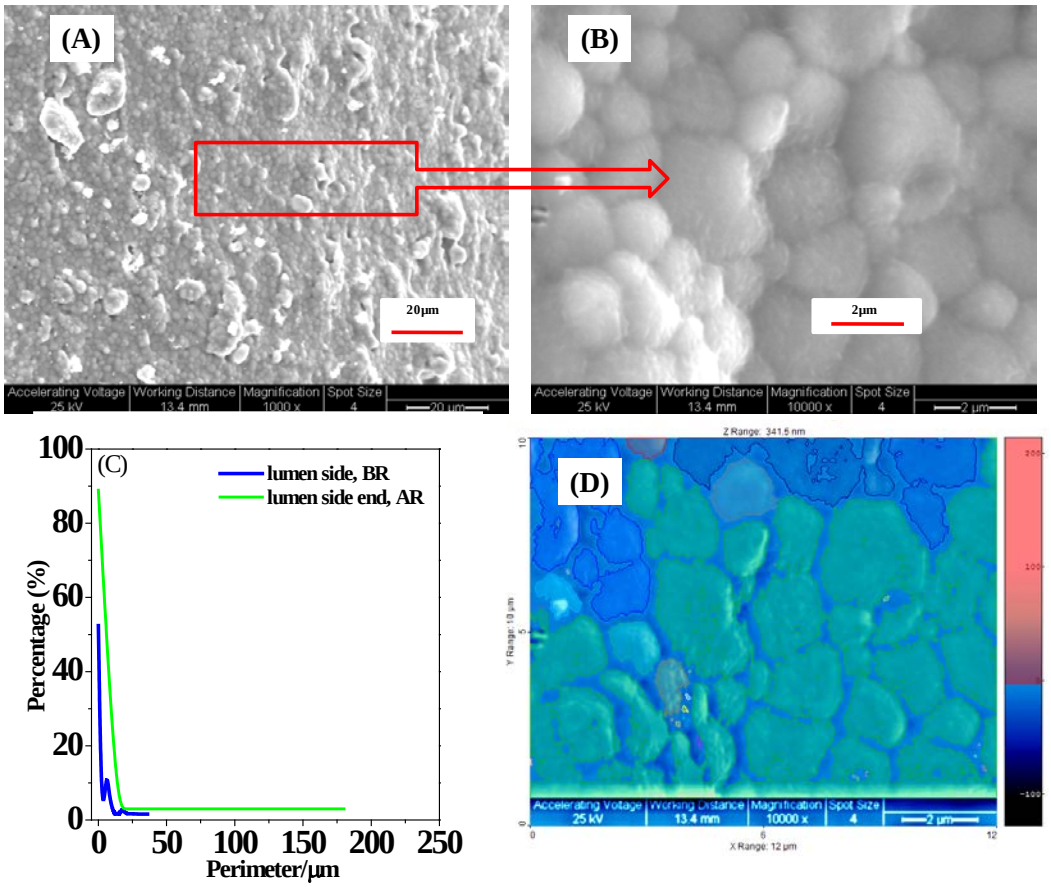

Figure 5.16 SEM micrograph end lumen side after oxygen fluxes measurements (A), images magnified (B), distribution of the grain boundary perimeter (D) and images simulated (C).

Note again that the range of the grain boundaries perimeter (i.e., 0.03 to 20 μm) for lumen side before and after reaction did not change (**figure 5.16C**). This range represents between

95 and 97 % of the overall grain boundary perimeter measured. These findings indicate that the distribution of the grain boundary of the end lumen and shell sides for Co_3O_4/LSCF6428-HFM did not vary after oxygen permeation experiment.

It is worth mentioning that small particles decorate the surface of the shell side and lumen side of the membrane. This can be attributed to the structural kinetic demixing of mobile cations of the hollow fibre membrane is caused by the cations diffusion under an oxygen chemical potential gradient **[22-25].**

5.5.3 Energy dispersive X- rays spectroscopy (EDXS)

In **table 5.1** is listed the EDXS results of different zones of the Co_3O_4/LSCF6428-HFM system before and after oxygen permeation experiments. It should be remarked that the values shown in **table 5.1** correspond to the average atomic %, except for the element S, Ca and Cl. Further details can be found in **appendix III.4, figure III.9;** where all values of the different zones and distances of the Co_3O_4/LSCF6428-HFM are tabulated. Oxygen concentrations were not considered because of its high content before and after reaction (see **appendix III.4, figures III.9** and **III.10**.

Nevertheless, it is clearly noticeable that there is a small reduction of the cobalt relative composition in the centre shell side after the oxygen permeation experiments (i.e. 33 %) compared to the cobalt concentration before reaction on the shell side (i.e. 35 %). This is probably due to the fact that part of the coated catalyst (i.e. Co_3O_4) on the LSCF6428-HFM was partially leached out during long operation time (i.e., 675 hours) at high temperature. Also, note that very small amounts of sulphur impurities were detected on the shell side before reaction, this is probably due to partial decomposition of the Polyethersulfone binder used during the preparation of the $La_{0.6}Sr_{0.4}Co_{0.2}Fe_{0.8O3-\delta}$ hollow fibre membrane (phase inversion methods), see **appendix I.1**. .

Table 5.1 Summary of EDXS results of different section of Co_3O_4/LSCF6428-HFM reactor before and after oxygen permeation

Membrane	*Condition*	*Section (side)*	*Average atomic %*						*Experimental stoichiometry*
			La	*Sr*	*Co*	*Fe*	*O*	*other*	
LSCF6428	**BR**	**Lumen**	**5.2**	**2.95**	**1.55**	**9.1**	**80.6**	**0.06Ca**	**La0.6:Sr0.4:Co0.2:Fe0.8**
Co_3O_4/LSCF6428	AR	Centre lumen	27.6	21.8	9.2	40.3		6.5S	La0.6:Sr0.4:Co0.2:Fe0.8
Co_3O_4/LSCF6428	AR	End lumen	29.2	22.4	10.4	37.5		1.5Ca	La0.6:Sr0.4:Co0.2:Fe0.8
Co_3O_4/LSCF6428	**BR**	**Shell**	**1.1**	**0.68**	**35.8**	**1.69**	**60.0**	**0.6S**	
Co_3O_4/LSCF6428	AR	Centre shell	22.5	15.9	33.2	28.2		1.9Cl	
Co_3O_4/LSCF6428	AR	End shell	28.2	22.3	10.3	38.9			
Co_3O_4/LSCF6428	AR	Centre cross section	31.9	19.4	10.5	38.2			La0.6:Sr0.4:Co0.2:Fe0.8
Co_3O_4/LSCF6428	AR	End cross section	30.3	21.1	9.9	38.1		6.5S	La0.6:Sr0.4:Co0.2:Fe0.8

BR: before reaction; AR: after reaction

EDXS spot analyses of the post operation Co_3O_4/LSCF6428-HFM for different zones along the surface of the membrane are shown in **table 5.1** and also in **appendix III.4** (**tables III.2 – III.9**). It can be appreciated that EDXS analysis of the centre lumen side surface after reaction displayed a uniform metal composition (i.e., La, Sr, Co and Fe) along the membrane and similar to the perovskite phase composition (i.e., $La_{0.6}Sr_{0.4}Co_{0.2}Fe_{0.8}O_{3-\delta}$) found in lumen side before reaction. Note that small amounts of sulphur were detected on this surface side (i.e. lumen side).

It is worth remarking that the EDXS analysis of the other sections of the membrane (i.e., end shell side and end lumen side) show similar metal composition than that of the perovskite phase ($La_{0.6}Sr_{0.4}Co_{0.2}Fe_{0.8}O_{3-\delta}$) before reaction.

According to the results obtained from XRD, SEM and EDXS analysis, both lumen side and shell side for the Co_3O_4/LSCF6428-HFM reactor after 675 hours of operation did not change. It was determined that the cobalt oxide catalyst coated on LSCF6428-HFM was deteriorated compared to the original uniform structure. This is probably due to the leaching of Co_3O_4 deposited on LSCF6428-HFM as a consequence of the high reaction temperature and long operation time. Also, it was determined that the grain boundary perimeter did not change in both end shell side and end lumen side and these were decorated with smaller particles. These particles were not analysed due to the poor quality of the images obtained by SEM.

It is worth remarking that both XRD and EDX data detected sulphur impurity, which can react with the oxygen molecular adsorption and elements segregated on membrane surface.

5.6. Oxygen flux for 5%Ni-LSCF6428/LSCF6428-HFM at 850°C and 900 °C

The study of oxygen release and uptake for 5%Ni-LSCF6428/LSCF6428 hollow fibre membranes reactor was carried out under different operations conditions (i.e., mode 1 and 2) at 850 °C and 900 °C.

In **figure 5.17** can be seen that a stabilization period for 5%Ni-LSCF6428/LSCF6428-HFM reactor under mode 2 was required. It can be observed that at the beginning both measurements (oxygen release and uptake) showed a similar trend. After approximately 466 minutes of run time the oxygen release started to increase until nearly 1194 min, where both measurements converge again. This stabilization period is possibly associated with the partial oxidation or/and sintering of the 5%Ni-LSCF6428 catalyst.

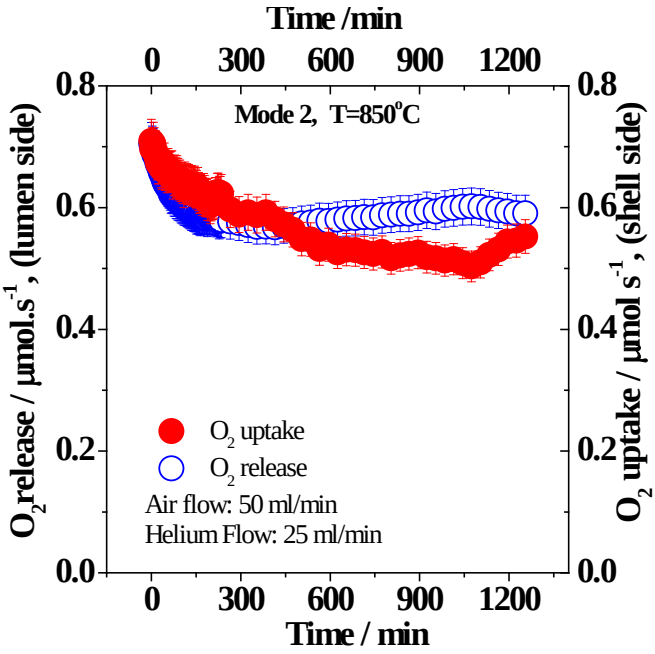

Figure 5.17 Oxygen release and oxygen uptake for 5%Ni-LSCF6428/LSCF6428 hollow fibre membranes reactor as a function of run time

The effect of helium flow rate on the oxygen flux is illustrated in **figure 5.18** for 5%Ni-LSCF6428/LSCF6428-HFM. It can be seen that the oxygen release and oxygen uptake measurements rose when increasing the helium flow rate. This is a consequence of diluting

the permeated oxygen and hence decreasing the oxygen partial pressure in the lumen side, which increases the driving force for oxygen transport across the membrane.

In addition, as is shown in **figure 5.18**, the oxygen release measurements and oxygen uptake for mode 2 of flow operation followed a similar trend. That is, both values were fairly similar. A similar trend showed for mode 1 of flow operation, except for air flow 75 ml (STP) min^{-1} where low values with respect to mode 2 (see **figure 5.18B**) were obtained. It is worth mentioning that mode 1 of flow operation measurements were carried out after mode 2 experiments. This unexpected finding for air flow of 75 ml (STP) min^{-1} in mode 1 is tentatively attributed to changes in the 5%Ni-LSCF6428 catalyst morphology because of oxidation or/and sintering (agglomeration) of the catalyst components as a consequence of long high thermal treatment during the experiments. This process provoked a diminution of the oxygen flux during the experiments likely due to the reduction of the surface area.

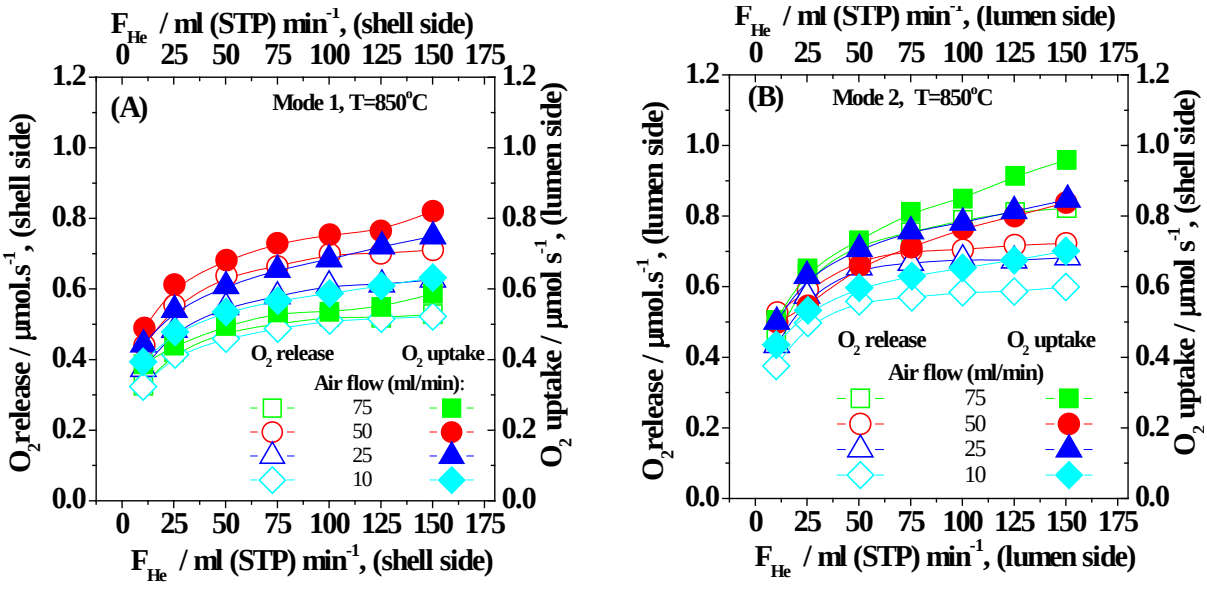

Figure 5.18 Dependence of the oxygen release and oxygen uptake against two modes of flow operation: mode 1 (A) and mode 2 (B) at 850 ˚C.

5.7. Reaction rate constants for two different modes of operation (i.e., mode 1 and mode 2) at 850 °C.

The apparent overall rate constants for 5%Ni-LSCF6428/LSCF6428-HFM against helium flow at 850ºC are given in **figure 5.19**. The model predicts that the apparent overall rate constants for 5%Ni-LSCF6428/LSCF6428-HFM appear to be slightly dependent upon helium flow eqn. (3.23); consequently the model may not be valid particularly at low helium flow rates. This is possibly due to the fact that the system did not reach a steady state condition. However, additional factors such as gas – solid mass transfer effects, deviation from plug flow behaviour, low Reynolds numbers ($\mathbf{Re < 2000}$) and incorrect form of the flux expression are also possible, see **appendix II.6, tables II.6** and **II.7**.

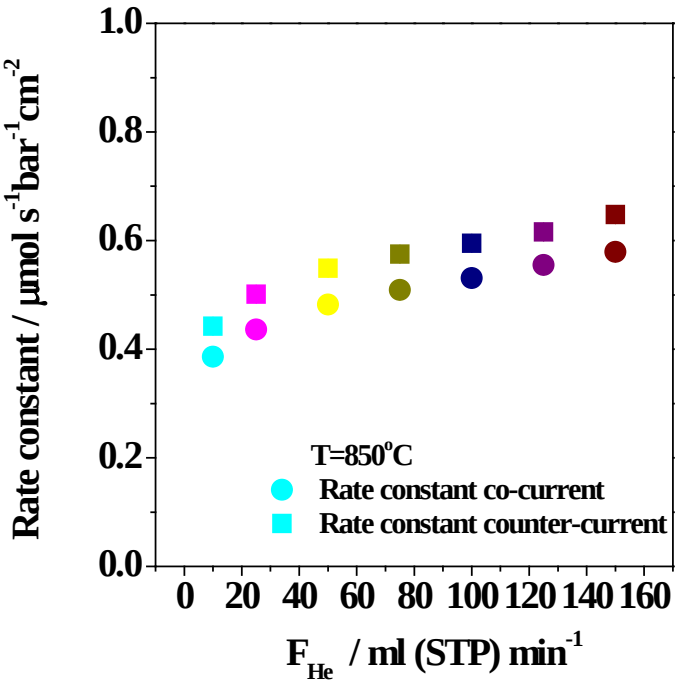

Figure 5.19 Influence of helium flow on the overall rate constant of the oxygen flux for unmodified and modified membrane at 850°C.

5.8. Influence of the temperature and reduction effect on the oxygen flux of the 5%Ni-LSCF6428/LSCF6428-HFM.

The temperature effect on oxygen release and uptake for 5%Ni/LSCF6428 hollow fibre membranes under mode 1 can be observed in **figure 5.20**. It is clearly illustrated that the oxygen release and uptake measurements at 900°C were comparable to those obtained at 850°C. This indicates that the oxygen partial pressure difference across the membrane did not vary significantly at 850°C and 900°C. This is likely due to changes in the catalyst morphology. Similar behaviour was observed in the experiment above carried out under mode 1 of operation for air flow 75 ml (STP) min^{-1} at 850°C, where the oxygen release and uptake behaviour was comparable with values obtained for air flow 10 ml (STP) min^{-1} (see **figure 5.18A**). This is probably due to the effects of sintering or/and oxidation of the catalyst (LSCF6428-supported nickel nanopowder). It is well-established that changes in the membrane phase structure affect the oxygen flux **[27-33]**.

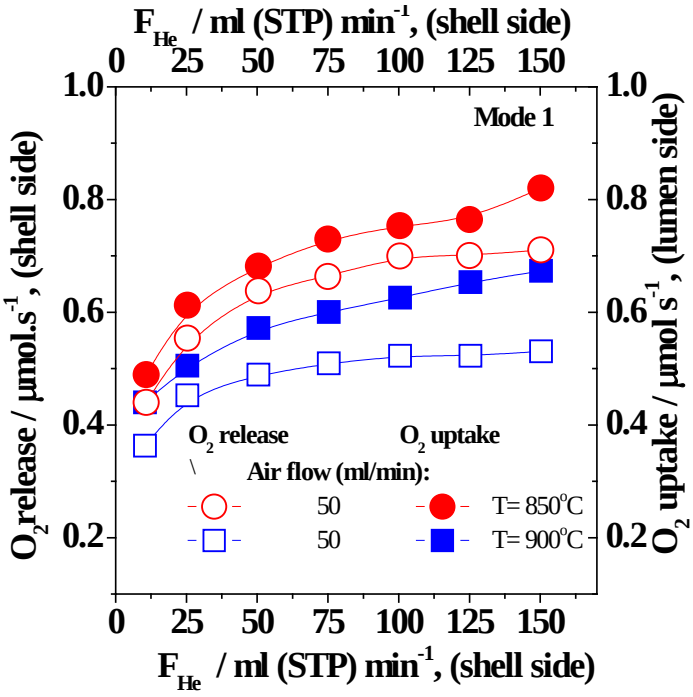

Figure 5.20 Dependence of the oxygen release and oxygen uptake against helium flow for 5%Ni/LSCF6428-HFM using an air feed flow rate of 50 ml (STP) min^{-1} at 850°C and 900°C.

The reduction of 5%Ni-LSCF6428/LSCF6428-HFM was carried out under the following procedure: the membrane reactor at 850 °C was cooled down up to 400 °C at approximately 0.4 °C min^{-1} under 9 ml min^{-1} air flow in lumen side. After reaching the temperature (400 °C), 30 ml (STP) min^{-1} of 5% H_2/He was supplied in the shell side while helium was co-current swept into the lumen side of the module during 30 or 60 minutes depending on the reduction time. Subsequently, the module temperature was increased up to 850°C at 0.4°C min^{-1} under a 9 ml (STP) min^{-1} He flow in both sides, see **figure 5.21.**

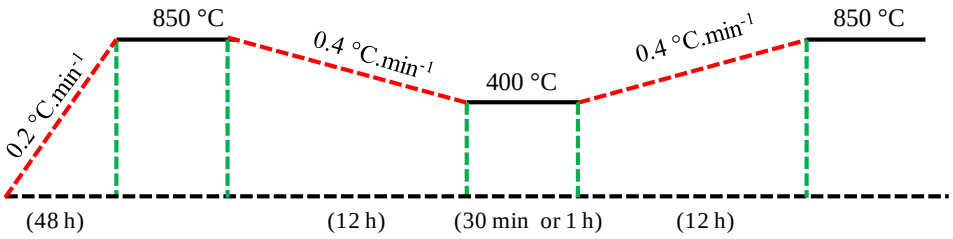

Figure 5.21 Schematic representation of the temperature programmed profile during the reduction of 5%Ni-LSCF6428/LSCF6428-HFM.

Figure 5.22 shows the oxygen release and uptake behaviour of 5%Ni-LSCF6428/LSCF6428-HFM for mode 1 of flow operation. The mode 1 corresponds to the air fed on the lumen side of the membranes and the helium sweep on the shell side (ALHS–air-lumen, helium-shell) in co-current.

As was expected, the oxygen release and oxygen uptake increased with rising helium flow rate. This is due to helium flow that induces the driving forces of oxygen migration across the membrane. Also, it can be observed that the oxygen uptake obtained after reduction was considerably higher than oxygen release compared to the oxygen flux measurements before reduction treatment, owing to reoxidation of the 5%Ni-LSCF6428 catalyst or/and LSCF6428 membrane. Note that the H_2 treatment for 30 and 60 minutes did not affect significantly the

oxygen uptake and release values, see **figure 5.22**. This indicates that 30 minutes is sufficient to reduce the 5%Ni-LSCF6428 catalyst.

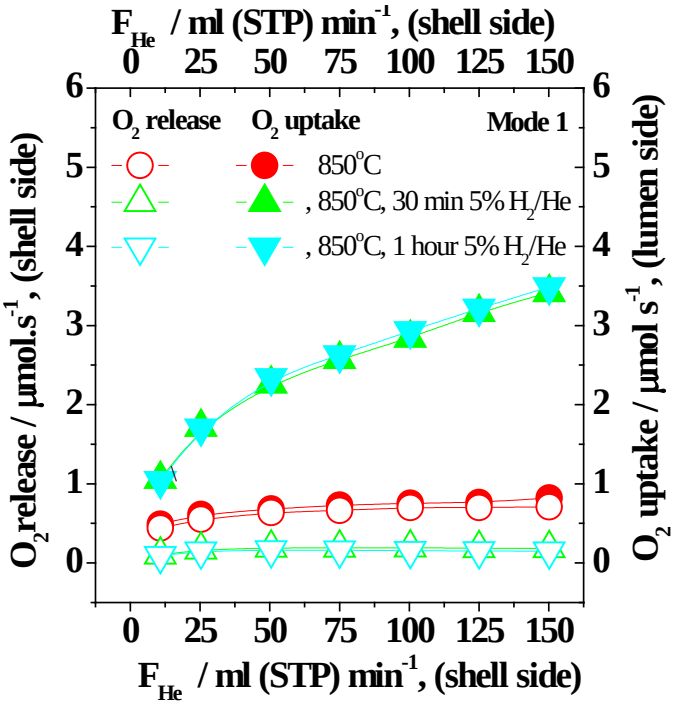

Figure 5.22 Comparison of oxygen release and uptake of the 5%Ni-LSCF6428/LSCF6428-HMF before and after H_2 reduction treatment.

In order to find out the stability of this membrane reactor, an experiment was carried out under mode 1 during 916 hours with 75 ml (STP) min^{-1} air flow supplied in lumen side and 50 ml (STP) min^{-1} He flow sweep in shell side, see **figure 5.23**.

It can be clearly noticed that the membrane reactor did not reach steady state after a long period of operation since the oxygen uptake was still higher than the oxygen release (i.e. comparable to the data shown in **figure 5.22**). This trend suggests that possibly the stoichiometry or/and morphology of the 5%Ni-LSCF6428 catalyst on LSCF6428 hollow fibre membrane reactor underwent an irreversible modification.

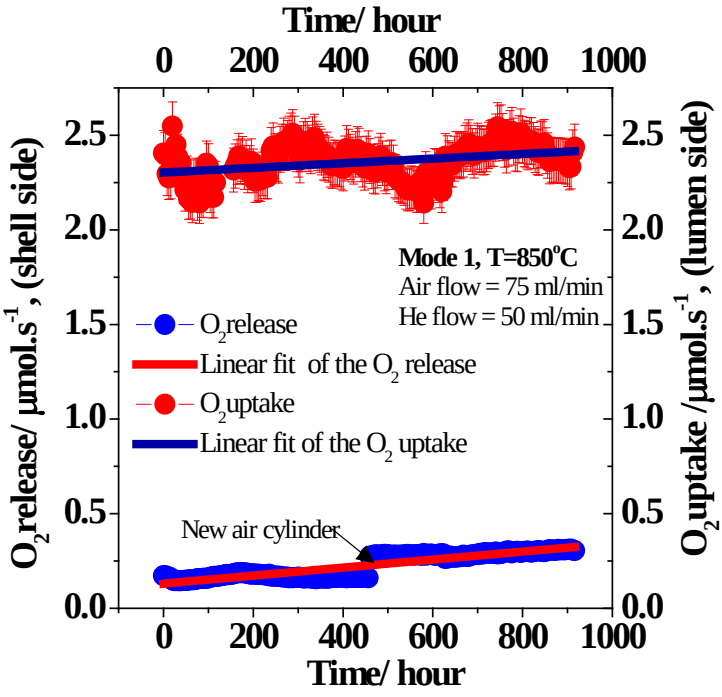

Figure 5.23 Oxygen release and oxygen uptake as a function of time on stream for 5%Ni-LSCF6428-HFM after H_2 reduction treatment.

5.9. Calculation and comparison of oxygen permeation resistance for 5%Ni-LSCF6428-HFM reactor.

The distributions of total permeation resistance of 5%Ni-LSCF6428-HFM reactor was determining using the eqns. (4.1) to (4.4) at 850°C [**3**] and the data are given in the **figure 5.24.** It can be observed that at low helium flow (i.e., 10 ml min^{-1}) the resistance of surface exchange at the oxygen lean side or lumen side ($\boldsymbol{R}_{ex}^{''}$) was between 54 and 51 %, indicating that $\boldsymbol{R}_{ex}^{''}$ controls the oxygen permeation rate. In contrast, $\boldsymbol{R}_{ex}^{'}$ (29-31 %) and $\boldsymbol{R}_{diff}$ (15-17 %) showed inferior contribution to the overall oxygen flux rate at 850°C, **appendix IV.1, figure IV.1**.

According to the results given in **figures 5.24**, $\boldsymbol{R}_{ex}^{''}$ and $\boldsymbol{R}_{ex}^{'}$ did not vary when increasing air flow rate. Furthermore, at helium flows between 25 and 75 ml min^{-1}, $\boldsymbol{R}_{ex}^{''}$ gradually increased up to 77 % while $\boldsymbol{R}_{ex}^{'}$ decreased and $\boldsymbol{R}_{diff}$ did not vary at helium flow above 10 ml

min^{-1}. This result suggests that oxygen permeation rate is limited by surface exchange on the oxygen lean side or lumen side ($R_{ex}^{''}$) at 850°C, **figures 5.24** and **appendix IV.1, figures IV.1.**

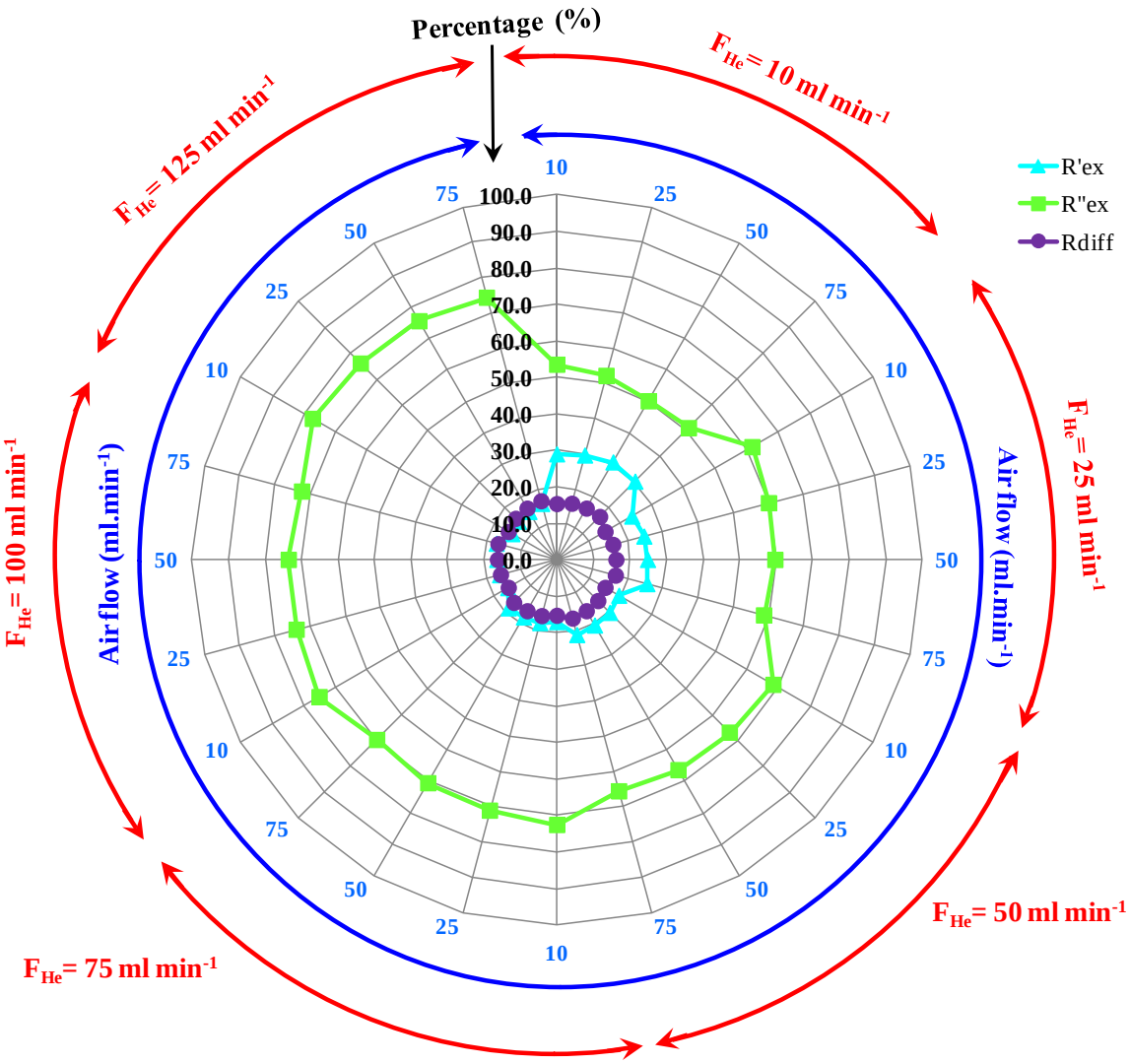

Figure 5.24 Effect of air and helium flows on the distribution of total permeation resistances for 5%Ni-LSCF6428-HFM at 850°C.

5.10. Characterization of the 5%Ni-LSCF6428/LSCF6428-HFM before and after oxygen fluxes by different techniques.

5.10.2. X ray-diffraction (XRD):

In **figure 5.25** are shown the XRD patterns for the 5%Ni-LSCF6428/HFM module before and after 1968 hours of oxygen flux experiments.

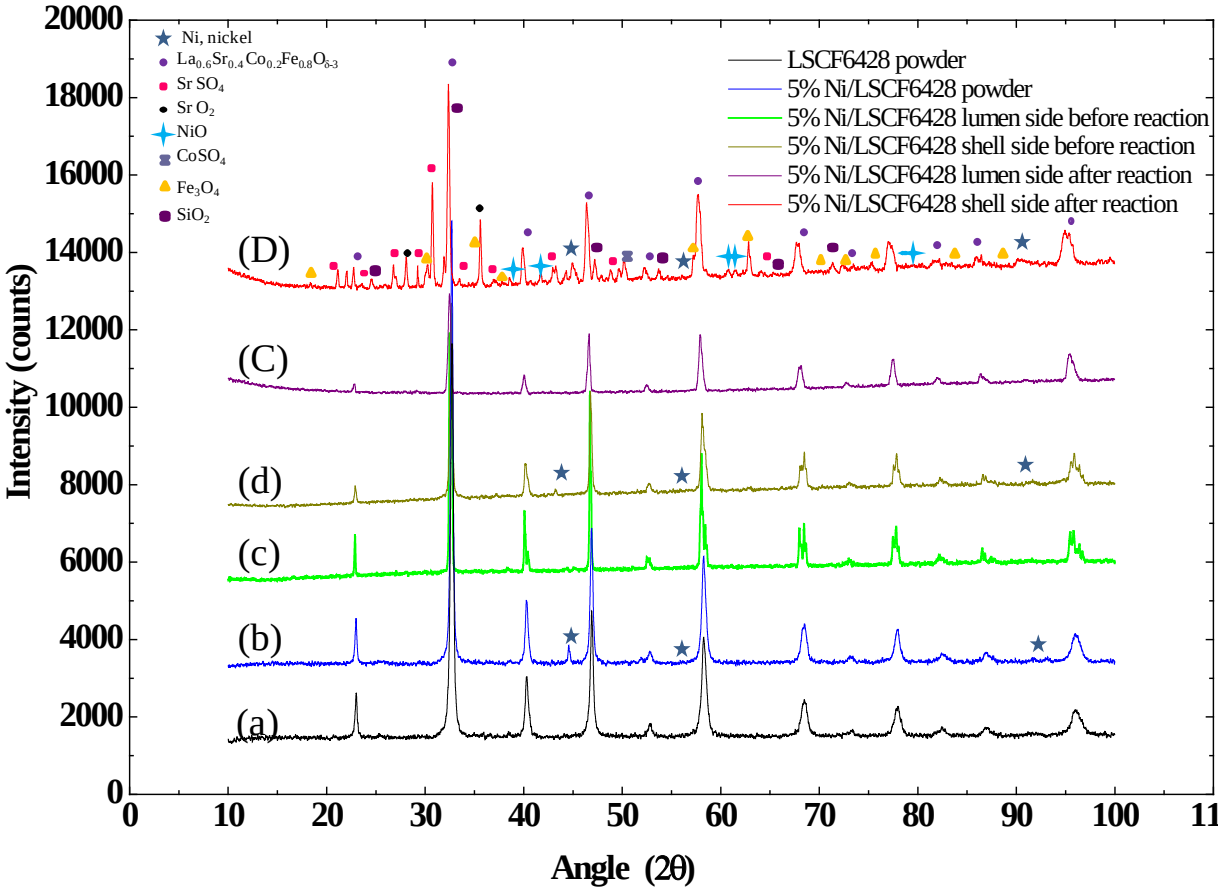

Figure 5.25 XRD profiles of the 5%Ni-LSCF6428/HFM. LSCF6428 powder (a), 5%Ni-LSCF6428/HFM powder (b), lumen side (c) and shell side (d) before the oxygen flux measurements. Centre lumen side (C) and centre shell side (D) after 1968 hours of experiments.

The diffraction profiles for 5%Ni-LSCF6428/HFM powder, lumen side and shell side before reaction are illustrated in **figures 5.25b, 5.25c** and **5.25d**, respectively. Three XRD profiles display the signs characteristic of the hollow fibre membrane (i.e. $La_{0.6}Sr_{0.4}Co_{0.8}Fe_{0.2}O_{3-\delta}$) as

the main crystalline phase **[34].** The 5%Ni-LSCF6428/LSCF6428-HFM powder and shell side before reaction present a second crystalline phase that corresponds to metallic nickel, Ni (00-004-0850). The crystal size for lumen side and shell side before oxygen permeation was around 26 nm (0.026 μm) and 25 nm (0.025 μm), respectively, **appendix IV.2, table IV.1**.

Figures 5.25C and **5.25D** correspond to the diffraction profiles for the centre lumen side and the centre shell side of 5%Ni-LSCF6428/LSCF6428-HFM after 1968 hours of operation. It can be clearly noted that the principal crystalline phase is LSCF6428 for both samples. Furthermore, other crystalline phases such as SrO_2 (00-007-0234), $SrSO_4$ (00-005-5935), $CoSO_4$ (10124-43-3), Fe_3O_4 (01-088-0315), NiO (1313-99-1) and SiO_2 (00-005-0490) were detected in the centre shell side (**figure 5.25D**). The crystal size for lumen side post operation did not change and was around 26 nm (0.026 μm). On the other hand, crystal size for shell side after oxygen permeation and methane conversion was around 32 nm (0.032 μm), **appendix IV.2, table IV.1**.

Considering the above-mentioned results we can assume that metallic nickel on 5%Ni-LSCF6428 catalyst changed its oxidation state from 0 (Ni^0) to 2+ (NiO) during the experiments, causing the drop of the oxygen flux. It can be also observed that the module reactor was contaminated by sulphur as revealed by the presence of $SrSO_4$ and $CoSO_4$ in the XRD analysis. Sulphur impurity, the H_2 reduction step and the segregation of iron, strontium and cobalt to produce crystalline metal oxides and sulphates may produce the diminution of oxygen permeation **[23, 35-37]**. Additionally, SiO_2 (silica) was detected in the hollow fibre membrane reactor after the reaction. The presence of this impurity is likely due to the sealant or quartz tube used to assemble the HF reactor, see **appendix IV.4, tables IV.11** and **IV.12.**

5.10.2. Scanning Electron Microscopy (SEM):

In **figure 5.26** are given the SEM micrographs of the shell side and cross section for 5%Ni-LSCF6428 catalyst deposited on LSCF6428 hollow fibre membrane before oxygen flux measurements.

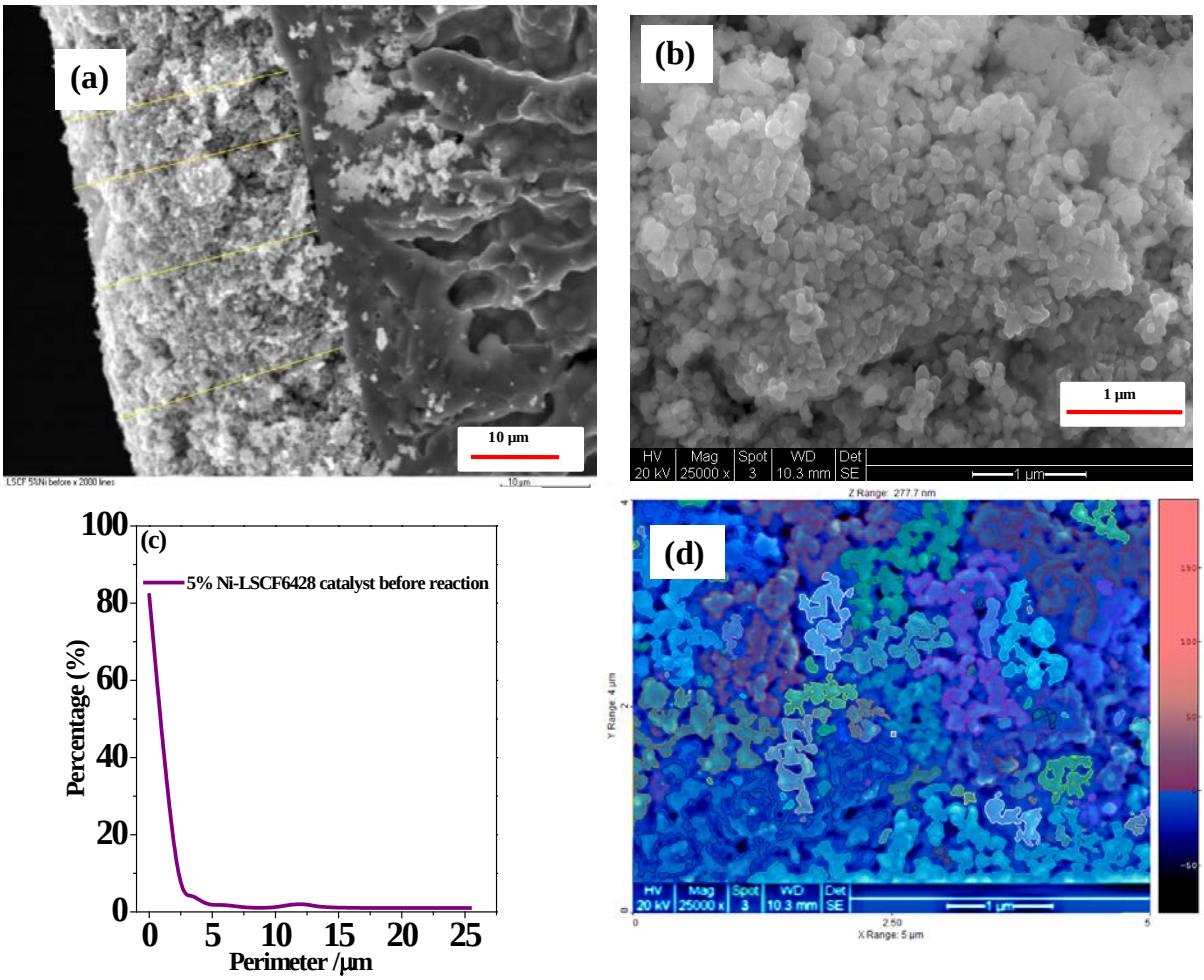

Figure 5.26 SEM images of the cross section of the 5%Ni/LSCF6428 catalysts on LSCF6428-HFM before reaction (a). 5%Ni/LSCF6428 catalysts on the shell side of LSCF6428-HFM before reaction (b), images simulated (d). Distribution of particle perimeter of the 5%Ni/LSCF6428 catalysts on LSCF6428-HFM (c)

The magnification images for shell side before reaction are shown in **figures 5.26b** and **5.24d**. Note that the thickness of 5%Ni-LSCF6428 catalyst was 26 µm **figures 5.26a** and the particle perimeter range is between 0.01 and 4.5 µm, which represent around 92% of the total

grain analysed. Also, the catalyst was well-distributed on the shell side of the LSCF6428-HFM (**figures 5.26a** and **5.26b**).

Figure 5.27 is given the magnification images of grain boundary for lumen side and shell side before reaction.

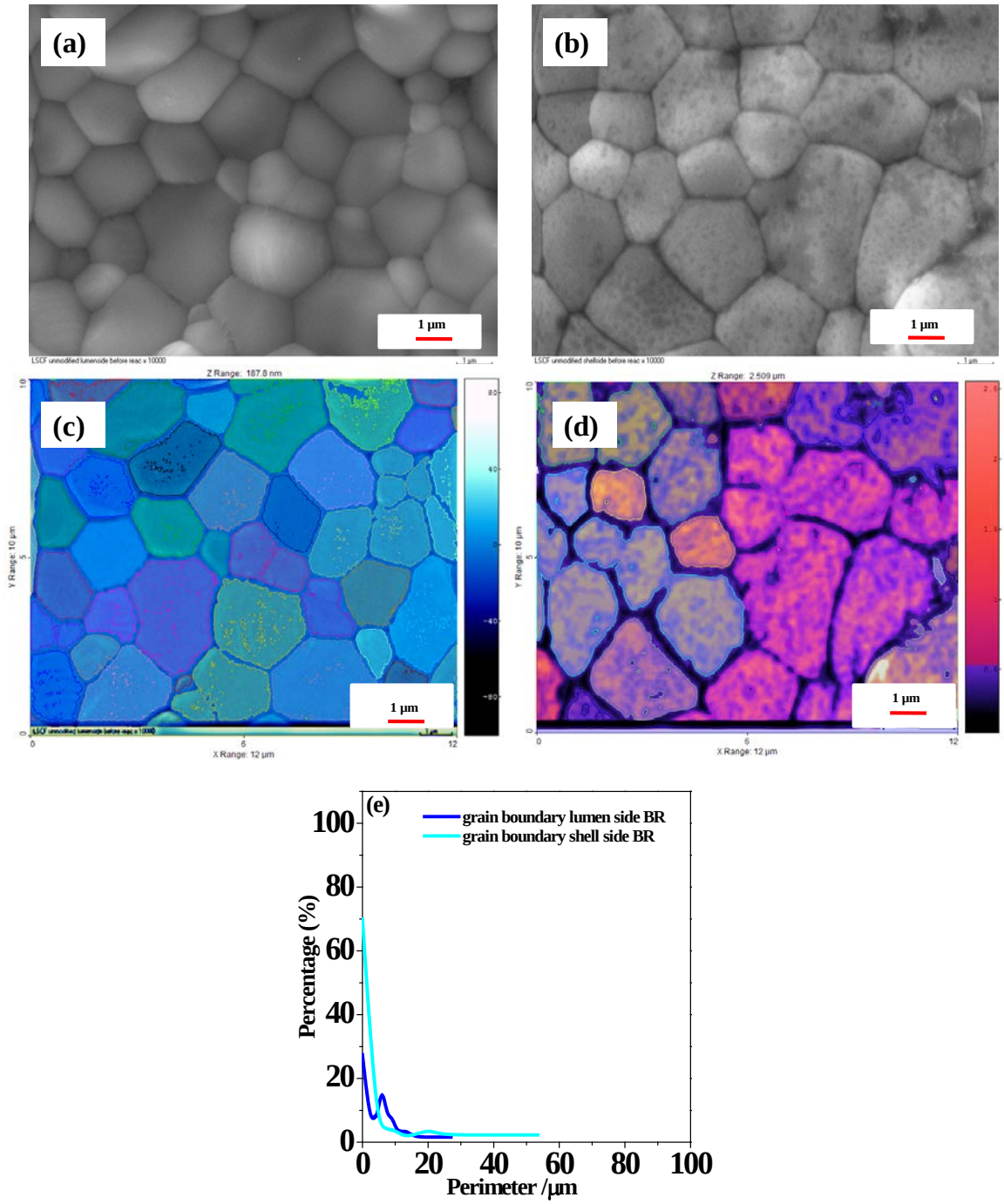

Figure 5.27 SEM micrographs of the lumen side (a) and shell side (b) before oxygen flux and images simulated of the lumen side (c) and shell side (d) before reaction. Distribution of grain boundary perimeter for both sides (e).

It can be noted that the grain boundary perimeter for lumen side exhibits a bimodal distribution with two ranges: 1) One between 0.02 and 4 µm that represents 38 % and 2) a second range between 4 and 16 µm, representing 53 % of the overall grain boundary perimeter (91 %). The remaining 9 % corresponds to grain boundaries with perimeters between 16 and 27 µm, according to the simulation of the images by SPIP 6.0.9**, figure 5.27e**. The grain boundary perimeters for shell side before reaction are between 0.02 to 20 µm, which corresponds to 93% of the total grains boundaries. Note that the distribution of the grain boundary perimeter for both sides is comparable, **figure 5.27e**.

The SEM images of the centre shell side of the 5%Ni-LSCF6428/LSCF6428-HFM after oxygen flux are shown in **figure 5.28**.

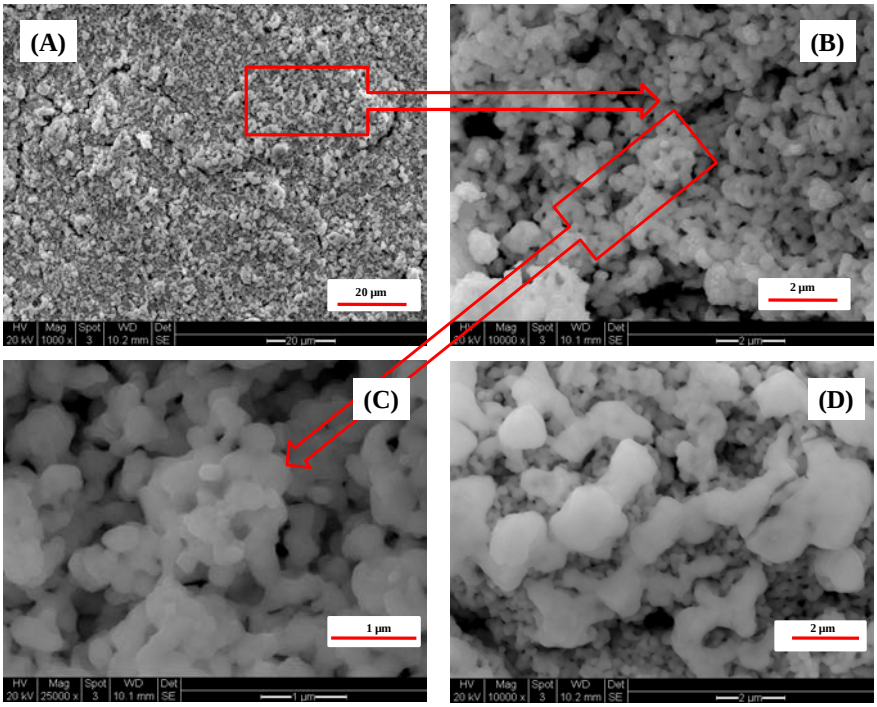

Figure 5.28 SEM images of the centre shell side of the post operation 5%Ni/LSCF6428-HFM (A) and images magnified (B), (C) and (D).

It can be clearly noted in the microstructure photographs (**figures 5.28C** and **5.28D**) that the grain perimeter of 5%Ni/LSCF6428 catalyst post reaction increased relative to the catalyst

grain size before reaction (**figure 5.26b**). It was not possible to obtain simulated images with good quality due to a poor contrast among the small particles of the catalyst for this reason the images were not included in the text.

This finding clearly shows that the catalyst particle underwent agglomeration and also oxidation (XRD result, **figure 5.25**) during the operation time. Both processes (i.e. agglomeration and oxidation) could take place simultaneously on HFM surface, which was caused by a decrease of oxygen flux. The H_2 treatment facilitated the formation of metallic Ni from nickel oxide but was unable to re-disperse it because of irreversible nature of the agglomeration process.

Figure 5.29 corresponds to centre lumen side of 5%Ni-LSCF6428/LSCF6428-HFM post reaction. It can be observed that the grain boundaries perimeter after reaction slightly increased (i.e., 0.07 to 30 μm) (**figures 5.29D** and **5.29E**) compared to the perimeters of the grain boundaries of the lumen side before reaction (i.e., 0.02 to 16 μm) for 91% of the overall grain boundary, see **figure 5.27**. Also, this membrane section showed small particles that decorates the surface of the membrane and cavities among the grain nodules (**figures 5.29B** and **5.29C**).

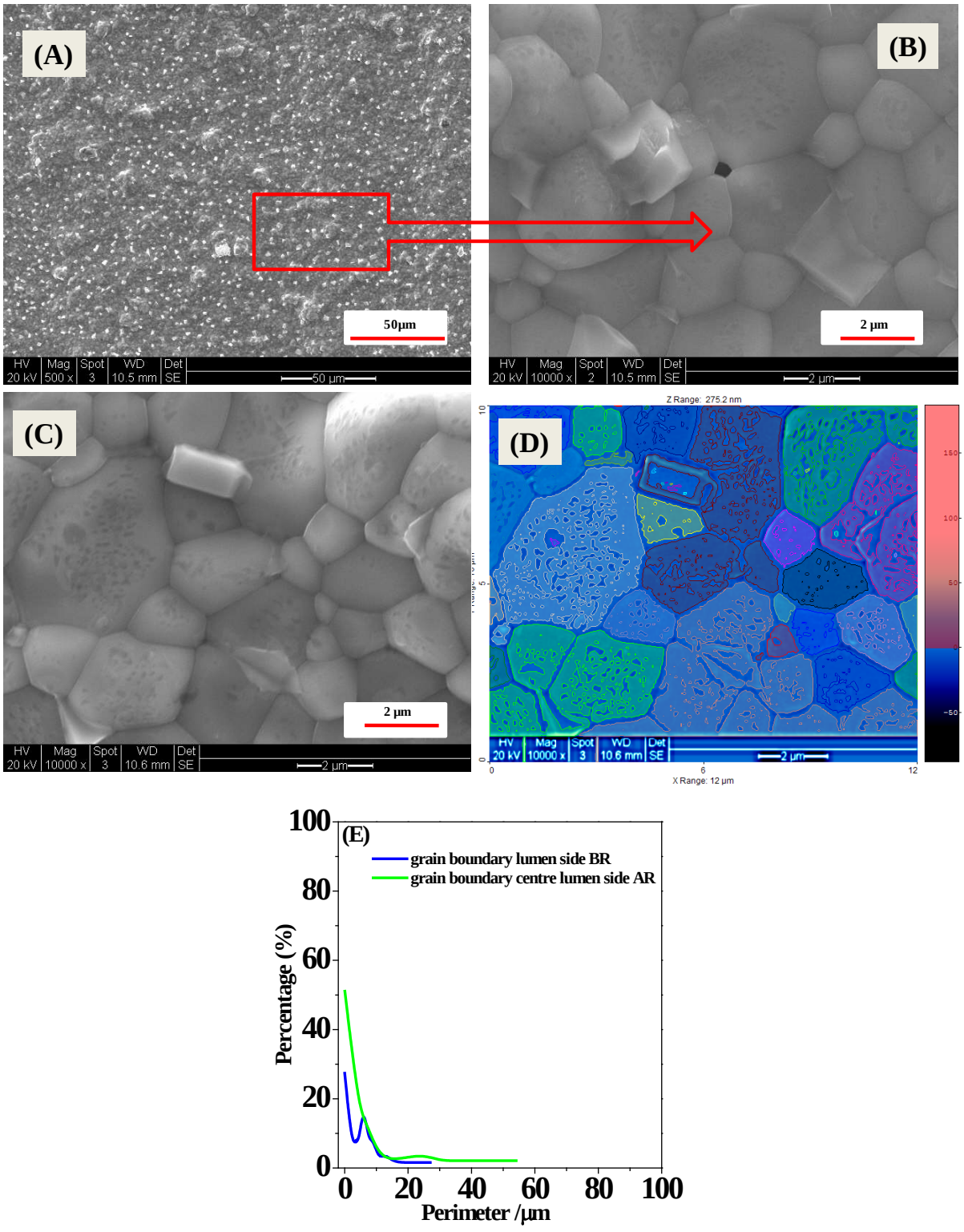

Figure 5.29 SEM images of the centre lumen side post reaction of the 5%Ni/LSCF6428-HFM (A) and image magnified (B) and (C). Images simulated of the lumen side after reaction (D) and distribution of particle perimeter of the 5%Ni/LSCF6428 catalysts on LSCF6428-HFM (E).

The microstructure of the 5%Ni/LSCF6428-HFM end lumen side post reaction is given in **figure 5.30**. According to the distribution of grain boundary perimeter for **figure 5.30B**, the grain boundaries perimeter of lumen side (i.e., 0.03 - 74 µm) varied significantly compared to that of the lumen side (i.e., 0.02 - 16 µm) before reaction, which represent 91% of the total grain boundary, see **figure 5.30D**.

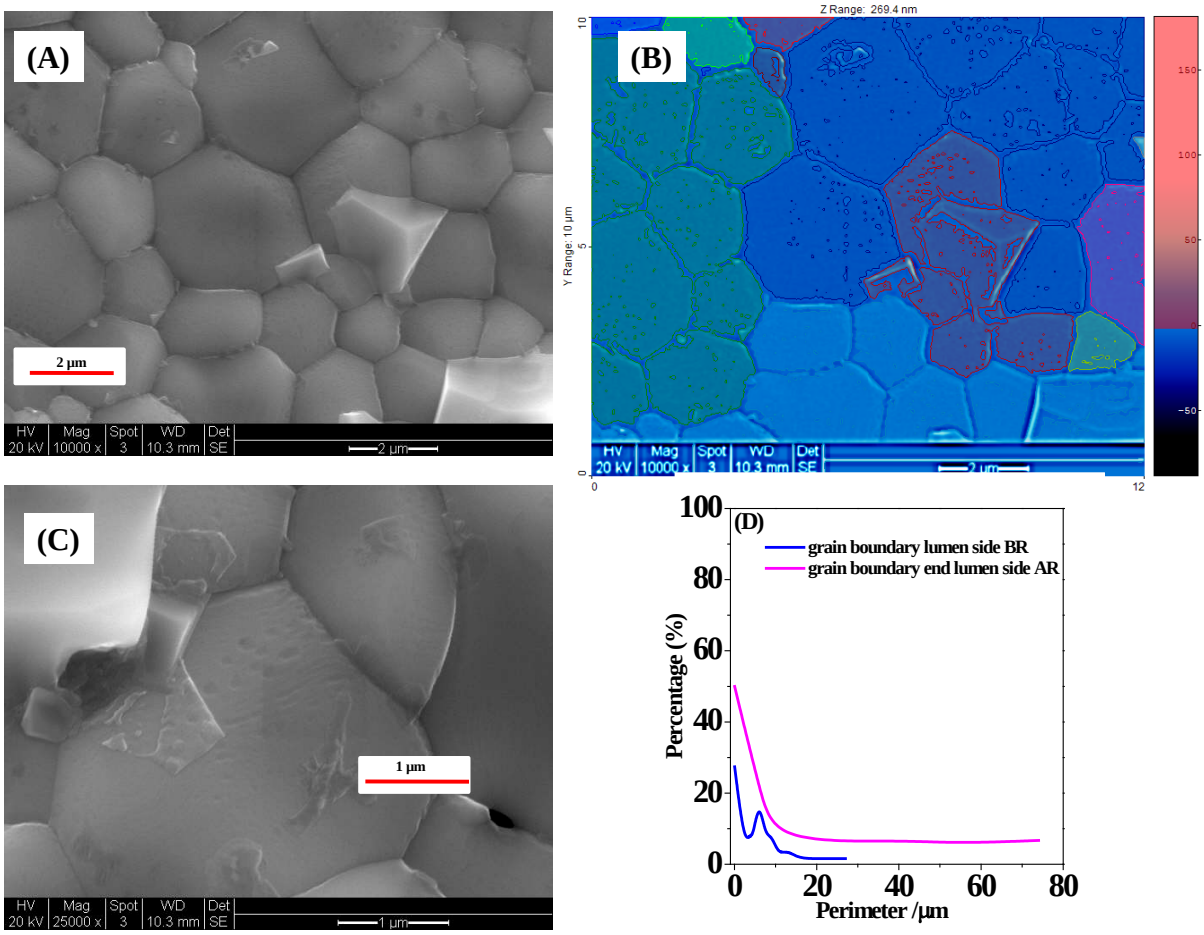

Figure 5.30 SEM micrograph of the end lumen side post reaction of the 5%Ni/LSCF6428-HFM (A), simulated image (B).magnified image (C) and distribution of grain boundary perimeter (D).

Also note that smaller particles decorate the surface of the lumen side and small cavities were created at the interface of the grain boundaries after reaction (**figures 5.30A** and **5.30C**), owing to the reducing atmosphere (H_2 and subsequently methane) before and during the partial oxidation of methane. This caused the interruption of the experiment because of a gas leak.

In **figure 5.31** is given the microstructure of the 5%Ni/LSCF6428-HFM end shell side post reaction. It can be noted in **figures 5.31A** and **5.31C** that the perimeter of the grain boundaries for shell side (i.e., 0.03 - 71 μm) vary slightly compared to the grain boundary perimeters for shell side before reaction (i.e., 0.02 - 20 μm), which corresponds to 93% of the total grains boundaries, see **figure 5.31C**.

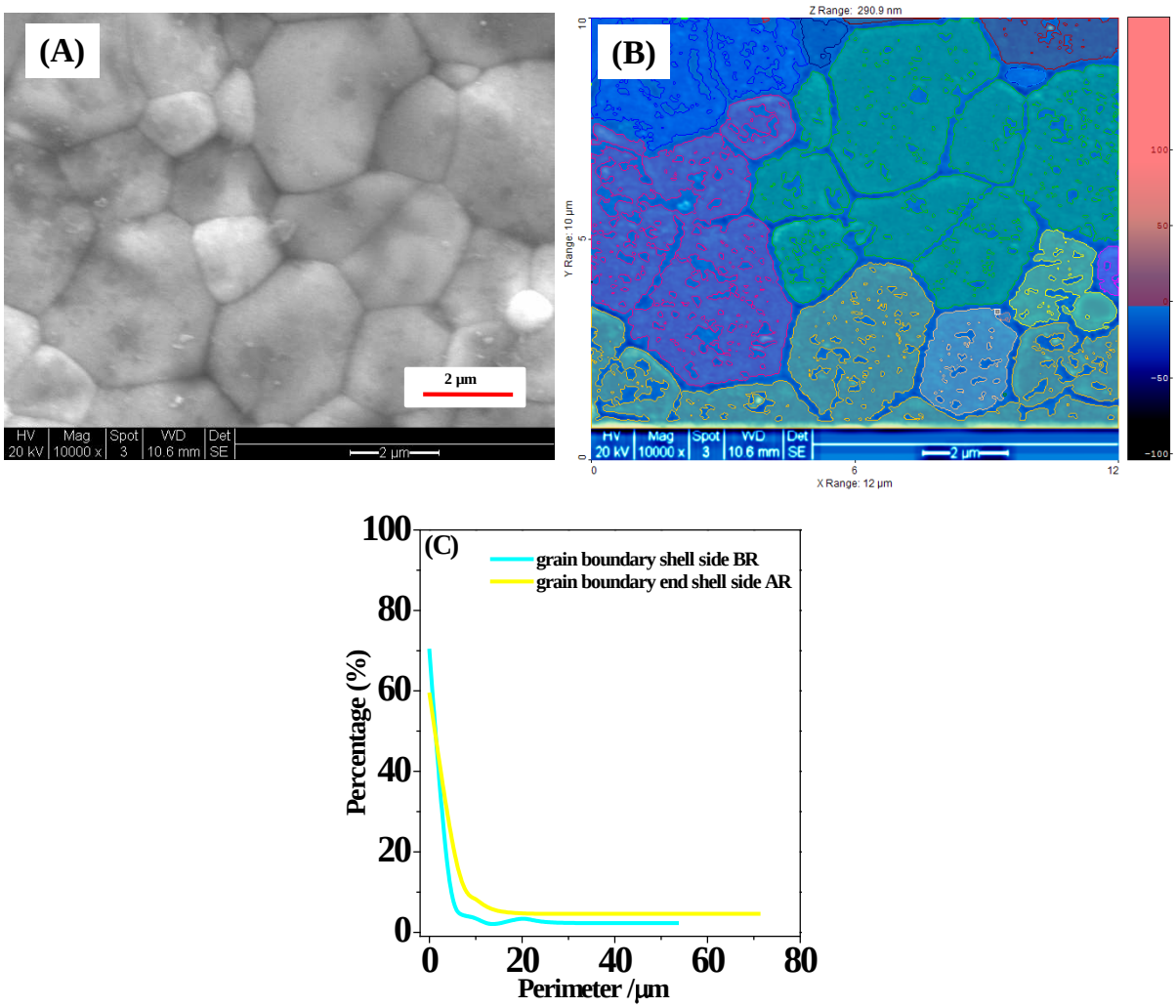

Figure 5.31 SEM micrograph of end shell side after oxygen flux measurements (A), image simulated (B) and distribution of the grain boundary perimeter (C).

Considering the above discussed XRD and SEM results for centre shell side of the 5%Ni/LSCF6428-HFM after 1968 hours of operation. One can suggest that the morphology of the catalyst changed as a consequence of an oxidation process of metallic nickel to NiO

and agglomeration of the particle due to its high thermal treatment (**figure 5.28**), which caused the diminution of the oxygen flux because of a reduction of the surface area available for the oxygen exchange reactions on the catalyst surface (5%Ni-LSCF6428).

Note that the module reactor was contaminated by sulphur, whose origins is tentatively attributed to air and helium gases employed during the experiments or more likely to the polyethersulfone (PESf) binder used in the manufacture of the membrane **[38-40].** The segregation of strontium and cobalt as crystalline oxide/sulphate phases (i.e., $CoSO_4$, SrO_2 and $SrSO_4$) were also observed by XRD (**figure 5.25**). These compositional changes of the LSCF6428 hollow fibre membrane could affect both the bulk diffusion and surface exchange kinetics of oxygen through the membrane, producing less oxygen fluxes than one would expect for a pure phase of LSCF6428 membrane **[41-43].** These crystalline oxide/sulphate phases have been previously observed elsewhere **[44-47]**.

5.10.3. Energy dispersive x-rays spectroscopy (EDXS)

In **table 5.2** are given the EDXS results of different zones for the 5%Ni-LSCF6428/LSCF6428-HFM before and post oxygen flux experiments. These zones are described in **Chapter 3 (figure 3.11**). It stands out that the value indicated in **table 5.2** is the average atomic %. For more details see **appendix IV.4**, where all values of EDX results for 5%Ni-LSCF6428/LSCF6428-HFM at different zones are given. Oxygen concentration was not considered because of its high content before and after reaction (see **appendix IV.4**).

On the other hand, it can be observed that there is a remarkable diminution of metal composition (i.e., La, Sr, Co, Fe and Ni depletion 6.3%, 3.3%, 1.6%, 7.8% and 1.6%, respectively) for 5%Ni-LSCF6428/LSCF6428-HFM in centre shell side after reaction compared with shell side before reaction. However, the overall stoichiometry of the 5%Ni-

LSCF6428/LSCF6428 membrane did not change considering the measurement error of EDXS analysis.

Furthermore, it is noticeable the presence of sulphur and carbon (1.0 % and 14%, respectively) on this membrane section, see **table 5.2** and **appendix IV.4**. Sulphur was already attributed to gas impurity or/and residuum of partial decomposition of polyethersulfone (PESf). Carbon deposition, on the other hand, is attributed to the methane conversion experiment; see **Chapter 6**, **section 6.3**. An overall diminution of the metal composition for La, Sr, Co and Fe (i.e., 4.9%, 3%, 1.6% and 6.9%) in the end shell side post reaction was observed compared to shell side before reaction of 5%Ni-LSCF6428/LSCF6428-HFM. However, the stoichiometry of the membrane bulk did not change. Both sulphur (1.2 %) and carbon (11.6%) were also detected in this section of the membrane, **table 5.2** and **appendix IV. 4.**

Comparing the lumen side before operation with centre lumen side after reaction it can be clearly established that the elemental compositions for La, Sr, Co and Fe diminished from 8.0%, 5.5%, 2.3% and 10.3 to 5.2 %, 3.36%, 1.3% and 8.3%, respectively. Meanwhile, the La, Sr, Co and Fe compositions in the end lumen side decreased up to 5.2%, 3.5%, 1.4% and 6.4% from 8.0%, 5.5%, 2.3% and 10.3 %, respectively. However, in both membrane sections the stoichiometry of the membrane bulk did not change (i.e. $La_{0.6}$:$Sr_{0.4}$:$Co_{0.2}$:$Fe_{0.8}$). Also, it is worth remarking that sulphur concentration around 0.30% was found in lumen side before reaction. This decreased to 0.1% in centre lumen side post reaction and increased up to 1.6 % in end lumen side after reaction; see **table 5.2** and **appendix IV.4.** The presence of sulphur content in lumen side before reaction is possibly originated by decomposition of the Polyethersulfone binder used during the preparation of the $La_{0.6}Sr_{0.4}Co_{0.2}Fe_{0.8}O_{3-\delta}$ hollow fibre membrane (phase inversion methods), see **appendix I.1**

Table 5.2 Summary of EDXS results of different zones of the 5%Ni-LSCF6428/LSCF6428-HFM before and after oxygen permeation and methane conversion.

Membrane	***Condition***	***Section (side)***	***Absolute atomic %***									***Experimental stoichiometry***
			La	***Sr***	***Co***	***Fe***	***O***	***Ni***	***S***	***Ca***	***C***	
LSCF6428	**BR**	**Lumen**	**8.0±0.9**	**5.5±0.8**	**2.3±0.6**	**10.3±1.2**	**73.8±13.5**		**0.3**	**0.5**		**La0.6:Sr0.4:Co0.2:Fe0.8**
LSCF6428	**BR**	**Shell**	**7.2**	**5.6**	**2.2**	**9.8**	**75.4**					**La0.6:Sr0.4:Co0.2:Fe0.8**
5%Ni-LSCF6428	**BR**	**Shell**	**7.4±0.8**	**4.7±0.9**	**2.2±0.5**	**9.1±1.1**	**74.9±14.0**	**1.7±0.6**				**La0.6:Sr0.4:Co0.2:Fe0.8**
5%Ni-LSCF6428	**BR**	**Cross**	**7.4±1.8**	**5.5±1.7**	**2.3±0.6**	**10.2±1.4**	**72.8±15.5**		**0.3**			**La0.6:Sr0.4:Co0.2:Fe0.8**
5%Ni-LSCF6428	AR	Centre lumen	5.2±1.9	3.4±2.2	1.3±0.7	8.3±1.2	68.9±11.2		0.14	0.5	13.6	La0.6:Sr0.4:Co0.2:Fe0.8
5%Ni-LSCF6428	AR	Centre shell	6.3±0.7	3.3±0.9	1.6±0.5	7.8±1.2	64.4±13.9	1.6±0.5	0.98		14.1	La0.6:Sr0.4:Co0.2:Fe0.8
5%Ni-LSCF6428	AR	Cross	7.8±1.8	3.2±2.8	2.3±0.6	10.5±1.3	73.6±13.5		0.98			La0.6:Sr0.4:Co0.2:Fe0.8
5%Ni-LSCF6428	AR	End shell	4.9±1.9	3.0±2.1	1.5±0.6	6.9±1.1	69.6±10.5	1.2±0.7	1.2		11.6	La0.6:Sr0.4:Co0.2:Fe0.8
5%Ni-LSCF6428	AR	End lumen	5.2±1.8	3.5±2.8	1.4±0.6	6.4±1.3	68.6±13.5		1.6		13.3	La0.6:Sr0.4:Co0.2:Fe0.8

An apparent sulphur accumulation was observed in end lumen side after reaction likely due to the descended temperature gradient from centre lumen side (850 °C) to end lumen side (400-300 °C), see **figure 3.4 (Chapter 3).**

According to the results obtained from XRD, SEM and EDXS analysis both the shell side and the lumen side of the 5%Ni-LSCF6428/LSCF6428-HFM module after 1968 hours of operation showed the following evidences:

The metallic nickel supported on LSCF6428 (catalyst) on shell side of the LSCF6428 hollow fibre membrane displayed morphology changes possibly due to the oxidation of metallic nickel to NiO by oxygen chemisorptions on active sites of the catalyst. A H_2 treatment process did not regenerate the initial oxygen flux of the membrane reactor. Furthermore, the particles were agglomerated owing to the long high thermal treatment during the experiments. All these changes could decrease the number of active sites in the catalyst, which was reflected on the diminution of oxygen flux during the experiments.

XRD characterisation of the module reactor after reaction showed the presence of sulphur and the segregation of iron, strontium and cobalt to form different crystalline oxide/sulphate phases, which may be detrimental to the 5%Ni/LSCF6428-HFM performance. Additionally, it can be noted that the hollow fibre membrane was contaminated by silica (SiO_2), which can likely come from the sealant or from the quartz tube whereas the detection of carbon was associated to residual carbon from partial oxidation of methane, see **Chapter 6**, **section 6.3.**

5.11. Comparison of the oxygen flux obtained from unmodified LSCF6428-HFM, Co_3O_4/LSCF6428-HFM and 5%Ni/LSCF6428-HFM membrane modules at 850 °C and 900 °C.

The effects of the helium flow rate on the oxygen permeation for LSCF6428-HFM, Co_3O_4/LSCF6428-HFM and 5%Ni-LSCF6428/LSCF6428-HFM reactors at the beginning of

the run under mode 1 and mode 2 at 850°C are illustrated in **figure 5.32**. It can be noted that the oxygen permeation rates rose when increasing the helium flow rate. This is a consequence of diluting the permeated oxygen that cause a decrease of the oxygen partial pressure in the helium side and created a larger oxygen partial pressure gradient, which promotes an increased driving force for oxygen transport across the membrane for both operation modes. Additionally, it is worth mentioning that the modified LSCF6428-HFM showed oxygen permeation between 2 and 3 folds above unmodified LSCF6428-HFM under two modes of flow operation (i.e. mode 1: ALHS–air-lumen, helium-shell and mode 2: ASHL–air-shell, helium-lumen). The enhancement in oxygen permeation is probably associated to the increase of the oxygen surface exchange rate since this is the limiting rate of the oxygen flux **[48-50].**

In **figure 5.32** is compared the oxygen permeation for both mode of flow operation (i.e. mode 1 versus mode 2). It can be seen that both Co_3O_4/LSCF6428-HFM and 5%Ni-LSCF6428/LSCF6428-HFM reactors presented a similar tendency of the oxygen permeation measurements for both modes of flow operation. Note that the oxygen permeation obtained from blank (LSCF6428-HFM) for both modes operation were also fairly comparable.

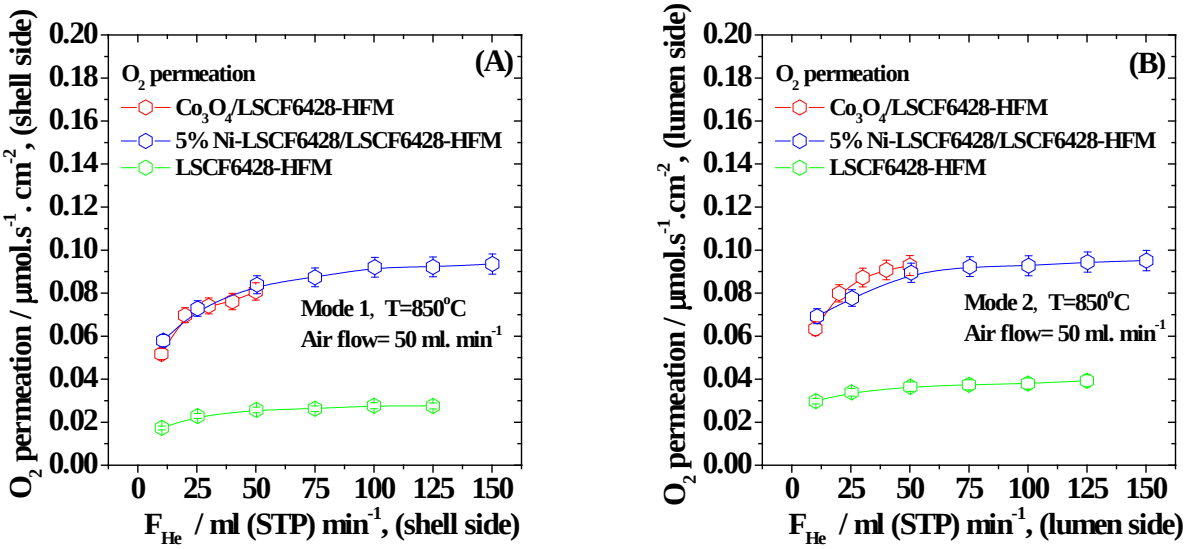

Figure 5.32 Dependence of the oxygen permeation against helium flow at 850°C for LSCF6428-HFM, Co_3O_4/LSCF6428-HFM and 5%Ni/LSCF6428-HFM using an air feed flow rate of 50 ml (STP) min^{-1} under mode 1 and 2.

Figure 5.33 shows the oxygen release and uptake measurements versus helium sweep gas flow rate at 850°C and air feed flow rate of 50 ml (STP) min^{-1} for unmodified LSCF6428, Co_3O_4/LSCF6428 and 5%Ni-LSCF6428/LSCF6428 hollow fibre membranes reactors. Both oxygen release and oxygen uptake increased with helium flow rate, due to the reduction of the oxygen partial pressure side in the side supplied with helium flow rate, which promotes an increased driving force for oxygen permeation.

Also, it can be observed that for Co_3O_4/LSCF6428-HFM the oxygen uptake values were slightly higher than the oxygen release, since the oxygen flux measurements were carried out before reaching steady state. In contrast for unmodified LSCF6428-HFM and 5%Ni-LSCF6428/LSCF6428-HFM the oxygen uptake was comparable to oxygen release because the module achieved the steady state before starting these experiments (**figure 5.33**).

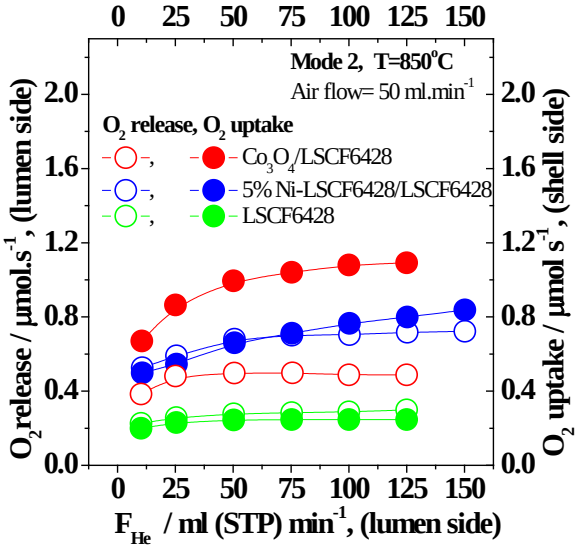

Figure 5.33 Dependence of the oxygen release and oxygen uptake against helium flow at 850°C for LSCF6428-HFM, Co_3O_4/LSCF6428-HFM and 5%Ni-LSCF6428.

To determine the temperature effect on oxygen permeation the unmodified LSCF6428, Co_3O_4/LSCF6428 and 5%Ni-LSCF6428/LSCF6428-HFM reactors were tested at 900°C under mode 2 with air feed flow rate of 50 ml (STP) min^{-1} (**figure 5.34**). As for previous data, it can be observed that the oxygen permeation increased with rising helium flow rate as

expected, because helium flows promotes the driving forces for oxygen migration across the membrane both unmodified membrane as modified membrane module.

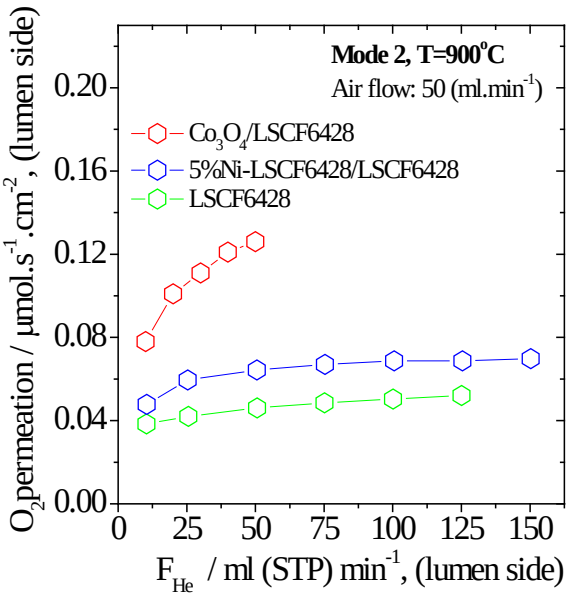

Figure 5.34 Dependence of the oxygen permeation versus helium flow at 900°C for LSCF6428-HFM, Co_3O_4/LSCF6428-HFM and 5%Ni/LSCF6428-HFM using an air feed flow rate of 50 ml (STP) min^{-1} under mode 2.

When one compares the oxygen permeation measurements at 850°C and 900°C for the three modules (**figures 5.32** and **5.34**) it can be observed that oxygen permeation improved when increasing temperature for LSCF6428-HFM and CO_3O_4/LSCF6428-HFM. However, the oxygen permeation measurements for 5%Ni-LSCF6428/LSCF6428-HFM at 900°C were comparable to those obtained at 850°C (**figure 5.32**). This indicates that the presence of nickel on the shell-side of the membrane has modified the nature of the rate determining step. According to the characterization data, this is most likely associated with the agglomeration of nickel nanoparticles during the long operation time. The oxygen permeation measurements for the modified membrane were in all cases higher than that for unmodified membrane, owing to the catalyst effect on the surface exchange reaction **[12, 44, 48, 51-53]**.

5.12. Comparison of the apparent overall rate constants for LSCF6428-HFM, Co_3O_4/LSCF6428-HFM and 5%Ni-LSCF6428/LSCF6428-HFM at 850°C

The apparent overall rate constants for LSCF6428-HFM, Co_3O_4/LSCF6428-HFM and 5%Ni-LSCF6428/LSCF6428-HFM against helium flow at 850ºC are given in **figure 5.35**.

In agreement with the model prediction, the apparent overall rate constants for Co_3O_4/LSCF6428-HFM and LSCF6428-HFM did not change with helium flow rate, particularly at helium flow above 20 ml min^{-1}. However, the apparent overall rate constant for 5%Ni-LSCF6428/LSCF6428-HFM appear to be dependent upon helium flow, indicating that the model may not be valid at helium flow rates below 50 ml min^{-1} because of relatively low Reynolds number (**Re < 2000**), producing laminar flows.

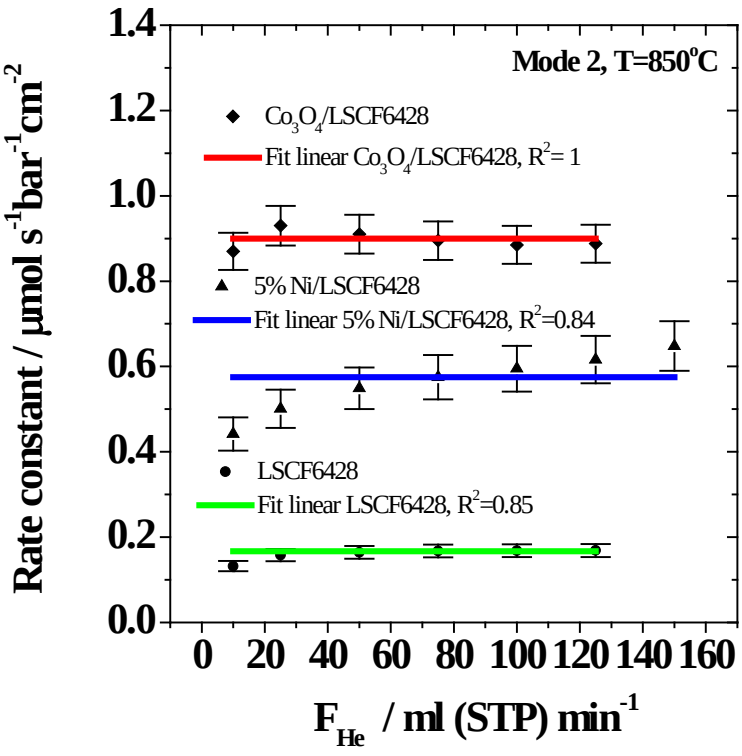

Figure 5.35 Influence of helium flow on the overall rate constant of the oxygen flux for unmodified and modified membrane at 850°C

According to characterization data, the 5%Ni-LSCF6428 catalyst suffered structural damages such as oxidation or/and sintering of the active component (agglomeration) due to long high thermal treatment during the experiments (see **figure 5.36**). This provoked a progressive catalyst deactivation that was reflected on the diminution of the oxygen flux during the experiments as a consequence of the reduction of the surface area available for the oxygen surface exchange reactions between 5%Ni/LSCF6428 catalyst and molecular oxygen. Yacou *et al*. also observed that palladium nanoparticles coated on LSCF6428-HFM were agglomerated after 24 hours of operation time at 850°C, which markedly decreased the oxygen flux **[52]**. However, additional factors such as mass transfer, Reynolds number, deviation from plug flow behaviour or incorrect form of the flux expression may also affect the fitting of the data.

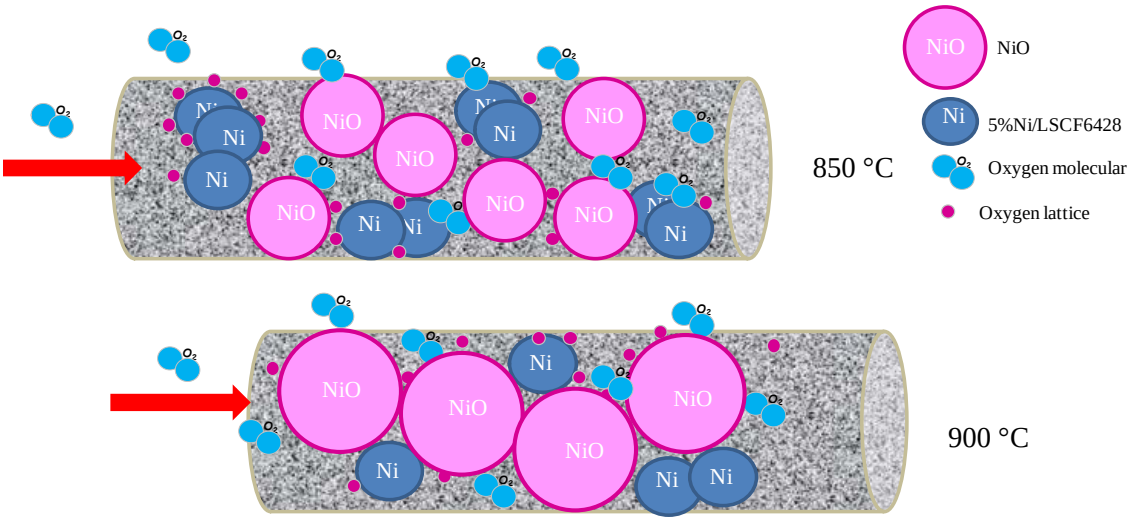

Figure 5.36 Schematic of the structural change of the 5%Ni/LSCF6428 catalyst at 850 °C and 900 °C.

Furthermore, it can be seen that the apparent overall rate constants for Co_3O_4/LSCF6428-HFM and 5%Ni/LSCF6428-HFM were 3-4 fold higher than those obtained for LSCF6428-HFM blank. This difference is tentatively attributed to two possible causes:

1. The presence of a catalyst on LSCF6428-HFM could affect the oxygen surface exchange rate and/or diffusion rate rather than the apparent activation energy or the rate-limiting step **[48]**.
2. The catalyst-modified membrane can create a new and energetically more favourable reaction path that reduces the activation energy of the reaction, (e.g. the dissociation of the oxygen molecule on the catalysts surface) **[10]**.

Additionally, oxygen flux improvements were reported for LSCF hollow fibres, modified with Pt **[55]** and Ag **[50].**

It is worth mentioning that the apparent overall rate constants for Co_3O_4/LSCF6428-HFM were 2 fold higher than that obtained for 5%Ni-LSCF6428/HFM (see **figure 5.35**), owing to its higher difference between the oxygen partial pressure across the membrane. The presence of a catalyst could promote the oxygen surface exchange rate and/or diffusion that would increase the force that drives oxygen transport through membrane **[48, 57]**. This is possibly due to the fact that cobalt ion in cobalt oxide (Co_3O_4) structure can easily change their valence Co^{3+} to Co^{2+} due to loses oxygen from the structure at elevated temperatures **[8]**. On the other hand, the partial oxidation of Ni nanoparticles to nickel oxide during the experiment induced its agglomeration, decreasing the surface area and hence the oxygen flux.

5.13. Conclusions

According to the above-discussed results for oxygen permeation experiments carried out in Co_3O_4/LSCF6428-HFM and 5%Ni-LSCF6428/LSCF6428-HFM reactors can be concluded the following:

1. The rise of helium flow rate promoted an increased driving force for oxygen migration across the membrane.

2. The oxygen permeation measurements from mode 1 and mode 2 for Co_3O_4/LSCF6428-HFM were different; due to presence of shell side-coated cobalt oxide catalyst, which apparently affected the exchange oxygen reaction rate on this side of the membrane.

3. The oxygen flux was strongly dependent upon the temperature and improved significantly with catalyst coated on LSCF6428-HFM whatever the type of catalyst.

4. In the membrane reactor steady state oxygen release and oxygen uptake reached similar values when oxygen incorporated into the LSCF6428-HFM was reduced to nearly zero.

5. The oxygen permeation rate is limited by surface exchange on the oxygen lean side or lumen side ($\boldsymbol{R}_{ex}^{''}$) at 850°C, according to the distribution of total oxygen permeation residence.

6. The apparent rate constant for Co_3O_4/LSCF6428-HFM reactor did not change with helium flow; possibly due to the presence of Co_3O_4 in the shell side that catalyses the dissociation of the oxygen molecule.

7. Cobalt oxide catalyst coated on LSCF6428-HFM was deteriorated from the original uniform coated structure after long operation time. According to XRD, SEM and EDX results, the grain boundary perimeter of Co_3O_4/LSCF6428-HFM did not change in both shell side and lumen side after the time of operation.

8. The morphology of the metallic nickel-supported LSCF6428 (catalyst) and coated on shell side of the LSCF6428 hollow fibre membrane changed after long operation time due to the agglomeration and oxidation of metallic Ni nanoparticles.

9. H_2 treatment process on 5%Ni-LSCF6428/LSCF6428-HFM module did not regenerate the initial oxygen flux of the membrane reactor, since the agglomeration of Ni nanoparticles was not reverted.

10. The apparent overall rate constant of 5%Ni-LSCF6428/LSCF6428-HFM appeared to be dependent of low helium flow rates. This finding was rationalised assuming that the system did not reach the steady state, however other factors such as mass transfer effect, low Reynolds numbers ($\mathbf{Re < 2000}$), deviation from plug flow behaviour or an incorrect flux expression may play an important role.

11. The presence of sulphur and the segregation of iron, strontium and cobalt to form different crystalline oxide/sulphate phases may be detrimental to the module (i.e., LSCF6428-HFM, Co_3O_4/LSCF6428-HFM and 5%Ni/LSCF6428-HFM) performance, according the XRD, SEM and EDX results.

12. The apparent overall rate constants for Co_3O_4/LSCF6428-HFM and 5%Ni/LSCF6428-HFM enhances 3-4 fold compared to LSCF6428-HFM blank. On the other hand, the apparent overall rate constants for Co_3O_4/LSCF6428-HFM were 2 fold higher than that obtained for 5%Ni-LSCF6428/HFM.

5.14. References

[1] X. Tan, Y. Liu and K. Li; AIChE Journal, 51, **2005**, 1991.

[2] A. Thursfield and I. Metcalfe; J. Solid Electrochem., 10**, 2006,** 604.

[3] S.J. Xu, W. J. Thomson, Chem. Engineering Science, 54, **1999**, 3839.

[4] Z. Shao, G. Xiong, H. Dong, W. Yang L. Lin; Separ. Purif. Technol, 25, **2001**, 97.

[5] M. H. R. Lankhorst and J. E. ten Elshof. J. Solid State Chem. **1997**, 130, 302.

[6] W. Zhang, J. Smit, van Sint Annaland, J. Kuipers; J. Membr. Sci. 291, **2007**, 19.

[7] X. Tan and K. Li; AlChE J., 48, 7, **2002**, 1469.

[8] J. Caro, H. H. Wang, C. Tablet, A. Kleinert, A. Feldhoff, T. Schiestel, M. Kilgus, P. Kölsch, S. Werth. Catal. Today 118, **2006**, 128.

[9] A. Thursfield and I. Metcalfe; J. Membr. Sci. 288, **2007,** 175.

[10] C. Yacou, J. Sunarso, C. X. C. Lin, S. Smart, S. Liu, J. C. Diniz da Costa; J. Membr. Sci. 380, **2011**, 223.

[11] V. G. Sathe, S.K. Paranjpe, V. Siruguri and A. V. Pimpale; J. Phys. Condens Matter, 10, **1998**, 4045.

[12] W. Jin, S. Li, P. Huang, N. Xu J. Shi and Y. S. Lin,; J. Membr. Sci. 166, **2000,** 13.

[13] J. E. ten Elshof, H. J. M. Bowmeester, H. Verweij; Appl. Catal. A: Gen.**,** 130, **1995**, 195.

[14] N. Xu, S. Li, W. Jin, J. Shi, Y. Lin; AlChE J. 45, **1999**, 12, 2519.

[15] S. Li, W. Jin, P. Huang, N. Xu, J.Shi, Y. S. Lin; J. Membr. Sci. 166, **2000**, 51.

[16] X. Tan and K. Li; Ind. Eng. Res. 45**, 2006,** 142.

[17] A. Thursfield and I. Metcalfe; J. Mater. Chem. 14, **2004,** 2475.

[18] X. Tan, Z. Wang, H. Liu, S. Liu; J. Membr. Sci. 324,**2008**, 128.

[19] V. V. Kharton, F. M. B. Marques, Curr. Opin. Solid State Mater. Sci. 34, **1999**, 1367.

[20] H. J. M. Bouwmeester, H. Kruidhof, A. J. Burggraaf, Solid State Ionics 72, **1994**, 185.

[21] K.Huang, J. B. Goodenough, J. Electrochem. Soc. 148, **2001**, E203.

[22] H. J. M. Bouwmeester; Catal Today, 82, **2003**, 141.

[23] B. Wang, B. Zydorczak, Z.T. Wu and K. Li; J. Membr. Sci., 344, **2009**, 101.

[24] R. H. E. van Doorn, H.J.M. Bouwmeester, A. J. Burggraf; Solid State Ionics 111, **1998**, 263.

[25] D. Schlehuber, E. Wessel, L. Singheiser, T. Markus; J. Membr. Sci., 351, **2010**, 16.

[26] B. Wang, B. Zydorczak, D. Poulidi I.S. Metcalfe, K. Li; J. Membr. Sci., 369, **2011**, 526.

[27] H.Wang, C. Tablet, A. Feldhoff, J. Caro; *J. Membr. Sci. 262*, **2005**, 20.

[28] P. Zeng, R. Ran, Z. Chen, H. Gu, Z. Shao, J. C. D. da Costa, S. Liu; *J. Membr. Sci. 302*, **2007**, 171.

[29] K. Zhang, Y. Yang, D. Ponnusamy, A. J. Jacobson, K. Salama,; *J. Mater. Sci. 34*, **1999**, 1367.

[30] S. Diethelm, J. V. Herle, J. Sfeir, P. Buffat; *J. Eur.Ceram. Soc. 25*, **2005**, 2191.

[31] H. Kusaba, Y. Shibata, K. Sasaki, Y. Teraoka; *Solid State Ionics 177,* **2006**, 2249.

[32] G. Etchegoyen, T. Chartier, P. Del-Gallo; *J. Solid State Electrochem. 10*, **2006**, 597.

[33] Q. Li, X. Zhu, Y. He, Y. Cong, W. Yang; J. Membr. Sci. 367, **2011**, 134.

[34] X. Tan, Z. Wang and K. Li; *Ind. Eng. Chem. Res. 49, 6, **2010**,* 2895.

[35] M. Martin, Materials in thermodynamic potential gradients, J. Chem. Thermodyn. 35, **2003**, 1291.

[36] A. P. Sutton, R. W. Balluffi, Interfaces in Crystalline Materials, Clarendon, Oxford, **1995.**

[37] X. Yin, Liang Hong, Zhaolin Liu, J. Membr. Sci. 311, **2008**, 89.

[38] V. G. Sathe, S. K. Paranjpe, V. Siruguri and A. V. Pimpale; J. Phys. Condens. tter, 10, **1998**, 4045.

[39] S. P. Deshmukh and K. Li; J. Membr. Sci. 150 (1), **1998**, 75.

[40] X. Y. Tan, Y. T. Liu, K. Li; AlChE J. 51 (7), **2005**, 1991.

[41] X. Tan., Y. Liu and K. Li; Ind. Eng. Chem. Res. 44, **2005**, 61.

[42] S. Liu, G.R. Gavalas; Ind. Eng. Chem. Res. 44, **2005**, 7633.

[43] S. Liu, X. Tan, Z. Shao, J. C. Diniz da Costa; AlChE J. 52, **2006**, 3452.

[44] C. Buysse, A. Kovalevsky, F. Snijkers, A. Buekenhoudt, S. Mullens, J. Luyten, J. Kretzschmar, S. Lenaerts; J.Membr. Sci. 359, **2010**,86.

[45] C. Y. Tsai, A. G. Dixon, W. R. Moser, Y.H. Ma, AlChE J. 43, **1997**, 2741.

[46] C. Y. Tsai, A. G. Dixon, W. R. Moser, Y.H. Ma, M.R. Pascucci; J. Am. Ceram. Soc., 81, **1998**, 1437.

[47] W. Jin, S. Li, P. Huang, N. Xu, J. Shi and Y.S. Lin; J. Membr. Sci., 166, **2000**, 13.

[48] R. H. E. van Doorn, H. J. M. Bouwmeester, A. J. Burggraf; Solid State Ionics 111, **1998**, 263.

[49] Y. Teraoka, Y. Honbe, J. Ishii, H. Furukawa, I. Moriguchi; Solid State Ionics, 152-153, **2002**, 681.

[50] T.H. Lee, Y. L. Yang, A. J. Jacobson, B. Abeles, M. Zhou; Solid State Ionics, 100, **1997**, 87.

[51] X. Tan, Z. Wang, H. Liu, S. Liu; J. Membr. Sci. 324, **2008**, 128.

[52] X. Tan, Z. Pang, Z. Gu, S. Liu; J. Membr. Sci. 302, **2007**, 109.

[53] S. Lee, K. S. Lee, S. K. Woo, J. W. Kim, T. Ishihara, D. Kyung Kim; Solid State Ionics, 158, **2003**, 287.

[54] A. Leo, S. Liu, J. C. Diniz da Costa, Z. Shao; Sci. and Techn. Adv. Mater., 7, **2006**, 819.

[55] J. A. Moulijn, Catalysis, Vol. 79, Second edition, Elsevier Science, **1995**, 80.

[56] A. Thursfield and I. Metcalfe; J. Membr. Sci. 288, **2007,** 175.

[57] H. Wang, S. Werth, T. Schiestel and J. Caro, Angew. Chem. 117, **2005**, 7066.

Chapter 6.

Methane conversion onLSCF6428-HFM and 5%Ni-LSCF6428/LSCF6428-HFM

6. Methane oxidation

The objective of this chapter is to provide the results of the methane conversion and products selectivities for LSCF6428 and 5%Ni-LSCF6428/LSCF6428 hollow fibre membrane reactors. Also, compare the apparent overall rate constant for both reactor under different gradients (i.e. Air/He and Air/CH_4) and O_2 at 850 °C. Characterization of the samples obtained from both reactors (i.e. LSCF6428HFM and 5%Ni-LSCF6428/LSCF6428-HFM) after methane oxidation has been done by different techniques such as XRD, SEM and EDX.

6.1. Oxidation of methane over unmodified LSCF6428 hollow fibre membrane.

The LSCF6428 hollow fibre membrane reactor for the POM experiments were assembled in the same fashion that those used for the oxygen permeation experiments and described in **Chapter 3, section 3.4, figure 3.2**. The experimental setup for the POM experiments is described in **Chapter 3, figure 3.9** under the following flow configurations:

1. 4% CH_4/He flow fed at 25 ml (STP) min^{-1} to the shell side of the reactor, while air flow rate 25 ml (STP) min^{-1} was co-currently introduced into to the lumen side (MSAL).

2. 4% CH_4/He flow supply in the lumen side of the reactor at 25 ml (STP) min^{-1}, whilst air flow rate 25 ml (STP) min^{-1} was sweep into shell side co-currently (MLAS).

The experiments were carried out at 850 °C and the products were analyzed on-line using two Varian 3900 chromatographs. The oxygen permeation flux was calculated from oxygen atoms of all the oxygen containing products eqn. (3.28), except the water, which was not measured from shell side. The conversion of methane was determined from eqn. (3.29). Also, the selectivities to carbon monoxide, carbon dioxide, ethane and ethylene products

were calculated using the equations shown in chapter 3 (i.e. eqns. (3.20) – (3.33)) and the carbon balances was calculated from eqn. (3.34). For more details see **Chapter 3**.

Figures 6.1 and **6.2** shows the conversion data obtained with unmodified hollow fibre membrane of LSCF6428, which was operated at 850°C for ca. 16 hours under two flow configurations (i.e. MSAL and MLAS).

When 4% CH_4/He is supplied into the shell side, the oxygen permeation slightly increased during the initial 45 min to obtain a constant value of 0.00033 μmol. $s^{-1}.cm^{-2}$. Meanwhile, the methane conversion was below 5% upon operation time (**figure 6.1A**). Also, it can be appreciated that C_2 product selectivity (i.e. C_2H_4 and C_2H_6 selectivities were 23 % and 60%, respectively) and this was much higher than CO selectivity (i.e. 10%), **figure 6.1B**. Comparable catalytic data have been obtained by Tan *et al*. **[1]** and Xu and Thomson **[2]** over LSCF6428. Elshof *et al*. **[3]** reported C_2 selectivities of up to 70% for methane conversion between 1 and 3 % over LSCF6482.

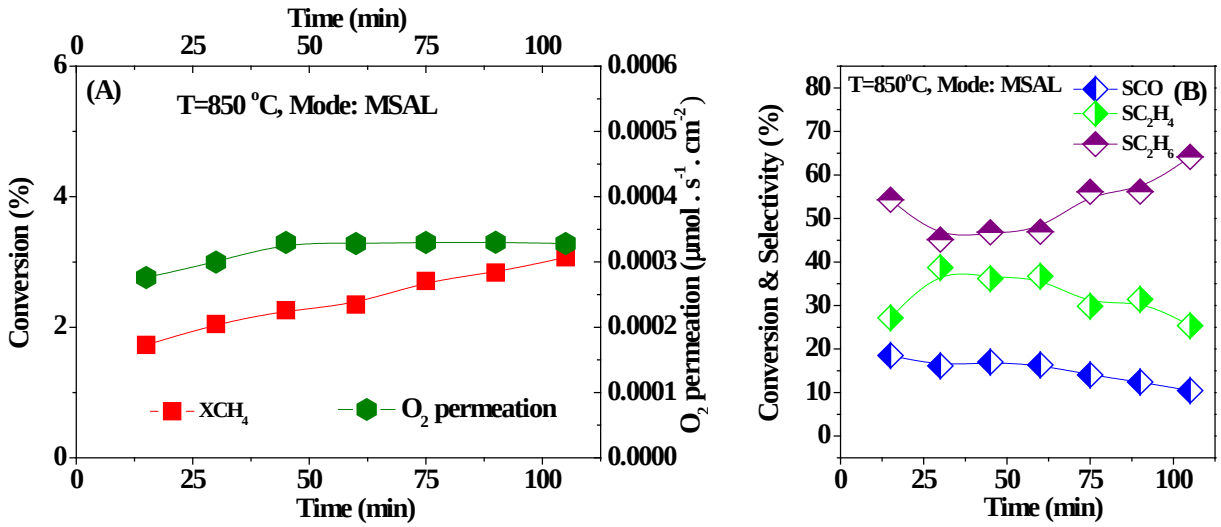

Figure 6.1 Catalytic performance of the POM on the LSCF6428-HFM reactor absent catalyst, where 4% CH_4/He flow supply in shell side while air flow rate sweep into to the lumen side (MSAL), co-current.

As LSCF6428-HFM reactor remained from the last experiment was with 4% CH_4/He flow supplied in the shell side while air flow rate swept into to the lumen side (MSAL), co-current.

It was decided to change the gas flow configuration (i.e. 4% CH_4/He flow was fed into the lumen side while air flow was introduced into the shell side (MLAS), co-current mode) on the HFM reactor and then it was tested for the methane oxidation reaction. It can be noted that oxygen permeation decreased slightly from (0.00045 to 0.00037) µmol s^{-1} cm^{-2} during the operation time. Methane conversion was approximately constant (i.e. 4%) during operation time (**figure 6.2A**).

Furthermore, it was found that CO and CO_2 selectivity decreases gradually from 5% to 0 % and 13% to 8 %, respectively during the time on stream. Note that SCO_2 is higher than SCO, this is tentatively attributed to the enrichment of oxygen in the lumen side because the air flow was supplied in this side during the previous experiment (mode: MSAL).

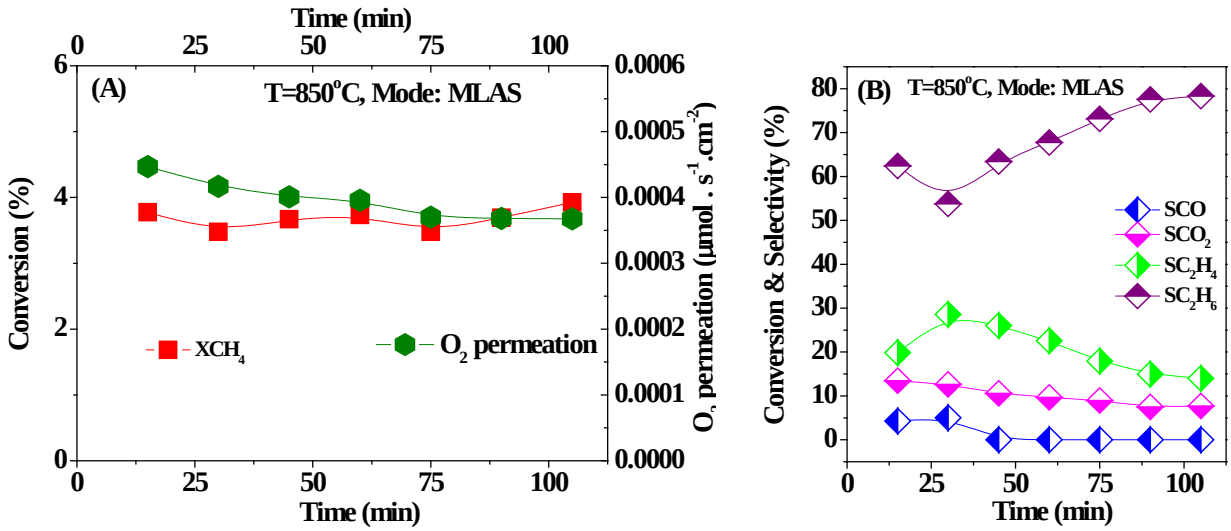

Figure 6.2 Catalytic performance of the methane oxidation reaction on the unmodified LSCF6428-HFM reactor, where 4% CH_4/He flow was supplied in lumen side and air flow fed into the shell side (MLAS) at 850 °C.

In addition, during the time on stream C_2H_6 selectivity rose slightly from 65% to 78%, while C_2H_4 selectivity declined slightly from 20% to 14% (**figure 6.2B**). The relatively low CO_x selectivity compared to C_2 selectivity would indicate that the amount of oxygen permeated was not sufficient for oxidizing the methane to CO and/or CO_2. Furthermore, the trend

observed for C_2H_6 and C_2H_4 suggests that C_2H_4 formation occurred through consecutive oxidation reactions eqns. (6.1) and (6.2) in agreement with a previous report **[4]**:

$$2CH_4 + O \rightarrow C_2H_6 + H_2O \quad (6.1)$$

$$C_2H_6 + O \rightarrow C_2H_4 + H_2O \quad (6.2)$$

In addition, the carbon deposited on the membrane surface was apparently between 10% and 20 %, according to the carbon balance (see **appendix V.1, figure V.1**). This finding is in line with a previous report **[5-6]**.

In **figure 6.3** are given the dependence of the methane conversion and product selectivity dependence with oxygen permeation under two flow operation modes (i.e. MSAL and MLAS) at 850 °C. Comparing the methane conversion versus oxygen permeation for both flow operation modes (**figure 6.3A**), shows that methane conversion for the MSAL operation mode increased slightly with rising oxygen permeation. On the other hand, methane conversion for the other operation mode (i.e. MLAS) did not vary markedly with change of the oxygen permeation. One should remark that methane conversions for MLAS operation mode were slightly higher than these obtained in MSAL mode as a consequence of the larger oxygen permeation values. It is well-established that different oxygen species exist at the membrane surface **[7-9]**, eqn. (6.3). However, not all these species are able to generate selective oxidation products from methane activation **[10, 11]**.

$$O_2(g) \longleftrightarrow O_2(ads) \xleftrightarrow{+e} O_2^- \xleftrightarrow{+e} O_2^{2-} \longleftrightarrow 2O^- \xleftrightarrow{+e} 2O_{lattice}^{2-} \quad (6.3).$$

According to Bielanski and Haber **[12]**, only the nucleophilic lattice oxygen ions (i.e. O^{2-}) conduce to selective oxidation products formation whereas that electrophilic oxygen species (i.e. O_2^-, O^- and $O_{2\,(ads)}$) generate total oxidation products. One can envisage that the activity-selectivity performance of the LSCF6428-HFM in methane conversion is likely

associated with the concentrations of electrophilic and nucleophilic oxygen species and also that different oxygen species produced depend upon the abundance of the oxygen vacancies (i.e. $V_0^{\bullet\bullet}$) in the membrane see eqn. (6.4)

$$\frac{1}{2}O_2 + V_0^{\bullet\bullet} + 2e' \rightarrow O^{2-} + 2h^{\bullet} \qquad (6.4)$$

The **figure 6.3B** are illustrates the C_2H_4, C_2H_6 selectivity against oxygen permeation for both modes of flow operation. It can be noted that the C_2H_6 and C_2H_4 selectivity exhibit the same behaviour for both flow operation modes, that is, C_2H_6 selectivity decreased with increasing of oxygen permeation whereas C_2H_4 selectivity showed an opposite trend. However, C_2H_6 selectivity was markedly higher than C_2H_4 selectivity, particularly for MLAS mode. Again, this trend can be rationalized assuming that C_2H_4 formation occurred via consecutive oxidation reactions of primarily formed C_2H_6, see eqn. (6.2).

In addition, **figure 6.3C** is presented the CO and CO_2 selectivity for both flow operation modes. It can be noted that the CO selectivity decreased while the oxygen permeation increased for MSAL mode, while no CO_2 was detected. In contrast, for MLAS mode, the CO_2 and CO selectivity increased when there was rising the oxygen permeation values.

It is worth mentioning that the oxygen permeation values for MLAS mode were higher than those values obtained in MSAL mode. This is likely due to high oxygen concentration in the lumen side, owing to the previous experiment under MSAL mode.

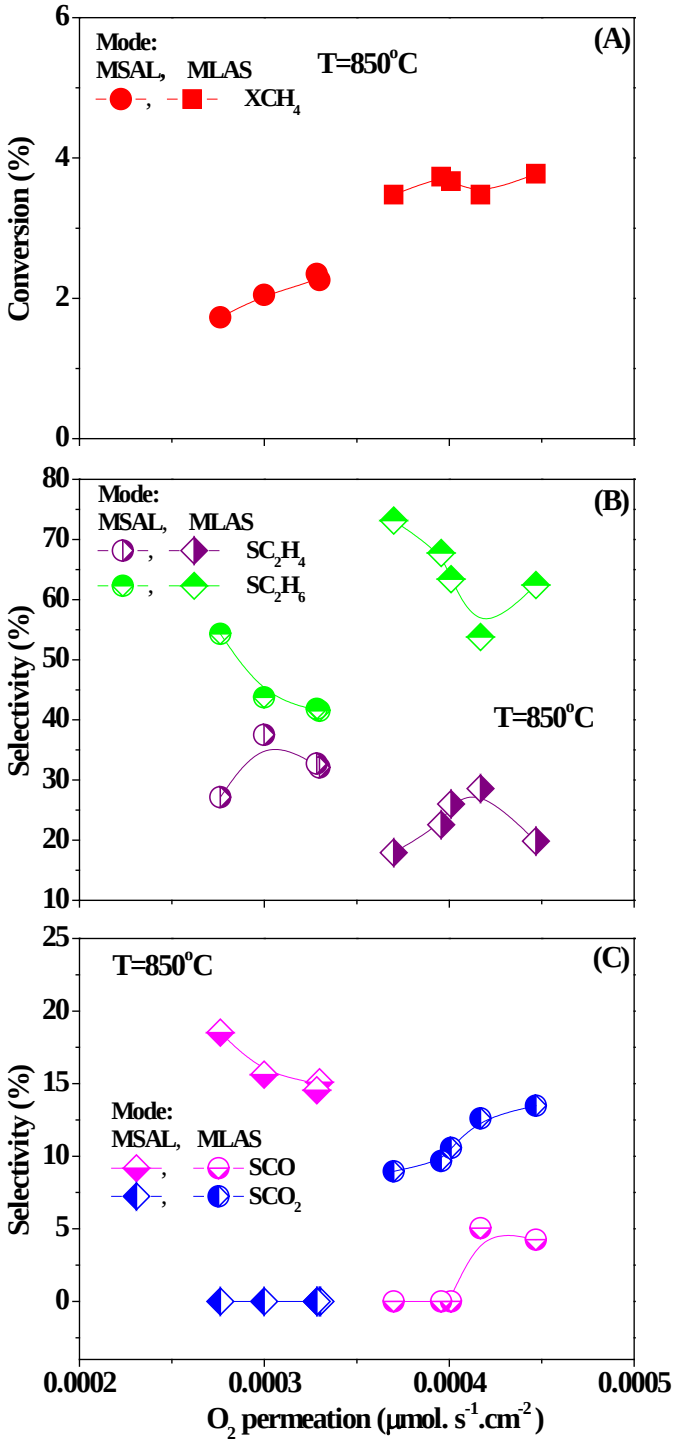

Figure 6.3 Dependence of methane conversion and product selectivity with oxygen permeation under two different flow operation modes at 850 °C. (A) Methane conversion, (B) C_2H_6 and C_2H_4 selectivity; (C) CO and CO_2 selectivity

Different oxygen species exist in the lumen side of the membrane likely due to different pathways and selectivity for the total methane oxidation (i.e. eqns. (6.5) and (6.8),

respectively) or/and consecutive oxidation from primary products (CO, C_2H_6 and C_2H_4) to CO_2, see eqns. (6.6), (6.7), (6.9) and (6.10).

$$CH_4 + 3O \rightarrow CO + 2H_2O \quad (6.5)$$

$$CO + H_2O \rightarrow CO_2 + H_2 \quad (6.6)$$

$$CO + O \rightarrow CO_2 \quad (6.7)$$

$$CH_4 + 4O \rightarrow CO_2 + 2H_2O \quad (6.8)$$

$$C_2H_6 + 7O \rightarrow 2CO_2 + 3H_2O \quad (6.9)$$

$$C_2H_4 + 6O \rightarrow 2CO_2 + 2H_2O \quad (6.10)$$

6.2. Characterization by different techniques of the unmodified LSCF6428-HFM reactor before and after methane conversion test.

6.2.1. X ray-diffraction (XRD):

The diffraction profiles for the unmodified LSCF 6428 hollow fibre membrane system before and after methane conversion are shown in **figure 6.4.** The XRD patterns for lumen side and shell side of unmodified LSCF 6428 hollow fibre membrane before reaction are shown in **Figures 6.4b** and **6.4c**, respectively. Both XRD profiles display the characteristic sign of the hollow fibre membrane (i.e. $La_{0.6}Sr_{0.4}Co_{0.8}Fe_{0.2}O_{3-\delta}$) as the main crystalline phase **[13]**.

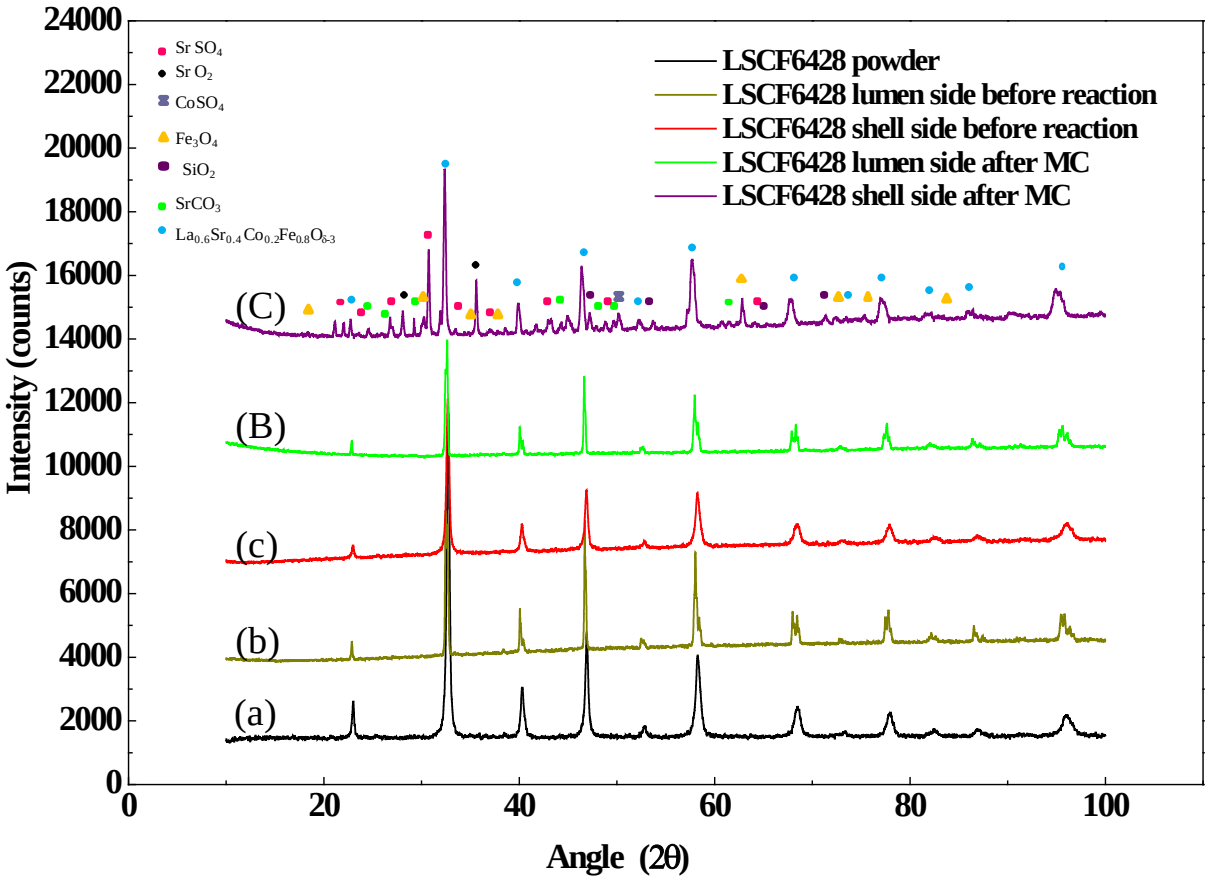

Figure.6.4. XRD patterns of the unmodified $La_{0.6}Sr_{0.4}Co_{0.2}Fe_{0.8}O_{3-\delta}$ hollow fibre membrane. LSCF6428 powder (a), Lumen side (b) and Shell side (c) before the oxygen flux measurements. Centre lumen side (B) and centre shell side (C) after methane conversion experiments.

The diffraction profiles for centre lumen side and centre shell side for unmodified LSCF6428-HFM reactors after methane conversion experiments are illustrated in **figures 6.4B** and **6.4C**. It can be clearly observed that the principal crystalline phase (i.e. LSCF6428) was detected in both sides (i.e. centre lumen and centre shell sides). However, other crystalline phases such as SrO_2 (00-005-0490), $SrSO_4$ (00-005-5935), $CoSO_4$ (10124-43-3), Fe_3O_4 (01-088-0315), SiO_2 (00-005-0490) and $SrCO_3$ (1633-05-2) were also observed for the centre shell side.

6.2.2. Scanning Electron Microscopy (SEM):

The SEM micrographs of the centre shell side of the $La_{0.6}Sr_{0.4}Co_{0.2}Fe_{0.8}O_{3-\delta}$ hollow fibre membrane before and after methane conversion are shown in **figures 6.5a** and **6.5A**, respectively.

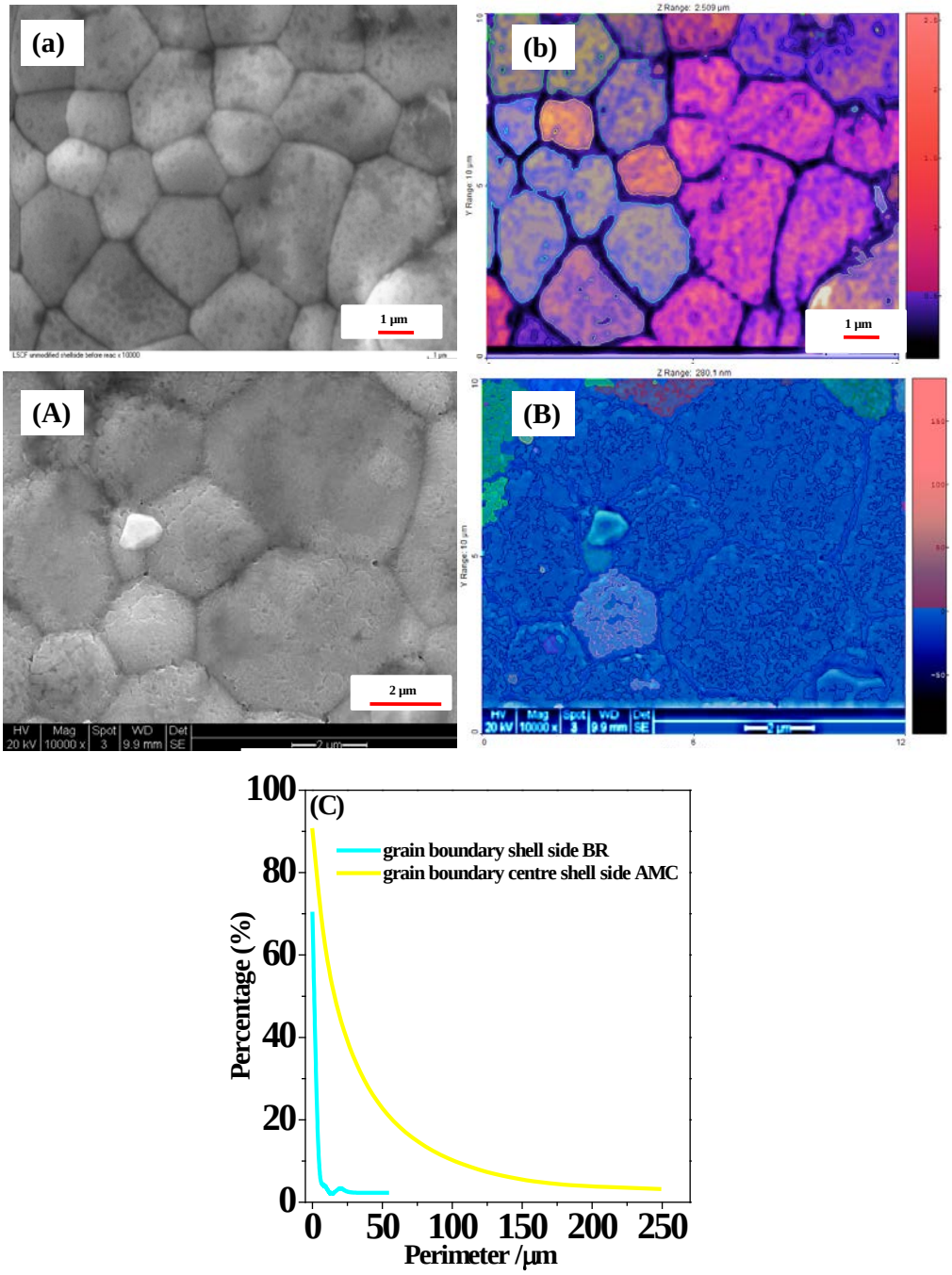

Figure 6.5 SEM images of the shell side (a) and simulate image (b) before reaction. SEM micrograph centre shell side (A), image simulate by SPIP6.0.9 (B). Distribution of the grain boundary perimeter shell side before and after methane conversion measurements (C).

Comparing the panoramic images of the centre shell side before and after methane conversion experiment, it is clearly illustrated that the smooth surface of the grain boundaries changed to rough surface due to the influence of the reducing gas atmosphere used (CH_4) and produced (CO) during the experiments (**figure 6.5a** and **6.5A**). Furthermore, the grain boundary perimeters slightly increased from (0.02 - 20 μm) before reaction to (0.03-175 μm) after methane conversion (**figure 6.5b**, **6.5B** and **6.5C**). These ranges of perimeters represent between 93% and 96% of the total grains boundaries analysed. The increase of the perimeters of the grain boundaries could be associated to the possible presence of hot spots during methane conversion reaction, see **appendix V.2, figure V.2.**

The microstructures of the centre lumen side for the unmodified LSCF6428-HFM before and after methane conversion are given in **figures 6.6a** and **6.6A**, respectively. It can be noted that the grain boundary perimeter after partial oxidation methane slightly increased up to (0.03 to 34 μm), which represent 97% of the total grain boundaries, compared to the grain boundary perimeter from the lumen side (0.02-16 μm) before reaction that correspond to 91% of the total grain boundaries, according to the simulation of the images by SPIP 6.0.9, **figure 6.6C** and **appendix V.2, figure V.3** Furthermore, it can be noted that small cavities or pores partially decorated with small particles appear at the interface of the grain boundaries after reaction (**figure 6.6A**).

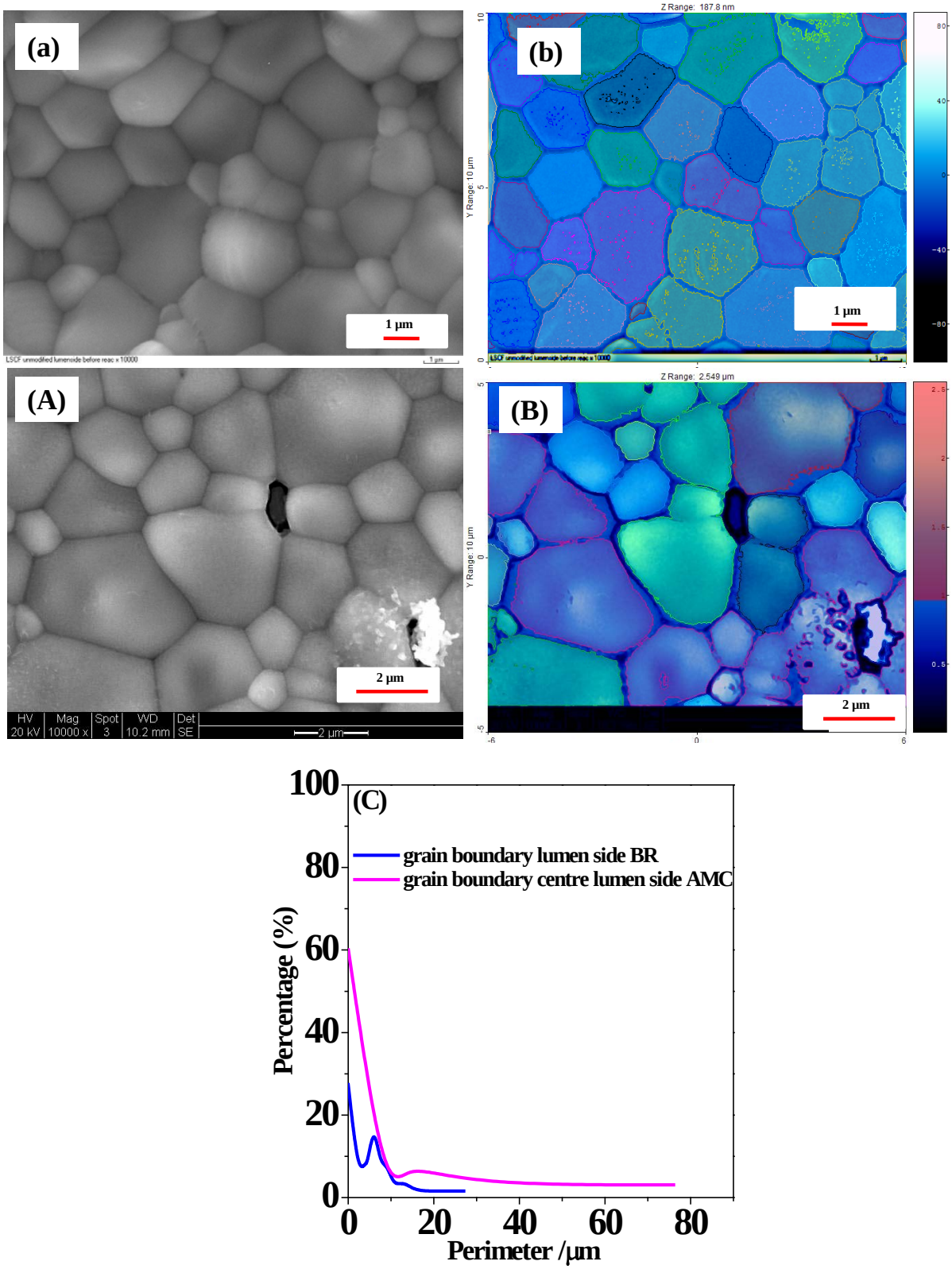

Figure 6.6 SEM images of the lumen side (a) and image simulated (b) before reaction and centre lumen side after methane conversion measurements (A) and image simulated (B). Distribution of the grain boundaries perimeter obtained by simulation with SPIP 6.0.9 (C)

Comparison of the microstructures from the centre shell side and the centre lumen side after methane conversion revealed that the external membrane side exhibits larger changes in the surface and morphology of the grain boundary than the centre lumen side surface, **appendix V.2, figures V.4** and **V.5**. This is probably due to the fact that the first experiment of methane conversion was under MSAL mode (i.e. 4%CH_4/He supplied in the shell side and air sweep in the lumen side). Then, it was changed the operation in MLAS mode (i.e. 4%CH_4/He supplied in the lumen side and air sweep in the shell side), where CH_4 reacted with relative high oxygen concentration in the lumen side because air was supplied in this side in previous experiments.

In **figure 6.7** is given the SEM photographs of the end shell side and end lumen side of the LSCF6428-HFM after methane conversion. The magnifications of the end shell side after reaction are shown in **figures 6.7A** and **6.7B**. It can be noted that the surface and morphology of the grain boundary severely changed as a consequence of the formation of small particles because of the relative high methane concentration in the module inlet (see **figure 6.8**).

On the other hand, the microstructures of end lumen side after methane conversion are shown in **figures 6.7C** and **6.7D**. It can be observed that the grain boundary perimeter slightly increased (i.e., 0.03 to 39 μm) compared to the grain boundary perimeter from the lumen side (i.e., 0.02-16 μm) before reaction, see **appendix V.2, figure V.6**. The former represents 97% whilst the later corresponds to 91% of the total grain boundaries simulated by SPIP 6.0.9, **figure 6.7 E**. In addition, small cavities or pores partially decorated with small particles appear at the interface of the grain boundaries after reaction (**figure 6.7C**). Note that the surface morphologies for the end lumen side compared to end shell side after methane conversion did not vary markedly (**figures 6.7C** and **6.7B**).

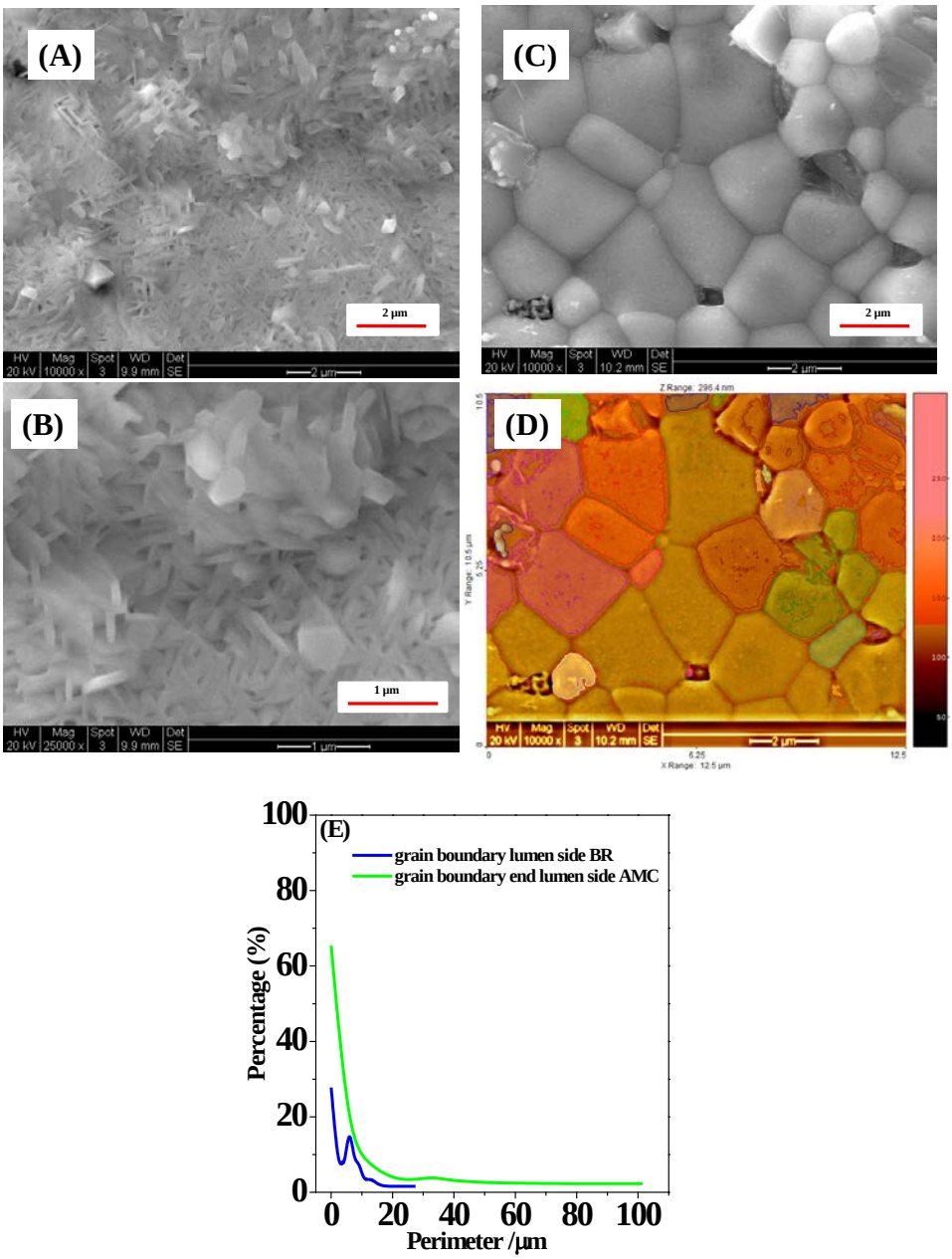

Figure 6.7 SEM micrograph of the end shell side (A) and image magnified (B). Microstructure of the end lumen side (C) and image simulated (D) after methane conversion measurements. Distribution of the grain boundary perimeter before and after methane conversion (E)

Comparing the centre shell side (**figure 6.5C**) with end shell side (**figures 6.7A** and **6.7B**) one can infer that the later side underwent further deterioration. This finding can be rationalised considering that in the module extreme, the oxygen permeation is lower than that in the centre shell side because of lower temperature, according to internal temperature profiles of the membrane module (**figure 3.4**, **Chapter 3**). This is reflected on a relatively

high methane concentration in the end shell side of the module and hence higher reducing character.

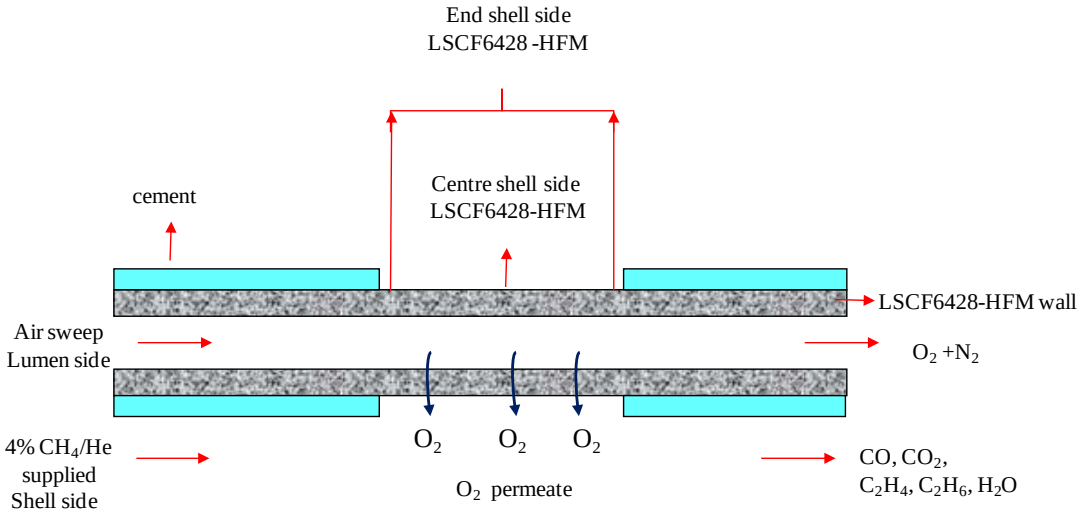

Figure 6.8 Diagram of the LSCF6428-HFM reactor with characterized zones and supplied gases.

6.2.3. Energy dispersive x-ray spectroscopy (EDXS)

In **table 6.1** is given the EDXS results for different zones of the LSCF6428 hollow fibre membrane before and after methane conversion. Further details can be found in **appendix V**, where all the EDXS results are given. Oxygen concentrations were not plotted because of its high content before and after reaction (see **appendix V.3**, **figure V.7**).

Comparison of the centre shell side of unmodified LSCF6428 post methane conversion with shell side before reaction indicates that the elemental compositions of the all metals decreased from (7.2% to 5 %) for La; (5.6% to 2.5 %) for Sr, (2.2% to 1.2 %) for Co and (9.8% to 6.1 %) for Fe. It is worth remarking that sulphur (0.3 %) and carbon (14.7 %) were also observed on this side of the membrane; see **table 6.1** and **appendix V.3** (**figure V.7**).

Table 6.1 Summary of EDXS results of different zones of the LSCF6428 hollow fibre membrane before and after partial oxidation of methane.

Membrane	***Condition***	***Section (side)***	***Absolute atomic %***							***Experimental stoichiometry***
			La	***Sr***	***Co***	***Fe***	***O***	***C***	***S***	
LSCF6428	**BR**	**Lumen**	**8**	**5.6**	**2.3**	**10.3**	**73.8**			**La0.6:Sr0.4:Co0.2:Fe0.8**
LSCF6428	AR	Centre lumen	7.6±0.9	3.5±1.1	1.2±0.5	8.8±1.1	74.6±9.5	2.3	0.9	
LSCF6428	AR	End lumen	7.5±0.6	3.41±0.6	1.2±0.5	9.02±1.1	64.8±12.9	13.0	0.98	
LSCF6428	**BR**	**Shell**	**7.2**	**5.6**	**2.2**	**9.8**	**75.4**			**La0.6:Sr0.4:Co0.2:Fe0.8**
LSCF6428	AR	Centre shell	5.0±0.78	2.5±1.1	1.2±0.59	6.1±1.2	70.0±11.6	14.7	0.3	
LSCF6428	AR	End shell	4.6±0.7	3.2±0.8	1.3±0.6	6.1±1.0	71.3±13.1	13.4	0.1	

Similar metal composition trend did show the end shell side after methane conversion. These changes in the elemental composition on the surface of HFM are attributed to the reducing gases used or generated during methane conversion and sulphur impurity. Similar tendency was reported by Tan *et al* **[14].**

Considering the above mentioned XRD, SEM and EDXS results from unmodified LSCF6428-HFM after methane conversion, it can be concluded that crystalline phases, morphology, perimeter and metal composition of the grain boundary changed on the centre shell side and the end shell side compared to the membrane composition before reaction. This is attributed to kinetic demixing of mobile cations and decomposition of the membrane due to the axial temperature generated by the exothermic reaction of methane combustion **[15]**.

Moreover, the membrane was contaminated by sulphur impurity which comes from air and helium gases employed during the experiments, polyethersulfone used during fabrication of the LSCF6428 hollow fibre and the cement used to assemble the reactor. It was also observed the segregation of strontium, cobalt and iron to form different crystalline oxide and sulphate phases such as SrO_2, $SrSO_4$, $CoSO_4$ and Fe_3O_4. Additionally, the formation of $SrCO_3$ was observed, owing to the reaction of CO_2 and/or CO with segregated strontium oxide, according to eqns. (6.11) and (6.12) **[14-20]**. According to the ΔG calculation at 850°C, the eqn. (6.12) would have a major contribution toward the formation of $SrCO_3$. (-258 kJ mol^{-1}) that the eqn. (6.11) (-53.2 kJ mol^{-1}), see **appendix V.4**, **figure V. 8**.

$$SrO + CO_2 \rightarrow SrCO_3 \qquad (6.11)$$

$$SrO_2 + CO \rightarrow SrCO_3 \qquad (6.12)$$

6.3. Oxidation of methane in a LSCF6428 hollow fibre membrane reactor modified with 5%Ni-LSCF6428 catalyst

The 5%Ni-LSCF6428 catalyst was coated on the outside surface of the LSCF6428-HFM, the micrographs is given in **figure 6.9**.

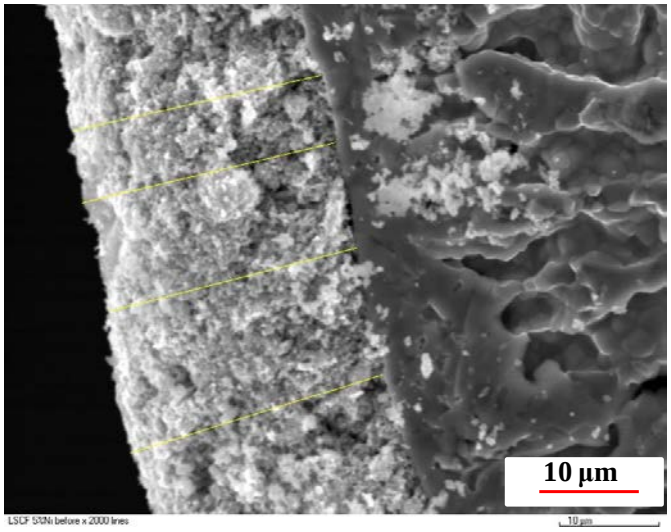

Figure 6.9 Cross section of SEM image for LSCF6428-HFM modified with 5%Ni-LSCF6428 catalyst layer.

The cross-section image for 5%Ni-LSCF6428 catalyst layer coated on the shell side of the LSCF6428 hollow fibre membrane presents a uniform and thin layer of approximately 26 µm thickness, see **figure 6.9**.

Four reactor modules were assembled to study the methane conversion on 5%Ni-LSCF6428/LSCF6428-HFM. Each module was operated for a period of 2-7 hours at 850 °C. This relatively short operation period is attributed to the removal of the perovskite-type structure lattice oxygen, owing to the reducing gas atmosphere generated by the catalytic reaction. This could cause the crystalline structure to collapse, which would be reflected by the membrane stoichiometry composition as a consequence of crystalline phase segregation (i.e. $SrCO_3$) **[14-20]**. Other factor that could damage the reactor is the high amount of heat

released by the methane combustion reaction, which can cause fracture due to the lattice expansion mismatch on opposite sides of the membrane **[13, 21-23]**.

Figure 6.10 shows the catalytic performance and oxygen flux for 5%Ni-LSCF6428/LSCF6428-HFM reactor as a function of operation time under mode MSAL (i.e. 10 ml (STP) min^{-1} of 4% CH_4/He flow was supplied in the shell side while in the lumen side sweep 10 ml (STP) min^{-1} of 2% O_2/He flow), co current at 850 °C.

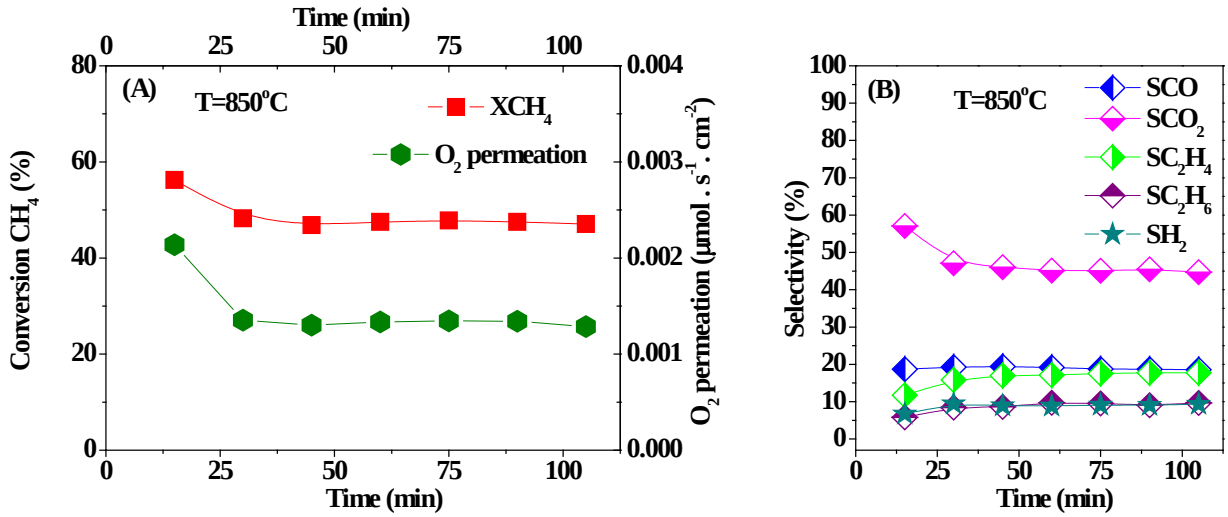

Figure 6.10 Catalytic performance and oxygen flux versus time on stream for 5%Ni-LSCF6428/LSCF6428-HFM reactor at 850 °C. 4% CH_4/He flow on the shell side and 2% O_2/He flow rate on the lumen side, both flows were 10 ml (STP) min^{-1}.

It should be remarked that this module was tested for 1968 hours in an oxygen permeation experiment and was treated with 30 ml (STP) min^{-1} of 5% H_2/He as was described in Chapter 5.

As can be seen in **figure 6.10A**, the oxygen permeation flux decreased slightly from 0.0021 to 0.0013 μmol s^{-1} cm^{-2} and also methane conversion gradually decreased from 56% to 47%. Nevertheless, a considerable improvement compared to blank of LSCF6428-HFM reactor (**figure 6.2A**) was obtained.

This is probably due to changes in the catalytic performance of the membrane reactor as presence of 5%Ni-LSCF6428 catalyst coated on surface of LSCF6428-HFM, which plays the following role: increases the oxygen transport through the hollow fibre membrane reactor and speeds up the methane oxidation reaction. In addition, this trend suggests that the methane conversion occurs mainly over the 5%Ni-LSCF6428 catalyst rather than the hollow fibre membrane **[4]**.

In **figure 6.10B** it can be observed that CO and H_2 selectivity was held constant (19% and 9%, respectively) during operation time. In contrast, CO_2 selectivity decreased initially from 57% to 45% during 30 minutes of reaction, but became constant during the remaining operation time. C_2 selectivity (C_2H_4 and C_2H_6), on the other hand, increased from 24% up to 27% during the methane conversion experiment. The carbon balance obtained for the module reactor (5%Ni-LSCF6428-HFM under MSAL mode) was approximately 30%, which suggests that nearly 70% of the carbon fed into the membrane reactor was deposited on the module surface (see **appendix V.5**, **figure V. 9**).

The above-mentioned results suggest that the three catalytic pathways can take place on 5%Ni-LSCF6428/LSCF6428-HFM: 1) Partial oxidation of methane to syngas ($CO + H_2$) on metallic nickel particles **[24-26]**. 2) Oxidative coupling of methane to C_2 and 3) total oxidation of methane to CO_2 products on NiO particles **[24-26]**. It should be remarked that the 5%Ni-LSCF6428/LSCF6428-HFM reactor employed in the experiment presented developed a leak after 105 min of operation under methane oxidation conditions. After so, the experiment was stopped immediately. The characterization of this module was reported in **Chapter 5, section 5.8.**

In **figure 6.11** describes the dependence of oxygen permeation, methane conversion and product selectivity over 5%Ni-LSCF6428/LSCF6428-HFM as a function of run time. On the

shell side was supplied with 4% CH_4/He and 2% O_2/He on the lumen side. Both gases were fed at 25 ml (STP) min^{-1} and the module was not treated with a H_2 flow.

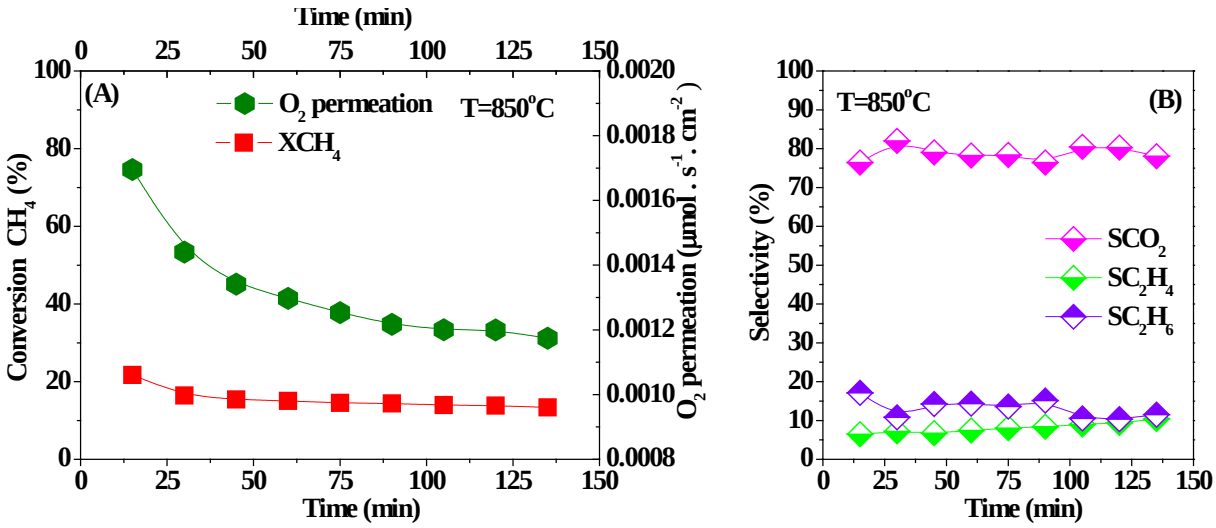

Figure 6.11 Dependence of oxygen permeation, methane conversion and product selectivity with time on stream for 5%Ni-LSCF6428/LSCF6428-HFM at 850 °C. 4% CH_4/He flow on the shell side and 2% O_2/He flow rate on the lumen side (25 ml (STP) min^{-1} in both sides).

It can be noted that the oxygen permeation and methane conversion into the hollow fibre membranes reactor decreased (i.e. from 0.0017 to 0.0012 μmol s^{-1} cm^{-2} and 22% to 13%, respectively) with increasing time on stream, see **figure 6.11A**. This is likely associated with changes in the 5%Ni-LSCF6428 catalyst coated on surface of LSCF6428-HFM that could affect the oxygen surface exchange rate and/or diffusion rate rather than the apparent activation energy or the rate-limiting step through the hollow fibre membrane reactor **[27].** Furthermore, the CO_2 selectivity is larger than 70 % and holds constant with increasing time on stream. Meanwhile, C_2 (C_2H_6 + C_2H_4) selectivity was steady (ca. 23%) during the operation time, see **figure 6.11B**. Based on the product distribution, the total oxidation of methane to CO_2 appears to be the main catalytic pathways. On the other hand, the carbon balance suggested that between 10% and 20 % of residual carbon remains on the catalyst surface, see **appendix V.5**, **figure V. 10**

The **figure 6.12** compares the methane conversion and the products selectivity obtained with the 5%Ni-LSCF6428/HFM reactor at similar reaction temperature but different gases flows (i.e. 10 and 25 ml (STP) min^{-1}) against oxygen permeation.

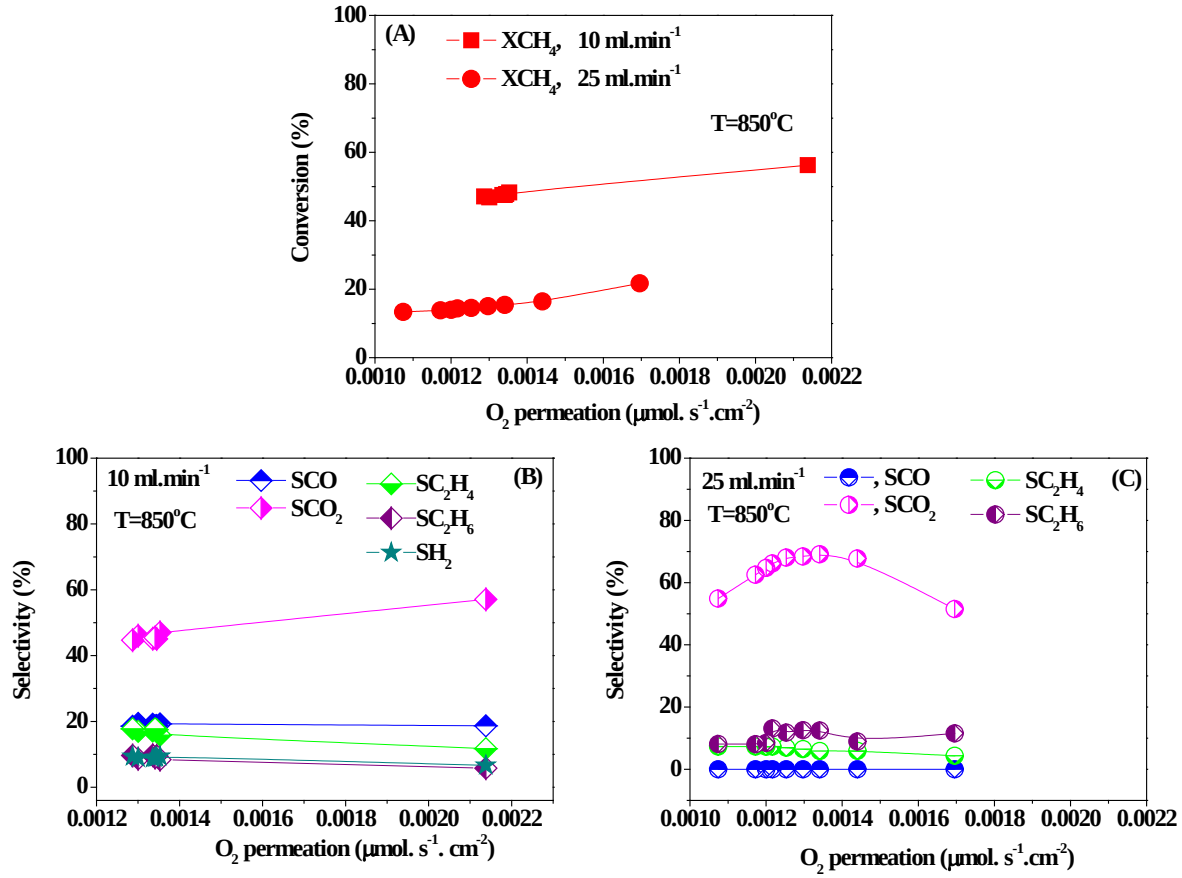

Figure 6.12 Comparison of methane conversion and selectivity of the products against oxygen permeation for two different flows on 5%Ni-LSCF6428/LSCF6428-HFM module at 850 °C. 4% CH_4/He flow on the shell side and 2% O_2/He flow rate on the lumen side (i.e. 10 and 25 $ml.min^{-1}$).

It was found be that the reactor under a low supplied flow (10 ml. min^{-1}) and H_2 treatment showed higher methane conversion than with high supplied flow (25 $ml.min^{-1}$) and no H_2 treatment. Additionally, CO_2 was a major product and C_2 (C_2H_6 and C_2H_4) were the minor products for both gas flows. Further, the H_2-treated module fed with low flows of 4% CH_4/He and 2% O_2/He produced syngas (i.e. CO and H_2) as a consequence of the hydrogen treatment; since the H_2 untreated reactor fed with a high flow did not produce syngas.

The methane conversion results and oxygen permeation for the 5%Ni-LSCF6428/LSCF6428-HFM reactor are shown in **figure 6.13**, when 4% CH_4/He was supplied on the shell side and air flow swept in the lumen side with a flow rate of 25 ml (STP) min^{-1} for both sides.

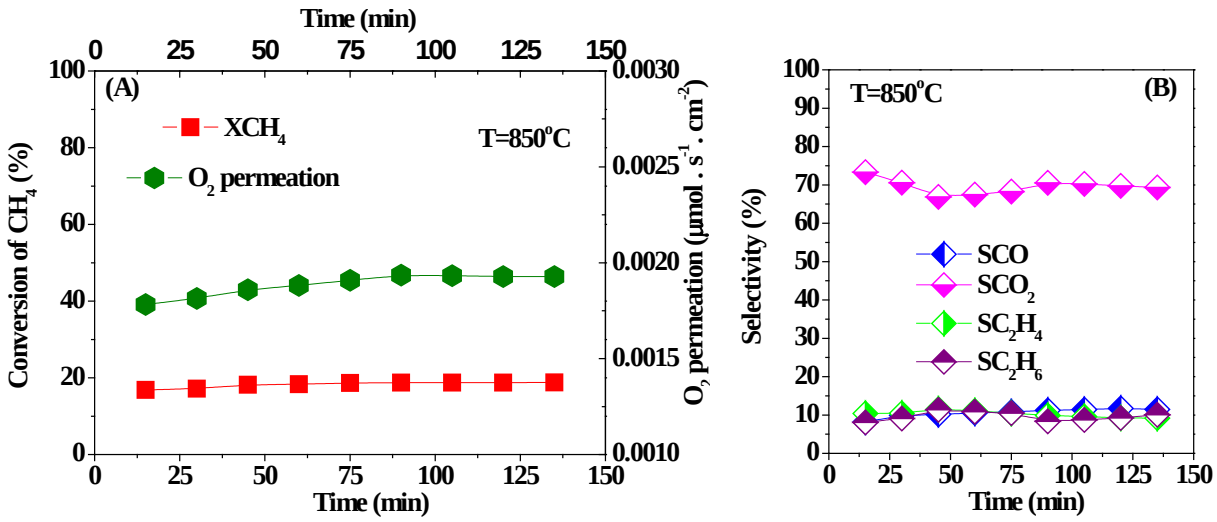

Figure 6.13 Catalytic performance of the methane conversion on LSCF6428-HFM coated 5%Ni-LSCF6428 reactor at 850 °C. Air flow fed on the lumen side and 4% CH_4/He on the shell side with flow of 25ml (STP) min^{-1} in both sides.

It was found that both oxygen permeation and methane conversion hold constant during operation time (i.e. 0.0019 μmol $s^{-1}cm^{-2}$ and 19%, respectively), see **figure 6.13A**. Furthermore, the CO_2 selectivity is slightly decreased from 73% to 69 % and CO, C_2H_4 and C_2H_6 selectivity presented a similar trend with and values between 8% and 11% for each product (**figure 6.13B**). Carbon balance for this case decreases from 100 to 97% (See **appendix V. 5**, **figure V.11**) this suggests that only small amounts of carbon (below 10 %) were deposited in the module.

The influence of oxygen concentration on oxygen permeation, methane conversion and products selectivity for 5%Ni-LSCF6428-HFM against time on stream at 850ºC is given in **figure 6.14**.

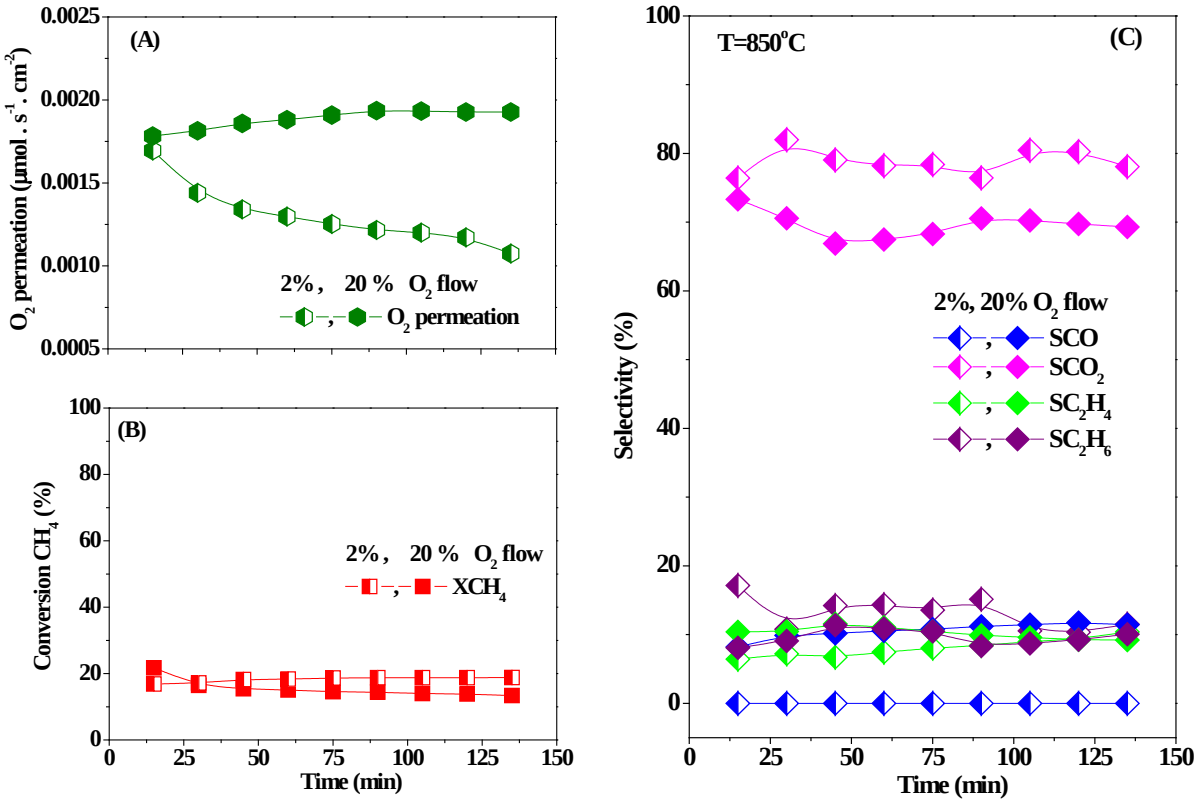

Figure 6.14 Influence of oxygen concentration on methane conversion and products selectivity for 5%Ni-modified LSCF6428-HFM reactor. 20% and 2% of O_2 flow fed on lumen side and 4% CH_4/He on the shell side with flow of 25ml (STP) min^{-1} in both sides.

As we expected, the oxygen permeation increases with increasing oxygen concentration. However, this was not reflected on methane conversion, which was between 15% and 20% whatever the oxygen concentration (i.e. 2% and 20%), see **figures 6.14A** and **6.14B**. Note that the main catalytic pathway for both oxygen concentrations is the total oxidation of methane to CO_2, according to product distribution, see **figure 6.14C**. Furthermore, at 20% of oxygen, CO was also observed as a product, likely due to the high lattice oxygen concentration on the membrane surface, according to eqn. (6.3).

The modification effect of the catalyst (i.e. 5% Ni-LSCF6428) coated on the hollow fibre membrane over methane conversion is shown in **figure 6.15**. Three effects of the 5%Ni-LSCF6428 catalyst on the membrane reactor performance were noted: **(i)** Oxygen permeation

increased from ca. 0.0003 µmol s^{-1} cm^{-2} to ca. 0.0019 µmol s^{-1} cm^{-2} as was expected **(ii)** Methane conversion increased from approximately 3% to 19% **(iii)** CO_x become the main reaction product, as a consequence of high oxygen permeation. Note that the unmodified HFM reactor favoured C_2 (C_2H_4 and C_2H_6) selectivity (i.e. oxidative coupling of methane). Both the products distribution and the high methane conversions suggest that CH_4 reacts with oxygen species that diffused over the catalyst to produce CO_x and H_2O. This would indicate that methane conversion occurs over the surface of 5%Ni-LSCF6428 catalyst and facilitates the total oxidation catalytic pathway **[1, 4]**.

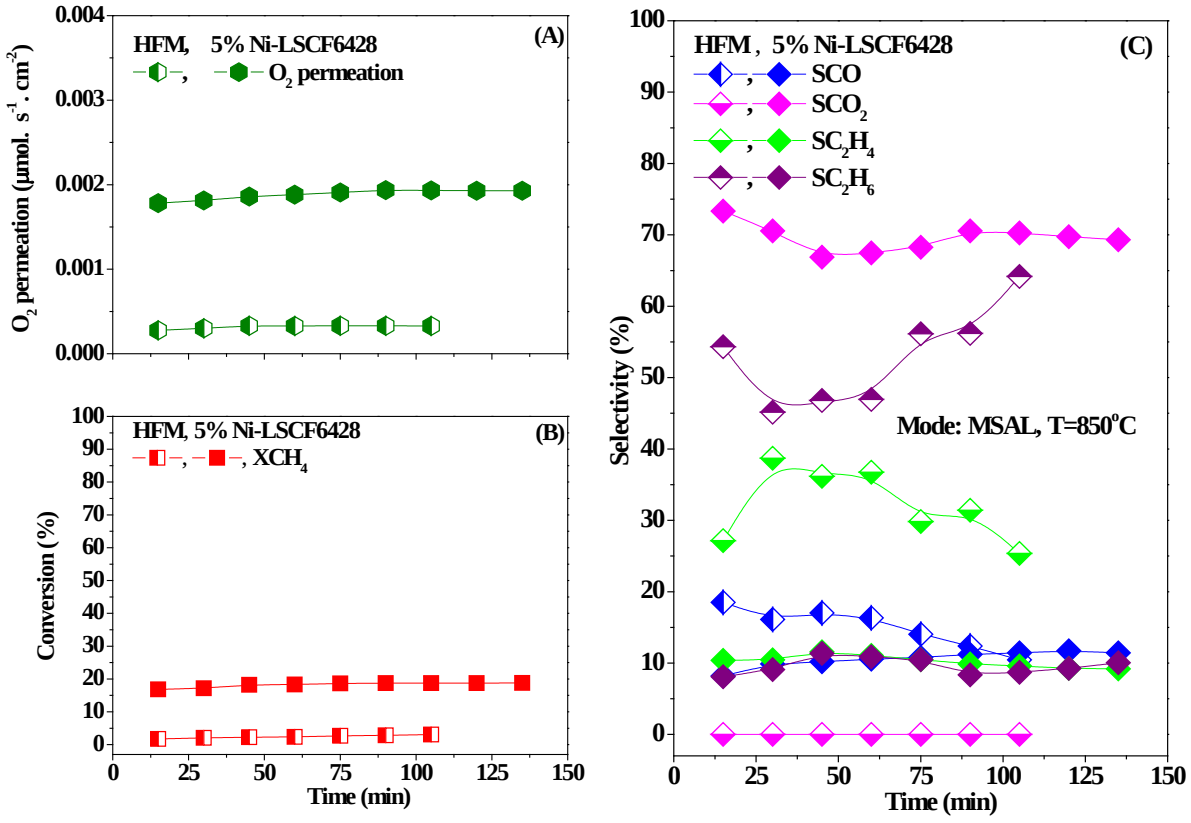

Figure 6.15 Dependence of the oxygen permeation, methane conversion and products selectivity against time on stream for unmodified and modified LSCF6428HFM at 850 °C. Air flow fed on the lumen side and 4% CH_4/He on the shell side with flow of 25ml (STP) min^{-1} in both sides.

6.4. Comparison of the apparent overall rate constants for LSCF6428-HFM, and 5%Ni-LSCF6428/LSCF6428-HFM under different atmosphere (He and CH_4) at 850 °C.

In **table 6.2** are given the apparent overall rate constants for LSCF6428-HFM and 5%Ni-LSCF6428/LSCF6428-HFM under different reducing gas atmosphere (i.e. He and CH_4).

Table 6.2 Apparent overall rate constant for LSCF6428-HFM and 5%Ni-LSCF6428/LSCF6428-HFM at 850 °C, where CH_4 or He flow supplied in the shell side and air sweep in the lumen side.

Catalyst	He flow ($ml.min^{-1}$)	4%CH_4 flow ($ml.min^{-1}$)	Percentage of oxygen (%)	O_2 flow ($ml.min^{-1}$)	Rate constant ($\mu mol.sec^{-1}.bar^{-1}cm^{-2}$)
Unmodified	25	-	20	25	0.16
Unmodified	-	25	20	25	0.26
5%Ni/LSCF64268	25	-	20	25	0.50
5%Ni/LSCF64268	-	10	2	10	nd
5%Ni/LSCF64268	-	25	2	25	nd
5%Ni/LSCF64268	-	25	20	25	0.76

Comparison the apparent overall rate constant for LSCF6428-HFM without catalyst obtained with different reducing atmospheres (CH_4 and He) under MSAL or ALHS mode, **table 6.2**. It is found that the apparent overall rate constant for Air/CH_4 gradient increased 1.5 fold (0.26 µmol s^{-1} bar^{-1} cm^{-2}) compared to Air/He gradient (0.16 µmol s^{-1} bar^{-1} cm^{-2}). This finding is likely due to the reducing character of CH_4 relative to He; the Air/CH_4 gradient is larger than Air/He gradient, therefore the oxygen concentration and driven force of the oxygen transport across the membrane is higher compared to Air/He gradient **[14]**. Moreover, the methane combustion is an exothermic reaction and releases a great amount of energy and hereby produces hot spots on the surface of the hollow fibre membrane reactor **[28]**. Helium, on the other hand, is inert on the HFM surface, facilitating a uniform temperature profile in the reactor **[14]**. A similar tendency was also observed in 5%Ni-

LSCF6428/LSCF6428-HFM reactor under Air/CH_4 gradient (i.e. 0.76 µmol s^{-1} bar^{-1} cm^{-2}) and Air/He gradient (i.e. 0.50 µmol s^{-1} $bar^{-1}cm^{-2}$), see **table 6.2**, in agreement with findings reported by Jin *et al*. **[29]**, Zeng *et al*. **[30]** and Xu and Thomson **[31]**.

On the other hand, comparison the apparent overall rate constant for the unmodified LSCF6428- HFM with the modified LSCF6428-HFM by 5%Ni-LSCF6428 catalyst under Air/He gradient shows that this increased from 0.16 µmol. s^{-1} bar^{-1} cm^{-2} to 0.50 µmol s^{-1} $bar^{-1}cm^{-2}$. This is tentatively attributed to the nickel catalyst that facilities the surface reaction of molecular oxygen and the possible enlargement of the surface area of the membrane by catalyst coated on the shell side.

Similar behaviour was observed under Air/CH_4 gradient for both the reactors unmodified LSCF6428-HFM (i.e. 0.26 µmol s^{-1} bar^{-1} cm^{-2}) and 5%Ni-LSCF6428-HFM (i.e. 0.76 µmol s^{-1} bar^{-1} cm^{-2}). This can be explained considering that the catalyst facilitates the dissociation of methane into methyl radical ($\bullet CH_3$) at the active sites on the catalyst surface. These active sites are usually reactive nucleophilic lattice oxygen ions (i.e. O^{2-}) and electrophilic oxygen species (i.e. O_2^-, O^- and $O_{2\,(ads)}$), which react with $\bullet CH_3$ to form products **[1, 12, 14, 32, 33]**.

In the experiments carried out at low oxygen concentration (i.e. 2%) it was not possible to determine the apparent rate constant due to low amount of oxygen permeated.

6.5. Characterization of the 5%Ni-LSCF6428/LSCF6428-HFM reactor before and after methane conversion by different techniques.

6.5.1 X ray-diffraction (XRD):

The XRD patterns of the 5%Ni-LSCF6428/LSCF 6428 hollow fibre membrane module before and after methane conversion are shown in **figure 6.16.**

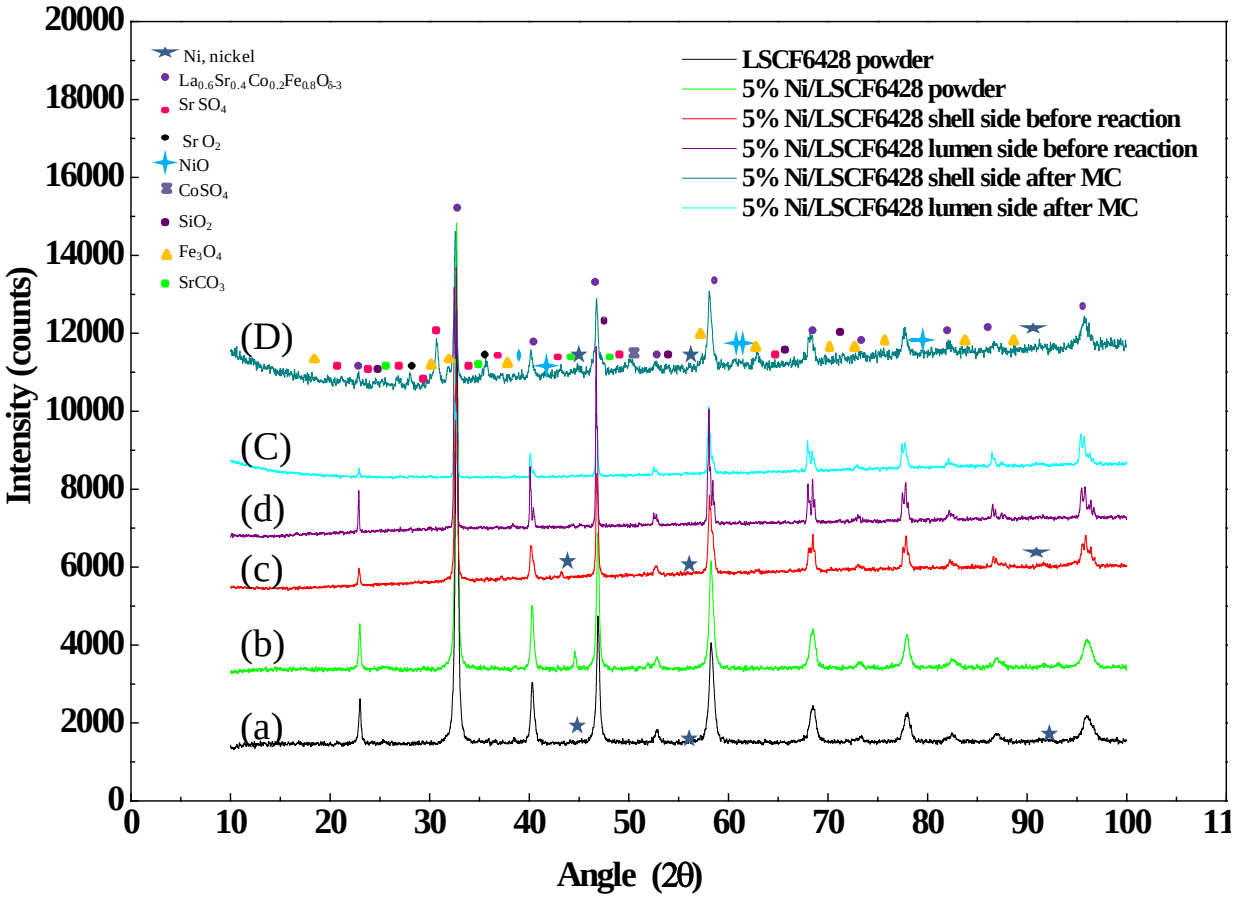

Figure.6.16 XRD patterns of the 5%Ni-LSCF6428/LSCF6428 hollow fibre membrane. LSCF6428 powder (a), 5%Ni/LSCF6428 powder (b), shell side (c) and lumen side (d) before the oxygen flux measurements. Centre lumen side (C) and centre shell side (D) after methane conversion experiments.

Both the shell side and lumen side samples exhibit the characteristic peaks of LSCF6428 as the major phase and only the 5%Ni-LSCF6428/LSCF6428-HFM powder and shell side before reaction presented a second crystalline phase that correspond to metallic nickel, Ni (00-004-0850). Furthermore, the diffraction profiles for centre lumen side and centre shell side post methane conversion experiments showed LSCF6428 as the main crystalline phase and other minor crystalline phases such as SrO_2 (00-007-0234), $SrSO_4$ (00-005-5935) and only for the centre shell side were observed $CoSO_4$ (10124-43-3), Fe_3O_4 (01-088-0315), NiO (1313-99-1), SiO_2 (00-005-0490) and $SrCO_3$ (1633-05-2), see **figure 6.16D**. It is worth mentioning that only one XRD profile from the lumen side and the shell side after methane

oxidation are shown in **figures 6.16 C** and **6.16D**, respectively; however other diffraction profiles are given in **appendix V.6**, **figure V.12**.

The above-mentioned XRD results show that the shell side of 5%Ni-LSCF6428-HFM after methane conversion exhibited certain impurities such as sulphur and silica detected as $SrSO_4$, $CoSO_4$ and SiO_2 crystalline phases, **figure 6.16D**. Similar sulphur-containing crystalline phases have been previously reported **[6, 17, 34-36]**. The formation of these phases was attributed to the presence of sulphur in the air and helium gases employed during the experiments. The polyethersulfone used during fabrication of the LSCF6428 hollow or/and the cement used in the reactor assemble. Additionally, $SrCO_3$ was observed as a consequence of the CO_2 interaction with segregated strontium oxide **[15-20]**.

6.5.2. Scanning Electron Microscopy (SEM):

The SEM photographs of the shell side and the lumen side of the modified LSCF6428-HFM pre operation are given in **figure 6.17**.

The magnification images for shell side before reaction is shown in **figure 6.17a**; it can be observed that the catalyst was well-distributed on the shell side of the LSCF6428-HFM. The particle perimeter range was between 0.01 and 4.5 μm, which represent around 92% of the total grain analysed in **figure 6.17e**, and **appendix V.7, figure V.13**.

Furthermore, note that the grain boundary perimeter for lumen side exhibits ranges between 0.02 to 16 μm, representing 91 % of the overall grain boundary perimeter, see **figure 6.17e** and **appendix V.2, figure V.3**. The deposition of 5%Ni/LSCF6428-HFM catalyst fully covered the grain boundary of the HFM.

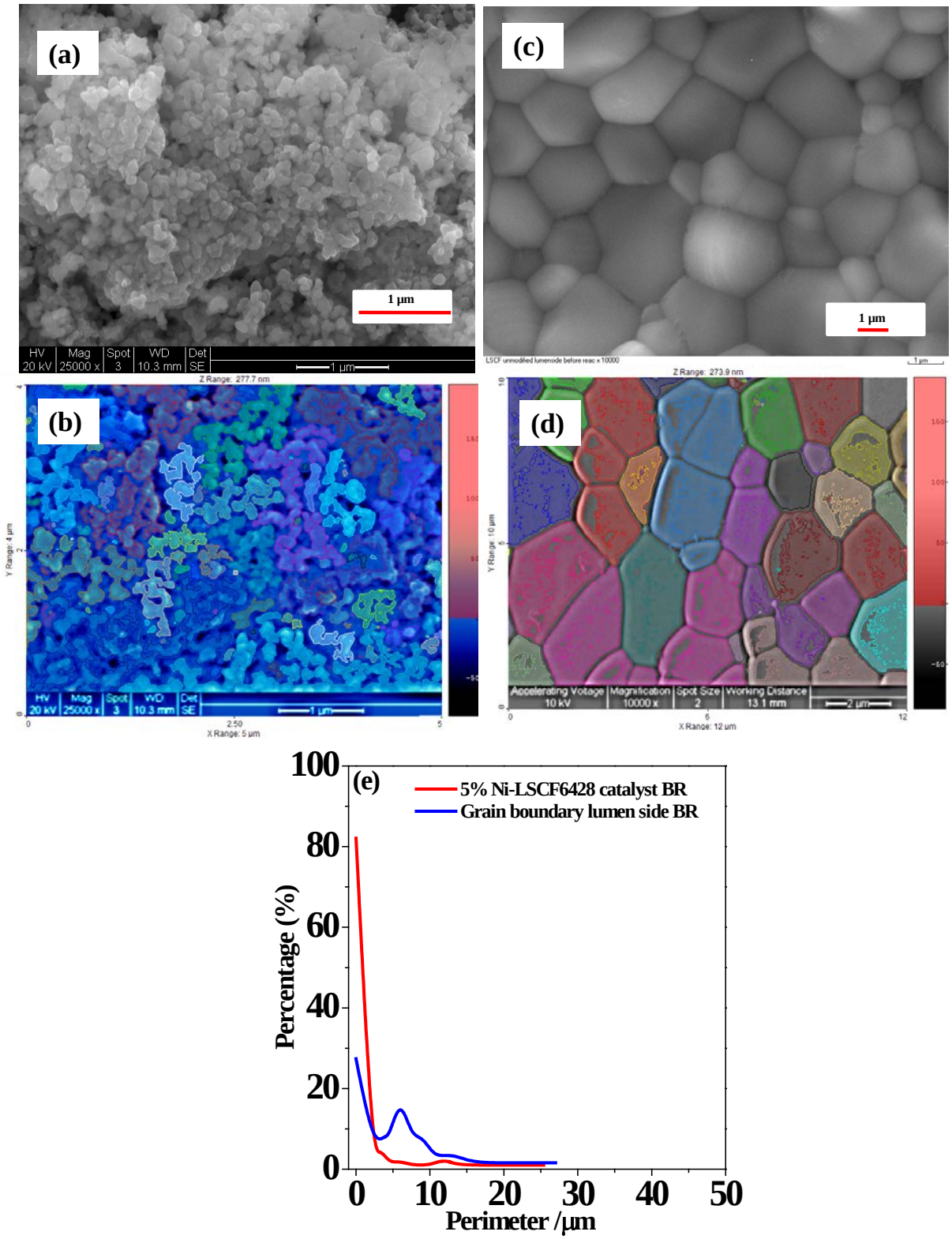

Figure 6.17 SEM images of the shell side before reaction (a), image simulated by SPIP 6.0.9 (b). SEM images of the grain boundary in lumen side before reaction (c), image simulated by SPIP 6.0.9 of the lumen side (d) and distribution of particle (5%Ni-LSCF6428 catalyst) and grain boundary perimeter (e).

The SEM photographs of the centre shell side and the centre lumen side of the modified LSCF6428-HFM post methane conversion are illustrated in **figure 6.18**. It can be clearly observed in the microstructure of the centre shell side after methane conversion (**figures 6.18A** and **6.18B**) that the grain size of 5%Ni/LSCF6428 catalyst increased compared to the grain size range before reaction (**figure 6.17a**). A similar finding was obtained with equivalent membrane reactor-deposited 5%Ni-LSCF6428 used in oxygen flux and methane oxidation and discussed in **Chapter 5**, **figure 5.28**. This was attributed to the agglomeration of catalyst particle and oxidation of Ni metal to NiO during the operation time. Also, note that the microstructure of the centre shell side after methane conversion was markedly affected by the reaction and product atmosphere (**figures 6.18A** and **6.18B**).

SEM pictures of the centre lumen side of 5%Ni-LSCF6428/LSCF6428-HFM post methane oxidation are shown in **figures 6.18C** and **6.18D**. It can be noted that the grain boundaries perimeter show significant changes with respect to the grain boundaries perimeter before reaction.

In addition, the surface morphology of grain boundaries was modified with small particles and cavities or pores among the grain boundaries due to high temperature and the reaction atmosphere (i.e. CH_4, CO and CO_2). The simulated image was not included in the text because of poor contrast between the remaining grain boundaries and the small particles, results a low quality simulated image.

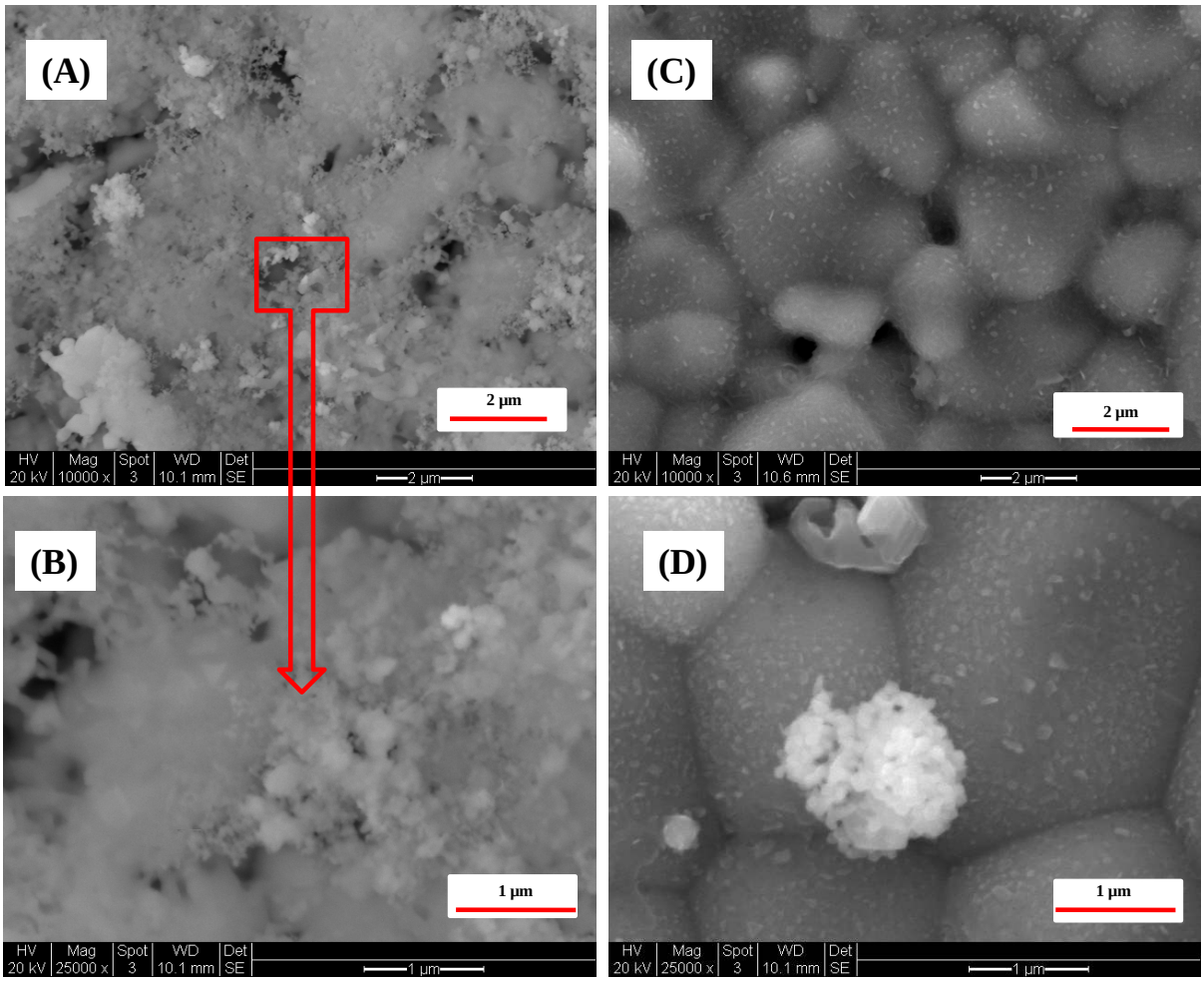

Figure 6.18 SEM microstructure of the centre shell side of 5%Ni-LSCF6428/LSCF6428-HFM (A), images magnified (B), the centre lumen side (C), Image magnified (D) after methane oxidation.

The microstructures of the end shell side and the end lumen side after methane oxidation are given in **figure 6.19**. These photographs show similar changes in the morphology both in the catalyst surface (i.e., end shell side) and in cavities or pores at the interfaces of the grain boundaries of the end lumen side compared to shell side and lumen side (see **figures 6.17a** and **6.17c**) before methane oxidation.

In addition, the grain boundary perimeter for end lumen side (i.e., 0.05 to 50 µm) with 97 % of the overall grain boundary perimeter analysed, see **figure 6.19E**, and **appendix V.7, figure V.15**, slightly increased compared to lumen side before reaction, which presented

grain boundary perimeter within 0.02 and 16 µm that correspond to 91 % of the overall grain boundary perimeter simulated, see **figure 6.19E**, and **appendix V.2, V.7; figures V.3**, **V.15**.

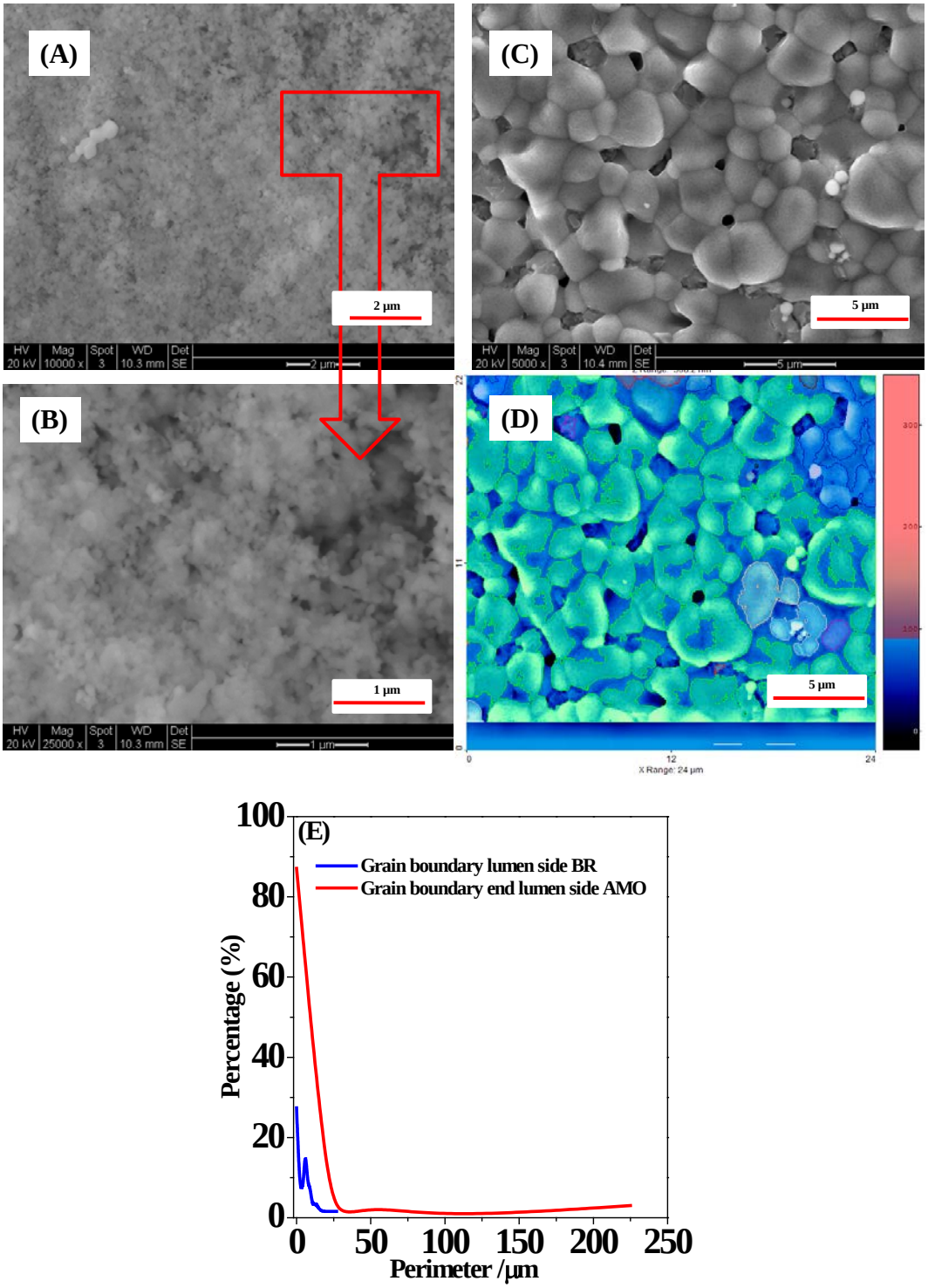

Figure 6.19 SEM microstructure of the end shell side (A), images magnified (B), the end lumen side (C), Image magnified (D) after methane conversion and distribution of the grain boundary perimeter (E).

Taking into account the above discussed XRD and SEM results for the centre shell side of the 5%Ni/LSCF6428-HFM after methane conversion. It can be noted that the morphology of the catalyst changes as a consequence of an oxidation process of metallic nickel to NiO and to the agglomeration of the particles due to the high thermal treatment (**figures 6.18A** and **6.18B**). Furthermore, re-dispersion of the catalyst during the methane conversion produced small particles on the catalyst surface (**figure 6.18A**).

6.5.3. Energy dispersive x-rays spectroscopy (EDXS)

The **table 6.3** shows the EDXS results for different zones of the 5%Ni-LSCF6428 hollow fibre membrane before and after methane conversion reaction. For more details see **appendix V**, where all the EDXS results are given. Oxygen composition was not plotted because of its high content (see **appendix V.8, figure V.16**).

Comparison of the centre shell side of 5%Ni-LSCF6428- HFM before reaction with the shell side after methane conversion, it can be noted that the elemental compositions decreased from (7.4% to 6.3%) for La; (4.7% to 3.3) for Sr, (9.1% to 7.8%) for Fe, (2.2 %to 1.6%) for Co, whist Ni (ca.1.6 %) contents did not change. In addition, it can be noted the presence of carbon (14.1 %) and sulphur (1.0%) on this membrane section, see **table 6.3** and **appendix V.8, tables V.1, V.2**

On the other hand, an overall diminution of the metal composition for La, Sr, Co and Fe (i.e., 5.29%, 3.4%, 1.3% and 8.3%, respectively) in the centre lumen side post methane conversion compared to lumen side before reaction of 5%Ni-LSCF6428/LSCF6428-HFM was observed. Also, it can be observed that sulphur content decreases (0.1%) compared to the fresh lumen side (0.3%), see **table 6.3**. A high carbon content was detected (i.e. 13.6%) in this area of the HFM.

Table 6.3 Summary of EDXS results of different zones of the 5%Ni-LSCF6428/LSCF6428-HFM before and after methane conversion.

Membrane	***Condition***	***Section (side)***	***Absolute atomic %***								***Experimental stoichiometry***
			La	***Sr***	***Co***	***Fe***	***O***	***Ni***	***S***	***Ca***	***C***	
LSCF6428	**BR**	**Lumen**	**8.0±0.9**	**5.5±0.8**	**2.3±0.6**	**10.3±1.2**	**73.8±13.5**		**0.3**	**0.5**		**La0.6:Sr0.4:Co0.2:Fe0.8**
LSCF6428	**BR**	**Shell**	**7.2**	**5.6**	**2.2**	**9.8**	**75.4**					**La0.6:Sr0.4:Co0.2:Fe0.8**
5%Ni-LSCF6428	**BR**	**Shell**	**7.4±0.8**	**4.7±0.9**	**2.2±0.5**	**9.1±1.1**	**74.9±14.0**	**1.7±0.6**				**La0.6:Sr0.4:Co0.2:Fe0.8**
5%Ni-LSCF6428	**BR**	**Cross**	**7.4±1.8**	**5.5±1.7**	**2.3±0.6**	**10.2±1.4**	**72.8±15.5**		**0.3**			**La0.6:Sr0.4:Co0.2:Fe0.8**
5%Ni-LSCF6428	AR	Centre lumen	5.2	3.4	1.3	8.3	68.9		0.14	0.5	13.6	
5%Ni-LSCF6428	AR	Centre shell	6.3	3.3	1.6	7.8	64.4	1.6	0.98		14.1	
5%Ni-LSCF6428	AR	Cross	4.7	2.8	1.4	6.2	70.4		1.26		13.2	
5%Ni-LSCF6428	AR	End shell	5.5	3	1.3	6.4	66.9	1.1	1		14.8	
5%Ni-LSCF6428	AR	End lumen	5.2	6.7	0.98	6.4	65.5		3.8		11.4	

Meanwhile, the end shell side showed a clear diminution of the metal compositions for Ni (1.7% to 1.1%), La (7.4% to 5.5%), Co (2.2% to 1.3%), Fe (9.1% to 6.4%), and Sr (4.7% to 3%). In addition, sulphur (1%) and carbon (14.8%) were detected on this membrane section; see **table 6.3** and **appendix V.8, table V.5**. Furthermore, at the end lumen side La, Co and Fe cations content decreased from 8% to 5.2%; 2.3% to 0.98% and 10.3% to 6.4%, respectively, whilst the remaining metal (i.e., Sr) concentration increased from 5.5% to 6.7%, see **table 6.3** and **appendix V.8**, **table V.6**. These changes in the elemental composition on the surface of HFM are a consequence of several factors such as the reducing gas mixture used (4%CH_4/He) or generated (CO) during methane conversion, impurities and the kinetic demixing of mobile cations of the membrane.

According to the results obtained from XRD, SEM and EDXS analysis on the shell side of the 5%Ni-LSCF6428/LSCF6428-HFM module after methane conversion suggest that the 5%Ni-LSCF6428 catalyst coated on the shell side of the LSCF6428 hollow fibre membrane displayed morphology changes likely due to the oxidation of metallic nickel to NiO by oxygen chemisorption on active sites of the catalyst. In addition, the particles were agglomerated by the high thermal treatment; furthermore carbon deposition on the HF membrane surface occurred during the experiments. These processes could affect the number of active sites in the catalyst, as reflected in the products selectivity during methane oxidation experiments.

XRD characterization of the module reactor after methane conversion showed different crystalline oxide/sulphate/carbonate phases (i.e. SrO_2, Fe_3O_4, $SrSO_4$, $CoSO_4$ and $SrCO_3$). The presence of sulphate and carbonate phases are attributed to sulphur impurities and reducing gases used/generated (i.e. CH_4 and CO), which could cause deterioration of the 5%Ni/LSCF6428-HFM performance. Also, it can be observed that the module was contaminated by silica (SiO_2), which can likely come from the sealant or from the quartz.

6.6. Thermodynamic calculation.

Figure 6.20 shows the standard Gibbs free energy for the oxidation of methane, ethane and ethylene at different temperatures.

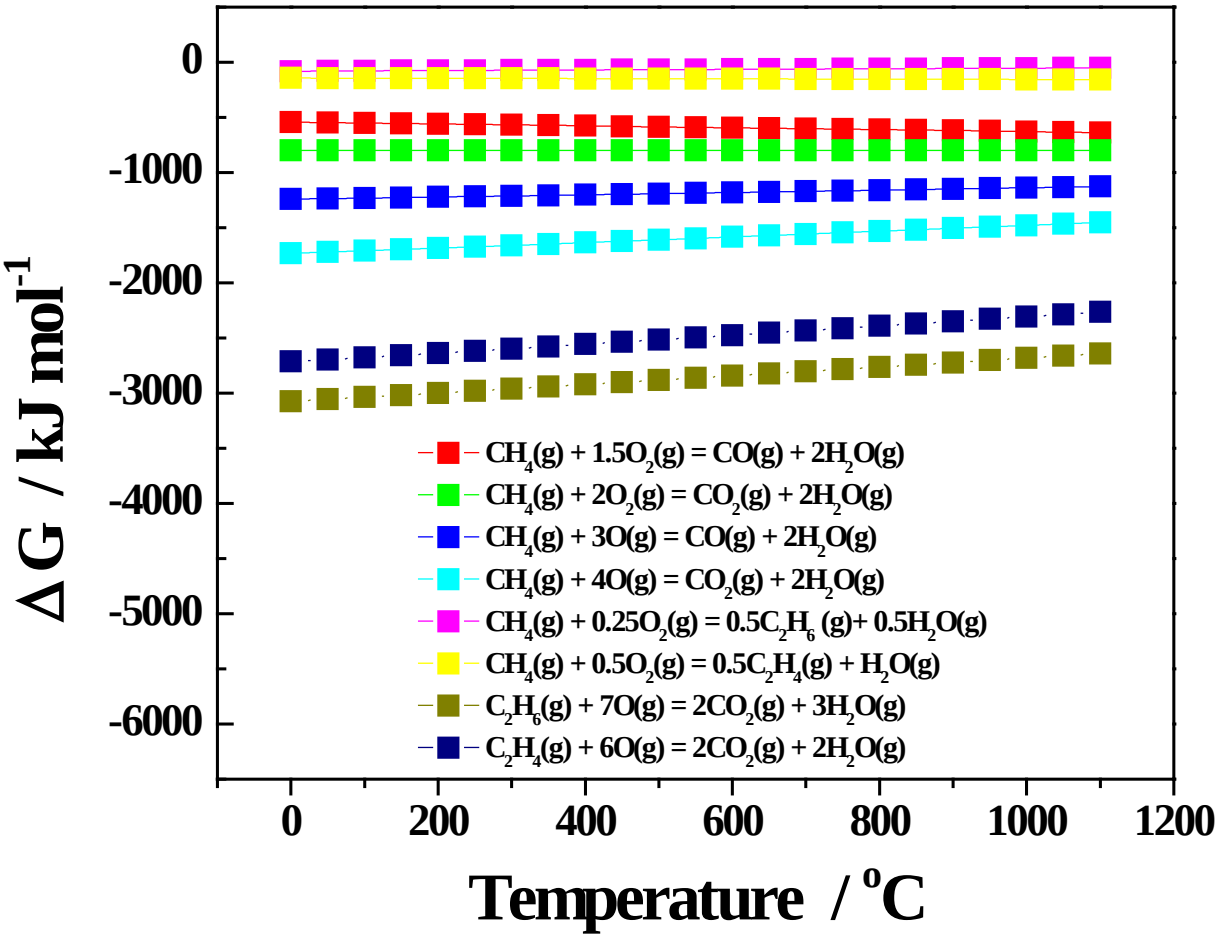

Figure 6.20 Dependence of standard Gibbs free energy with temperature for partial and total oxidation of methane, ethane and ethylene.

It can be observed that the total oxidation reactions of methane and C_2 are thermodynamically favourable because of their lower ΔG. Furthermore, the total oxidation of methane is more favourable that the partial oxidation of methane at high oxygen concentration, according to thermodynamic calculation, **figure 6.20.** These findings are in agreement with experimental results obtained in this work.

The thermodynamic stability of perovskite phases under O_2/CH_4 atmosphere was evaluated. The standard Gibbs free energy for single perovskite phases, rather than LSCF6428 perovskite due to absence of thermodynamic data, were calculated and given in **figure 6.21**. It can be appreciated that $LaCoO_3$ perovskite exhibits lower ΔG compared to $LaFeO_3$ and $Sr_2Fe_2O_5$ perovskites.

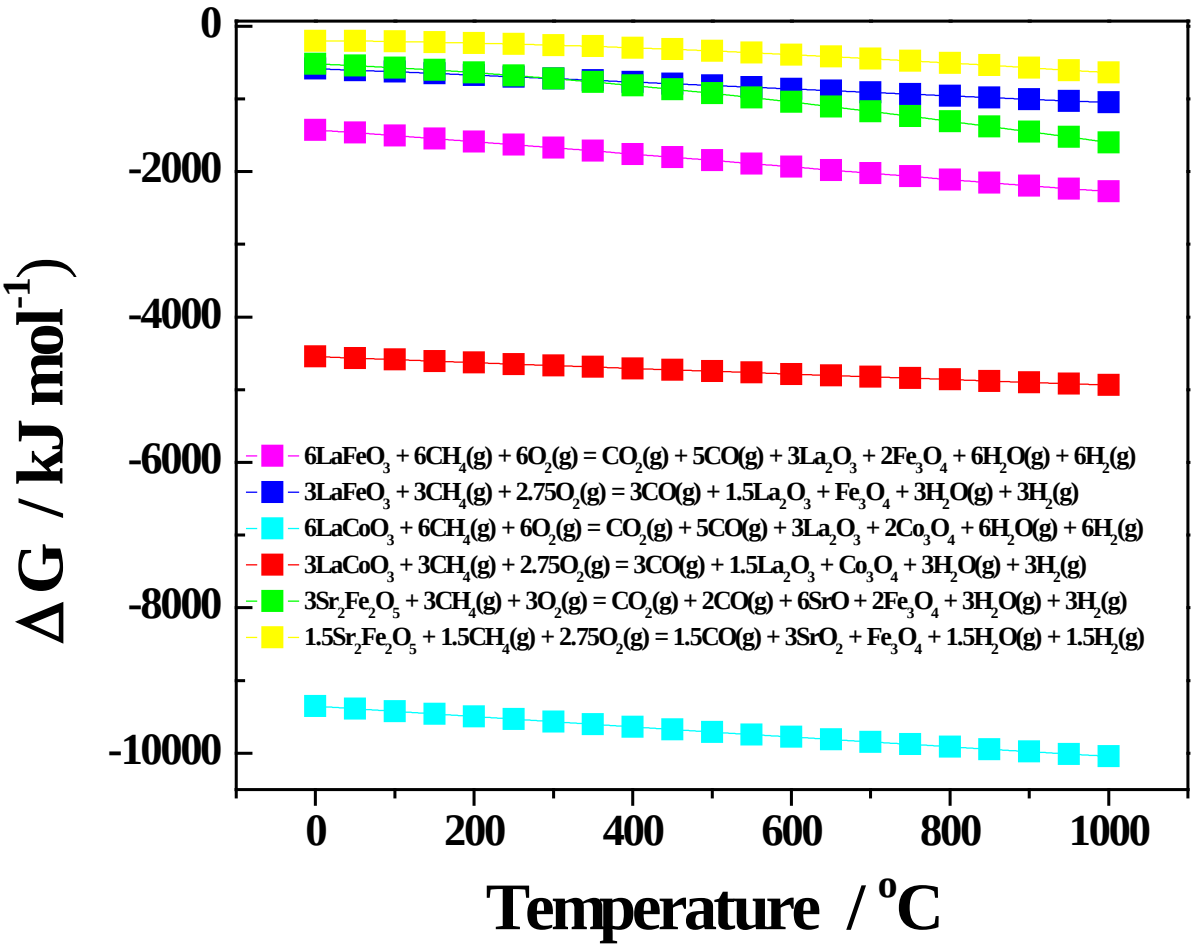

Figure 6.21 Dependence of standard Gibbs free energy with temperature for total and partial oxidations of methane reactions over $LaCoO_3$, $LaFeO_3$ and $Sr_2Fe_2O_5$ perovskites.

According to the results given in **figure 6.21**, the $LaCoO_3$ perovskite was selected to find out its stability under O_2/CH_4 atmosphere. Below are shown the standard Gibbs free energy for various oxidations of methane reactions at $LaCoO_3$ perovskite model (**figure 6.22**).

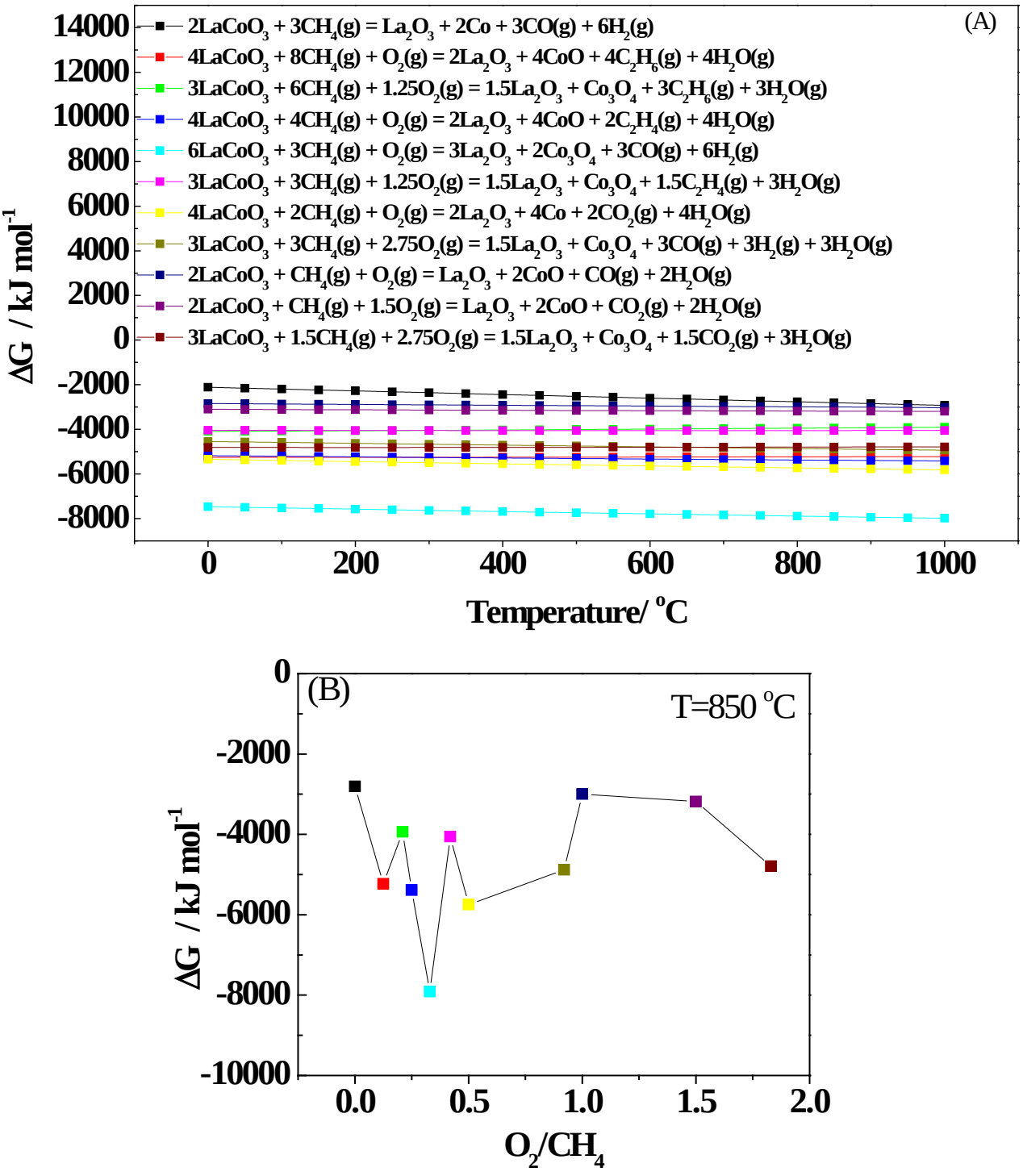

Figure 6.22 Dependence of standard Gibbs free energy with temperature for various oxidations of methane reactions of the $LaCoO_3$ perovskite (A), dependence of the standard Gibbs free energy versus O_2/CH_4 ratio for $LaCoO_3$ perovskite at 850 °C (B).

It can be noted that the reactions that exhibit an O_2/CH_4 ratio of 0.33 is thermodynamically more favourable because of its lower ΔG , see **figure 6.22A** and eqn. (6.13).

$$LaCoO_3 + 3CH_4(g) + O_2(g) \rightarrow 3La_2O_3 + 2Co_3O_4 + 3CO(g) + 6H_2(g) \qquad (6.13)$$

The dependence of ΔG at 850°C with the O_2/CH_4 ratio indicates that the $LaCoO_3$ perovskite is less stable at O_2/CH_4 ratio below 0.5, see **figure 6.22B**. At the operation condition carried out the experiments in this work, it was observed $CoSO_4$ rather than Co_3O_4 and/or CoO because of its sulphurization with sulphur impurity. Also, note that the production of C_2 (i.e. C_2H_4 and C_2H_6) and syngas are thermodynamically favourable. On the other hand, the total oxidation of methane to CO_2 are thermodynamically favourable when the ratio is between 0.5 and 2, see **figure 6.22B**. This finding suggests that high O_2/CH_4 ratio would improve the $LaCoO_3$ perovskite stability relative to low O_2/CH_4 ratio (i.e., below 0.5).

Additional evidence that support the above-discussed thermodynamic data is given in the phase diagram for La-Co-O system (see **figure 6.23**). It can be observed that Co_3O_4 and La_2O_3 are thermodynamically favourable under different partial pressure of oxygen at 850°C.

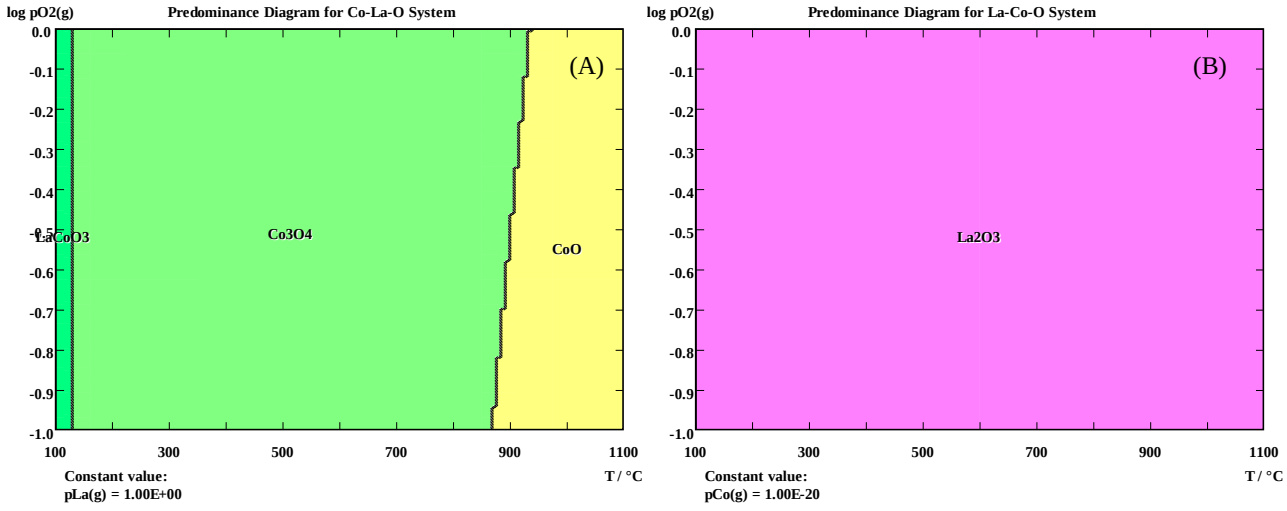

Figure 6.23 Phase diagram for $LaCoO_3$ system in function of $\log pO_2$ against temperature**.**

Similar thermodynamic studies were carried out for $LaFeO_3$ and $Sr_2Fe_2O_5$ perovskites and are given in **appendix V.9, figures V.22** to **V.25**. It can be noted that the phase more

thermodynamic stable are La_2O_3 and Fe_3O_4 for La-Fe-O system while SrO_2, Fe_2O_3 and Fe_3O_4 were the most stable phases for Sr-Fe-O system at 850°C. These findings are in agreement with experimental results obtained in this work, which suggests that the thermodynamic calculation for single perovskite phases can give some insight into the phase evolution of $La_{0.6}Sr_{0.4}Co_{0.2}Fe_{0.8}O_{3-\delta}$ perovskite.

6.7. Conclusions

The results discussed above for the methane conversion experiments using unmodified LSCF6428-HFM and 5%Ni-LSCF6428/LSCF6428-HFM reactors lead to the following conclusions:

Unmodified LSCF6428-HFM reactor:

1. The unmodified LSCF6428-HFM reactor favoured the formation of C_2 products (C_2H_6 + C_2H_4) at methane conversion below 5% when Air/4% CH_4 gradients operated under MSAL and MLAS modes.

2. The activity-selectivity performance of the unmodified and modified LSCF6428-HFM in methane conversion is likely associated to the concentrations of electrophilic (i.e. O_2^-, O^- and $O_{2\ (ads)}$) that generate total oxidation products and nucleophilic oxygen species (i.e. O^{2-}) that conduced to formation of selective oxidations and also that different oxygen species produced depend upon the abundance of the oxygen vacancies (i.e. $V_0^{\bullet\bullet}$) in the membrane.

5%Ni-LSCF6428/LSCF6428-HFM reactor:

3. The 5%Ni-LSCF6428/LSCF6428-HFM module reduced with hydrogen and operated with 2% O_2/4%CH_4 gradient showed the production of syngas (CO + H_2) (i.e., 28 %) with H_2 /CO ratio of 0.5, carbon dioxide (i.e., 45%) and C_2 product (i.e., 27%). It is proposed that two main catalytic pathways can take place on 5%Ni-LSCF6428/LSCF6428-HFM: partial oxidation of methane to syngas (CO + H_2) on metallic nickel particles and oxidative coupling methane to C_2 and CO_2 products on NiO particles.

4. The 5%Ni-LSCF6428/LSCF6428-HFM module unreduced and operated with 4% O_2/4%CH_4 gradient facilitated the formation of carbon dioxide (ca. 71 %) whilst CO, C_2H_4 and C_2H_6 selectivities were around 19 %. No hydrogen formation was observed.

5. The increase of oxygen concentration from 2% to 20% improves oxygen permeation ca. 2 fold, but this was not reflected on methane conversion (15% and 20%). The main catalytic pathway at low oxygen concentration and H_2 reduction treatment was partial oxidation of methane to C_2 and syngas. At high oxygen concentration and no H_2 treatment the total oxidation of methane to CO_2 was the main pathway in agreement with the thermodynamic calculation data.

6. The modification of the LSCF6428-HFM with 5% Ni-LSCF6428 catalyst increases the performance of reactor and oxygen permeation 6 fold compared to the unmodified LSCF6428-HFM. In addition, CO_x become the main reaction product, instead the unmodified HFM reactor favoured the C_2 (C_2H_4 and C_2H_6) selectivity (i.e., oxidative coupling of methane).

7. According to the products distribution and the high methane conversions it is proposed that CH_4 reacts with oxygen species that diffused or dissociated over the catalyst to produce CO_x and H_2O. This would indicate that methane conversion occurs over the surface of 5%Ni-LSCF6428 catalyst and facilitates the total oxidation catalytic pathway.

8. The presence of 5%Ni-LSCF6428 catalyst improved 3 fold the apparent overall rate constant under Air/CH_4 gradient relative to unmodified LSCF6428-HFM. A similar trend was obtained for Air/He gradient, which reflects the positive effect of the catalyst on the oxygen flux.

9. The morphology of the catalyst (centre shell side) and metal composition of the grain boundary (centre lumen side and end lumen side) of the 5%Ni-LSCF6428-HFM after methane conversion significantly changed relative to the modified membrane before reaction. The centre shell side and the end shell side of the unmodified LSCF6428-HFM reactor also showed changes in crystalline phases, morphology and metal composition of the grain boundary compared to the fresh unmodified membrane. This is tentatively attributed to kinetic demixing of mobile cations and decomposition of the membrane due to the axial temperature generated by the exothermic reaction of methane combustion.

10. Both LSCF6428-HFM and 5%Ni/LSCF6428-HFM reactors showed the presence of $SrSO_4$ and $CoSO_4$ because of the contamination by sulphur impurities, which is tentatively attributed to the air gas employed during the experiments. Sulphur impurity could also be produced by polyethersulfone employed during fabrication of the LSCF6428 hollow and the cement used to assemble the reactor.

11. The segregation of strontium, cobalt and iron to form different crystalline oxide/carbonate/sulphate phases such as Fe_3O_4, SrO_2, $SrCO_3$, $SrSO_4$ and $CoSO_4$ occurred on LSCF6428-HFM and 5%Ni/LSCF6428-HFM reactors. Thermodynamic calculation and diagram of phases supported the formation of these species under Air/CH_4 gradient and sulphur impurity.

6.8. Reference

[1] X. Tan, Z. Pang, Z. Gu, S. Liu, J. Membr. Sci. 302, **2007,** 109.

[2] Xu, S.; Thomson, W. AlChe J. 43, **1997**, 2731.

[3] Elshof, J. E.; Bouwmeester, H. J. M.; Verweij, H. Appl. Catal. A. Gen. 130, **1995**, 195.

[4] E. V. Kondratenko, H. Wang, V. A. Kondratenko, J. Caro; J. Mol. Catal. A: Chemical 297**, 2009**, 142.

[5] X. Tan and K. Li; Ind. Eng. Chem. Res. 45, **2006**, 142.

[6] A. Thursfield . I. S. Metcalfe; J Solid State Electrochem., 10, **2006**, 604.

[7] X. Tan, Y. Liu and K. Li, AIChE Journal, 51, **2005,** 1991.

[8] Z. Shao, G. Xiong, H. Dong, W. Yang L. Lin, Separ. Purif. Technol, 25, **2001**, 97.

[9] P.J. Gellings and H.J.M. Bouwmeester Catalysis Today, **58**, **2000,** 1.

[10] V. A. Shevts, V. M. Vrotyntsev, V. B. Kazansky; Kinet Catal. **1996**, 10: 356. 30.

[11] V.B. Kazansky Kinet. Catal. **1997**, 18: 43, 24.

[12] A. Bielanski, J. Haber; In: Oxygen in Catalysis, Marcel Dekker, Inn., New York, **1991**

[13] V. G. Sathe, S. K. Paranjpe, V. Siruguri and A. V. Pimpale. J. Phys. Condens. Matter, 10, **1998**, 4045.

[14] X. Tan, K. Li, A. Thursfield, I. S. Metcalfe; Catal Today, 131, **2008**, 292.

[15] W.T. Stephens, T. J. Mazanec, H. U. Anderson; Solid State Ionics, 129, **2000**, 271.

[16] H. Liu, Z. Pang, X. Tan, Z. Shao, J. Surnaso, R. Ding, S. Liu; Ceramics international, 35,4, **2009**,1435.

[17] J. E. Ten Elshof, H.J. M. Bouwmeester, H. Verweij; Appl. Catal. A: Gen. 130, **1995**, 195.

[18] U. Balanchandran. J. T. Dusek, P. S. Maiya, B. Ma, R. L. Mieville, M. S. Kleefish, C. A. Udovich; Catal. Today 36, **1997**, 265.

[19] U. Balachandran, J. T. Dusek, S. M. Sweeney, R.B. Poeppel, R. L. Mieville, P.S. Maiya, M. S. Kleefish, S. Pei, T.P. Kobylinski, C.A. Udovich and A. C. Bose; Am. Ceram. Soc. Bull. 74, **1995**, 71.

[20] U. Balachandran, J. T. Dusek, R. L. Mieville, R. B. Poeppel, M. S. Kleefish, S. Pei, T. P. Kobylinski, C. A. Udovich and A. C. Bose; Appl. Catal. A. 133, **1995**, 19.

[21] F. A. N. Fernandes, C. P. Souza, J. F. Souza, Engenharia Termica (Termal Engineering), 1, 5, **2006**, 40.

[22] H. J. M. Bouwmeester; Catal Today, 82, **2003**, 141.

[23] S. Pei, M.S. Kleefish, T. P. Kobylinski, J. Faber, C. A. Udovich, V. Zhang-McCoy, B. Dabrowski, U. Balachandran, R. L. Mieville, R. B. Poeppel; Catal Lett. 30, **1995**, 201.

[24] Y. Matsuma, T. Nakamori, Appl. Catal. A: General 258, **2004**, 107.

[25] J. Li, K. J. Smith Appl. Catal A: General 349, **2008**, 116.

[26] Y. Lu, J-Z. Xue, X.J. Ding, S. K. Shen, J. of Natural Gas Chemist. 5, 1, **1996**, 45.

[27] R. H. E. van Doorn, H. J. M. Bouwmeester, A. J. Burggraf; Solid State Ionics 111, **1998**, 263.

[28] J. Caro, K. J. Caspary, C. Hamel, B. Hoting, P. Kölsch, B. Langanke, K. Nassauer, T. Schiestel, A. Schmidt, R. Schomäcker, A. Seidel-Morgenstern, E. Tsotsas, I. Voigt, H. Wang, R. Warsitz, S. Werth and A. Wolf**;** Ind. Eng. Chem. Res. 46, **2007,** 2286.

[29] W. Jin, S. Li, P. Huang, N. Xu, J. Shi, Y. S. Lin; J. Membr. Sci. 166, **2000**, 13.

[30] Y. Zeng, Y.S. Lin, S. L. Swartz; J. Membr. Sci. 150, **1998**, 87.

[31] S. Xu, W. J. Thomson, Ind. Eng. Chem. Res. 37, **1998**,1290.

[32] C. Yacou, J. Sunarso, C. X. C. Lin, S. Smart, S. Liu, J. C. Diniz da Costa; J. Membr. Sci. 380, **2011**, 223.

[33] Y. S. Lin and Y. Zeng, J. of Catal. 164, **1996**, 220.

[34] N. Xu, S. Li, W. Jin, J. Shi, Y. Lin, AlChE J. 45, **1999**, 12, 2519.

[35] S. Li, W. Jin, P. Huang, N. Xu, J. Shi, Y. S. Lin, J. Membr. Sci. 166, **2000**, 51.

[36] A. Thursfield, I.S. Metcalfe, J. Membr. Sci. 288, **2007**, 175.

Chapter 7.

Overall conclusions

7. Overall conclusions and recommendations

7.1. Overall conclusions

The results discussed above for both oxygen flux and methane conversion experiments carried out in unmodified LSCF6428-HFM, Co_3O_4/LSCF6428-HFM and 5%Ni-LSCF6428/LSCF6428-HFM reactors lead to the following conclusions:

Mixed Ionic and Electronic Conducting (MIEC) membranes (i.e. LSCF6428-HFM) reactors are of interest because they have the potential to provide a clean, efficient and economic route to separate oxygen from air. Furthermore, this technology could possibly revolutionize the chemical industry where a continuous oxygen supply is required as in many industrial processes such as: the partial oxidation of methane (POM) and the oxidative-coupling of methane (OCM). In addition, the MIEC ceramic membrane has the potential advantage that could be integrated the oxygen separation and syngas processes into a single compact ceramic membrane reactor.

Oxygen flux across the membranes can be enhanced with rising helium flow rate because high helium flow rate reduces oxygen partial pressure on the helium flow side, producing an increase of oxygen partial pressure difference across the membrane. This driving force promotes the diffusion of the lattice oxygen from high oxygen partial pressure to lower oxygen partial pressure.

Unmodified and modified LSCF6428-HFM reactors exhibit stable oxygen flux under Air/He gradient. In addition, they show good thermal and mechanical stability of the hollow fibre geometry. However, under continuous long tern operation conditions the LSCF6428 hollow fibre membrane reactor showed signs of kinetic demixing of mobile cations and the presence

of sulphur contamination. This may be detrimental to the module (i.e., LSCF6428-HFM, Co_3O_4/LSCF6428-HFM and 5%Ni/LSCF6428-HFM) performance.

A kinetic model assuming plug flow was developed and successfully applied for calculating the overall rate constants for LSCF6428-HFM and modified LSCF6428-HFM under oxygen flux and methane oxidation experiments. The data are fairly well fitted at high helium flow rates, but at low helium flows the model is invalid possibly due to mass transfer effects and low Reynolds numbers ($\mathbf{Re < 2000}$).

The oxygen permeation rate is limited by surface exchange on the oxygen lean side or lumen side ($\boldsymbol{R}_{ex}^{''}$) at 850°C and 900°C and the contribution of bulk diffusion on the oxygen permeation rate increased with a rise in the temperature (900°C), according to distribution of total oxygen permeation residence for unmodified and modified LSCF6428-HFM reactor.

The oxygen flux significantly improved with catalyst coated on LSCF6428-HFM whatever the type of catalyst. When LSCF6428-HFM was coated with Co_3O_4 catalyst, the oxygen permeation measurements from mode 1 (ALHS) and mode 2 (ASHL) were different. In addition, the apparent rate constant for Co_3O_4/LSCF6428-HFM reactor did not change with helium flow.

The morphology of LSCF6428-HFM coated with 5 % Ni/LSCF6428 catalyst changed after a long operation time as a consequence of Ni nanoparticles agglomeration and oxidation to nickel oxide. This could decrease the number of active site in the catalyst and hence the oxygen fluxes. A H_2 treatment process on the 5%Ni-LSCF6428/LSCF6428-HFM module did not recover the initial oxygen flux of the membrane reactor. On the other hand, the apparent overall rate constants for Co_3O_4/LSCF6428-HFM and 5%Ni/LSCF6428-HFM enhanced 3-4 fold compared to unmodified LSCF6428-HFM. Comparison of both modified HFM reactors showed that the apparent overall rate constants for Co_3O_4/LSCF6428-HFM were 2 fold higher than that obtained for 5%Ni-LSCF6428/HFM.

Comparison of the results from unmodified and modified LSCF6428-HFM, show that the oxygen fluxes is considerably enhanced when the membrane was operated not only under Air/CH_4 compared to Air/He gradients but also when oxygen concentration increased from 2 to 20%. The activity-selectivity performance in methane conversion is likely associated to the concentrations of electrophilic species (i.e. O_2^-, O^- and $O_{2\ (ads)}$) that facilitate total oxidation products and nucleophilic oxygen species (i.e. O^{2-}) that conduce to the formation of selective oxidations. Furthermore, the modification of the LSCF6428-HFM with 5% Ni-LSCF6428 catalyst increased the reactor performance and oxygen permeation 6 fold compared with unmodified LSCF6428-HFM. In addition, CO_x became the main reaction product and the unmodified HFM reactor favoured the C_2 (C_2H_4 and C_2H_6) selectivity (i.e. oxidative coupling of methane).

Two main catalytic pathways take place on 5%Ni-LSCF6428/LSCF6428-HFM when the module received H_2 treatment: **1)** partial oxidation of methane to syngas (CO + H_2) on metallic nickel particles (H_2-treated) and **2)** oxidative coupling of methane to C_2 and CO_2 products on NiO particle (without H_2-treatement). Additionally, syngas (CO + H_2) selectivity was 28 % and the ratio H_2 /CO was 0.5.

The presence of 5%Ni-LSCF6428 catalyst improved 3-fold the apparent overall rate constant under an Air/CH_4 gradient relative to unmodified LSCF6428-HFM. A similar trend was obtained for Air/He gradient, which reflects the positive effect of the catalyst on the oxygen flux. On the other hand, the carbon deposited on modified and unmodified HFM reactors was between 10% and 15%.

The morphology of the catalyst (centre shell side) and metal composition of the grain boundary (centre lumen side and end lumen side) of 5%Ni-LSCF6428-HFM after methane conversion varied significantly compared to the modified membrane before reaction. In

addition, the centre shell side and end shell side of the unmodified LSCF6428-HFM reactor showed changes in crystalline phases, morphology and metal composition of the grain boundary compared with fresh unmodified membrane.

Both LSCF6428-HFM and 5%Ni/LSCF6428-HFM reactors after methane conversion exhibited the presence of sulphur and the segregation of iron, strontium and cobalt to form different crystalline oxide/sulphate phases such as SrO_2, $SrSO_4$, $CoSO_4$ and Fe_3O_4. In addition, CO_2 generated during the reaction produced $SrCO_3$, from the reaction of CO_2 with segregated strontium oxide. Thermodynamic calculation and phases diagrams also showed that these phases are facilitated under Air/CH_4 gradient and sulphur impurity.

A summary of the possible methane oxidation pathways obtained from unmodified LSCF6428-HFM and modified LSCF6428-HFM at 850 °C is given in **figure 7.1**. Note that the catalytic routes are dependent upon flow operation modes, oxygen concentration, H_2 treatment and catalyst.

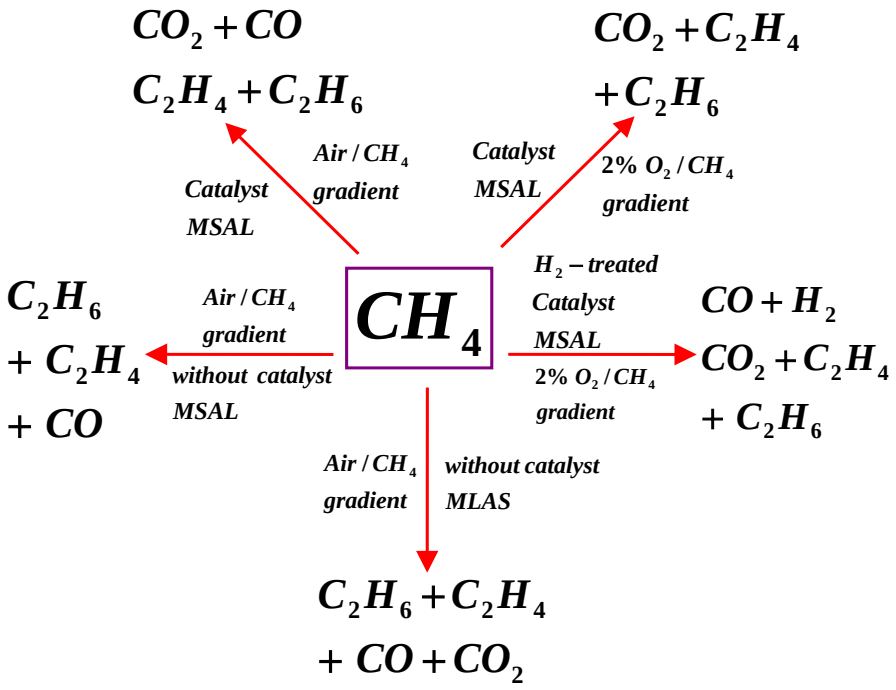

Figure 7.1 Summary of methane oxidation routes for 5%Ni-LSCF6428/LSCF6428-HFM reactor.

7.2.Recommendations for future works

1. The assemble LSCF6428 hollow fibre membrane reactor quite often presented a problem of sealing between the two ends of the membrane with cement, owing to the high temperatures that produce cement fracture and thereby generate gas leaks in the module. We recommend using a high temperature resistant silicone sealant to seal the ends of the membrane.

2. During the methane conversion reaction on unmodified and modified LSCF6428-HFM reactors, usually large amount of water is produced. It is suggested that the quantity of water be measured in future experiments to obtain a more reliable material balance.

3. Nickel is an active and economical catalyst for the partial methane oxidation (POM) reaction and modified with other active components such as Cobalt (Co), Iron (Fe) or noble metal such as Ruthenium (Ru), Platinum (Pt) and Palladium (Pd) could improve the stability and assist in the reduction of carbon deposition **[1]**. The relative order of activity for the partial oxidation catalyst has been determined as: $\boldsymbol{Ru > Rh, Ni, Ir > Pt > Pd}$. The preparation method and support properties also affect the activity of the catalyst. A tentative good formulation could be Ru-Ni-CeO_2 catalyst, which has capability for oxygen storage and can help oxidation of surface carbon which is deposited. The addition of the rare earth oxide (CeO_2) also could stabilize the support and prevent the sintering during the reaction **[1]**. Additionally, Ru favours higher methane activity and selectivity to syngas (CO and H_2).

4. During the oxygen flux and methane conversion experiments sulphur impurities were observed whose origins is tentatively attributed to: **(*i*)** air and helium gases employed

during the experiments, ***(ii)*** the polyethersulfone (PESf) binder used in the manufacture of the membrane, ***(iii)*** the cement used in the reactor assemble. This sulphur can affect the membrane surface area and form different crystalline sulphate phases (i.e. $SrSO_4$, and $CoSO_4$) with strontium and cobalt segregated. Therefore, it is recommended to investigate exhaustively the source(s) that produces sulphur on the membrane and its influence on the membrane oxygen flux.

5. Use a different approach for determining the non-stoichiometric oxygen incorporated into LSCF6428-HFM. Initially, take fresh reactor of LSCF6428-HFM and heated up to 850°C under an air flow on both sides. After the reactor reaches a steady state, based on the oxygen permeation measurements, the air flow is stopped and switched a helium flow over both sides of the membrane reactor. Then, the liberated oxygen from the structure of LSCF6428 perovskite is measured and then compared it with the value of non-stoichiometric oxygen (**δ**) reported in this work and the literature.

6. Make a calibration at different concentration of oxygen, particularly at low oxygen concentrations (below 2 %) to ensure that the measurements of oxygen permeation at low air flow rate are accurate.

7. Characterize the hollow fibre membrane by X-ray photoelectron spectroscopy (XPS) to measure quantitatively the elemental composition (i.e., empirical formula, the chemical state and electronic state of the elements) that exist at the membrane surface.

8. In order to assess leak growth of the LSCF6428 hollow fibre membrane under the operation temperature (800-1000°C) the rate of He leak as a function of time needs to be measured. In addition, find out the magnitude of the leak activation energy to provide information on the underlying mechanism of the leak formation and leak growth.

7.3. Reference

[1] A. P.E. York, T. Xiao and M. L. H. Green, Topic Catal., 22, 3-4, **2003**, 345.

Appendix.

Appendix I- Appendix V

Appendix I:

I.1. Preparation of the $La_{0.6}Sr_{0.4}Co_{0.2}Fe_{0.8O3-\delta}$ hollow fibre membrane

The LSCF6428 hollow fibre membranes were prepared and supplied by Imperial College London. They were made in one step using a combined phase-inversion/sintering technique as previously described by Li and co-workers [**1, 2, and 3** from **Chapter 3**].

I.2. Reactants

Powder samples of this composition ($La_{0.6}Sr_{0.4}Co_{0.2}Fe_{0.8O3-\delta}$) with surface area = 6.0m^2/g were obtained from Praxair Surface technologies, USA. The polymer used as binder, solvent and additive for preparation the starting mixture are: Polyethersulfone (PESf) [Radel A-300, Ameco Performance, USA], N-methyl-2-pyrrolidone (NMP) [Synthesis grade, Merck], Polyvinylpyrrolidone (PVP, K16-18) [Acros Organic, Mw=8000]. The internal and external coagulants are deionized water and tap water, respectively.

I.3. Fabrication of the $La_{0.6}Sr_{0.4}Co_{0.2}Fe_{0.8}O_{3-\delta}$ hollow fibre membranes

The LSCF6428 hollow fibre membrane was fabricated the following manner:

A calculated quantity of PESf with the additive PVP was dissolved in the weighed NMP solvent in a 250 ml wide-neck bottle.

When the polymer solution was obtained, the LSCF6428 powder previously weighed was added carefully.

This solution was stirred for at least 48 h using a Heidolph RZR 2000 stirrer at a speed of around 300 rpm to make sure that the powder was well-dispersed in the polymer solution.

The starting solution was degassed at room temperature for 30 min and then transferred to a stainless steel reservoir where it was pressurized up to 0.5 bars with nitrogen.

It was used a spinneret to obtain the hollow fibre precursors.

Both tap water and deionized water were employed as the internal and external coagulants respectively.

The hollow fibre precursors were then immersed in a water bath for 24 hours to improve the solidification process.

Finally, the precursors were thermally treated under air at 600 °C for 2 hours to burn off the organic polymer binder and subsequently treated at 1100-1280 °C for 4 hours for densification via sintering to take place. [**1-3**].

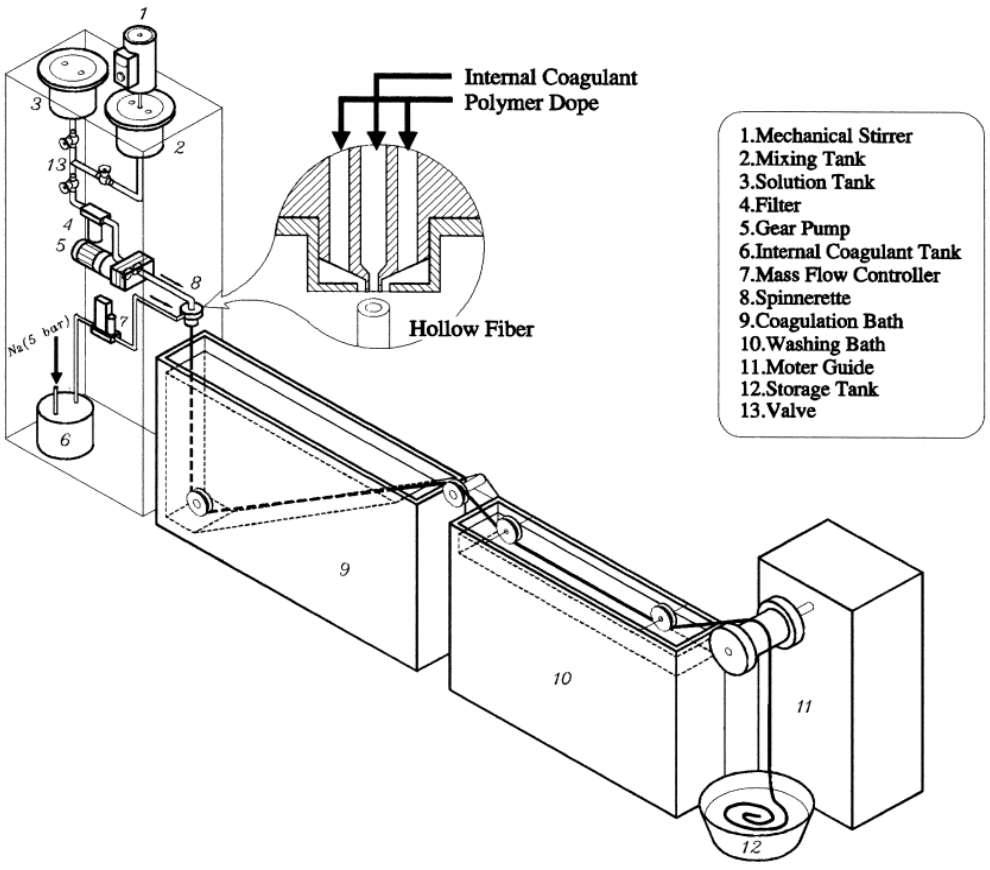

Figure I.1 Apparatus to fabricate the LSCF6428 hollow fibre membrane **[1].**

1.4. Average surface loading of the catalytically modified LSCF6428 HFM.

- **Co_3O_4 catalyst**:

Weight of 1 HFM unmodified (5 cm of large): $\mathbf{0.3678\ g}$

Weight of 1 HFM modified with Co_3O_4 (5 cm of large): $\mathbf{0.3758\ g}$

Amount of Co_3O_4 deposited on 1 HFM: $\mathbf{0.008\ gr \approx 8\ mg}$

Amount of Co_3O_4 deposited on 4 HFM: $\mathbf{0.032\ gr \approx 32\ mg}$

Surface area of catalysts coated on HFM:

$$S_a = \frac{2\pi * r_0}{\ln(r_0)} n * L = 3.308\, cm^2 \qquad \text{(I.1)}$$

The external radius of the HFM (0.07 cm) is r_0, n is the number of HFM used for assemble reactor (i.e., 4) and L is the length of HFM coated by catalyst (5 cm).

The average surface loading of the catalyst on the 4 HFM is given by the below expression:

$$\frac{Amount\ \ of\ \ catalyst\ \ deposited\ \ on\ 4\ \ HFM}{Surface\ \ area\ \ of\ \ catalyst} = \frac{32\ mg}{3.308\ cm^2} = 9.67\ mg\, cm^{-2} \qquad \text{(I.2)}$$

- **5% Ni/ LSCF6428 catalyst:**

Weight of 1 LSCF6428-HFM unmodified (5 cm of large): $\mathbf{0.3119 g}$

Weight of 1 LSCF6428-HFM modified with 5% Ni/ LSCF6428 (5 cm of large): $\mathbf{0.3589 g}$

Amount of 5% Ni/ LSCF6428 deposited on 1 HFM: $\mathbf{0.3119 - 0.3589 = 0.047\ g = 47\ mg}$

Amount of 5% Ni/ LSCF6428 deposited on 4 HFM: $\mathbf{0.188\ g = 188\ mg}$

Surface area of 5% Ni/ LSCF6428 catalyst coated on HFM: $\mathbf{3.308\ cm^{-2}}$

The average surface loading of the catalyst on the 4HFM is given by the below expression:

$$S_{asl} = \frac{Amount\ \ of\ \ catalyst\ \ deposited\ on\ 4\ HFM}{Surface\ area\ of\ \ catalyst} = \frac{188\,mg}{3.308\,cm^2} = 56.8\ mg\,cm^{-2} \approx 57\ mg\ \ cm^{-2} \quad \text{(I.3)}$$

$$g\ \ Ni = \frac{Amount\ \ of\ \ catalyst\ \ deposited\ \ on1\ \ HFM * 5\%}{100\%} = \frac{0.047g * 5\%}{100\%} = 2.35x10^{-3}g \quad \text{(I.4)}$$

Weight of nickel for 4 HFM is: $2.35x10^{-3}\,g * 4 = 9.4x10^{-3}\ \ g$

$$\%\ \ Ni = \frac{g\ \ of\ \ \ Nickel\ \ for\ \ \ 4HFM}{weight\ \ of\ \ \ 5\%Ni\,/\,LSCF\,6428\ \ deposited\ \ on\ \ 4HFM} * 100 = \frac{9.4x10^{-3}\ \ g}{0.188\ \ g}100 = 5\% \quad \text{(I.5)}$$

I.5. Calibration plots for different gases employed in the experiments:

- ***Calibration curve for air gas injections using air gas flow of 50 ml.min^{-1}***

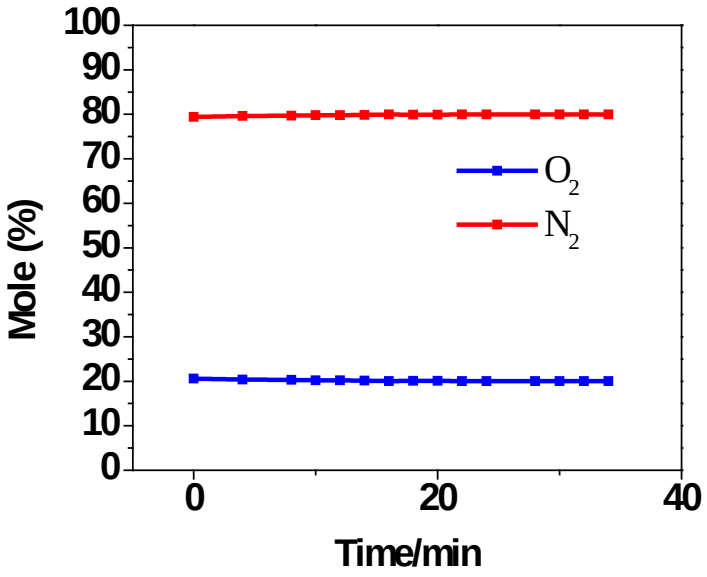

Figure I.2 Single point calibration curve for air flow.

- ***Calibration curve of mixture of N_2 (2%), O_2 (2%) and H_2 (1%), balance in helium. Mixture gas flow (50 ml.min^{-1})***

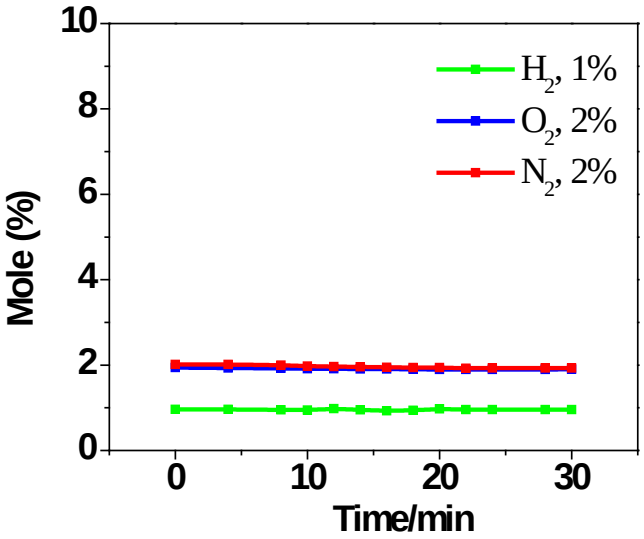

Figure I.3 Single point calibration curve for the injections of the mixture 1% H_2, 2%O_2 and 2%N_2, balance in helium.

- ***Calibration of GCB with mixture of H_2 (2%), O_2 (0.5%), N_2 (2%), CO (2%), CO_2 (2%), C_2H_4 (2%) and C_2H_6 (2%) balance in helium. Mixture gas flow (50 ml.min^{-1}).***

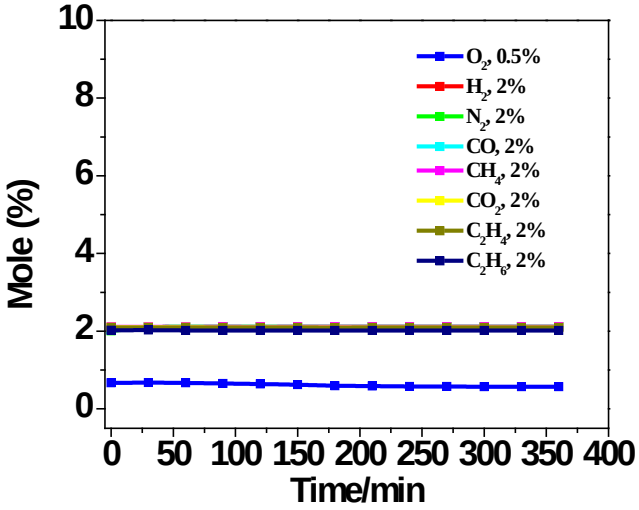

Figure I.4 Single point calibration curve for mixture 0.5%O_2, 2%H_2, 2%N_2, 2%CO, 2%CH_4, 2%CO_2, 2%C_2H_4 and 2%C_2H_6, balance in helium.

It is worth remarking that all the injections showed excellent reproducibility since the error of the measurements were below 5 %.

Appendix II

II.1. Enlargement of oxygen release using mode 1 and mode 2, obtained figure 4.1

Figure II.1 shows the magnification of the oxygen release data discussed in **Chapter 4, figure 4.1.**

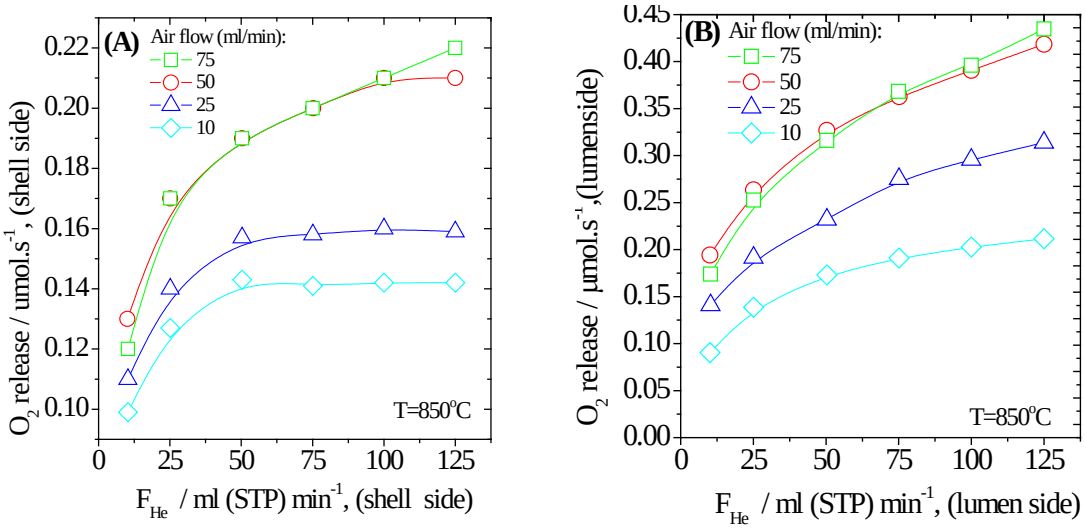

Figure.II.1 Oxygen release against helium flow. (A) mode 1: air flow feed in lumen side and (B) mode 2: air flow feed in shell side

II.2. Oxygen release and oxygen uptake against time of operation

Figure II.2 corresponds to the magnification of the oxygen release and oxygen uptake, data discussed in **Chapter 4, figure 4.2**.

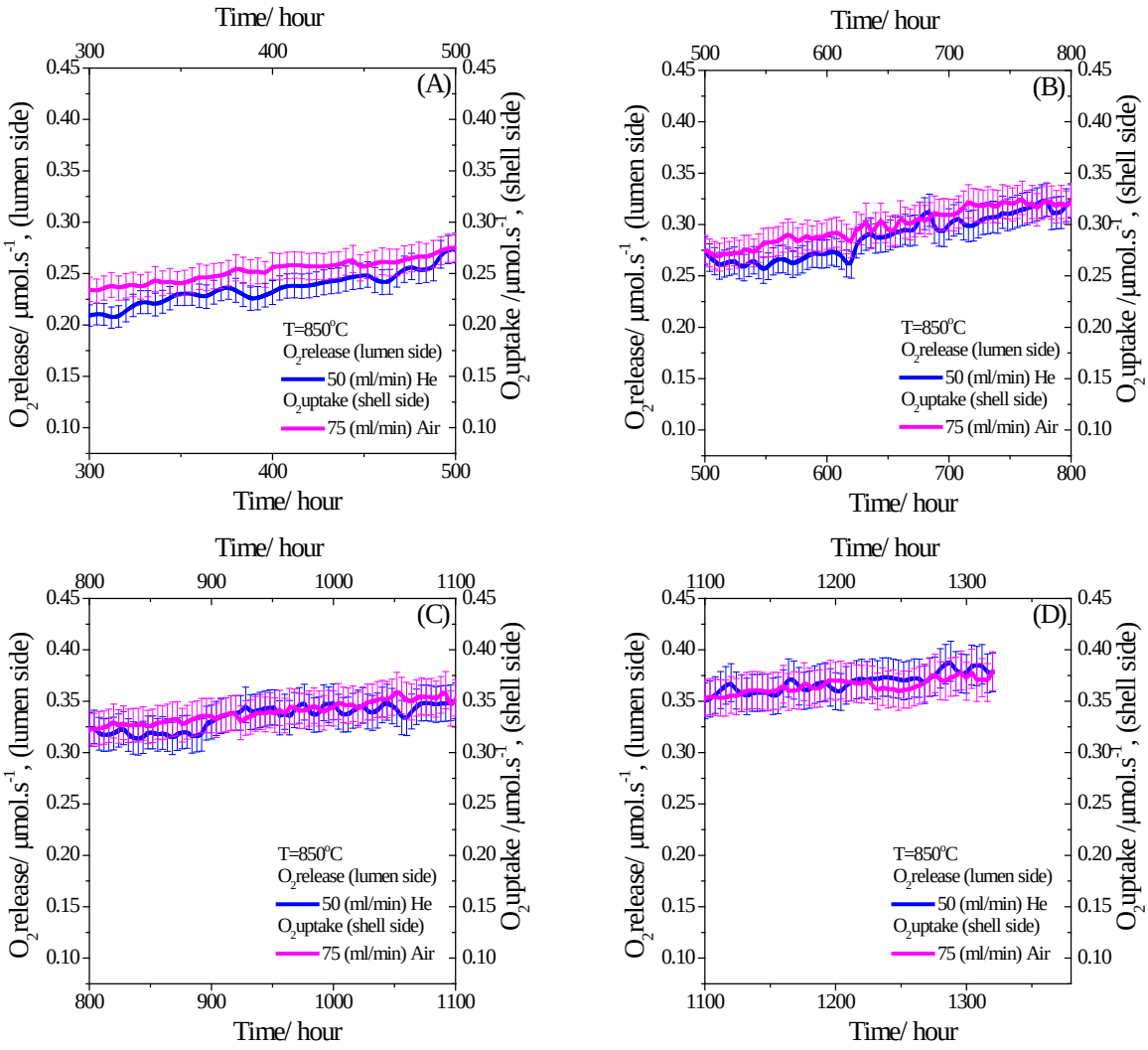

Figure.II.2 Oxygen release and oxygen uptake with accuracy 5% versus time of operation, (A), (B), (C) and (D).

Figure II.3 corresponds to the percentages of the nitrogen in lumen side versus time of operation, according to the data discussed in **Chapter 4, figure 4.2.**

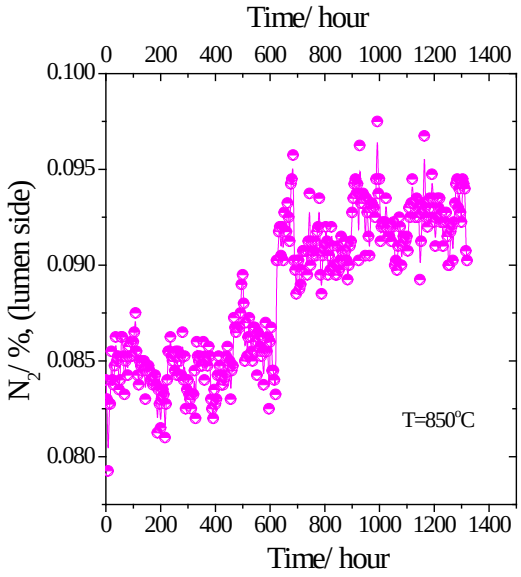

Figure.II.3 Percentages of nitrogen in lumen side versus time of operation

II.3. Statistical regression of oxygen uptake and release obtained at long operation time:

The statistical regression calculation for oxygen uptake and release obtained are given below:

Automatic injection systems can produce remarkably repeatable results because they inject in precisely the same way time and time again. To calculate the residual standard deviation (%RSD) on the peak that is obtained from six repetitive injections of a sample can be done using the following equation.

$$\%RSD = \frac{\sigma_{n-1}}{\bar{x}} * 100$$

Table II.1 Summary output of the residual standard deviation for GCA

Peak area	Standard deviations (σ)	Average peak – areas (x)	%RSD	%RSD
2.704	0.006	2.697	0.235	0.20%
2.703				
2.698				
2.695				
2.693				
2.689				

Table II.2 Summary output of the residual standard deviation for GCB

Peak area	Standard deviations (σ)	Average peak – areas (x)	%RSD	%RSD
18.651	0.0179	18.618	0.0966	0.10%
18.641				
18.627				
18.617				
18.612				
18.603				

Oxygen uptake

$$O_{2\ uptake} = n_{O_{2\ in}} - \left(n_{O_{2\ out}} + \frac{n'_{N_{2\ out}}}{4} \right) \tag{II.1}$$

Propagation of errors for Oxygen uptake

$$P = \left(n_{O_{2\ out}} + \frac{n'_{N_{2\ out}}}{4} \right) \tag{II.2}$$

$$\Delta P = \sqrt{\left(\frac{\partial P}{\partial nO_{2_{out}}} \right)^2 \Delta nO_{2_{out}}{}^2 + \left(\frac{\partial P}{\partial nN'_{2_{out}}} \right)^2 \Delta nN'_{2_{out}}} \tag{II.3}$$

$$\Delta P = \sqrt{\Delta nO_{2_{out}}{}^2 + \frac{1}{16} \Delta nN'_{2_{out}}} \tag{II.4}$$

$$\Delta P = 0.0078 \tag{II.5}$$

$$O_{2\ uptake} = n_{O_{2\ in}} - P \tag{II.6}$$

$$\Delta O_{2_{uptake}} = \sqrt{\Delta nO_{2_{in}}{}^2 + \Delta P^2} \tag{II.7}$$

$$\Delta O_{2_{uptake}} = 0.008 \tag{II.8}$$

$$\text{Relative error} = \frac{O_{2\ uptake}}{\Delta O_{2\ uptake}} * 100 = 4.48 \quad \text{(II.9)}$$

Oxygen release

$$O_{2\ release} = \left(n'_{O_{2\ out}} - \frac{n'_{N_{2\ out}}}{4} \right) n'_{He_{in}} \quad \text{(II.10)}$$

Propagation of errors for oxygen release

$$Q = \left(n'_{O_{2\ out}} + \frac{n'_{N_{2\ out}}}{4} \right) \quad \text{(II.11)}$$

$$\Delta Q = \sqrt{\left(\frac{\partial Q}{\partial nO'_{2\ out}} \right)^2 \Delta nO'^{\ 2}_{2\ out} + \left(\frac{\partial Q}{\partial nN'_{2_{out}}} \right)^2 \Delta nN'_{2_{out}}} \quad \text{(II.12)}$$

$$\Delta Q = \sqrt{\Delta nO'^{\ 2}_{2\ out} + \frac{1}{16} \Delta nN'_{2_{out}}} \quad \text{(II.13)}$$

$$\Delta Q = 0.000153 \quad \text{(II.14)}$$

$$\Delta O_{2\ release} = \sqrt{\left(\frac{\partial O_{2\ release}}{\partial Q} \right)^2 \Delta Q^2 + \left(\frac{\partial O_{2\ release}}{\partial nHe'_{in}} \right)^2 \Delta nHe'_{in}} \quad \text{(II.15)}$$

This term $\left(\frac{\partial O_{2\ release}}{\partial nHe'_{in}} \right)^2 \Delta nHe'_{in} = 0$, because in the experiment Helium flow was constant (51.5 ml/min)

Therefore,

$$\Delta O_{2\ release} = nHe'_{in}\ \Delta Q \quad \text{(II.16)}$$

$$\Delta O_{2\ release} = 0.005845 \quad \text{(II.17)}$$

$$\text{Relative error} = \frac{O_{2\ release}}{\Delta O_{2\ release}} * 100 = 4.93 \quad \text{(II.18)}$$

II.4. Confidence Intervals for the rate of oxygen incorporated was calculated using regression statistics

Table II. 3. Summary output of the rate of oxygen incorporated regression statistic.

Multiple R	R Square	Adjusted R Square	Standard Error	Observations
0.8615	0.7423	0.7415	0.0078	331

Table II. 4. Summary output of the rate of oxygen incorporated regression statistic (ANOVA).

	df	*SS*	*MS*	*F*	*Significance F*
Regression	1	0.058	0.058	947.505	7E-99
Residual	329	0.020	6.125E-05		
Total	330	0.078			

Table II. 5. Summary output of the rate of oxygen incorporated

	Intercept	*X variable 1*
Coefficient	0.037	-3.5E-05
Standard error	0.0009	1E-06
T stat	43.49	-30.78
P-value	1.8E-138	7E-99
Lower 95%	0.036	-3.7E-05
Upper 95%	0.039	-3.2E-05

For calculating the confidence interval for the oxygen incorporated, the following equation was used

$$a + bX \pm t(RSD)\sqrt{\frac{1}{n} + \frac{(x)^2}{(n-1)\,(SD\ of\ \ x)^2}} \qquad \text{(II.19)}$$

Where regression coefficients a and b are the value of the intercept and slope respectively obtained from a straight line (Y), t is infinity degree of freedom at a 95% level of confidence = 1.96, n is the number of measurements = 330, ***SD of x*** is the standard deviation of the time and ***RSD*** is the residual standard deviation that can be obtained from eqn. (II.20).

$$RSD\sqrt{\frac{residual\ \ sum\ of\ \ squares}{Degrees\ of\ \ \ freedom}} \qquad \text{(II.20)}$$

II.5. Apparent rate constant for the oxygen incorporation

The determination of the apparent rate constant for the oxygen incorporation into LSCF6428 hollow fibre membranes was calculated assuming that the reaction is first order, see **figure II.4**

$$A \rightarrow B, \qquad r_A = kN_A/V \qquad \text{(II.21)}$$

Where r_A is reaction rate, N_A is moles of A, (V) is volume and (t) is time.

$$\int_0^t dt = -\int_{N_{A_0}}^{N_A} \frac{dN_A}{r_A}\frac{1}{V} \qquad \text{(II.22)}$$

Substituting $r_A\,V = k\ N_A$ from eqn. (II.21), and resolving the integral; the eqn. (II.23) is obtained,

$$\ln\frac{N_A}{N_{A_0}} = -k\ t \qquad \text{(II.23)}$$

The rate constant (k) was obtaining by plotting, see **figure II.4**,

$$t \quad vs. \quad \ln \frac{O_2 uptake - O_2 \ release}{nO_2 in} \tag{II.24}$$

The slope of the resulting line corresponds to:

$$k = m * n_{O_2\ in} / S_A P \tag{II.25}$$

Where, $n_{O_2\ in}$ is the molar flow of the oxygen at the inlet in the shell side (µmol s^{-1}), S_A is the superficial active membrane area for oxygen permeation and P is pressure (bar).

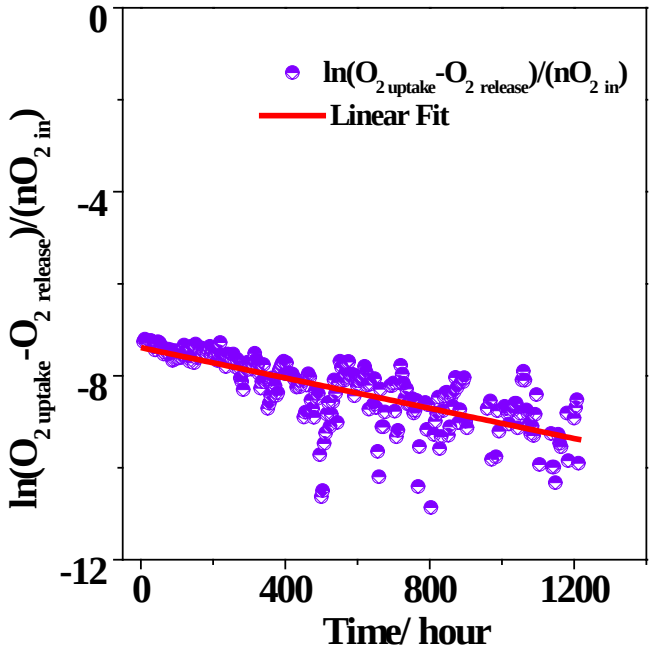

Figure.II.4 Apparent rate constant for oxygen incorporated.

II.6. Apparent rate constant for different helium flow under two modes of flow operation at 850 and 900°C: (A) Mode 2 (co-current) and (B) Mode 3 (counter-current)

These apparent rate constants are given in **Chapter 4, figure 4.6.**

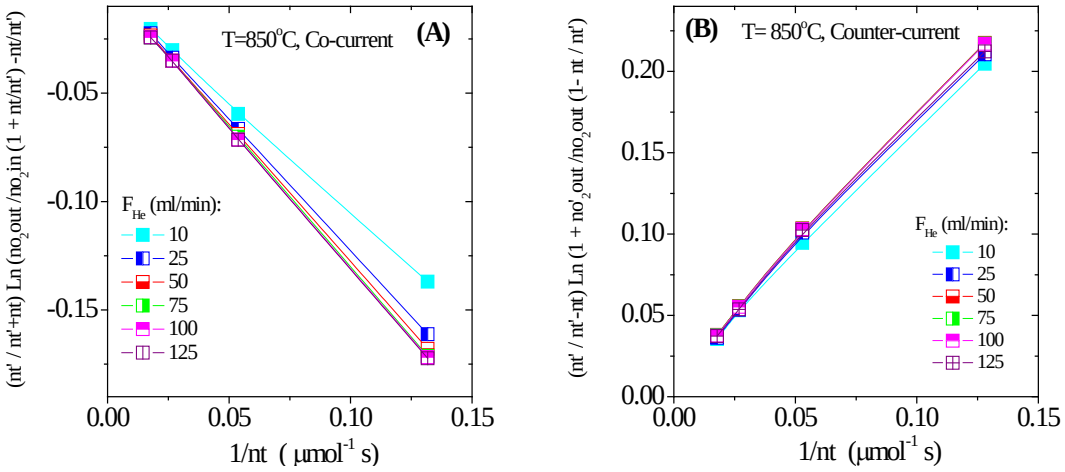

Figure.II.5 Reaction rate constant for different helium flows under two modes of flow operation at 850°C. (A) mode 2 (co-current) and (B) mode 3 (counter-current)

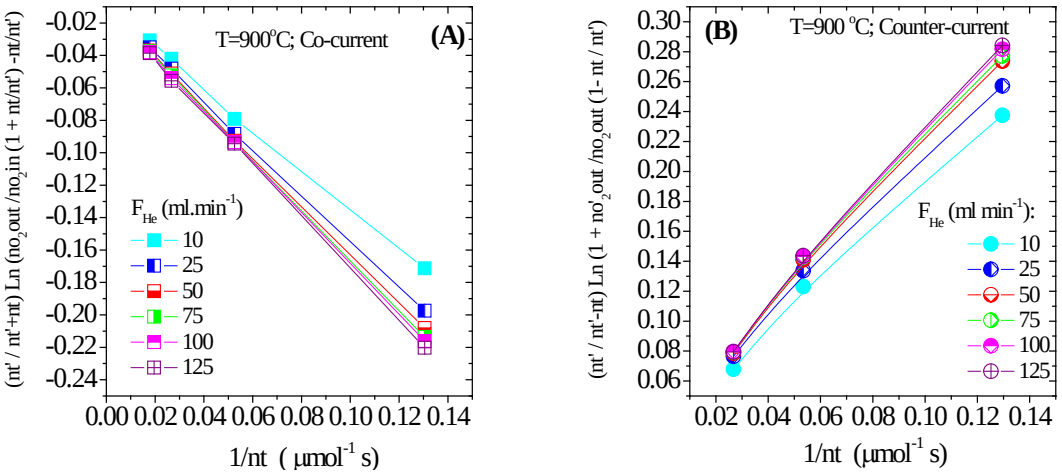

Figure.II.6 Reaction rate constant for different helium lows under two modes of flow operation at 900°C. (A) mode 2 (co-current) and (B) mode 3 (counter-current)

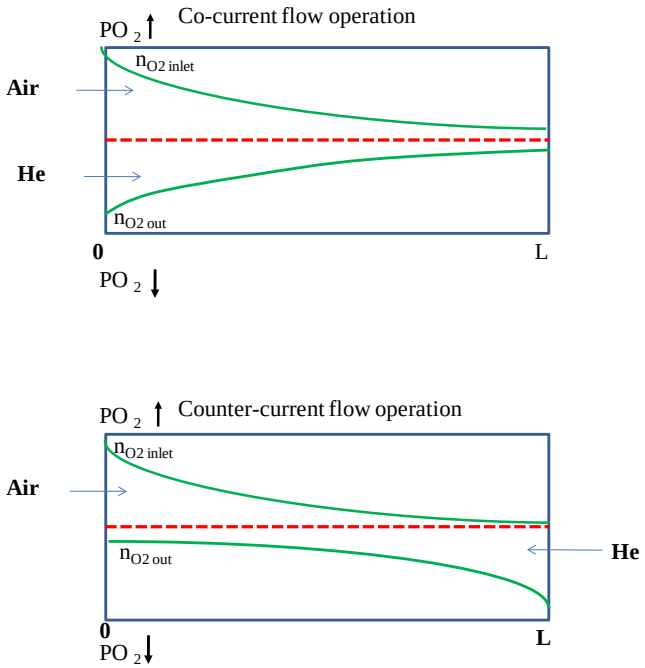

Figure II.7 Profiles of oxygen inlet (nO_2 inlet) and oxygen outlet (nO_2out) across membrane for mode 2 (co-current) and mode 3 (counter-current).

II.7. Reynolds number

Reynolds number (Re) can be defined for a number of different situations where a fluid or gas is in relative movement to a surface. These definitions generally include the gas properties such as density, viscosity, velocity and characteristic length or characteristic dimension (radius inter of the hollow fibre membrane).

Reynolds number is defined as: $\mathbf{Re} = \frac{\rho V D}{\mu}$, (II.26)

Where:

- V is the mean velocity of the object relative to the gas (m/s)
- D is the hollow fibre membrane diameter inter (m)
- μ is the dynamic viscosity of the gas ($Pa\ s\ or\ N\ s/m^2\ or\ Kg/m\ s$)

The Reynolds numbers are used to characterize different flow regimes, such as:

1. ***Laminar flow*** occurs at low Reynolds numbers (**Re < 2000**) and tends to have a lower velocity, where viscous forces are dominant, and is characterized by smooth and constant fluid motion.

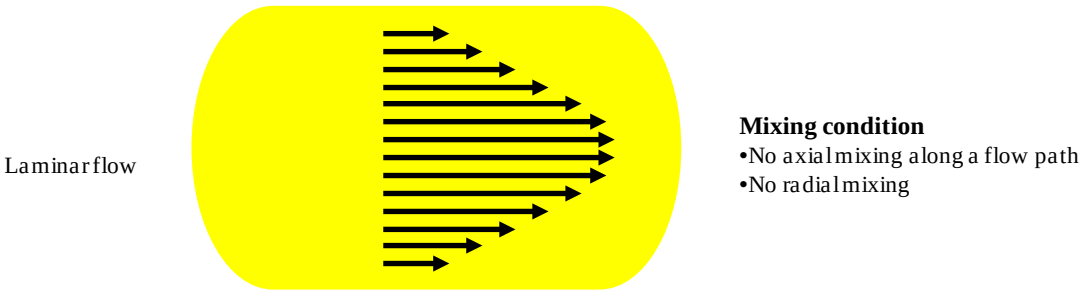

Figure II.8 Schematic *representation* of the laminar flow into tubular reactor

2. ***Turbulent flow*** occurs at high Reynolds numbers (**Re > 4000**) and is dominated by inertial forces, which tends to produce chaotic and unstable flow. Turbulent flow is irregular and travels at a higher speed, whose cross section can be assumed constant or flat.

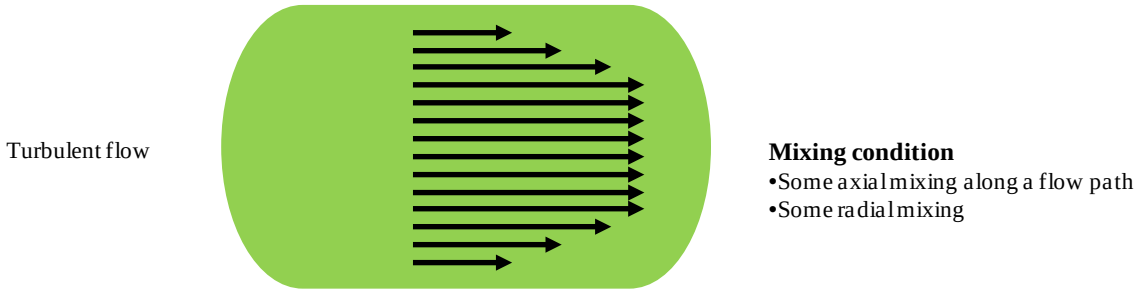

Figure II.9 Schematic representation of the turbulent flow into tubular reactor

3. ***Transitional flow*** is a mixture of laminar and turbulent flows with turbulence in the centre of the pipe and laminar flow near the edges (**2000 < Re < 4000**). These flows are uniform at medium velocity and depend on pipe roughness.

Below is shown the Reynolds numbers for different flow of air and oxygen, considering the following gas properties: **Density of air**: 1.205 kg m^{-3}; **Viscosity of air:** 0.0000185 N.s.m^{-2}; **Density of O_2**: 1.354 kg m^{-3}; **Viscosity of O_2**: 0.00001909 N.s.m^{-2}; **Diameter:** 0.001 m

$cross\ section = \pi\ r_0\ r_i = 0.011\ cm^2$, where r_i and r_0 are inner and outer radius of a typical hollow fibre (0.05 cm and 0.07 cm) and $Velocity = Flow\ rate / cross\ section\ of\ the\ HFM$

Table II. 6 Reynolds numbers for air in LSCF6428HFM-reactor.

Flow ($cm^3\ s^{-1}$)	Velocity ($m\ s^{-1}$)	Re	Type flow
10	9.094547	592	Laminar
25	22.73637	1481	Laminar
50	45.47273	2962	Transient
75	68.20910	4443	Turbulent
100	90.94547	5924	Turbulent
125	113.6818	7405	Turbulent
150	136.4182	8886	Turbulent
175	159.1546	10367	Turbulent
200	181.8909	11847	Turbulent

Table II. 7 Reynolds numbers for O_2 in LSCF6428HFM-reactor

Flow ($cm^3\ s^{-1}$)	Velocity ($m\ s^{-1}$)	Re	Type flow
10	9.094547	645	Laminar
25	22.73637	1613	Laminar
50	45.47273	3225	Transient
75	68.20910	4838	Turbulent
100	90.94547	6451	Turbulent
125	113.6818	8063	Turbulent
150	136.4182	9676	Turbulent
175	159.1546	11288	Turbulent
200	181.8909	12901	Turbulent

II.8. Distribution of total permeation resistance of unmodified LSCF6428-HFM reactor calculated with eqns (4.1), (4.2), (4.3) and (4.4) and is described in Chapter 4.

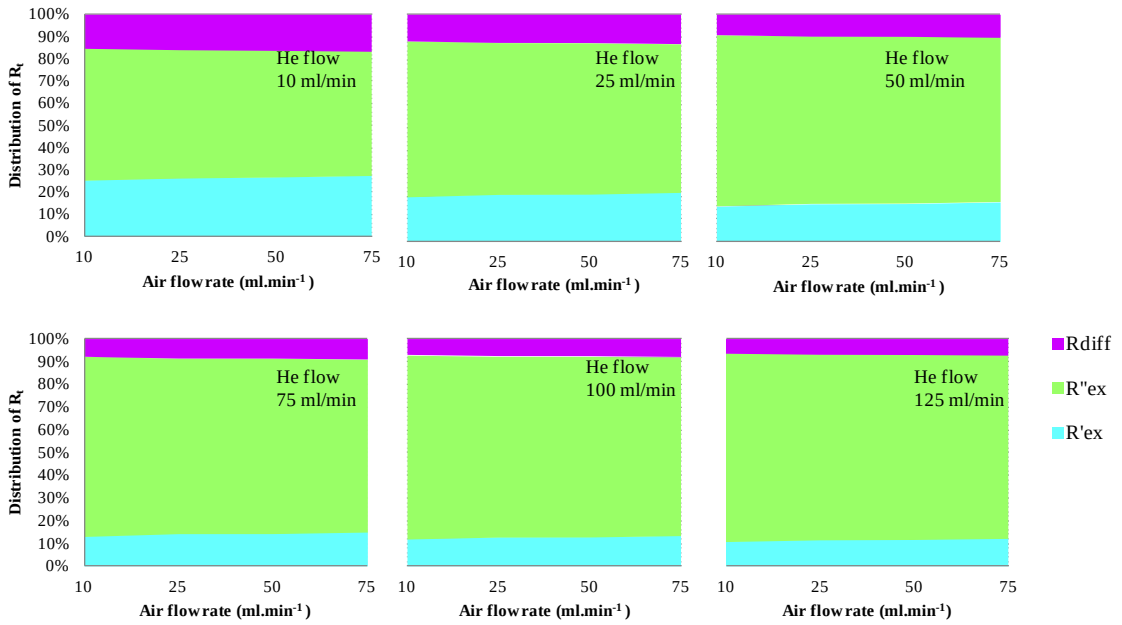

Figure II.10 Effect of air flow on distribution of total permeation resistance of unmodified LSCF6428-HFM reactor at 850°C.

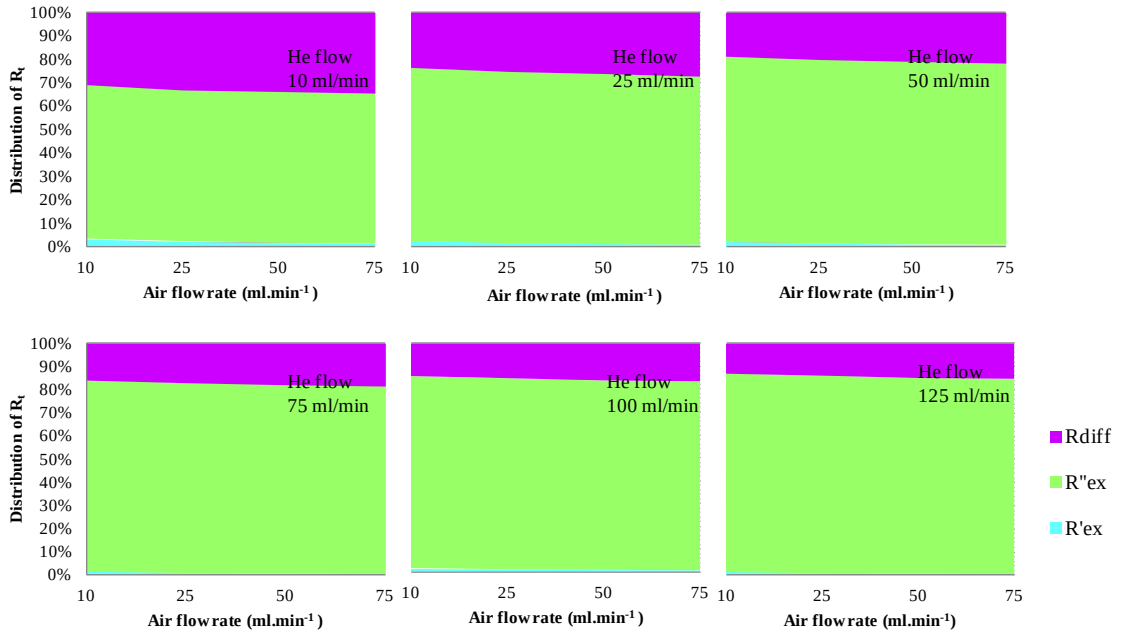

Figure II.11 Effect of air flow on distribution of total permeation resistance of unmodified LSCF6428-HFM reactor at 900°C.

II.9. Residence time or holding time for LSCF6428-HFM

Residence time or holding time (τ) is a representation of how long it takes for the gas concentration to significantly change in the reactor and is calculated by dividing membrane volume (shell or lumen side) by the volumetric flow.

$$\tau_s = \frac{volumen\ of\ \ membrane}{volumetric\ \ flow\ rate} \qquad \text{(II.27)}$$

Holding time in lumen side (τ_l):

$$volumen = \pi\ r_i^2 z\ n = 0.16\ \text{cm}^3, \qquad \text{(II.28)}$$

Where, r_i is the inner radius of a typical hollow fibre (0.05 cm), n is the number of hollow fibres used for assembled reactor and z is the isothermal zone centre of hollow fibre membrane reactor (5 cm)

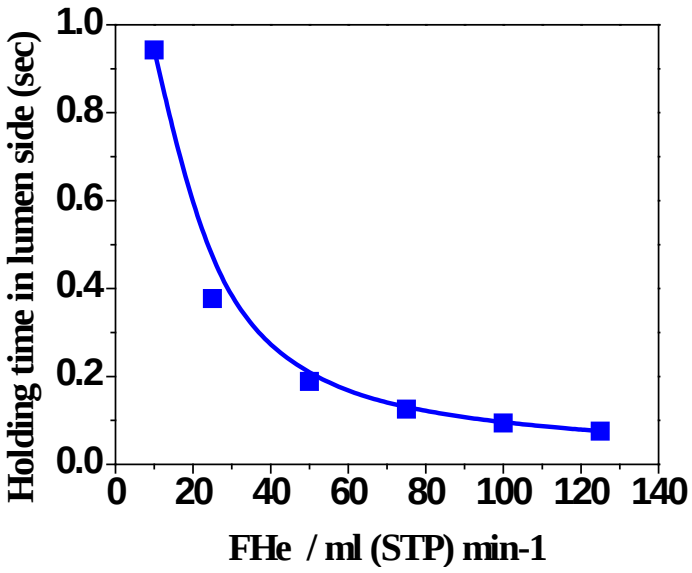

Figure II.12 Resistance time in lumen side of the *LSCF6428-HFM reactor*

Holding time in Shell side (τ_s):

$$volume = \frac{2\pi(r_0 - r_{in})}{\ln(r_o / r_{in})} n\, r_q, \qquad l = 21.3\ \text{cm}^3, \tag{II.29}$$

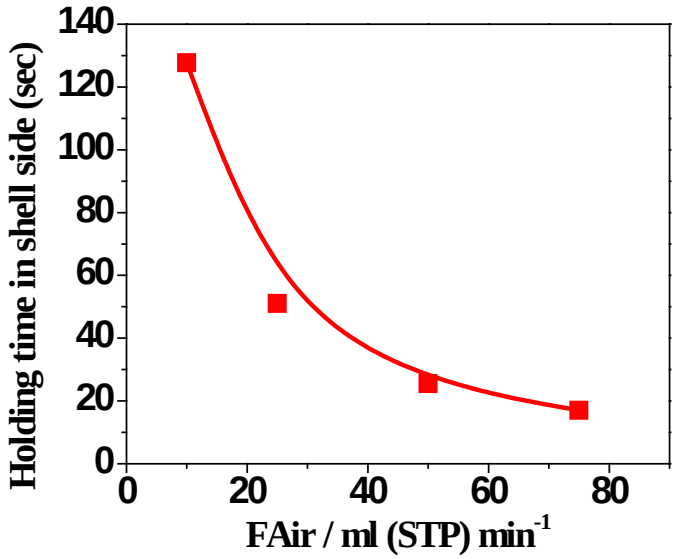

Figure II.13 Resistance time in shell side of the *LSCF6428-HFM reactor*

II.10. Activation energy (E_a) for unmodified LSCF6428-HFM, values reported in Chapter 4

Activation energy (E_a) was calculated using the Arrhenius equation:

$$k = A\exp(-E_a / RT) \tag{II.30}$$

Where, k is the rate constant, R is the ideal gas constant (8.314 $J.K^{-1}.mol^{-1}$) and T is the temperature (Kelvin)

Applying logarithm on both side of eqn. (II.30), it can be obtained

$$\ln(k) = (-E_a / R)\ (1/T) + \ln(A) \quad \text{(II.31)}$$

Plotting $\ln(k)$ vs. $1/T$, we can obtain the activation energy through the slope(m).

$$y = mx + c \quad \text{(II.32)}$$

$$E_a = mR, \ \ (kJ.mol^{-1}) \quad \text{(II.33)}$$

Table.II.8 Activation Energy for unmodified LSCF6428-HFM

Helium flow (ml mol^{-1})	Ea (kJ mol^{-1})
10	44
25	37
50	40
75	40
100	43

II.11. Determination of the crystallite size by XRD method using Scherrer equation for unmodified LSCF6428-HFM, data given in Chapter 4

Table. II.9 Crystal size determined by Scherrer equation for unmodified LSCF6428-HFM

Membrane zone	Condition	2θ	Crystal size (um)	Crystal size (nm)
Lumen side	BR	32.64	0.022	22.0
Shell side	BR	32.68	0.023	23.3
Lumen side	AR	32.56	0.025	25.4
Shell side	AR	32.68	0.024	24.0

II.12 Distribution of the of the pore area and grain boundary perimeter using SPIP 6.0.9 software for unmodified LSCF6428-HFM, data given in Chapter 4

- **Cross section of unmodified LSCF6428-HFM**

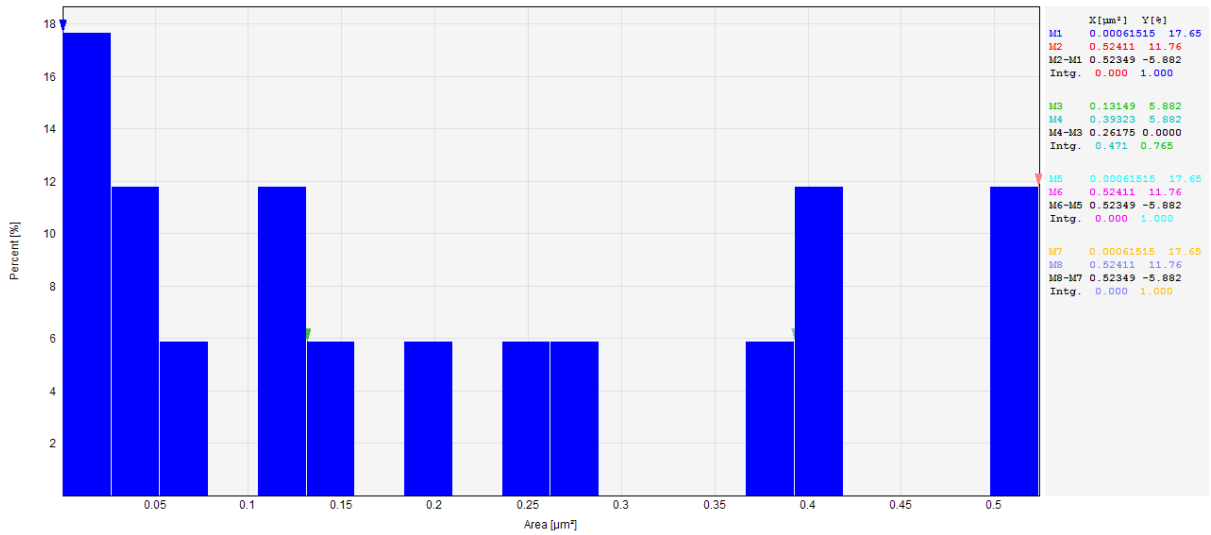

Figure II.14 Distribution of the pore area of cross section before reaction, data obtained by SPIP 6.0.9

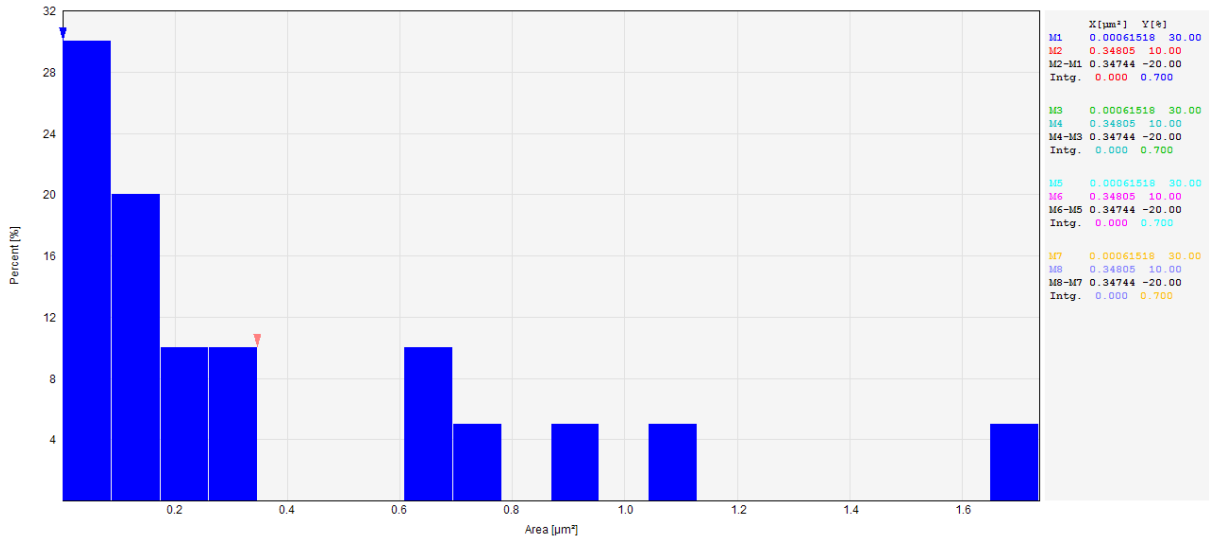

Figure II.15 Distribution of the pore area of cross section after reaction, data obtained by SPIP 6.0.9

- **Lumen side for unmodified LSCF6428-HFM.**

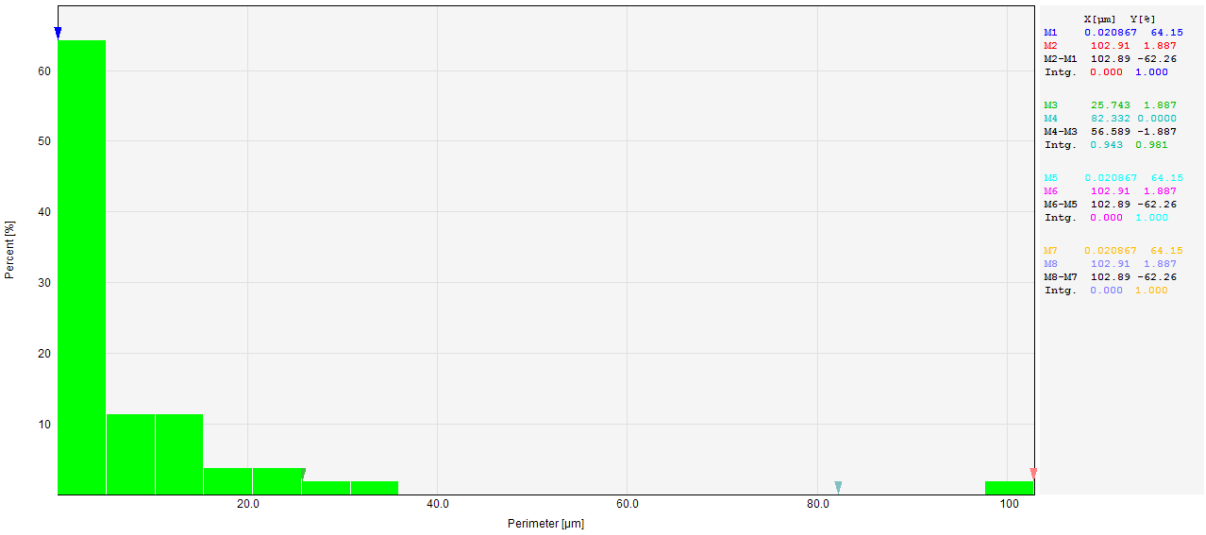

Figure II.16 Distribution of the grain boundary perimeter of lumen side before reaction, data obtained by SPIP 6.0.9

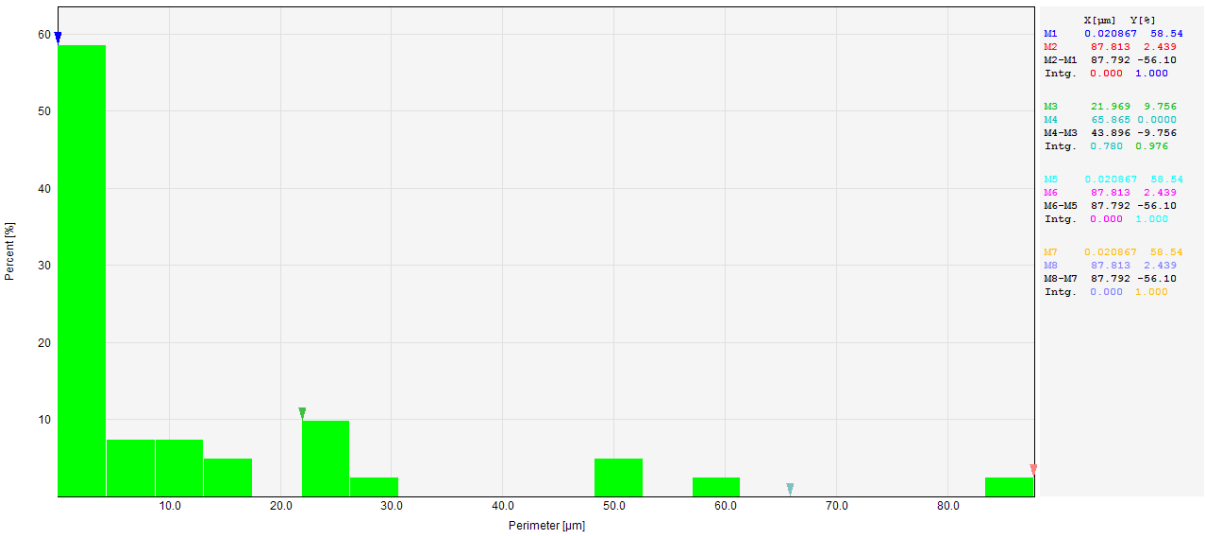

Figure II.17 Distribution of the grain boundary perimeter of centre lumen side after reaction, data obtained by SPIP 6.0.9

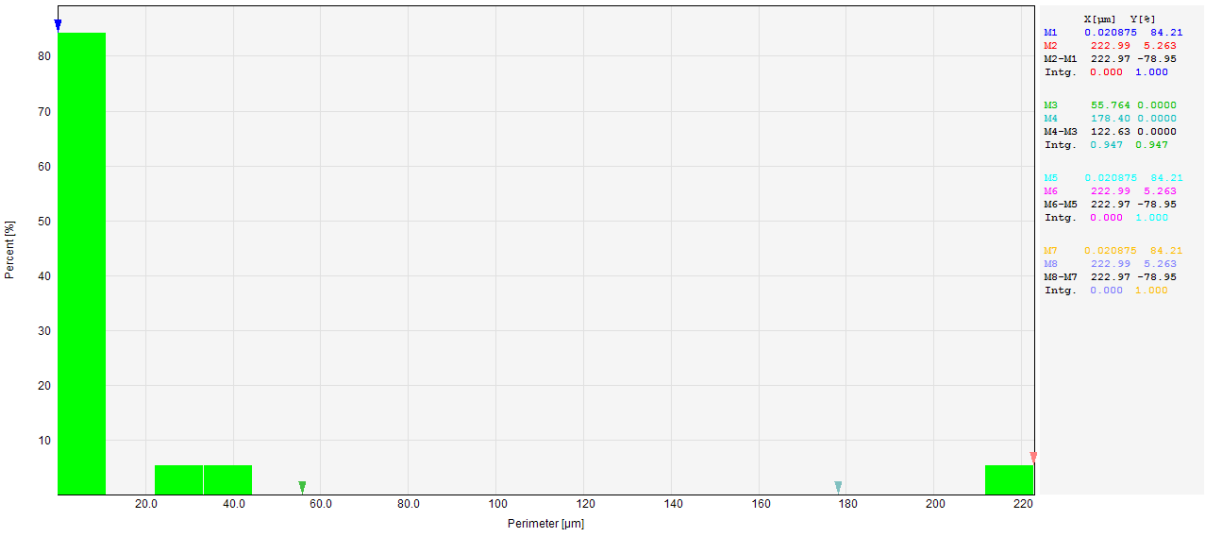

Figure II.18 Distribution of the grain boundary perimeter of end lumen side after reaction, data obtained by SPIP 6.0.9

- **Shell side for unmodified LSCF6428-HFM**

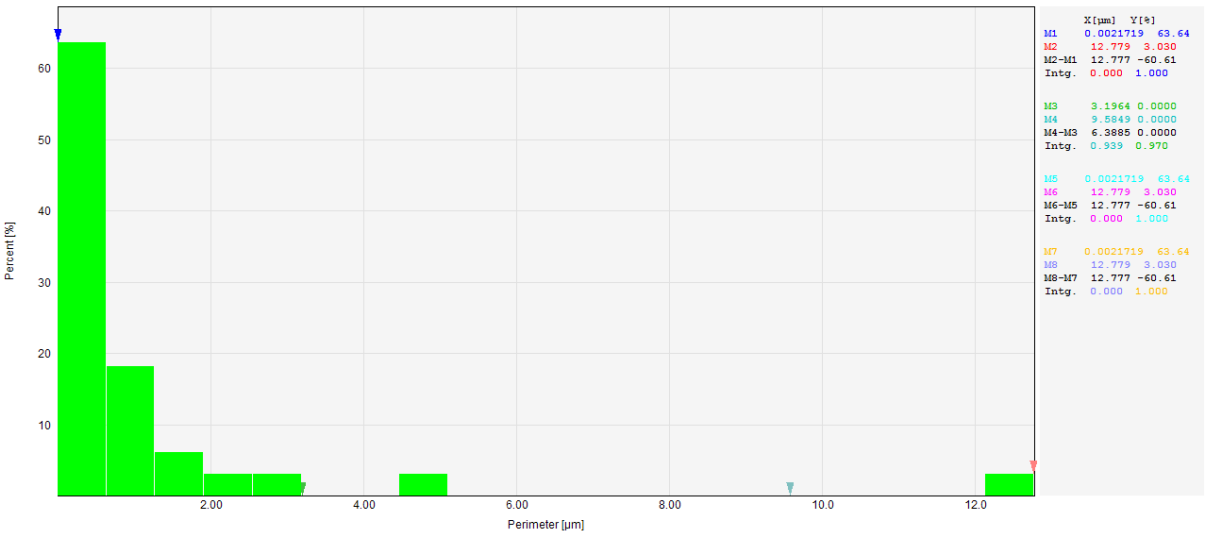

Figure II.19 Distribution of the grain boundary perimeter of end shell side before reaction, data obtained by SPIP 6.0.9

II.13. EDXS profile of the different zones of the LSCF6428-HFM before and after oxygen permeation measurements, which was describe in Chapter 4.

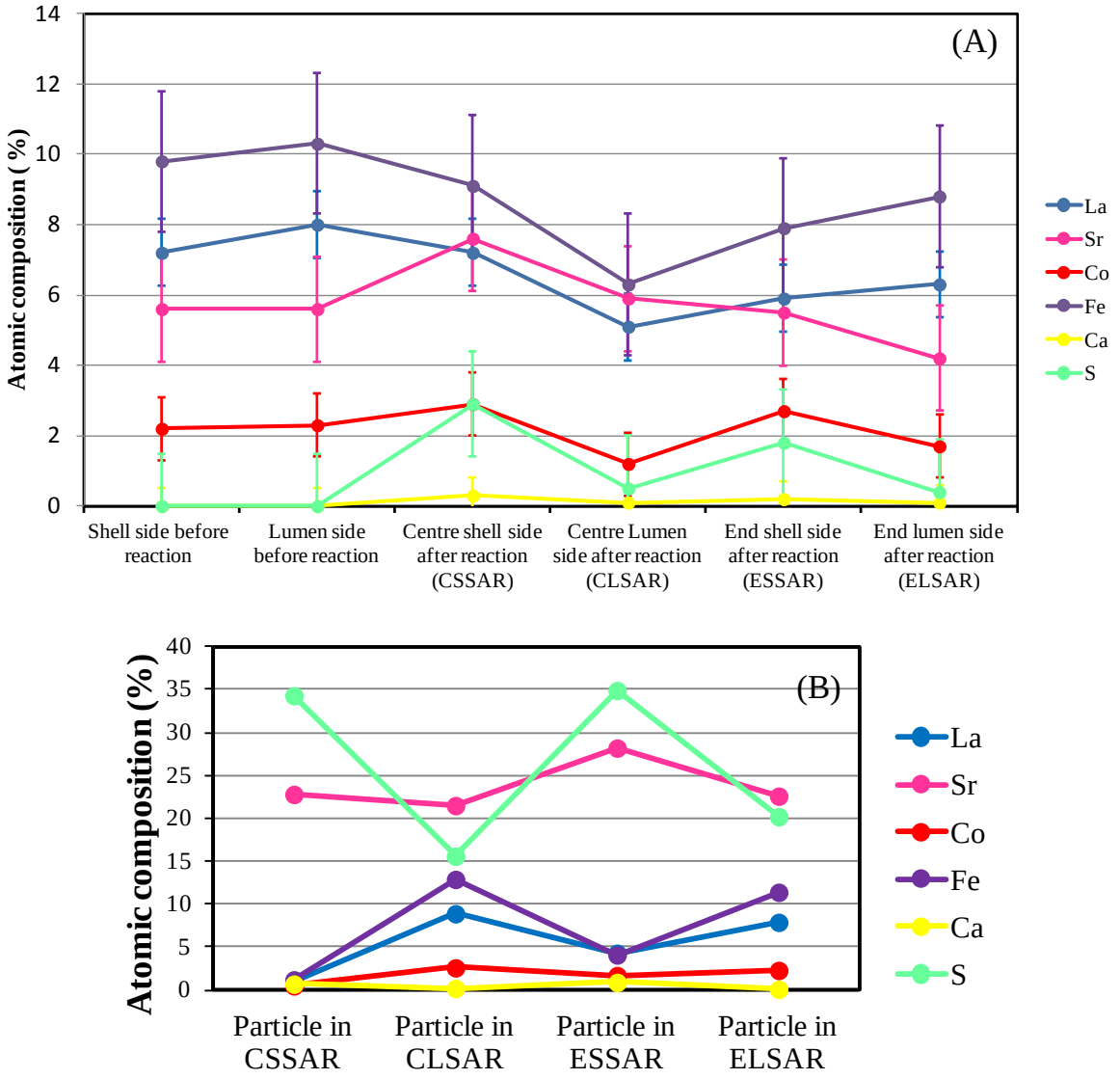

Figure II.20 EDXS results of different zones of the LSCF6428-HFM before and after oxygen permeation measurements (A). EDXS results for particles in different zones of membrane (B).

Table II.10 EDXS of the unmodified LCF6428-HFM centre lumen side after reaction

*** PUzaf results ***					
elem/line	P/B	B	F	c(atom)	confid._h_
O K-ser	@	1.00000	1.00000	50.41	+- 9.52
Al K-ser	@134.9	1.00789	1.00738	30.54	+- 5.42
La L-ser	@135.7	1.03605	1.05237	5.10	+- 0.92
Fe K-alpha	@ 83.4	1.04394	1.04435	6.31	+- 1.11
Co K-alpha	@ 15.6	1.04589	1.05479	1.16	+- 0.50
Sr L-ser	@ 58.9	1.01270	1.01150	5.85	+- 1.13
S K-ser	@ 3.9	1.01875	1.01370	0.54	+- 0.53
Ca K-alpha	@ 1.0	1.03035	1.06907	0.10	+- 0.24
standardless				100.00	[2s]

Table II.11 EDXS of the particle of unmodified LCF6428-HFM centre lumen side after reaction

*** PUzaf results ***					
elem/line	P/B	B	F	c(atom)	confid._h_
O K-ser	@	1.00000	1.00000	24.90	+- 4.47
Al K-ser	@ 31.6	1.00939	1.01262	13.40	+- 2.38
S K-ser	@ 59.0	1.02233	1.01065	15.58	+- 1.92
La L-ser	@125.6	1.04294	1.05300	8.97	+- 1.11
Fe K-alpha	@ 89.3	1.05234	1.04478	12.88	+- 1.78
Co K-alpha	@ 18.3	1.05466	1.05512	2.60	+- 0.96
Sr L-ser	@114.7	1.01513	1.01080	21.48	+- 3.03
Ca K-alpha	@ 1.0	1.03614	1.05305	0.18	+- 0.36
standardless				100.00	[2s]

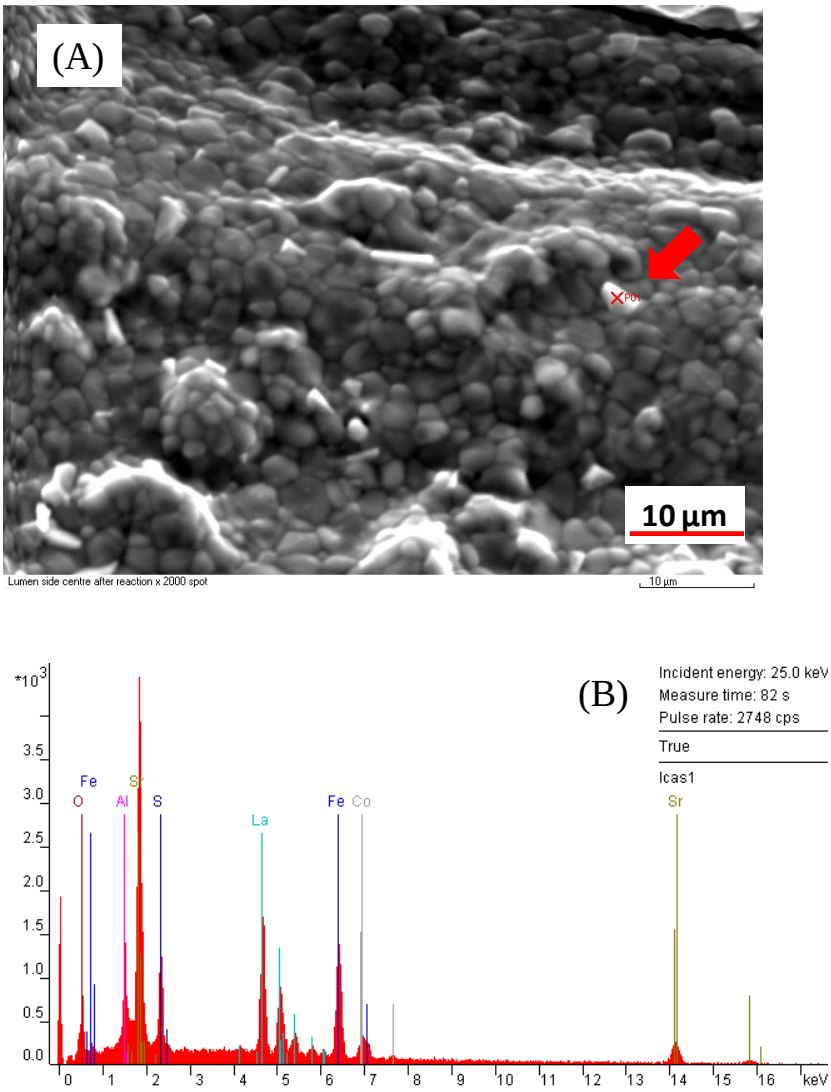

Figure II.21 SEM image and EDXS profile of the particle of unmodified LCF6428-HFM centre lumen side after reaction

Table II.12 EDXS of the unmodified LCF6428-HFM end lumen side after reaction

```
------------------------------------------------------------------
*** PUzaf results ***
elem/line____P/B_____B_____F_____________c(atom)__confid._h_
O  K-ser   @       1.00000 1.00000          73.75  +-12.91
Al K-ser   @ 22.2  1.00827 1.00776           4.89  +- 0.92
S  K-ser   @  2.6  1.01966 1.01833           0.35  +- 0.18
La L-ser   @170.5  1.03782 1.05221           6.30  +- 0.66
Fe K-alpha @116.9  1.04610 1.03991           8.76  +- 1.05
Co K-alpha @ 22.7  1.04814 1.04885           1.67  +- 0.50
Sr L-ser   @ 43.6  1.01332 1.01460           4.22  +- 0.63
Ca K-alpha @  0.7  1.03183 1.09425           0.07  +- 0.15
------------------------------------------------------------------
standardless                                100.00     [2s]
```

Table II.13 EDXS of the particle of unmodified LCF6428-HFM end lumen side after reaction

```
------------------------------------------------------------------
*** PUzaf results ***
elem/line____P/B_____B_____F_____________c(atom)__confid._h_
O  K-ser   @       1.00000 1.00000          26.18  +- 4.83
Al K-ser   @ 22.3  1.00929 1.01390           9.31  +- 2.16
S  K-ser   @ 77.6  1.02207 1.00974          20.20  +- 2.77
La L-ser   @113.1  1.04245 1.05351           7.94  +- 1.19
Fe K-alpha @ 80.8  1.05174 1.04631          11.43  +- 1.74
Co K-alpha @ 16.6  1.05403 1.05711           2.30  +- 1.02
Sr L-ser   @122.5  1.01495 1.01068          22.58  +- 3.66
Ca K-alpha @  0.3  1.03573 1.04823           0.06  +- 0.25
------------------------------------------------------------------
standardless                                100.00     [2s]
```

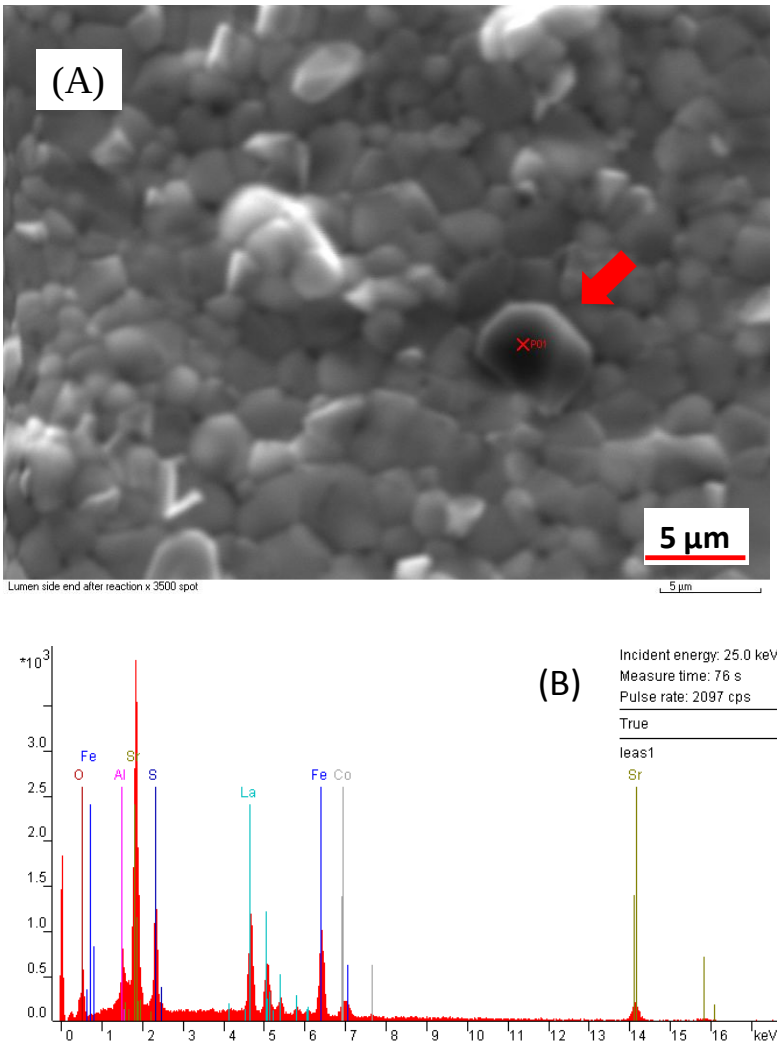

Figure II.22 SEM image and EDXS profile of the particle of unmodified LCF6428-HFM end lumen side after reaction

Table II.14 EDXS of the unmodified LCF6428-HFM centre shell side after reaction

elem/line	P/B	B	F	c(atom)	confid._h_
O K-ser	@	1.00000	1.00000	64.74	+-11.61
Al K-ser	@ 22.9	1.00870	1.00903	5.27	+- 1.06
S K-ser	@ 20.5	1.02068	1.01558	2.92	+- 0.57
Ca K-alpha	@ 3.2	1.03348	1.07899	0.32	+- 0.23
La L-ser	@185.9	1.03977	1.05199	7.20	+- 0.78
Fe K-alpha	@115.4	1.04848	1.04170	9.05	+- 1.17
Co K-alpha	@ 37.7	1.05063	1.05000	2.91	+- 0.59
Sr L-ser	@ 74.9	1.01401	1.01323	7.58	+- 1.06
standardless				100.00	[2s]

*** PUzaf results ***

Table II.15 EDXS of the particle of unmodified LCF6428-HFM centre shell side after reaction

elem/line	P/B	B	F	c(atom)	confid._h_
O K-ser	@	1.00000	1.00000	34.87	+- 5.98
Al K-ser	@ 20.4	1.00800	1.02557	4.64	+- 0.94
S K-ser	@238.6	1.01901	1.00465	34.26	+- 3.89
Ca K-alpha	@ 7.1	1.03077	1.01930	0.74	+- 0.25
La L-ser	@ 26.6	1.03655	1.05950	1.01	+- 0.28
Fe K-alpha	@ 15.7	1.04455	1.06741	1.17	+- 0.36
Co K-alpha	@ 7.2	1.04653	1.08461	0.52	+- 0.28
Sr L-ser	@224.0	1.01288	1.00944	22.80	+- 3.63
standardless				100.00	[2s]

*** PUzaf results ***

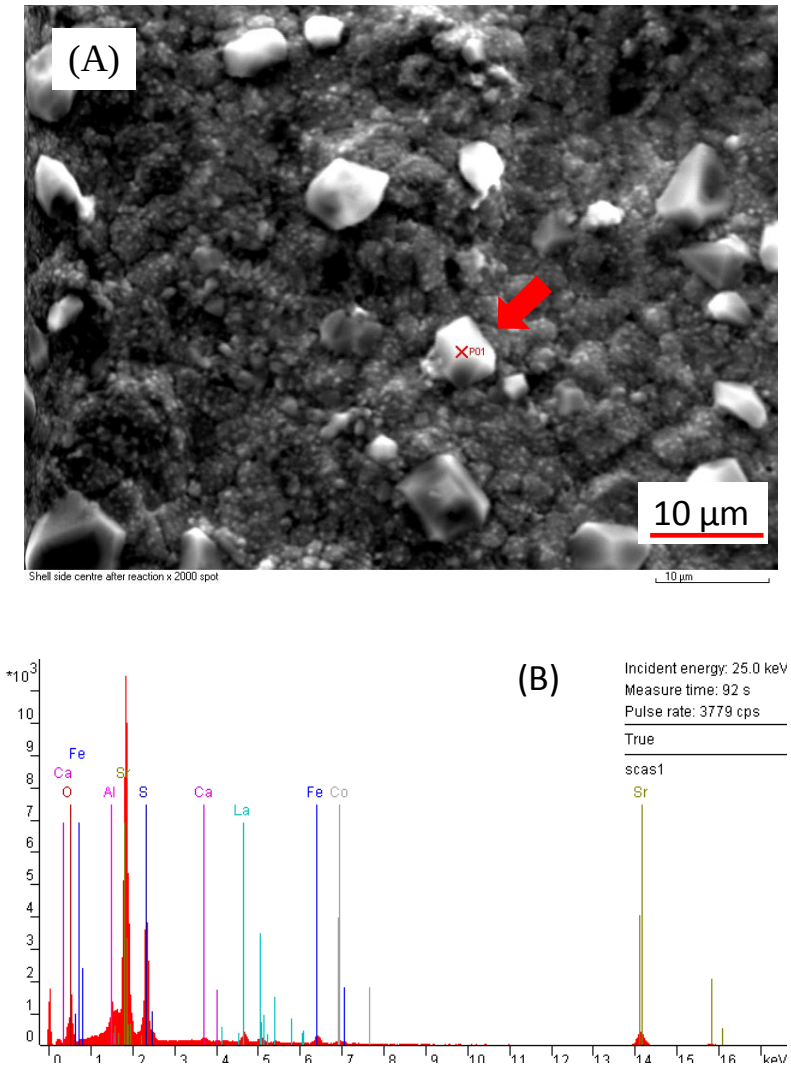

Figure II.23 SEM image and EDXS profile of the particle of unmodified LCF6428-HFM centre shell side after reaction

Table II.16 EDXS of the unmodified LCF6428-HFM end shell side after reaction

elem/line	P/B	B	F	c(atom)	confid. h
O K-ser	@	1.00000	1.00000	73.09	+-13.05
Al K-ser	@ 13.1	1.00828	1.00856	2.89	+- 0.65
S K-ser	@ 13.3	1.01968	1.01637	1.81	+- 0.38
Ca K-alpha	@ 1.9	1.03186	1.08325	0.18	+- 0.16
La L-ser	@161.3	1.03785	1.05368	5.94	+- 0.66
Fe K-alpha	@105.3	1.04613	1.04197	7.85	+- 1.03
Co K-alpha	@ 37.0	1.04818	1.04990	2.72	+- 0.55
Sr L-ser	@ 57.2	1.01333	1.01373	5.52	+- 0.81
standardless				100.00	[2s]

Table II.17 EDXS of the particle of unmodified LCF6428-HFM end shell side after reaction

```
------------------------------------------------------------------
*** PUzaf results ***
elem/line____P/B_____B_____F_____________c(atom)__confid._h_
O  K-ser   @       1.00000 1.00000          19.67  +- 3.55
Al K-ser   @ 20.4  1.00887 1.02017           6.21  +- 1.33
S  K-ser   @182.3  1.02109 1.00659          34.91  +- 3.91
Ca K-alpha @  6.4  1.03414 1.03015           0.89  +- 0.29
La L-ser   @ 83.9  1.04056 1.05411           4.29  +- 0.55
Fe K-alpha @ 40.6  1.04944 1.05611           4.13  +- 0.65
Co K-alpha @ 17.3  1.05163 1.06921           1.73  +- 0.46
Sr L-ser   @207.7  1.01429 1.00977          28.17  +- 4.39
------------------------------------------------------------------
standardless                                100.00     [2s]
```

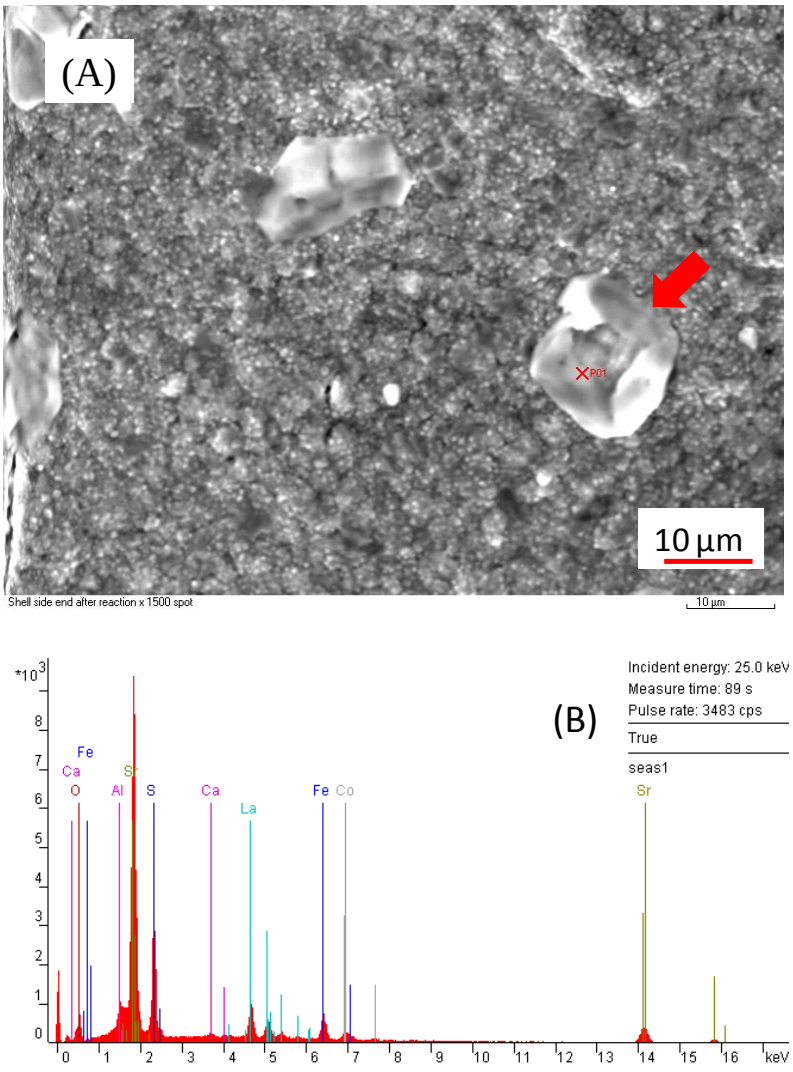

Figure II.24 SEM image and EDXS profile of the particle of unmodified LCF6428-HFM end shell side after reaction

II.14. Thermodynamics calculation used in chapters 4, 5 and 6

Below is given the thermodynamic equations, whose applications are illustrated with an example.

- **Temperature Dependence of Enthalpy Changes:**

The enthalpy changes for chemical reaction can be deduced for a range of temperature.

For a chemical reaction:

$$\mathbf{Re}ac\,\mathbf{tan}ts \rightarrow \mathbf{Pr}oducts \qquad \text{(II.34)}$$

The enthalpy change for the reaction can be written as:

$$\Delta H = \Delta H_{\mathbf{Pr}oducts} - \Delta H_{reac\,\mathbf{tan}ts} \qquad \text{(II.35)}$$

The enthalpies of the products and reactants involve the sum of the molar enthalpies of the different products and reactants present in the chemical reaction.

The derivative with respect to temperature is given in eqn. (II.36):

$$\left[\partial(\Delta H)/\partial T\right]_P = \left[\partial(\Delta H_{prod})/\partial T\right]_P - \left[\partial(\Delta H_{react})/\partial T\right]_P \qquad \text{(II.36)}$$

Also, we can write this, using heat-capacity terms:

$$\left[\partial(\Delta H)/\partial T\right]_P = (Cp)_{prod} - (Cp)_{react} = \Delta Cp \qquad \text{(II.37)}$$

Where $(Cp)_{prod}$ ***and*** $(Cp)_{react}$ imply the sum of the heat capacities of the products and reactants.

Integrating the enthalpy of reaction from T_1 ***to*** T_2, it is obtained eqn. (II.39)

$$\int_{T_1}^{T_2} \left[\partial(\Delta H)/\partial T\right]_P = \int_{T_1}^{T_2} \Delta Cp\, dT \qquad \text{(II.38)}$$

$$\Delta H_{T_2} - \Delta H_{T_1} = \int_{T_1}^{T_2} \Delta Cp \; dT \qquad \text{(II.39)}$$

According to Leitner *et al.*, the heat capacity of solid mixed oxides is given by eqn. (II.40)

$$Cp = a + bT + \left(c / T^2\right) \qquad \text{(II.40)}$$

$$\Delta H_{T_2} - \Delta H_{T_1} = \int_{T_1}^{T_2} \Delta(a + bT + (c / T^2)\; dT \qquad \text{(II.41)}$$

Substituting Cp into the eqn. (II.39) and resolving the integral, it is obtained the following eqn.

$$\Delta H_{T_2} - \Delta H_{T_1} = \Delta a\left(T_2 - T_1\right) + \left(1/2\right)\left(\Delta b\right)\left(T_2^2 - T_1^2\right) - \left(\Delta c\right)\left[\left(1/T_2\right) - \left(1/T_1\right)\right] \qquad \text{(II.42)}$$

Using eqn. (II.41), the enthalpy change at one temperature from the enthalpy change at another temperature can be calculated. General expression for temperature dependence of the reaction enthalpy change is given below

$$\Delta H_T = \Delta aT + \left(1/2\right)\left(\Delta b\right)\left(T^2\right) - \left(\Delta c\right)\left(1/T\right) + cons\tan t \qquad \text{(II.43)}$$

The constant term is evaluated by using the enthalpy change for the reaction at 25°C. After calculating the constant term, the equation can be used to calculate the enthalpy change at any other temperature.

Example

Calculate the enthalpy change for $CO(g) + H_2O(g) \rightarrow CO_2(g) + H_2(g)$ at 1123 K. Standard enthalpies of formation of CO(g), H_2O(g), CO_2(g) and H_2(g) are -110.52, -241.82, -393.51 and 0 kJ mol^{-1}, respectively.

$$CO(g) + H_2O(g) \rightarrow CO_2(g) + H_2(g)$$

$$\Delta H_f^0 = -110.52 \quad -241.82 \quad -393.51 \quad 0$$

The enthalpy change for the reaction is given below

$$\Delta_r H_{298}^0 = -393.51 + 0 - (-110.52 + (-241.82)) \tag{II.44}$$

$$\Delta_r H_{298}^0 = -41.17 kJ\ mol^{-1} \tag{II.45}$$

Determination of the enthalpy change at 1123 K using the values of a, b and c

$$CO(g) + H_2O(g) \rightarrow CO_2(g) + H_2\ (g)$$

a terms	**28.41**	**30.54**	**44.22**	**27.28**
b terms	**0.00410**	**0.01029**	**0.00879**	**0.00326**
c terms	**−46,000**	**0**	**−862,000**	**50,000**

Where,

$$\Delta a = 44.22 + 27.28 - (28.41 + 30.54) = 12.55 \tag{II.46}$$

$$\Delta b = 0.00879 + 0.00326 - (0.00410 + 0.01029) = -2.34x10^{-3} \tag{II.47}$$

$$\Delta c = -862000 + 50000 - (-46000 + 0) = -7.66x10^5 \tag{II.48}$$

Substituting the value of $\Delta H_{298}^0 = 41.138\ kJ\ mol^{-1}$, $\Delta a, \Delta b, \Delta c$ and $T = 298.15\ K$ in eqn.(II.42), the value of the constant can be obtained.

$$\Delta H_{298} = (12.55)(298) + (1/2)\left(-2.34x10^{-3}\right)(298)^2 - \left(-7.66x10^5\right)(1/298) + const \tag{II.49}$$

$$\Delta H_{298} = 3739.9 - 103.901 + 2570.469 + const \tag{II.50}$$

$$-41138 = 6206.469 + const \tag{II.51}$$

$$const = -47344.5 \;\; J\,mol^{-1} \;\; or \;\; 47.3445 \;\; k.mol^{-1} \qquad \text{(II.52)}$$

For $T = 1123\,K$

$$\Delta H_{298} = (12.55)(1123) + (1/2)\left(-2.34x10^{-3}\right)\left(1123^2\right) - \left(-7.66x10^{5}\right)(1/1123) - 473445 \qquad \text{(II.53)}$$

$$\Delta H_{1123} = -34.0443 \;\; kJ\,mol^{-1}$$

- **Calculation of the Gibbs energy change**

Calculate the standard Gibbs energy change at 298 K for the below reaction

$$CO(g) + H_2O(g) \rightarrow CO_2(g) + H_2\,(g)$$

$$\Delta H_f^0 = -110.52 \quad -241.82 \quad -393.51 \quad 0$$

Using standard values of $\Delta_f H^{\circ}_{298}$ and S^0_{298} for reactants and products along eqns. (II.54) and (II.57) is possible to determine the enthalpy and entropy of reaction.

Using eqn. (II.54)

$$\Delta_r H^0_{298} = \sum v_i \Delta_f H^o_{298}(products) - \sum v_i \Delta_f H^o_{298}(reac\tan ts) \qquad \text{(II.54)}$$

$$= 1x\Delta_f H^o_{298}(CO_2)(g) + 1x\Delta_f H^o_{298}(H_2)(g) - \left[1x\Delta_f H^o_{298}(CO)(g) + \Delta_f H^o_{298}(H_2O)(g)\right] \qquad \text{(II.55)}$$

$$= -393.51\,kJmol^{-1} + 0kJmol^{-1} - \left[-110.52\,kJmol^{-1} + (-241.82\,kJmol^{-1}\right] \qquad \text{(II.56)}$$

$$\Delta_r H^0_{298} = -41.138\,kJ\,mol^{-1}$$

In the same way, using Eqn. (II.57) for calculating entropy;

$$\Delta_r S^0_{298} = \sum v_i S^o_{298}(products) - \sum v_i S^o_{298}(reac\tan ts) \qquad \text{(II.57)}$$

$$\Delta_r S^0_{298} = 1xS^0_{298}(CO_2)(g) + 1xS^0_{298}(H_2)(g) - \left[1xS^o_{298}(CO) + 1xS^o_{298}(H_2O)(g)\right] \quad \text{(II.58)}$$

$$\Delta_r S^0_{298} = 213.8 \ \ Jmol^{-1}K^{-1} + 130.7 \ Jmol^{-1}K^{-1} - \left[197.7 Jmol^{-1}K^{-1} + 188.8 Jmol^{-1}K^{-1}\right] \quad \text{(II.59)}$$

$$\Delta_r S^0_{298} = 344.5 \ \ Jmol^{-1}K^{-1} - \left[386.5 Jmol^{-1}K^{-1}\right] \quad \text{(II.60)}$$

$$\Delta_r S^0_{298} = -42.045 \ Jmol^{-1}K^{-1}$$

The Gibbs energy of reaction can be determined using eqn. (II.61)

$$\Delta_r G^0 = \Delta_r H^0 - T\Delta_r S^0 \quad \text{(II.61)}$$

$$\Delta_r G^0_{298} = \Delta_r H^0_{298} - T\Delta_r S^0_{298} \quad \text{(II.62)}$$

$$\Delta_r G^0_{298} = -41138 \ J \ mol^{-1} - \left(298K \ \ x(-42.045 \ J \ mol^{-1} \ K^{-1})\right) \quad \text{(II.63)}$$

$$\Delta_r G^0_{298} = -28{,}608 \ J \ mol^{-1} = -28.608 \ kJ \ \text{mol}^{-1}$$

- **Calculation of the change of Gibbs energy with temperature**

Calculate the standard Gibbs energy change for $CO(g) + H_2O(g) \rightarrow CO_2(g) + H_2\ (g)$ at 1123 K.

The standard enthalpy and entropy of reaction at 298 K was calculated using Eqns (II.54) and (II.57). The change in the heat capacity on reaction was calculated using eqn. (II.64).

$$\Delta_r C^0_P = \sum v_i C^0_P(products) - \sum v_i C^0_P(reactants) \quad \text{(II.64)}$$

$$\Delta_r C^0_P = \left[1xC^0_P(CO_2)(g) + 1xC^0_P(H_2)(g)\right] - \left(1xC^0_P(CO) + 1xC^0_P(H_2O)(g)\right) \quad \text{(II.65)}$$

$$\Delta_r C^0_P = \left[42.8 Jmol^{-1}K^{-1} + 28.8 \ Jmol^{-1}K^{-1}\right] - \left(29.1 \ Jmol^{-1}K^{-1} + 33.6 \ Jmol^{-1}K^{-1}\right) \quad \text{(II.66)}$$

$$\Delta_r C^0_P = \left[71.6 \ Jmol^{-1}K^{-1}\right] - \left(62.7 \ Jmol^{-1}K^{-1}\right) \quad \text{(II.67)}$$

$$\Delta_r C_P^0 = 8.9 J mol^{-1} K^{-1}$$

Then, the standard enthalpy at 1123 K was determined using Eqns (II.68).

$$\Delta_r H_{T_2}^0 = \Delta_r H_{T_1}^0 + \Delta C_P^0 (T_2 - T_1) \quad \text{(II.68)}$$

$$\Delta_r H_{1123}^0 = \Delta_r H_{298}^0 + \Delta C_P^0 (1123K - 298K) \quad \text{(II.69)}$$

$$\Delta_r H_{1123}^0 = -41170\ J\ mol^{-1} + (8.9\ J\ mol^{-1} K^{-1} x\ 825K) \quad \text{(II.70)}$$

$$\Delta_r H_{1123}^0 = -33618\ J\, mol^{-1} \quad or \quad -33.618\ kJ\ mol^{-1}$$

The reaction entropy at 1223K was determined using eqn. (II.71).

$$\Delta S_{T_2}^0 = \Delta S_{T_1}^0 + \Delta C_P^0 \ln\left(T_2 / T_1\right) \quad \text{II.71)}$$

$$\Delta S_{1123}^0 = \Delta S_{298}^0 + \Delta C_P^0 \ln\left(1123 / 298\right) \quad \text{(II.72)}$$

$$\Delta S_{1123}^0 = -42\ J\ mol^{-1} K^{-1} + \left[\left(8.9 J\ mol^{-1} K^{-1}\right) \ln\left(1123K / 298K\right)\right] \quad \text{(II.73)}$$

$$\Delta S_{1123}^0 = -30.857\ \text{J mol}^{-1}\text{K}^{-1}$$

Combining the values for the enthalpy and entropy changes at 1123 K using eqn. (II.74), we can obtain the value of Gibbs energy of reaction at 1123 K

$$\Delta_r G_{1123}^0 = \Delta_r H_{1123}^0 - T\Delta_r S_{1123}^0 \quad \text{(II.74)}$$

$$\Delta_r G_{1123}^0 = -33827.5\ J\ mol^{-1} - (1123K * (-30.193\ J\ mol^{-1}\ K^{-1})) \quad \text{(II.75)}$$

$$\Delta_r G_{1123}^0 = 1034.4\ J\ mol^{-1} \quad or \quad 1.034\ kJ\ mol^{-1} \quad \text{(II.76)}$$

II.15. Thermodynamic calculations for various reactions that involve H_2S and S_2O in different perovskite

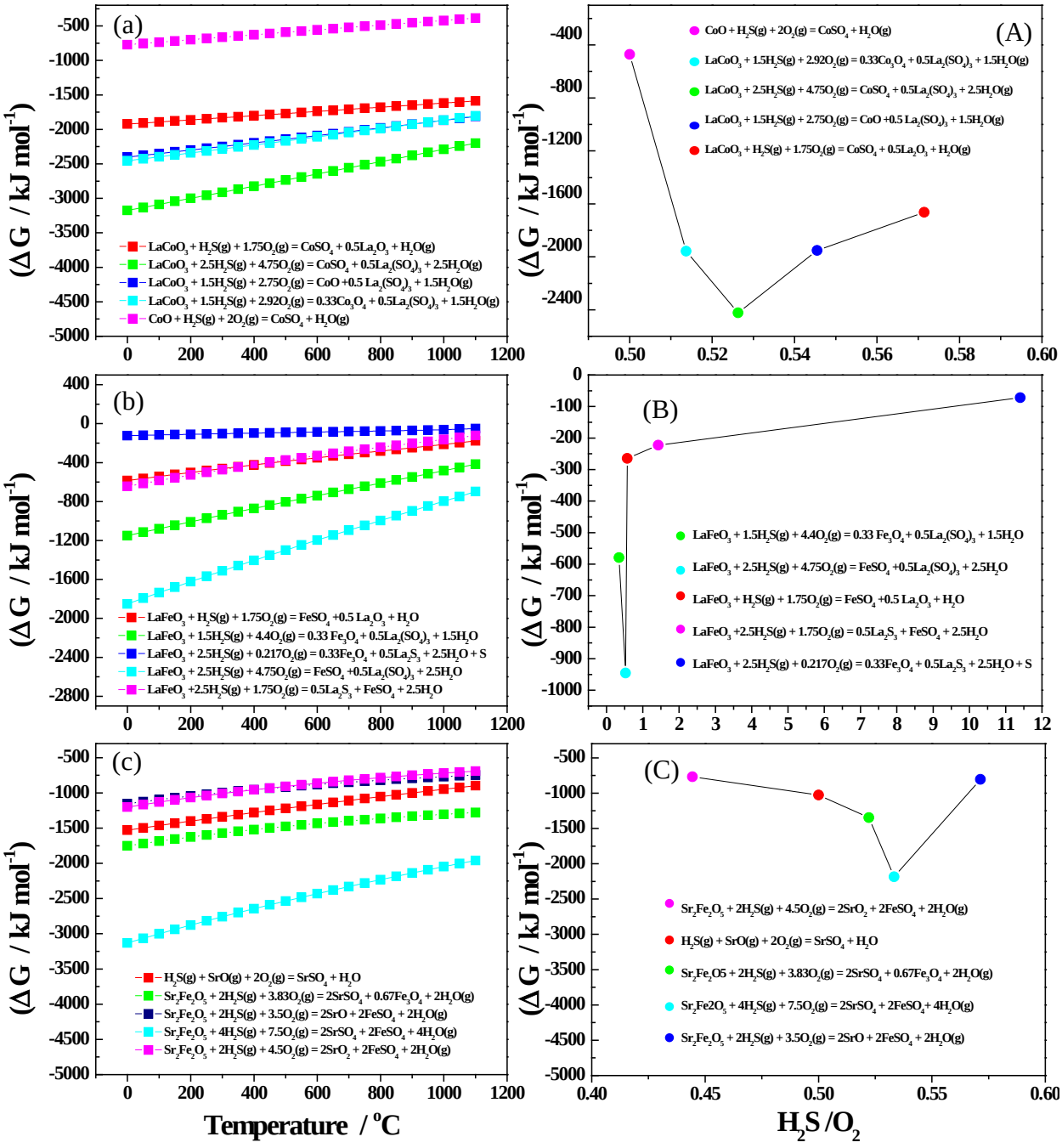

Figure II.25 Dependence of standard Gibbs free energy with temperature for H_2S as sulphurisation agent of different perovskites.

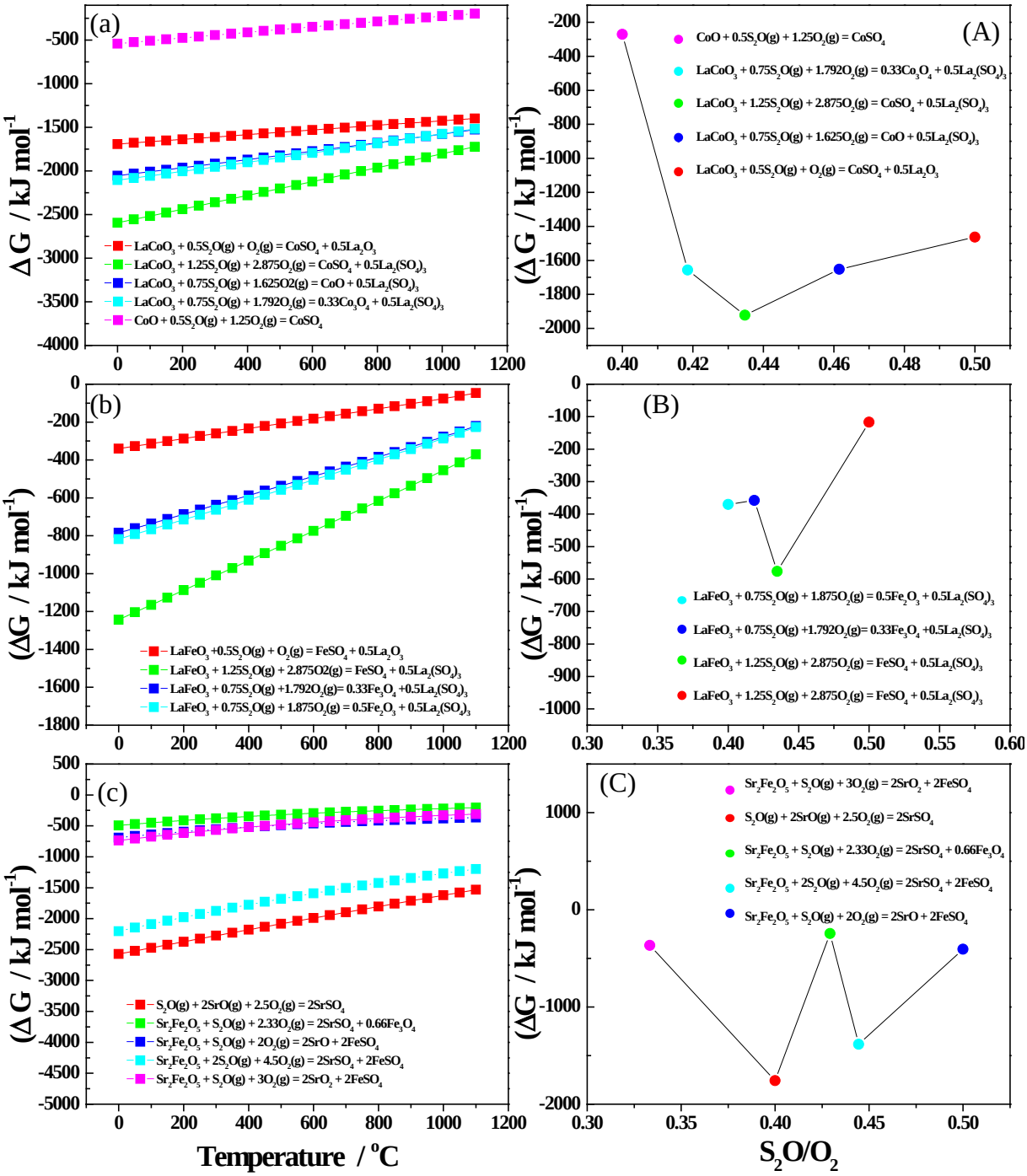

Figure II.26 Dependence of standard Gibbs free energy with temperature for S_2O as sulphurisation agent of different perovskites.

II.16 Reference

[1] J. Leitner, P. Chuchvalec, D. Sedmidubsky, A. Strejc and P. Abrman, Thermochimica Acta, **2003**, 395, 27.

Appendix III

III.1. Distribution of the total permeation resistance of Co_3O_4/LSCF6428-HFM reactor using eqns. (4.1),(4.2), (4.3) and (4.4) in the Chapter 5.

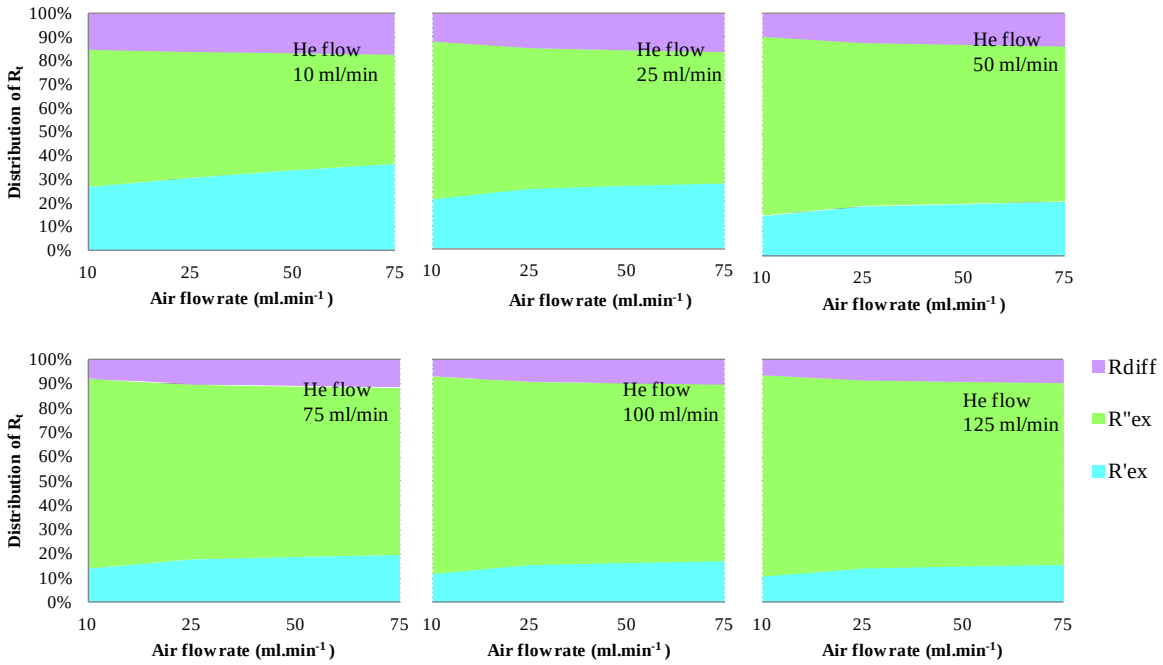

Figure III.1 Effect of the air flow on distribution of the total permeation resistance of Co_3O_4/LSCF6428-HFM reactor at 850°C.

III.2. XRD method using Scherrer equation for determining the crystallite size of Co_3O_4/LSCF6428-HFM

Table.III.1 Crystal size determined by Scherrer equation for Co_3O_4/LSCF6428-HFM

Membrane side	Condition	2θ	Crystal size (um)	Crystal size (nm)
Lumen	BR	32.64	0.022	22.0
Shell	BR	32.68	0.023	23.3
Centre lumen	AR	32.56	0.022	22.2
Centre shell	AR	32.63	0.026	25.8
End lumen	AR	32.73	0.022	21.5
End shell	AR	32.87	0.026	25.7

III.3. Distribution of the grain boundary perimeter of Co_3O_4/LSCF6428-HFM using SPIP 6.0.9 software, data showed in Chapter 5.

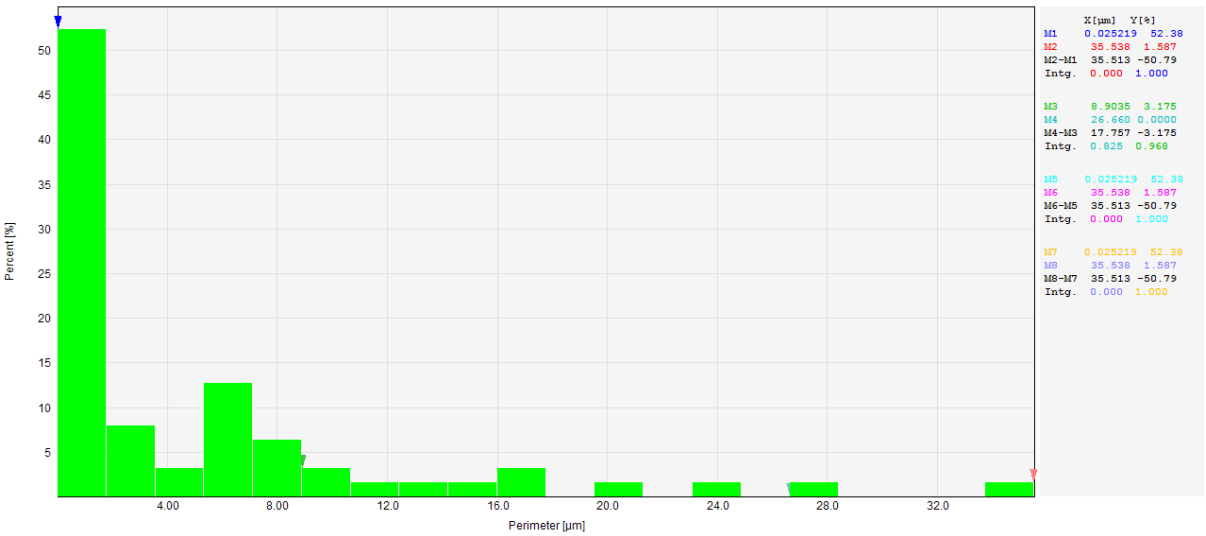

Figure III.2 Distribution of the grain boundary perimeter of LSCF6428-HFM lumen side before reaction, data obtained by SPIP 6.0.9

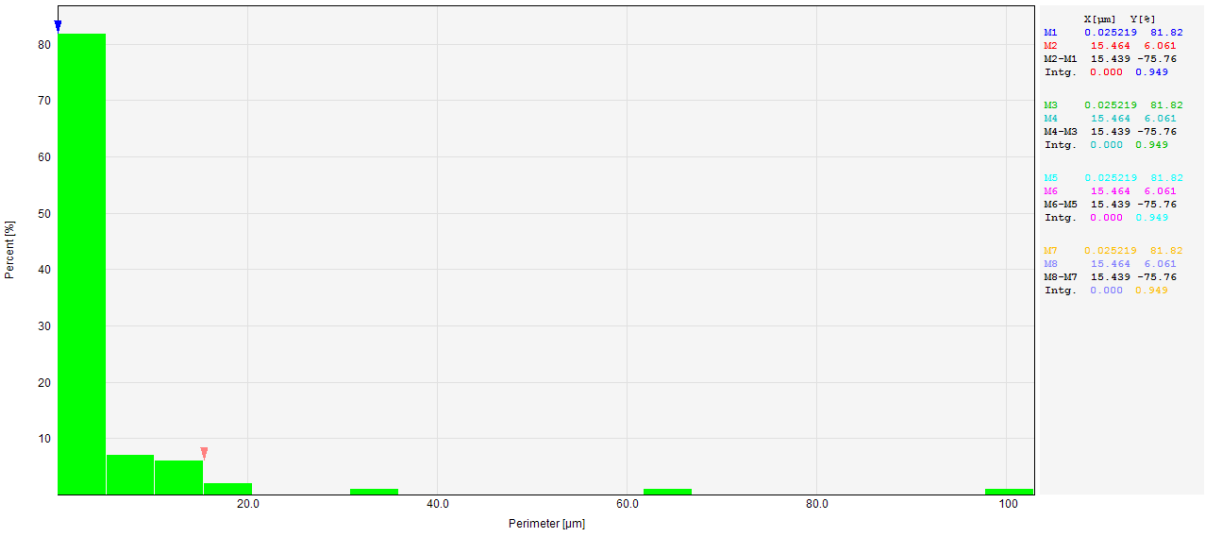

Figure III.3 Distribution of the grain boundary perimeter of LSCF6428-HFM shell side before reaction, data obtained by SPIP 6.0.9

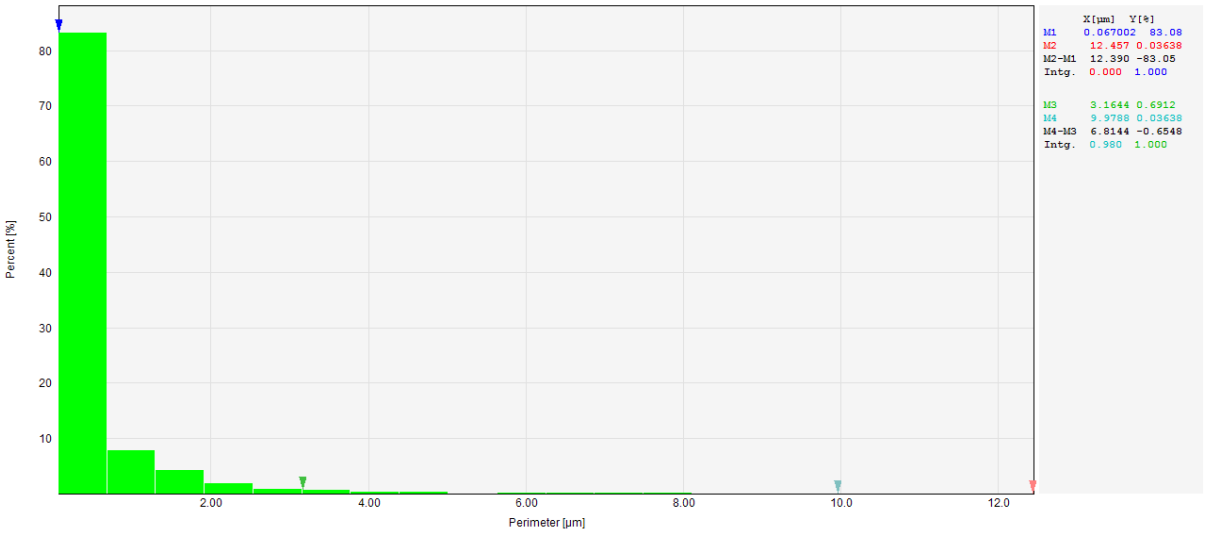

Figure III.4 Distribution of the particle perimeter of Co_3O_4 catalyst before reaction, data obtained by SPIP 6.0.9

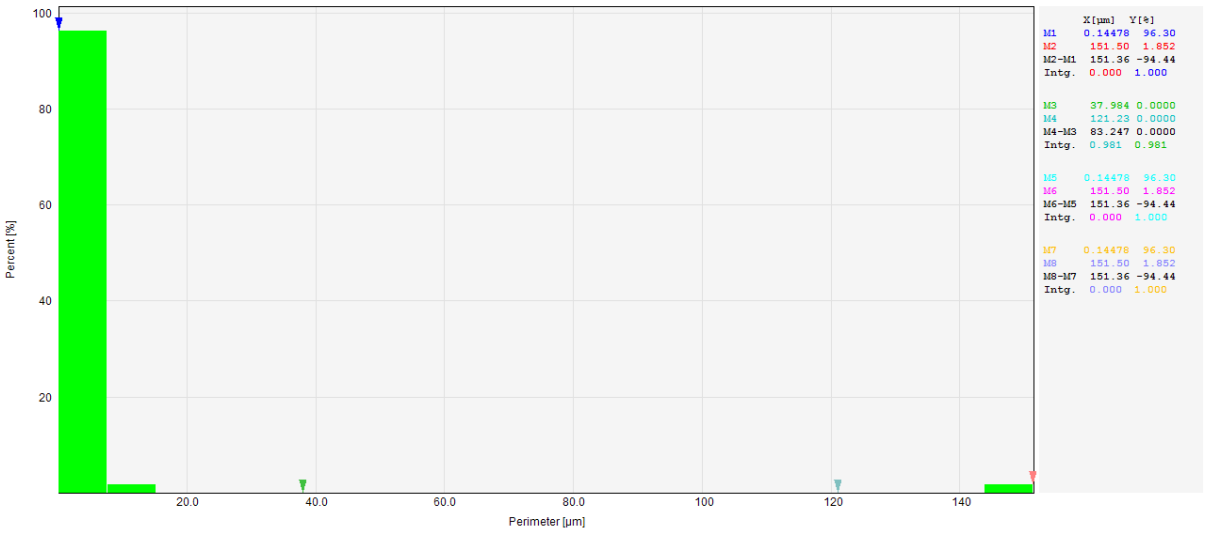

Figure III.5 Distribution of the particle perimeter of Co_3O_4 catalyst after reaction, data obtained by SPIP 6.0.9

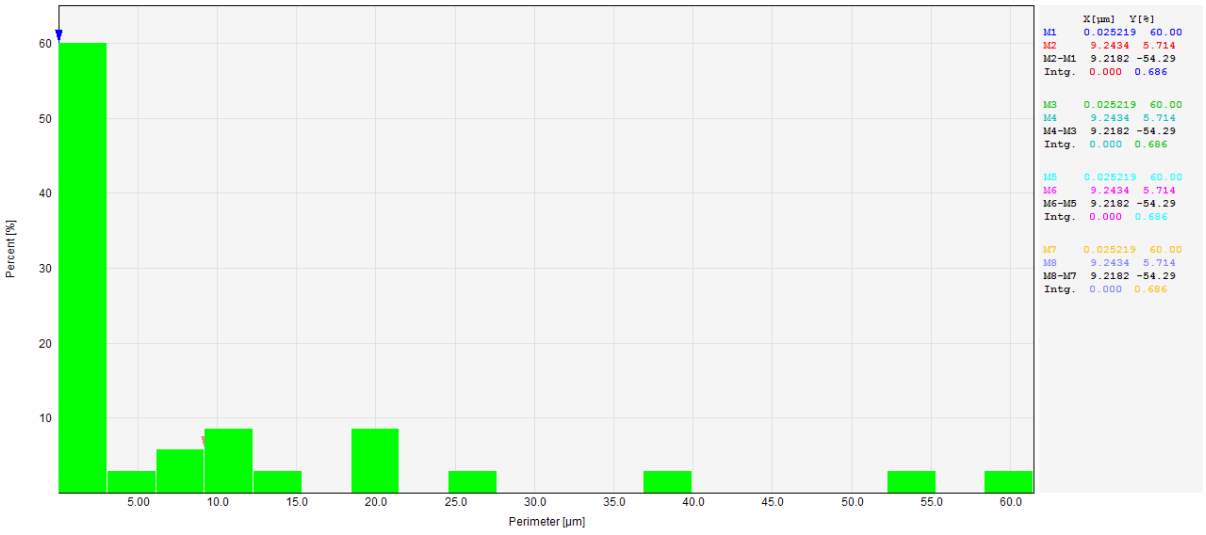

Figure III.6 Distribution of the grain boundary perimeter of Co_3O_4/LSCF6428-HFM centre lumen side after reaction, data obtained by SPIP 6.0.9

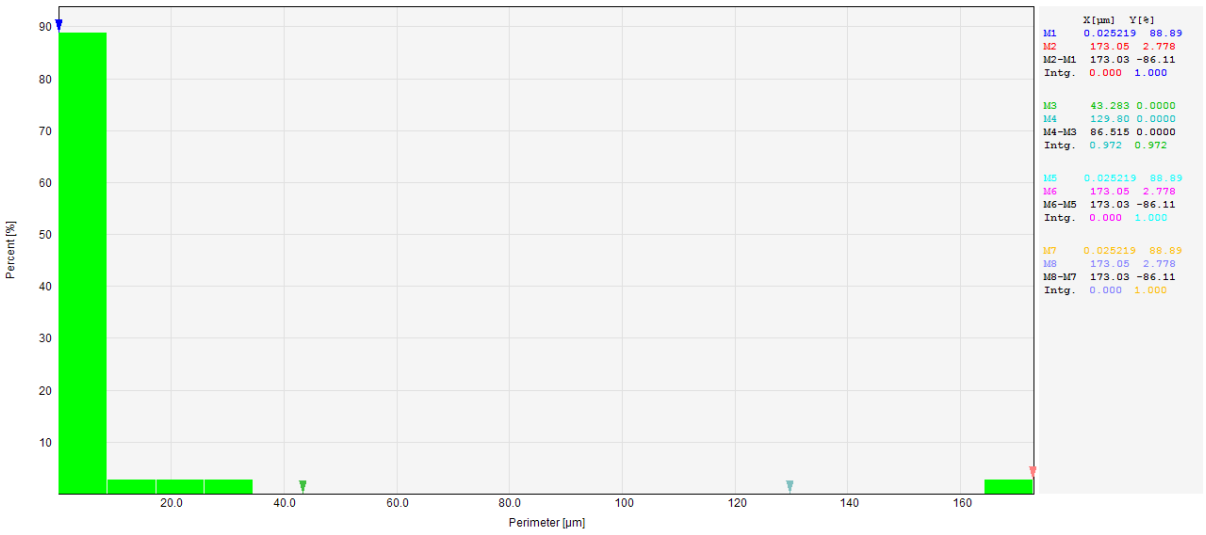

Figure III.7 Distribution of the grain boundary perimeter of Co_3O_4/LSCF6428-HFM end lumen side after reaction, data obtained by SPIP 6.0.9

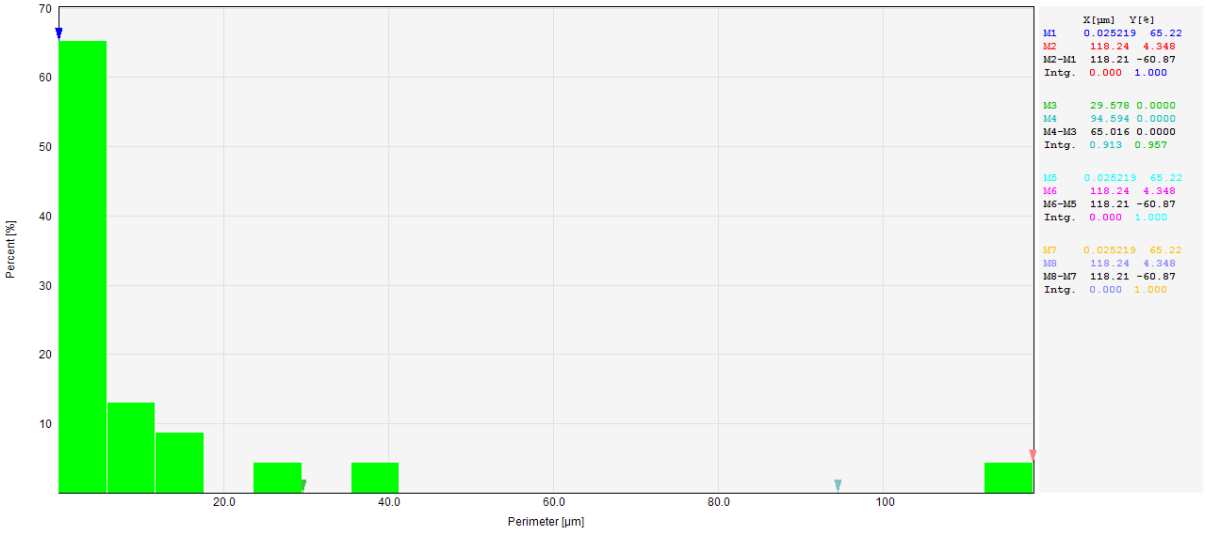

Figure III.8 Distribution of the grain boundary perimeter of Co_3O_4/LSCF6428-HFM end shell side after reaction, data obtained by SPIP 6.0.9

III.4. EDXS results of the Co_3O_4/LSCF6428-HFM reactor before and after reaction, data described in Chapter 5

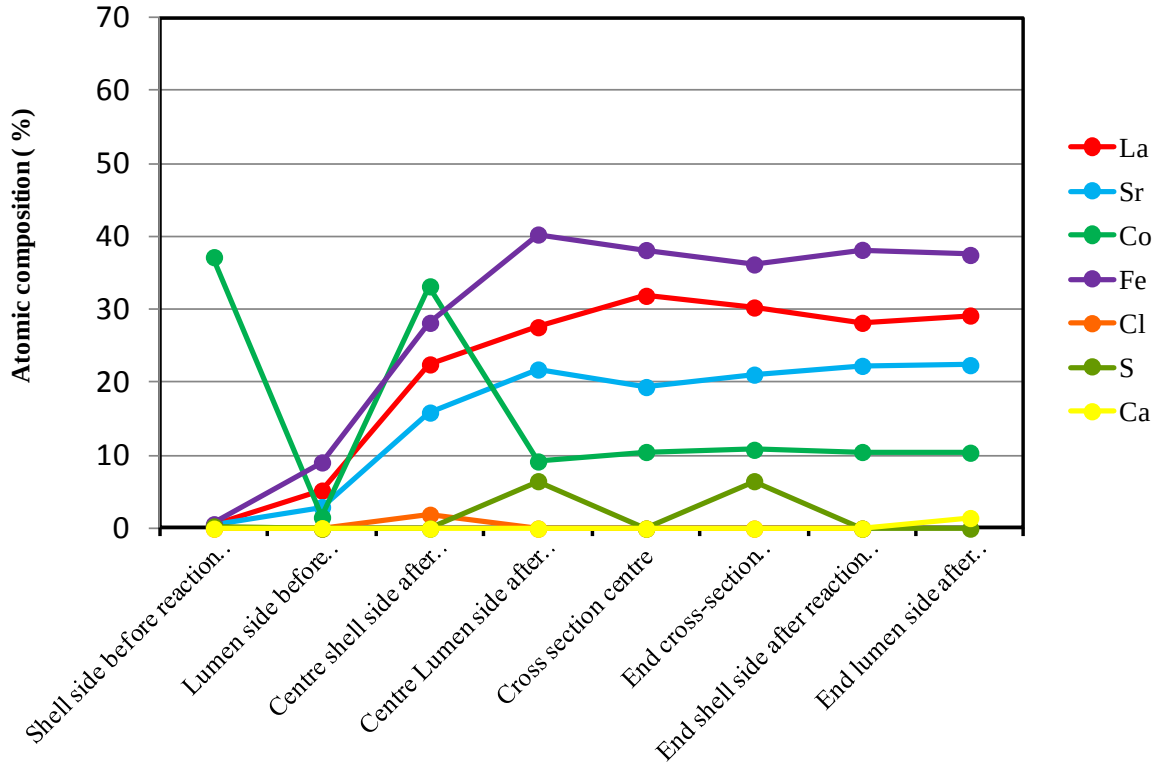

Figure III.9 EDXS results of the different zones of the Co_3O_4/LSCF6428-HFM before and after oxygen permeation measurements

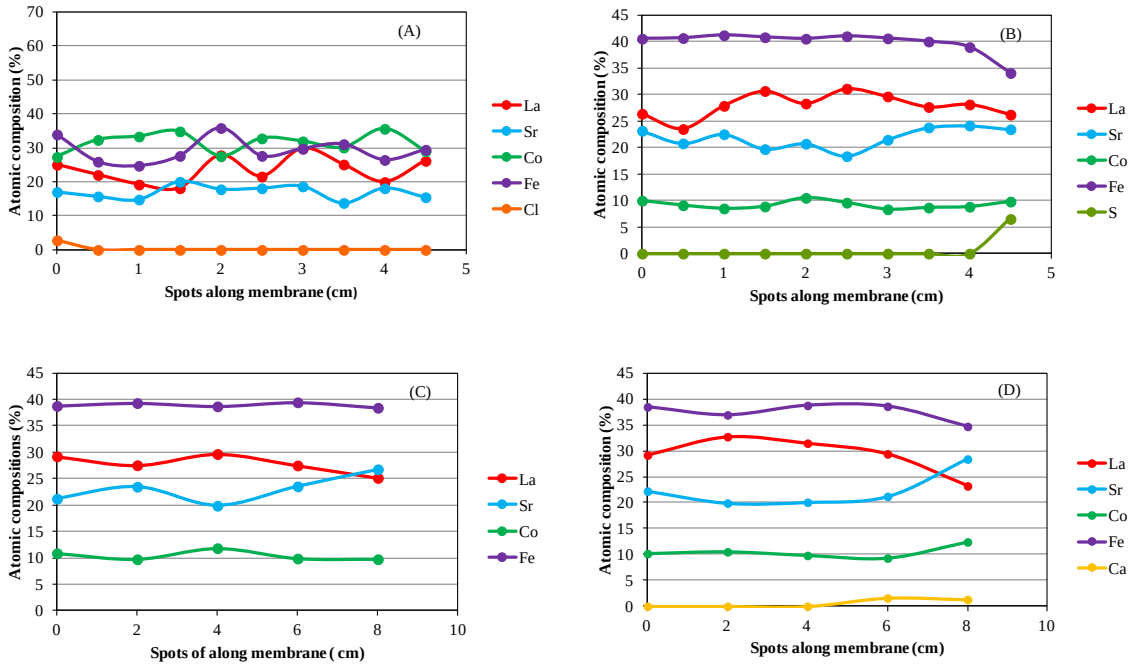

Figure III.10 EDXS results of the different zones of the Co_3O_4/LSCF6428-HFM after oxygen permeation measurements. Centre shell side (A), centre lumen side (B), end shell side (C) and end lumen side (D).

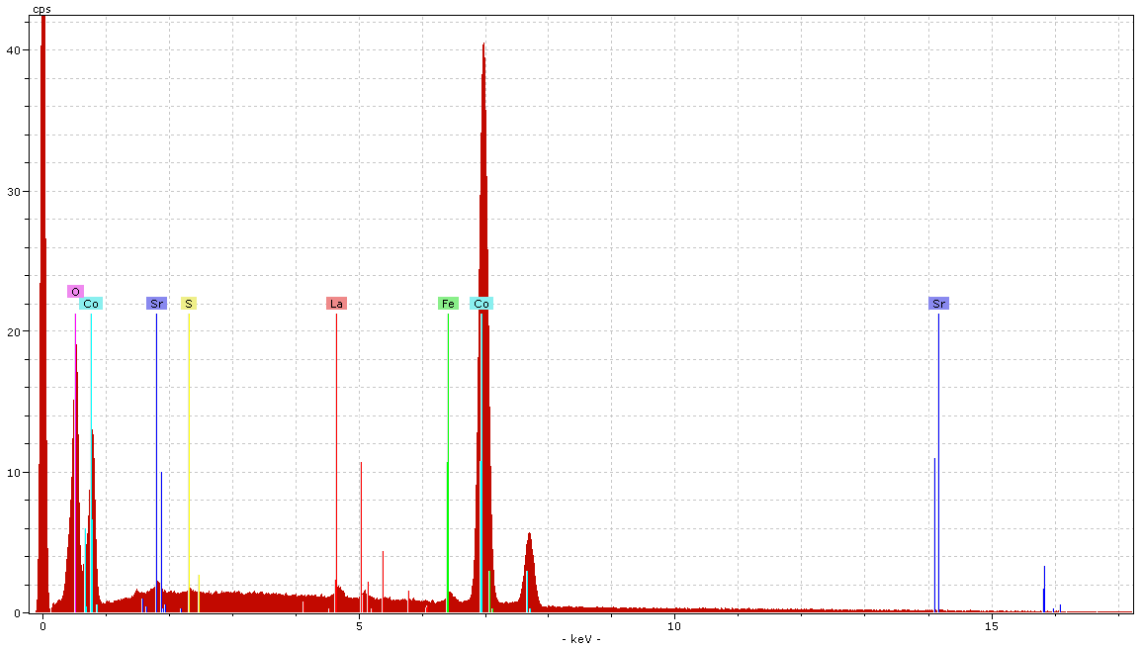

Figure III.11 EDXS profile of the Co_3O_4/LSCF6428-HFM shell side before reaction

Table II.2 EDXS results of the Co_3O_4/LSCF6428-HFM shell side before reaction

Element	norm. C [wt.-%]	Atom. C [at.-%]
Lanthanum	1.82	0.43
Iron	1.01	0.60
Strontium	0.98	0.37
Cobalt	66.29	37.16
Oxygen	29.61	61.14
Sulfur	0.29	0.30

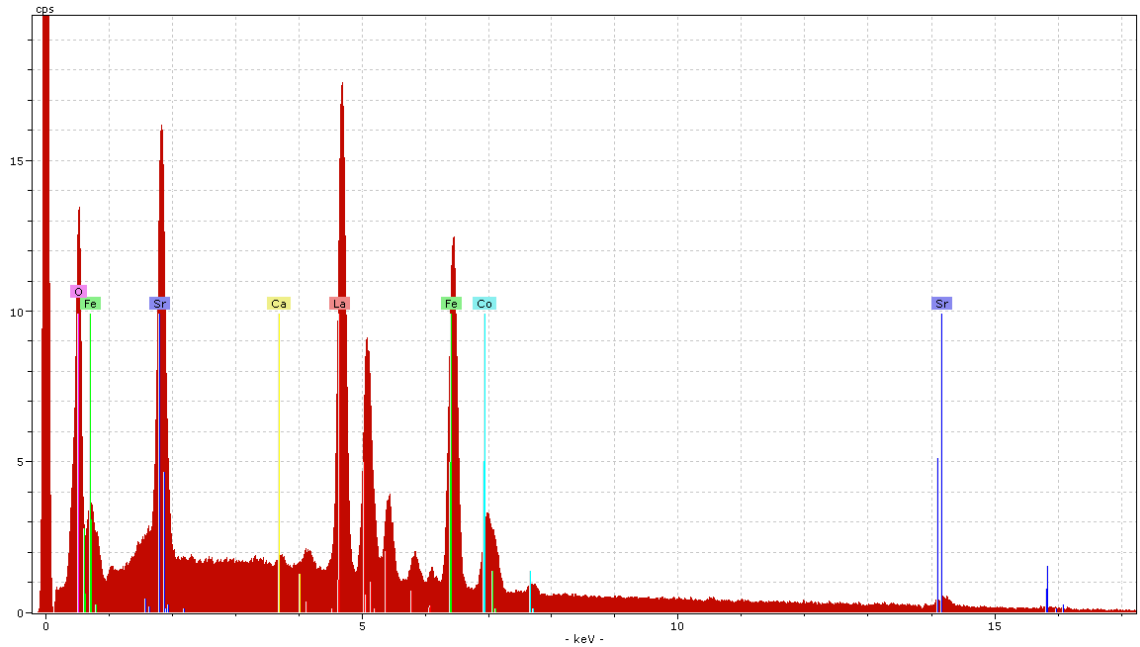

Figure III.12 EDXS profile of the Co_3O_4/LSCF6428-HFM lumen side before reaction

Table II.3 EDXS results of the Co_3O_4/LSCF6428-HFM lumen side before reaction

Element	norm. C [wt.-%]	Atom. C [at.-%]
Lanthanum	27.33	5.21
Iron	17.14	9.07
Strontium	8.74	2.95
Cobalt	3.09	1.55
Oxygen	43.62	80.56
Calcium	0.08	0.06

Table III.4 EDXS results of the centre cross section of Co_3O_4/LSCF6428-HFM reactor after oxygen permeation.

			Absolute atomic %			
Points	***Position***		***La***	***Sr***	***Co***	***Fe***
	cm	μm				
1	0	0	33.0	17.1	10.1	39.7
2	0.5	29	28.4	21.7	10.2	39.7
3	1	59	29.7	20.1	11.1	39.1
4	1.5	88	39.5	12.4	8.8	39.4
5	2	118	39.1	23.5	9.5	28.0
6	2.5	147	35.1	15.5	14.9	34.4
7	3	176	32.9	15.2	11.4	40.4
8	3.5	206	29.4	21.5	8.9	40.2
9	4	235	26.1	17.5	18.5	37.8
10	4.5	265	33.7	19.3	8.2	38.8
11	5	294	28.6	22.6	9.1	39.8
12	5.5	324	31.8	19.5	8.5	40.2
13	6	353	27.5	26.7	7.4	38.4

Table III.5 EDXS results of the end cross section of Co_3O_4/LSCF6428-HFM reactor after oxygen permeation.

			Absolute atomic %				
Points	***Position***		***La***	***Sr***	***Co***	***Fe***	***others***
	cm	μm					
1	0	0	28.4	24.0	9.2	37.8	
2	0.5	29	33.9	18.1	9.4	38.6	
3	1	59	22.9	30.8	10.5	38.7	
4	1.5	88	33.1	14.9	12.5	39.9	
5	2	118	36.7	19.6	11.3	35.4	
6	2.5	147	35.4	13.8	11.2	39.6	
7	3	176	26.1	27.0	10.0	36.9	
8	3.5	206	27.5	18.1	10.6	38.8	
9	4	235	27.5	21.1	8.9	42.5	
10	4.5	265	26.9	23.3	7.6	35.7	6.5S
11	5	294	35.8	26.1	9.4	36.7	
12	5.5	324	34.4	14.2	11.3	38.4	
13	6	353	24.9	23.7	7.5	35.7	

Table III.6 EDXS results of the end lumen side of Co_3O_4/LSCF6428-HFM reactor after oxygen permeation.

	Absolute atomic %				
Points	***La***	***Sr***	***Co***	***Fe***	***Other***
1	29.2	22.2	10.2	38.5	
2	32.7	19.9	10.5	36.9	
3	31.5	20.1	9.8	38.7	
4	29.4	21.2	9.3	38.6	1.6Ca
5	23.2	28.4	12.4	34.7	1.3Ca

Table III.7 EDXS results of the end shell side of Co_3O_4/LSCF6428-HFM reactor after oxygen permeation.

	Absolute atomic %				
Points	***La***	***Sr***	***Co***	***Fe***	***Other***
1	29.2	21.2	10.9	38.8	
2	27.5	23.5	9.7	39.3	
3	29.7	19.9	11.8	38.7	
4	27.5	23.5	9.6	39.4	
5	27.1	23.8	9.7	38.4	

Appendix IV

IV.1. Distribution of the total permeation resistance of 5%Ni-LSCF6428/LSCF6428-HFM reactor, data obtained using eqns (4.)1, (4.2), (4.3) and (4.4) in Chapter 5

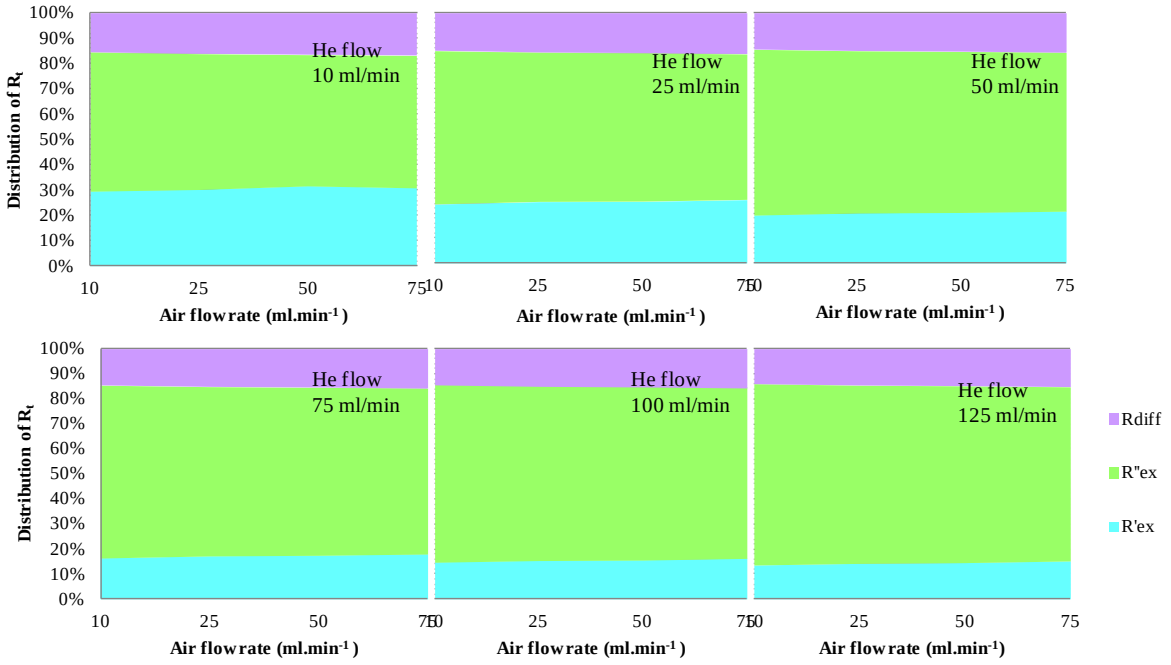

Figure IV.1 Effect of air flow on the distribution of the total permeation resistance of 5%Ni-LSCF6428/LSCF6428-HFM reactor at 850°C.

IV.2. XRD method using Scherrer equation for determining the crystallite size of 5%Ni-LSCF6428/LSCF6428-HFM, data discussed in Chapter 5.

Table. IV.1 Crystal size determined by Scherrer equation of 5%Ni-LSCF6428/LSCF6428-HFM

Membrane zone	Condition	2θ	Crystal size (um)	Crystal size (nm)
Lumen side	BR	32.54	0.026	26.2
Shell side	BR	32.68	0.025	24.7
Centre lumen side	BR	32.44	0.026	25.6
Centre shell side	BR	32.34	0.032	31.8

IV.3. Distribution of the particle and grain boundary perimeter of 5%Ni-LSCF6428/LSCF6428-HFM using SPIP 6.0.9 software, data showed in Chapter 5

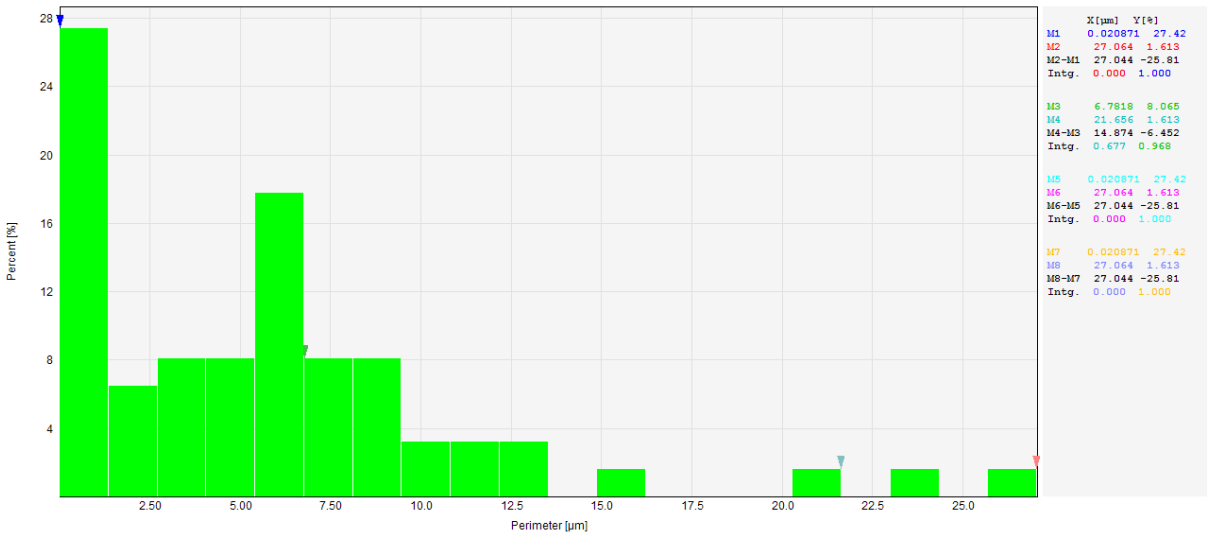

Figure IV.2 Distribution of the grain boundary perimeter of 5%Ni-LSCF6428-HFM lumen side before reaction, data obtained by SPIP 6.0.9

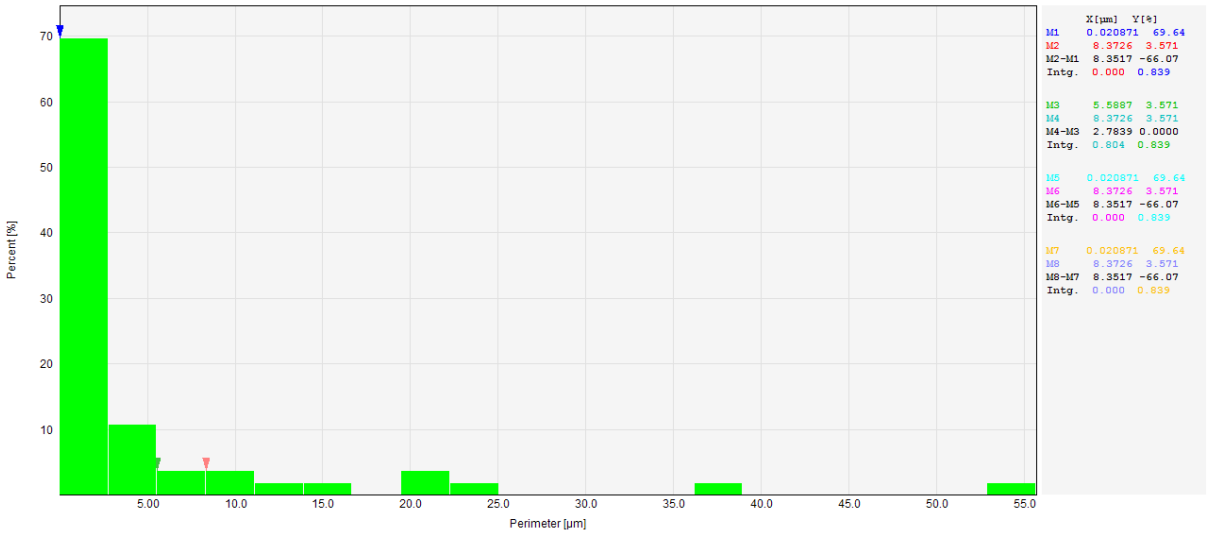

Figure IV.3 Distribution of the grain boundary perimeter of 5%Ni-LSCF6428-HFM shell side before reaction, data obtained by SPIP 6.0.9

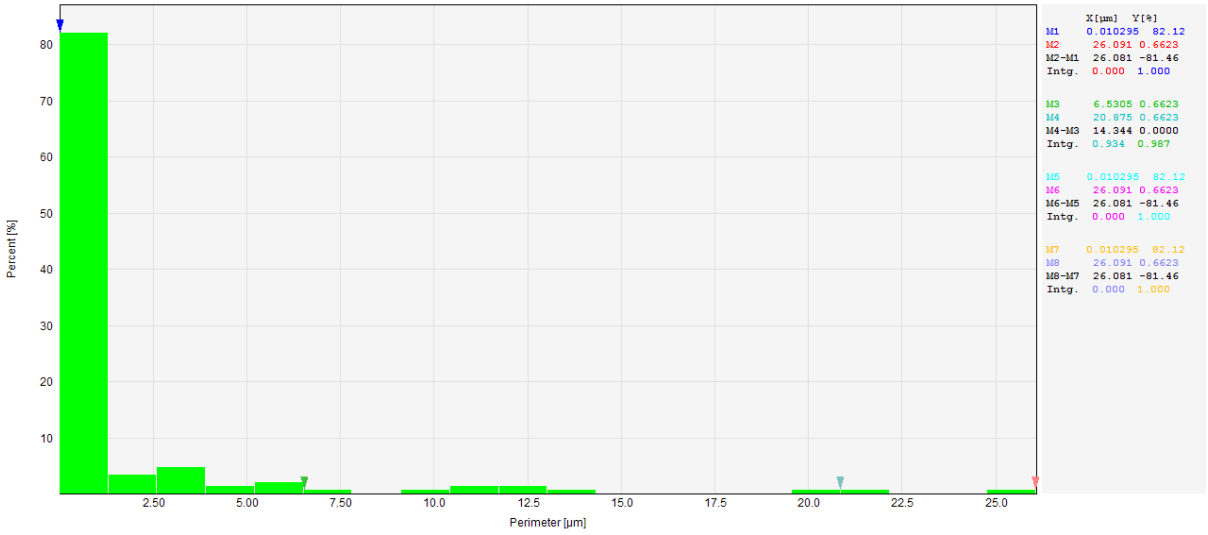

Figure IV.4 Distribution of the particle of 5%Ni-LSCF6428-HFM catalyst before reaction, data obtained by SPIP 6.0.9

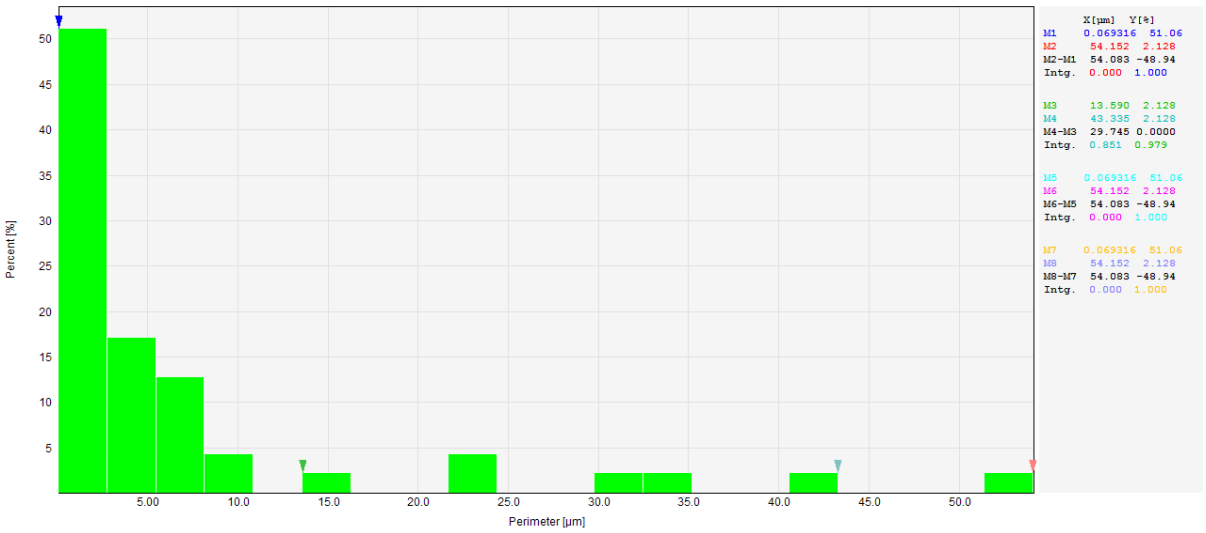

Figure IV.5 Distribution of the grain boundary perimeter of 5%Ni-LSCF6428-HFM centre lumen side after reaction, data obtained by SPIP 6.0.9

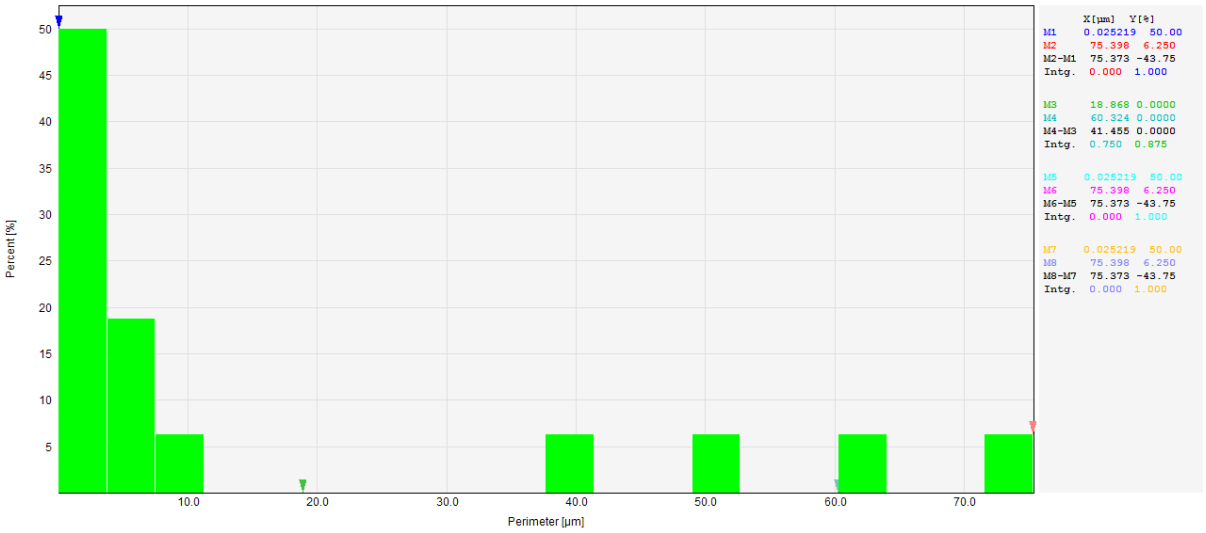

Figure IV.6 Distribution of the grain boundary perimeter of 5%Ni-LSCF6428-HFM end lumen side after reaction, data obtained by SPIP 6.0.9

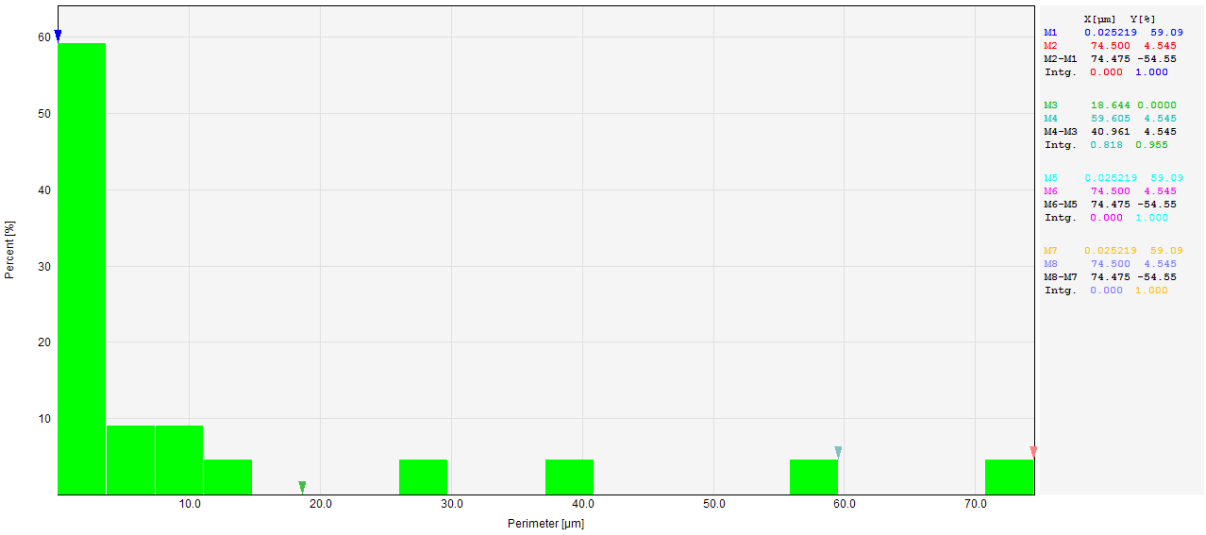

Figure IV.7 Distribution of the grain boundary perimeter of 5%Ni-LSCF6428-HFM end shell side after reaction, data obtained by SPIP 6.0.9

IV.4. EDXS results of the 5%Ni-LSCF6428-LSCF6428-HFM before and after oxygen flux, data discussed in Chapter 5

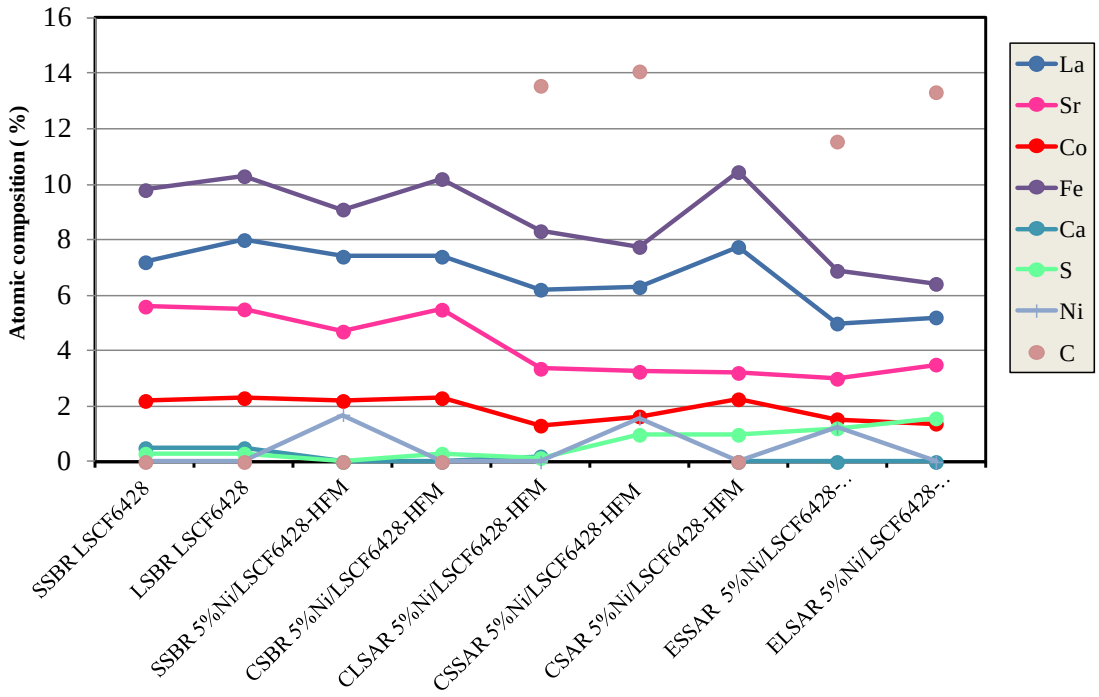

Figure IV.8 Comparison of the EDXS results between LSCF6428-HFM and 5%Ni/LSCF6428-HFM in different zones of the membrane before and after oxygen flux measurements.

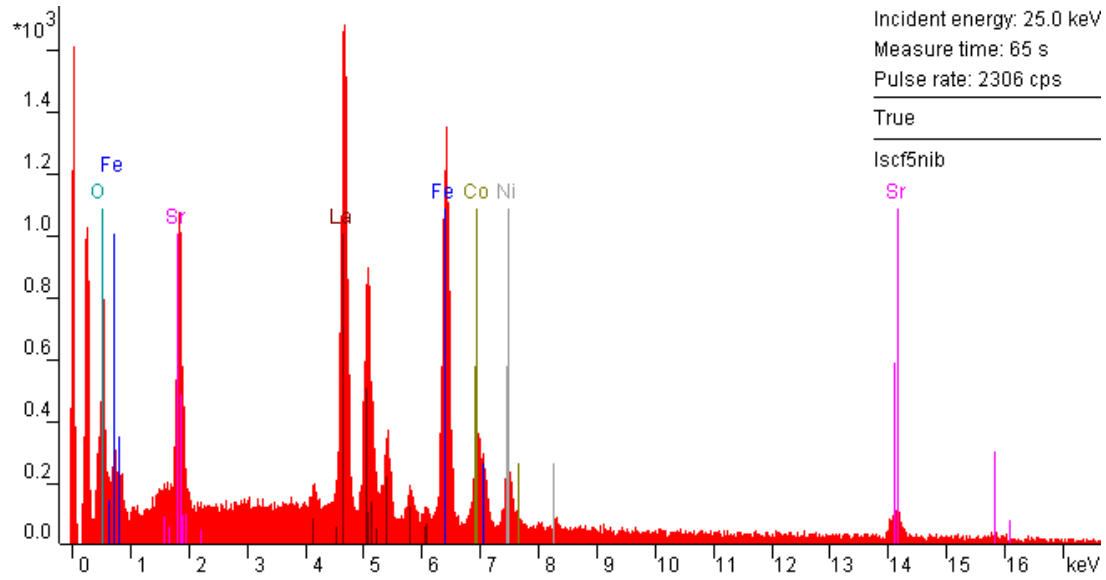

Figure IV.9 EDXS profile of the 5%Ni-LSCF6428/LSCF6428-HFM shell side before reaction

Table IV.2 EDXS results of the 5%Ni-LSCF6428/LSCF6428-HFM shell side before reaction

elem/line	P/B	B	F	c(atom)	confid. h
O K-ser	@	1.00000	1.00000	74.92	+-13.47
La L-ser	@192.3	1.03952	1.05193	7.40	+- 0.84
Fe K-alpha	@117.0	1.04817	1.04488	9.09	+- 1.21
Co K-alpha	@ 29.2	1.05031	1.04876	2.24	+- 0.54
Ni K-alpha	@ 22.1	1.05237	1.05607	1.69	+- 0.55
Sr L-ser	46.6	1.01392	1.01496	4.66	+- 0.83
standardless				100.00	[2s]

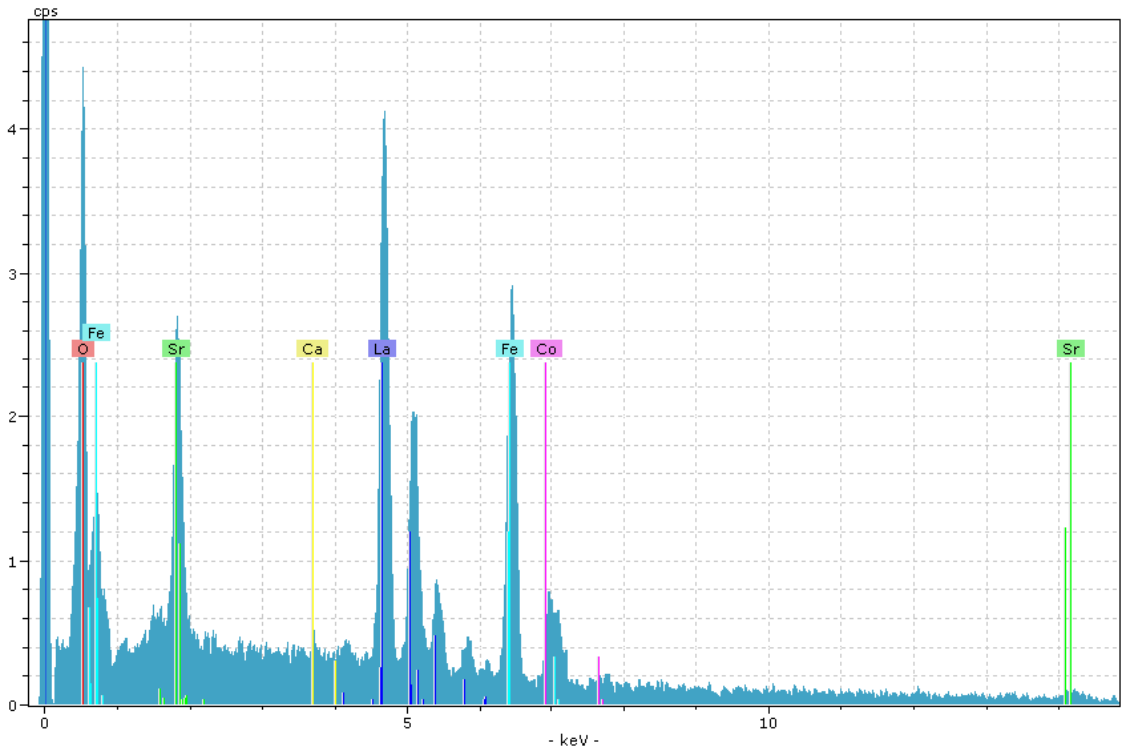

Figure IV.10 EDXS profile of the 5%Ni-LSCF6428/LSCF6428-HFM lumen side before reaction

Table IV.3 EDXS results of the 5%Ni-LSCF6428/LSCF6428-HFM lumen side before reaction

```
------------------------------------------------------------------
*** PUzaf results ***
elem/line____P/B_____B_______F_____________c(atom)__confid._h_
O  K-ser   @       1.00000 1.00000            73.09  +-13.46
La L-ser   @192.3  1.03952 1.05193             8.00  +- 0.85
Fe K-alpha @117.0  1.04817 1.04488            10.30  +- 1.20
Co K-alpha @ 29.2  1.05031 1.04876             2.30  +- 0.53
Sr L-ser     46.6  1.01392 1.01496             5.52  +- 0.84
S  K-ser   @182.3  1.02109 1.00659            .0.31  +- 3.93
Ca K-alpha @  1.9  1.03186 1.08325             0.48  +- 0.16
------------------------------------------------------------------
standardless                                100.00     [2s]
```

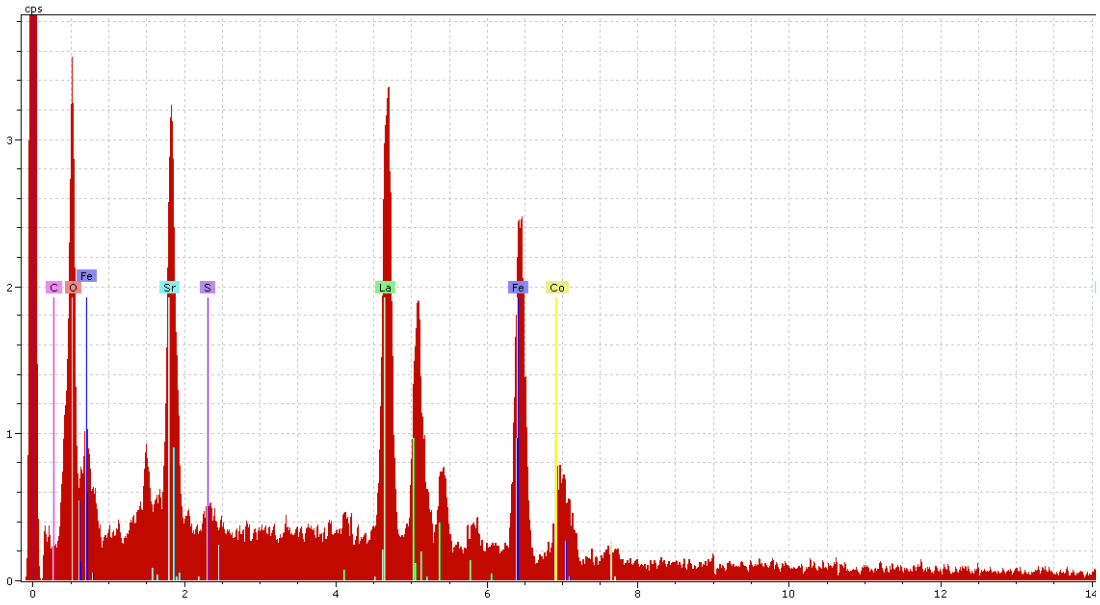

Figure IV.11 EDXS profile of the cross section of 5%Ni-LSCF6428/LSCF6428-HFM before reaction

Table IV.4 EDXS results of the cross section of 5%Ni-LSCF6428/LSCF6428-HFM before reaction

```
------------------------------------------------------------------
*** PUzaf results ***
elem/line____P/B______B_______F_________________c(atom)__confid._h_
O  K-ser   @       1.00000 1.00000               72.82  +-15.47
La L-ser   @192.3  1.03952 1.05193                7.40  +- 1.84
Fe K-alpha @117.0  1.04817 1.04488               10.16  +- 1.41
Co K-alpha @ 29.2  1.05031 1.04876                2.30  +- 0.64
Sr L-ser     46.6  1.01392 1.01496                5.49  +- 1.73
S  K-ser   @182.3  1.02109 1.00659               .0.30  +- 3.82
------------------------------------------------------------------
standardless                                    100.00     [2s]
```

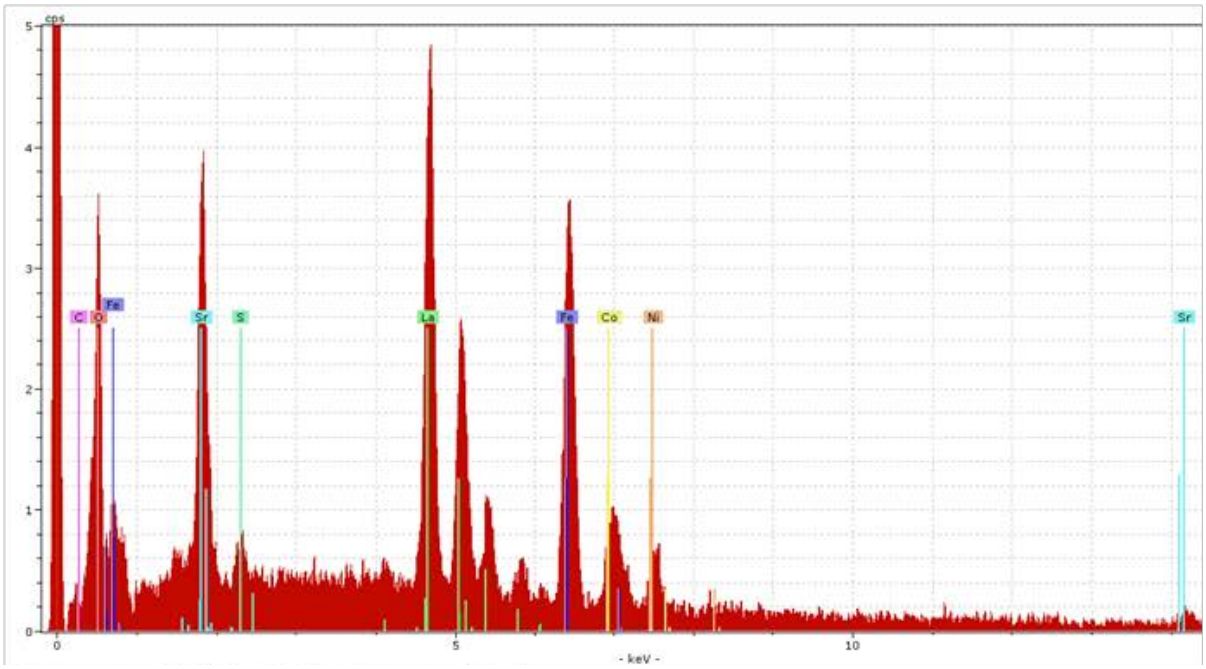

Figure IV.12 EDXS profile of the 5%Ni-LSCF6428/LSCF6428-HFM centre shell side after reaction

Table IV.5 EDXS results of the centre shell side of 5%Ni-LSCF6428/LSCF6428-HFM after reaction

*** PUzaf results ***						
elem/line		P/B	B	F	c(atom)	confid._h_
O K-ser	@		1.00000	1.00000	64.43	+-13.93
La L-ser	@	192.3	1.03952	1.05193	6.29	+- 0.74
Fe K-alpha	@	117.0	1.04817	1.04488	7.75	+- 1.20
Co K-alpha	@	29.2	1.05031	1.04876	1.64	+- 0.54
Sr L-ser	@	46.6	1.01392	1.01496	3.25	+- 0.92
S K-ser	@	182.3	1.02109	1.00659	0.98	+- 3.90
Ni K-alpha	@	22.1	1.05237	1.05607	1.57	+- 0.54
C K-ser	@	22.3	1.00929	1.01390	14.08	+- 2.16
standardless					100.00	[2s]

Table IV.6 EDXS results of the centre lumen side of 5%Ni-LSCF6428/LSCF6428-HFM after reaction

*** PUzaf results ***						
elem/line		P/B	B	F	c(atom)	confid._h_
O K-ser	@		1.00000	1.00000	68.92	+-11.20
La L-ser	@	192.3	1.03952	1.05193	5.21	+- 1.96
Fe K-alpha	@	117.0	1.04817	1.04488	8.32	+- 1.18
Co K-alpha	@	29.2	1.05031	1.04876	1.31	+- 0.72
Sr L-ser	@	46.6	1.01392	1.01496	3.36	+- 2.17
S K-ser	@	182.3	1.02109	1.00659	0.14	+- 3.92
C K-ser	@	22.3	1.00929	1.01390	13.56	+- 2.20
Ca K-alpha	@	1.9	1.03186	1.08325	0.48	+- 0.16
standardless					100.00	[2s]

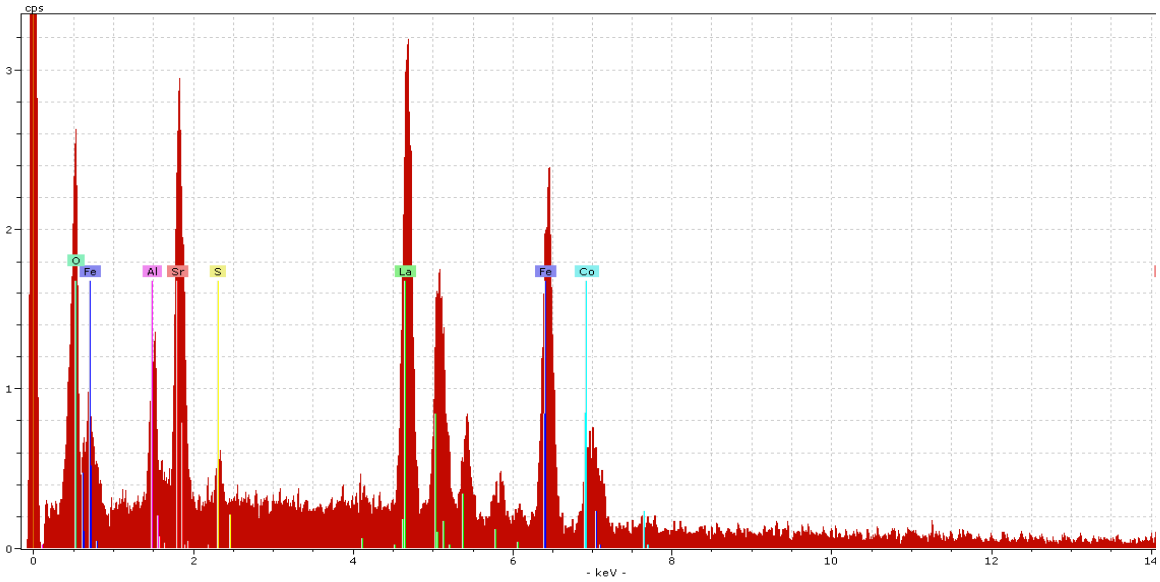

Figure IV.13 EDXS profile of the cross section of 5%Ni-LSCF6428/LSCF6428-HFM after reaction

Table IV.7 EDXS results of cross section of the 5%Ni-LSCF6428/LSCF6428-HFM after reaction

```
------------------------------------------------------------------
*** PUzaf results ***
elem/line____P/B_____B_______F_____________c(atom)__confid._h_
O  K-ser   @       1.00000 1.00000             73.58  +-13.49
La L-ser   @192.3  1.03952 1.05193              7.75  +- 1.84
Fe K-alpha @117.0  1.04817 1.04488             10.45  +- 1.31
Co K-alpha @ 29.2  1.05031 1.04876              2.26  +- 0.64
Sr L-ser     46.6  1.01392 1.01496              3.21  +- 2.83
S  K-ser   @182.3  1.02109 1.00659             .0.98  +- 3.82
Al K-ser   @ 20.4  1.00887 1.02017              1.78  +- 1.33
------------------------------------------------------------------
standardless                                 100.00     [2s]
```

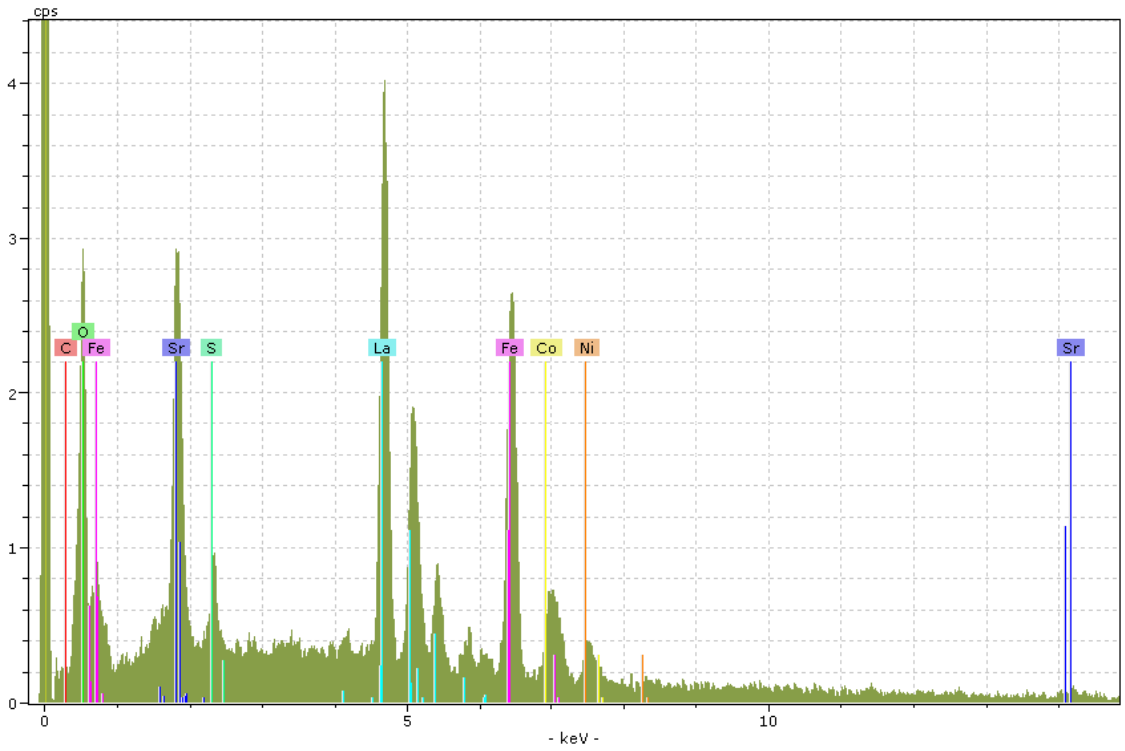

Figure IV.14 EDXS profile of the end shell side of 5%Ni-LSCF6428/LSCF6428-HFM after reaction

Table IV.8 EDXS results of the end shell side of 5%Ni-LSCF6428/LSCF6428-HFM after reaction

elem/line	P/B	B	F	c(atom)	confid._h_
O K-ser	@	1.00000	1.00000	69.56	+-10.50
La L-ser	@ 192.3	1.03952	1.05193	4.99	+- 1.92
Fe K-alpha	@ 117.0	1.04817	1.04488	6.89	+- 1.11
Co K-alpha	@ 29.2	1.05031	1.04876	1.54	+- 0.55
Sr L-ser	@ 46.6	1.01392	1.01496	3.00	+- 2.07
S K-ser	@ 182.3	1.02109	1.00659	1.21	+- 3.92
C K-ser	@ 22.3	1.00929	1.01390	11.55	+- 2.21
Ni K-alpha	@ 22.1..	1.05237.	1.05607	1.24	+- 0.54
standardless				100.00	[2s]

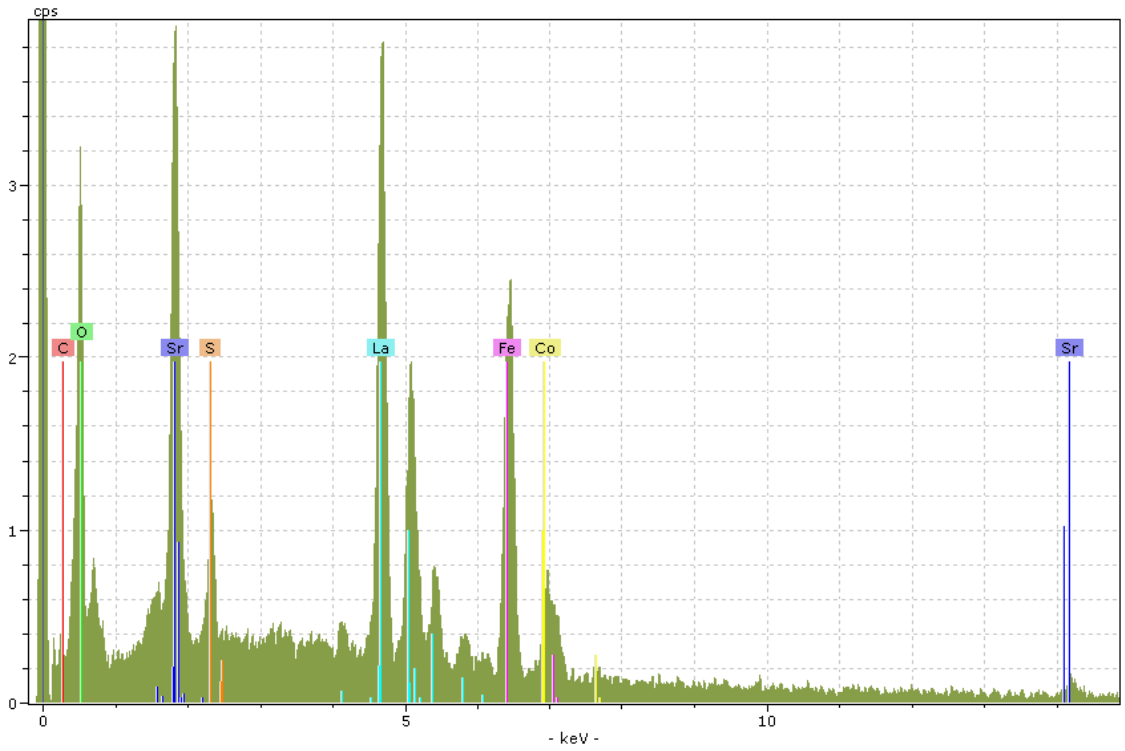

Figure IV.15 EDXS profile of the end lumen side of 5%Ni-LSCF6428/LSCF6428-HFM after reaction

Table IV.9 EDXS results of the end lumen side of 5%Ni-LSCF6428/LSCF6428-HFM after reaction

```
------------------------------------------------------------------
*** PUzaf results ***
elem/line____P/B_____B_____F_____________c(atom)__confid._h_
O  K-ser   @       1.00000 1.00000          68.59  +-13.50
La L-ser   @192.3  1.03952 1.05193           5.21  +- 1.84
Fe K-alpha @117.0  1.04817 1.04488           6.42  +- 1.33
Co K-alpha @ 29.2  1.05031 1.04876           1.38  +- 0.63
Sr L-ser     46.6  1.01392 1.01496           3.51  +- 2.83
S  K-ser   @182.3  1.02109 1.00659          .1.57  +- 3.80
C K-ser    @ 22.3  1.00929 1.01390          13.33  +- 2.21
------------------------------------------------------------------
standardless                                100.00     [2s]
```

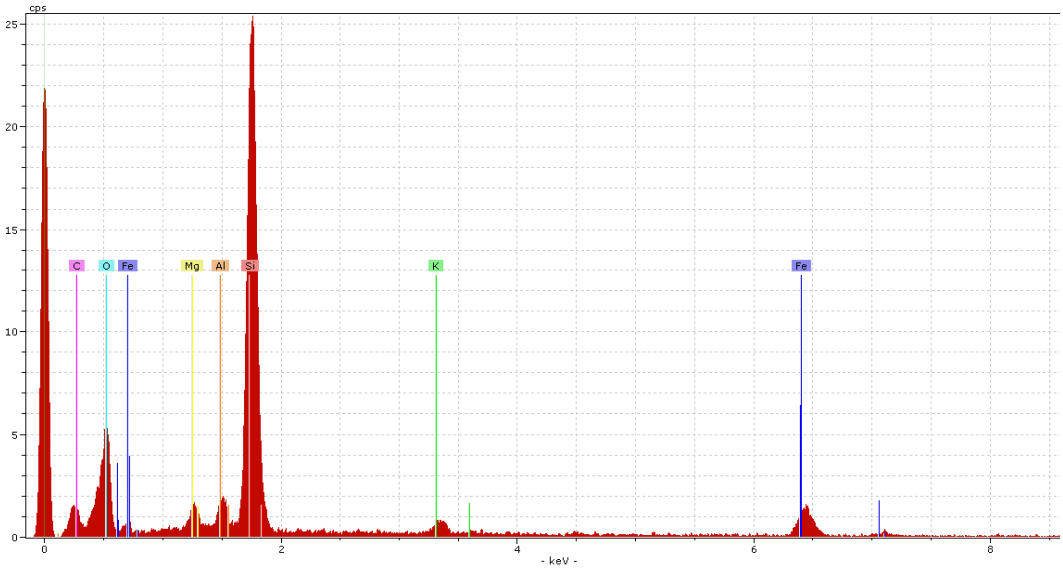

Figure IV.16 EDXS profile of the red sealant for assembling the 5%Ni-LSCF6428/LSCF6428-HFM reactor.

Table IV.10 EDXS results of the red sealant for assembling the 5%Ni-LSCF6428/LSCF6428-HFM reactor.

Element	norm. C [wt.-%]	Atom. C [at.-%]
Silicon	27.35	20.08
Potassium	2.17	1.14
Iron	11.82	4.36
Oxygen	56.13	72.35
Carbon	0.02	0.04
Magnesium	1.23	1.04
Aluminium	1.28	0.98

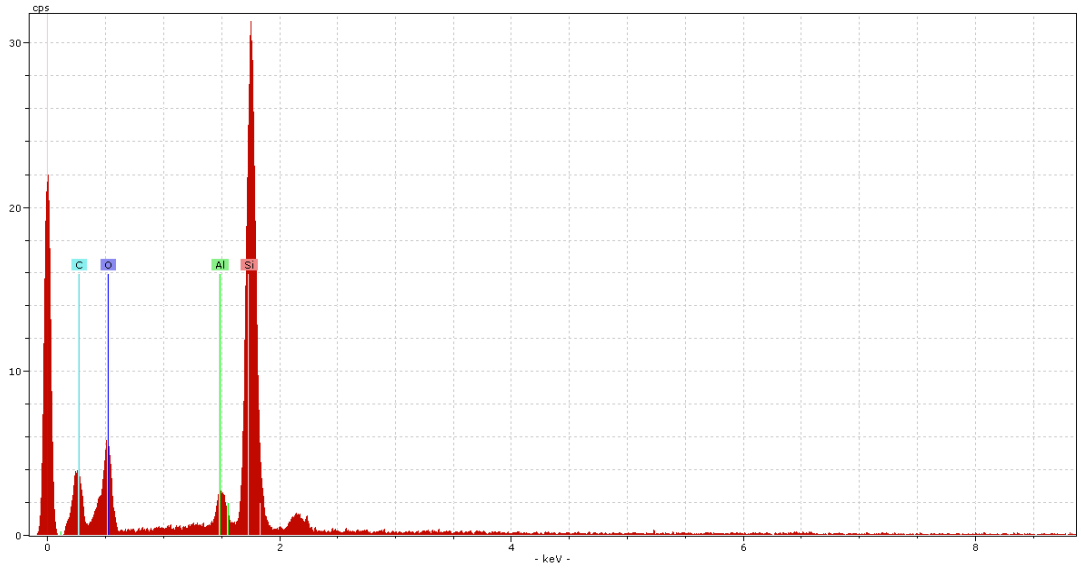

Figure IV.17 EDXS profile of the transparent sealant for assembling the 5%Ni-LSCF6428/LSCF6428-HFM reactor.

Table IV. 11 EDXS results of the transparent sealant for assembling the 5%Ni-LSCF6428/LSCF6428-HFM reactor.

Element	norm. C [wt.-%]	Atom. C [at.-%]
Silicon	15.76	8.89
Aluminium	1.05	0.62
Oxygen	58.51	57.94
Carbon	24.68	32.55

Appendix V

V.1. Carbon balances of the unmodified LSCF6428-HFM under mode 2 of the flow operation obtained after partial oxidation of methane, data showed in Chapter 6

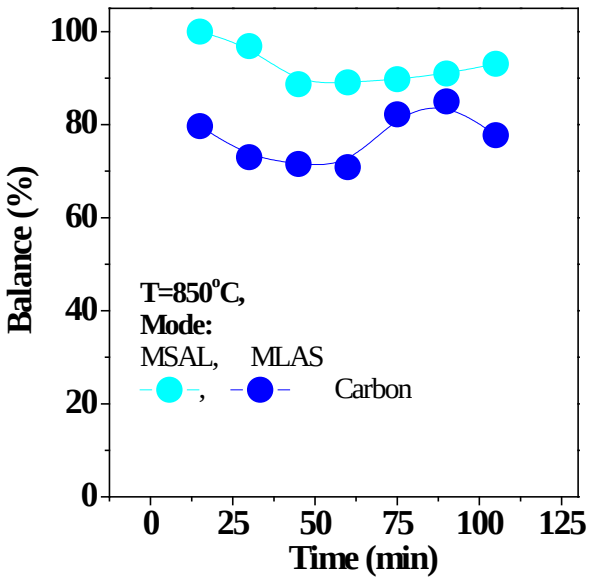

Figure V.1 Comparison of the carbon balances of LSCF6428-HFM without catalyst at two modes of flow operation at 850 °C for POM.

V.2. Distribution of the particle and grain boundary perimeter of unmodified LSCF6428-HFM before and after methane conversion using SPIP 6.0.9 software, data showed in Chapter 6

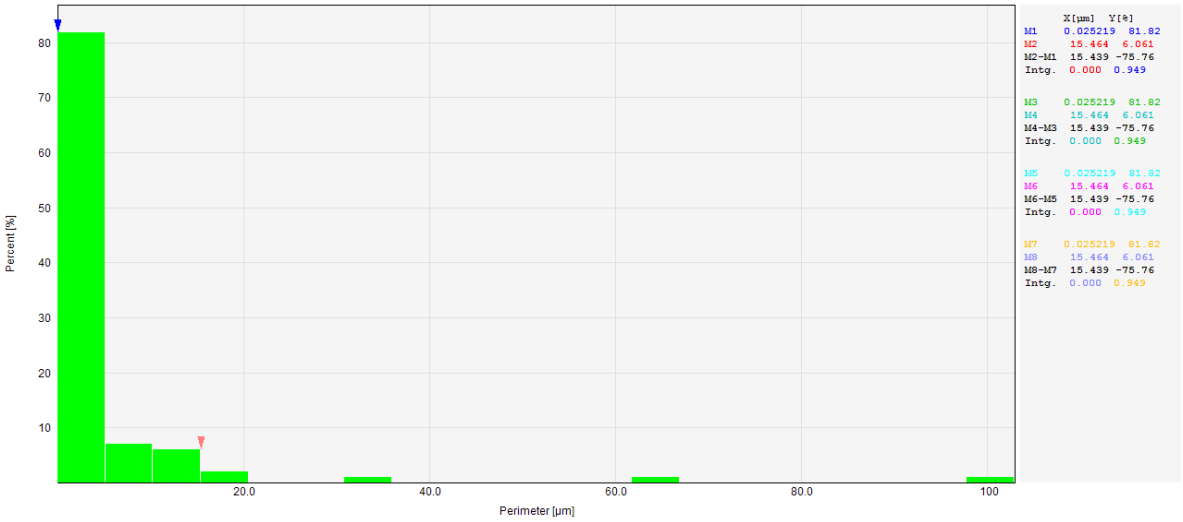

Figure V.2 Distribution of the grain boundary perimeter of LSCF6428-HFM shell side reactor before methane conversion, data obtained by SPIP 6.0.9

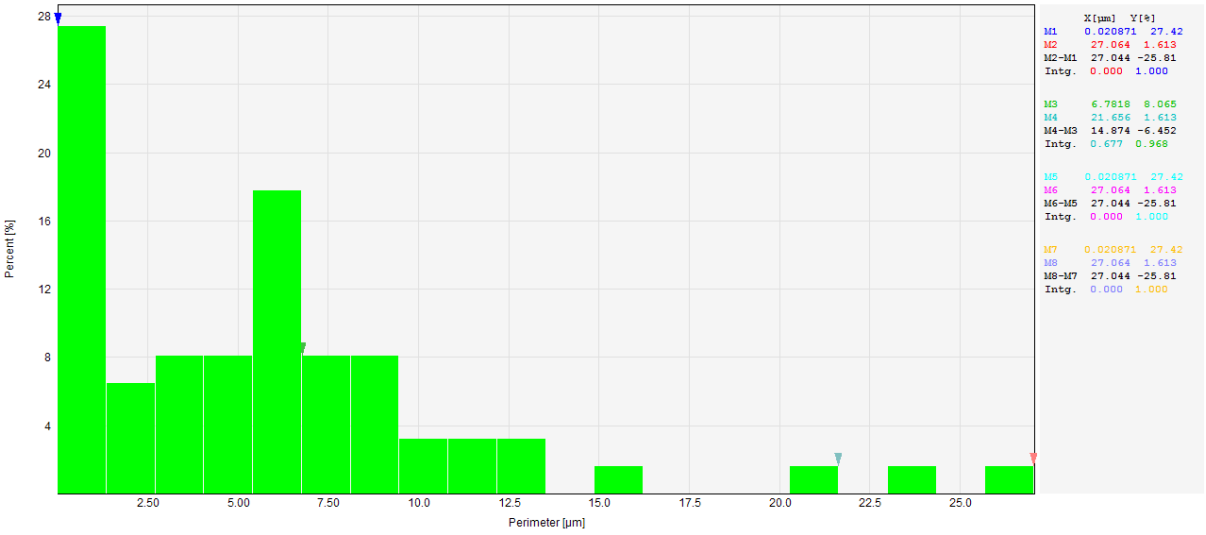

Figure V.3 Distribution of the grain boundary perimeter of LSCF6428-HFM lumen side before methane conversion, data obtained by SPIP 6.0.9

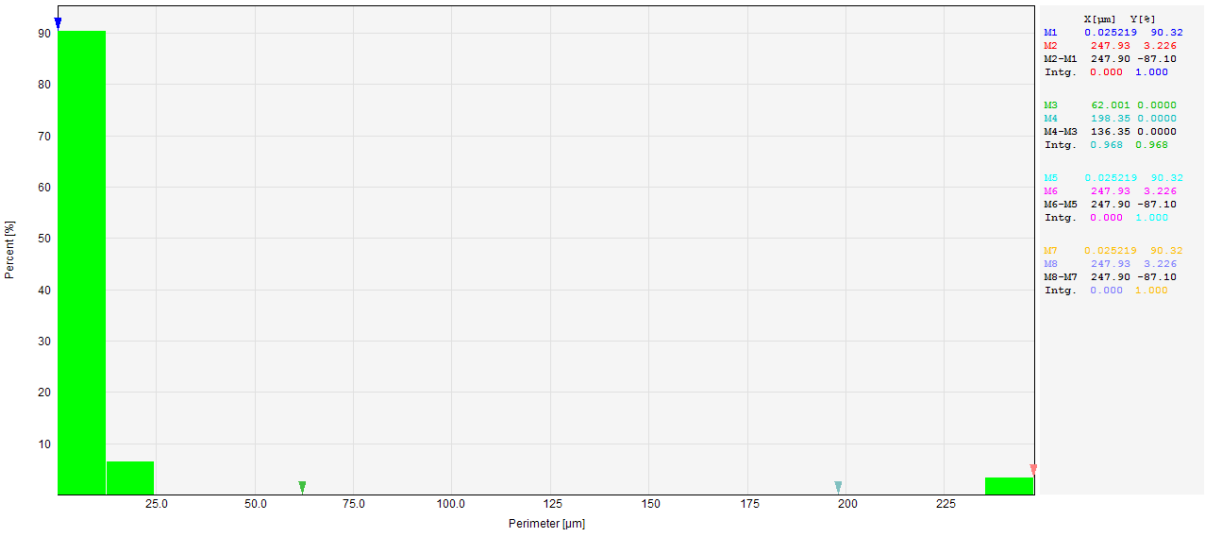

Figure V.4 Distribution of the grain boundary perimeter of LSCF6428-HFM centre shell side after methane conversion, data obtained by SPIP 6.0.9

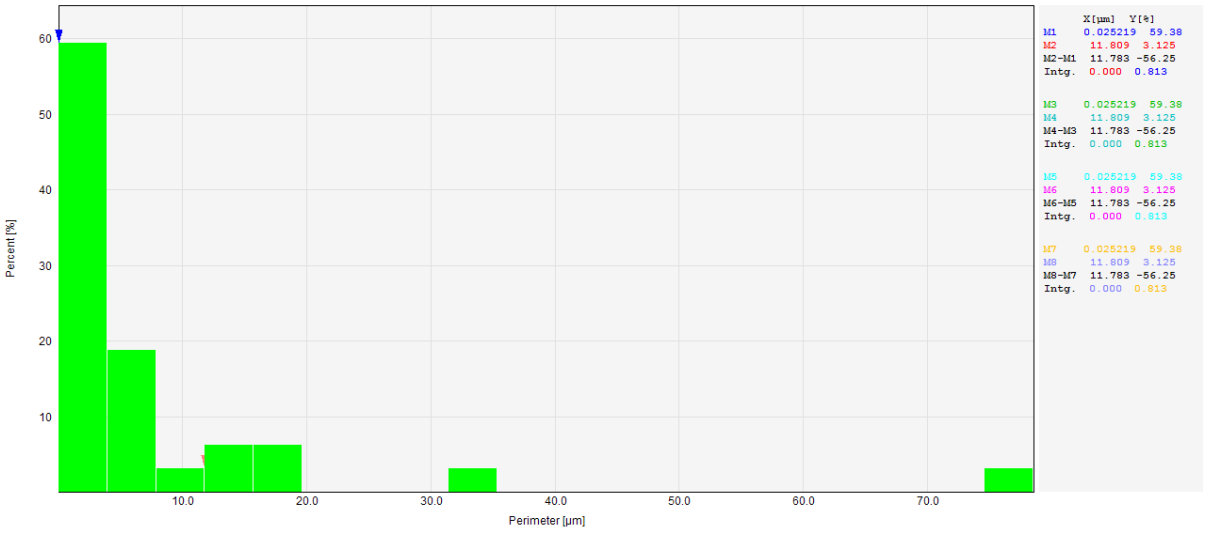

Figure V.5 Distribution of the grain boundary perimeter of LSCF6428-HFM centre lumen side after methane conversion, data obtained by SPIP 6.0.9

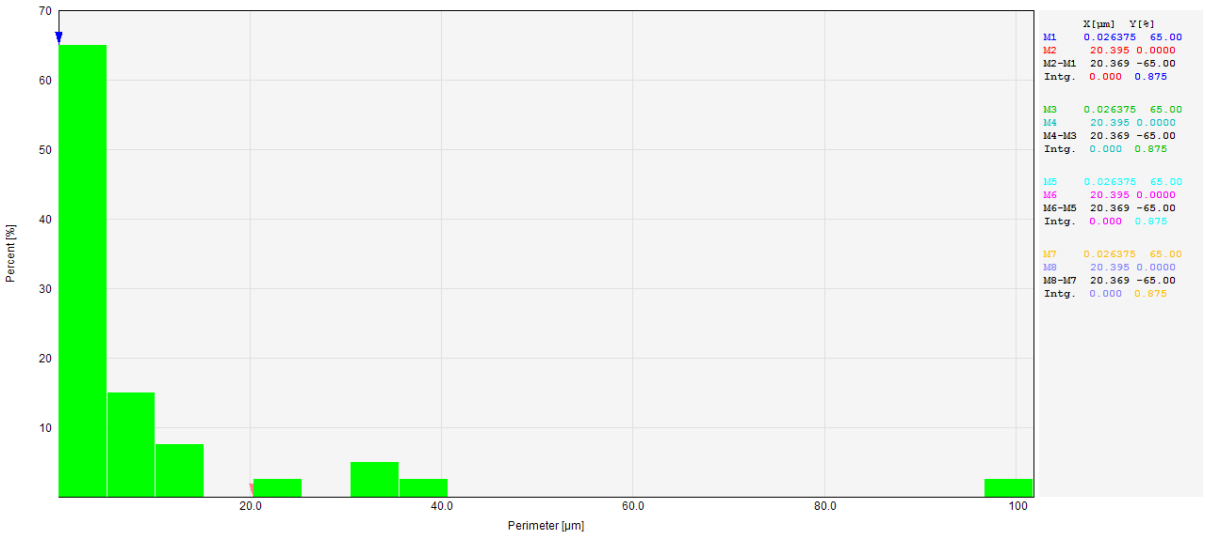

Figure V.6 Distribution of the grain boundary perimeter of LSCF6428-HFM end lumen side before methane conversion, data obtained by SPIP 6.0.9

V.3. EDXS results of the unmodified LSCF6428-HFM reactor before and after methane conversion, data discussed in Chapter 6

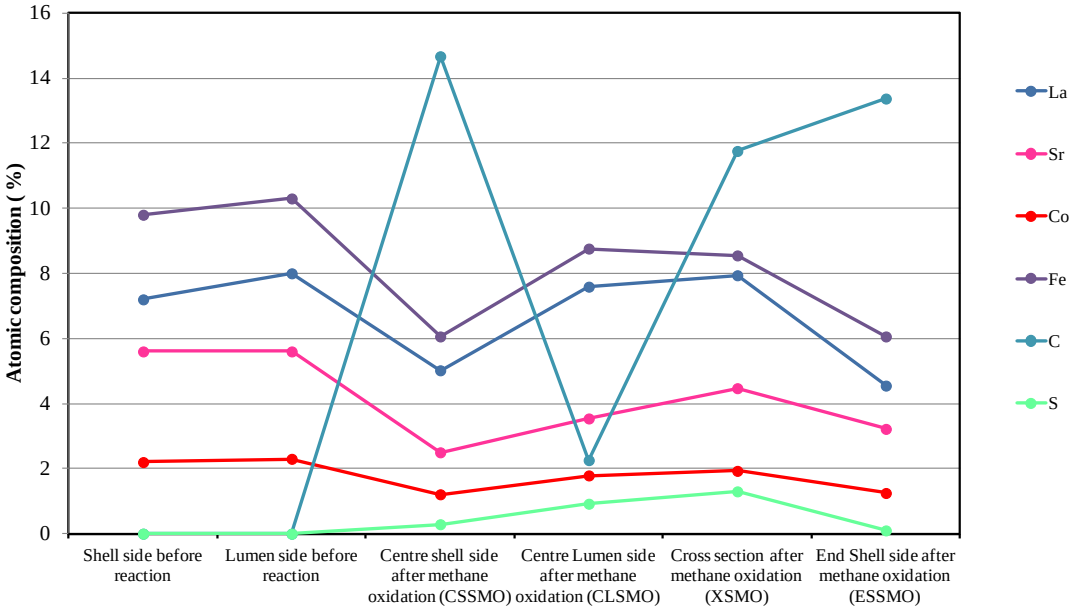

Figure V.7 EDXS results for different zones of the LSCF6428-HFM pre- and post-methane conversion.

V.4. Dependence of standard Gibbs free energy with temperature for $SrCO_3$, data discussed in Chapter 6, section 6.2.3.

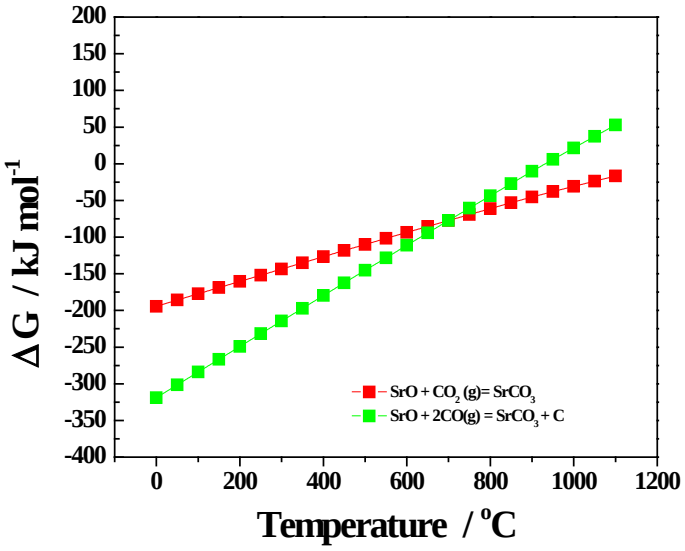

Figure V.8 Dependence of standard Gibbs free energy with temperature for the formation of $SrCO_3$.

V.5. Carbon balances of the 5%Ni-LSCF6428/LSCF6428-HFM under mode 2 of the flow operation obtained after partial oxidation of methane, data showed in Chapter 6

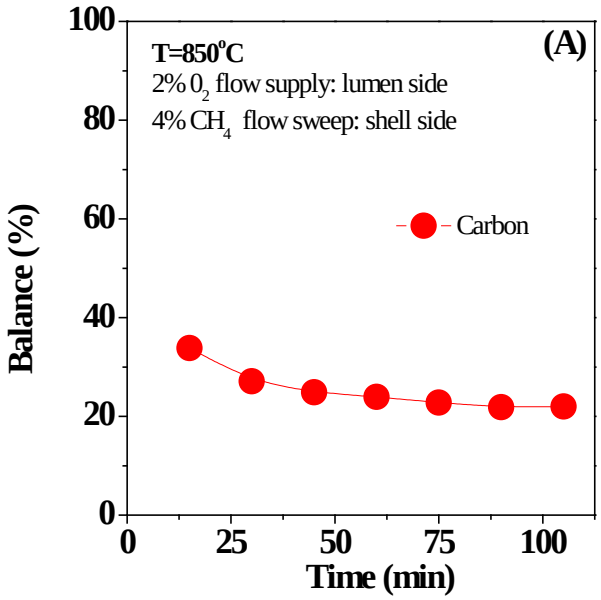

Figure V.9 Carbon balance as a function of time on stream for LSCF6428-HFM modified with 5%Ni-LSCF6428 catalyst under MSAL mode at 850 °C. 4% methane flow on the shell side (10 ml (STP) min^{-1}) and 2% O_2 flow rate on the lumen side (10ml (STP) min^{-1}).

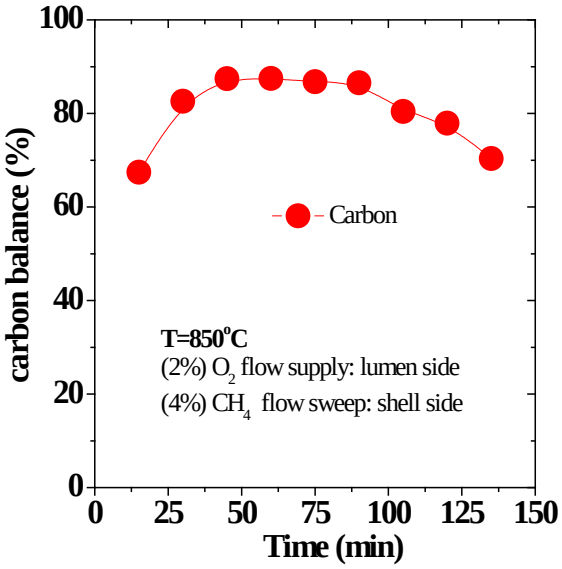

Figure V.10 Carbon balance as a function of time on stream into 5%Ni-LSCF6428/LSCF6428-HFM reactor at 850 °C under MSAL mode, 4% methane flow on the shell side and 2% O_2 flow rate on the lumen side both flow was at 25 ml (STP) min^{-1}.

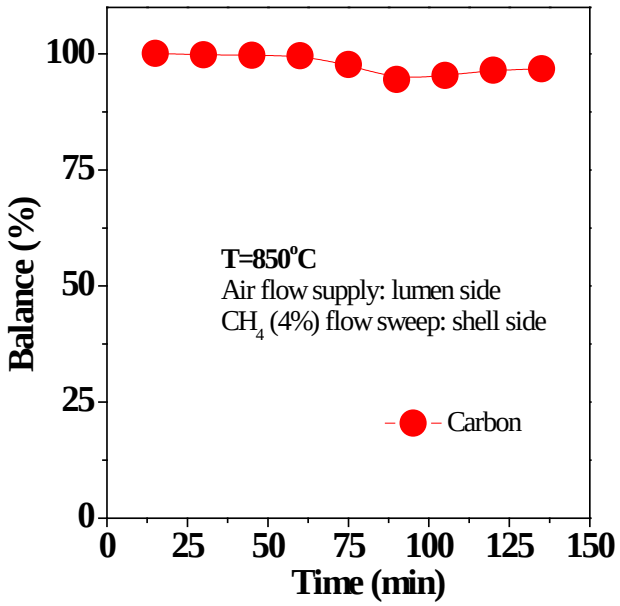

Figure V.11 Balance of carbon as a function of the operation time for LSCF6428-HFM modified with 5%Ni-LSCF6428 catalyst under modes MSAL at 850 °C. 4% methane flow on the shell side and air flow rate on the lumen side, both flows was 25 ml (STP) min^{-1}).

V.6. XRD of the 5%Ni-LSCF6428/LSCF6428-HFM before and after methane conversion, data discussed in Chapter 6

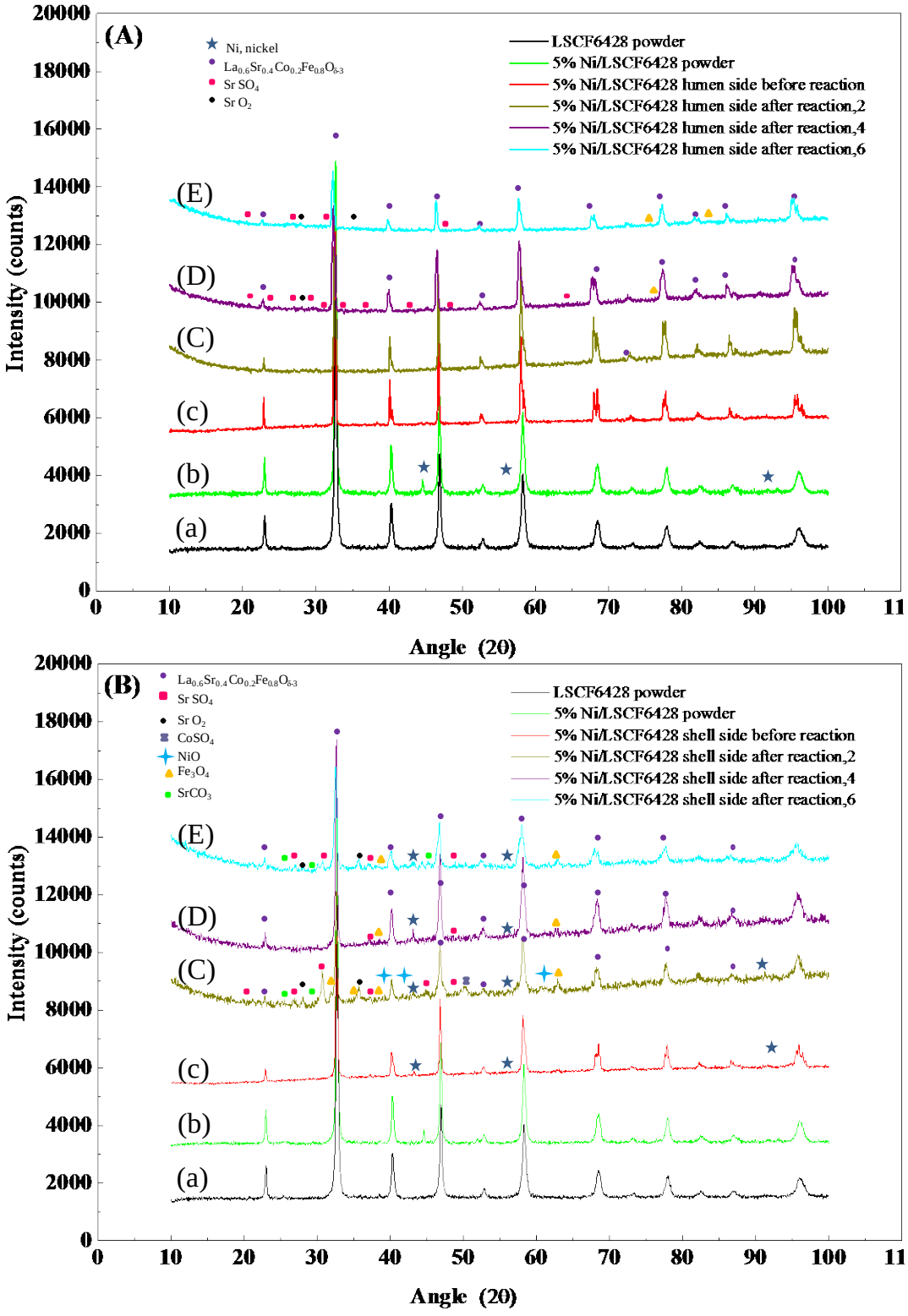

Figure.V.12 XRD patterns of the 5%Ni-LSCF6428/LSCF6428-HFM. Shell side before and after methane conversion (A) and lumen side before and after methane conversion experiments (B).

V.7. Distribution of the particle and grain boundary perimeter of 5%Ni-LSCF6428/LSCF6428-HFM before and after methane conversion using SPIP 6.0.9 software, data showed in Chapter 6

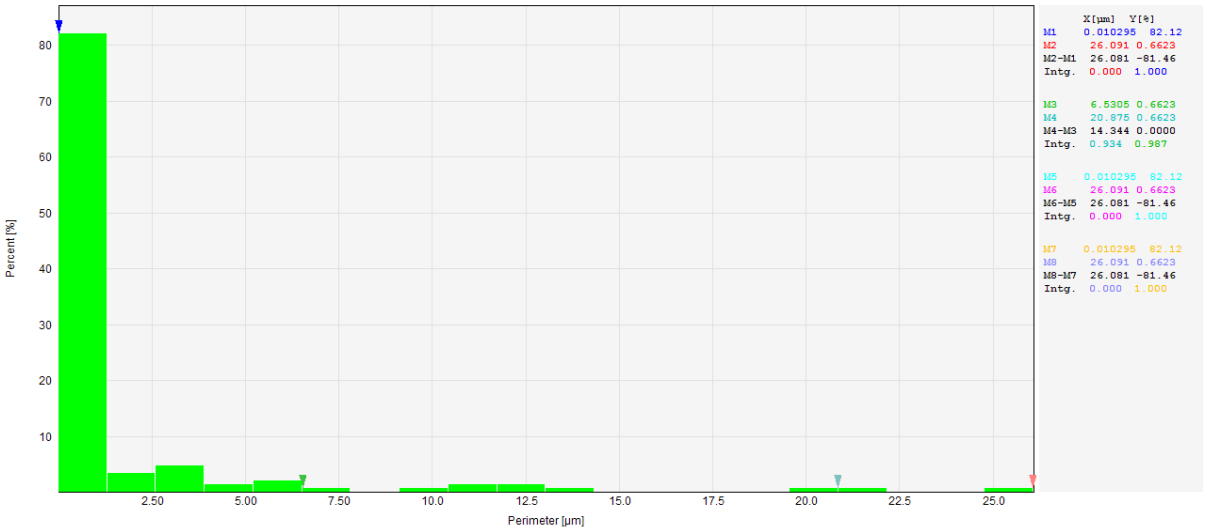

Figure V.13 Distribution of the particle perimeter of catalyst 5%Ni- LSCF6428 coated on shell side of LSCF6428-HFM before methane conversion, data obtained by SPIP 6.0.9

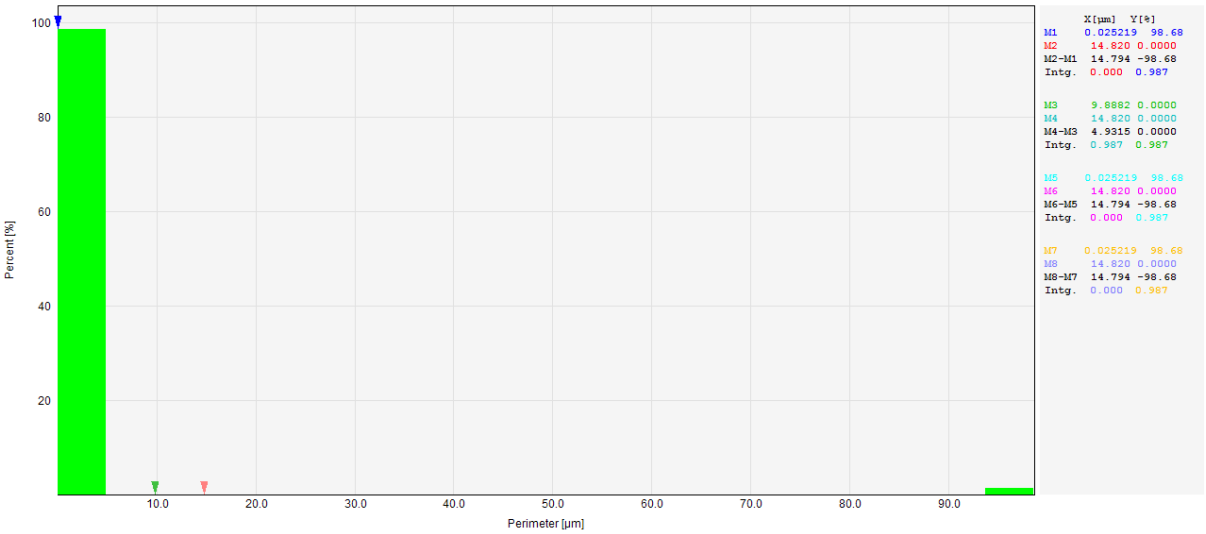

Figure V.14 Distribution of the grain boundary perimeter of 5%Ni- LSCF6428/LSCF6428-HFM centre lumen side after methane conversion, data obtained by SPIP 6.0.9

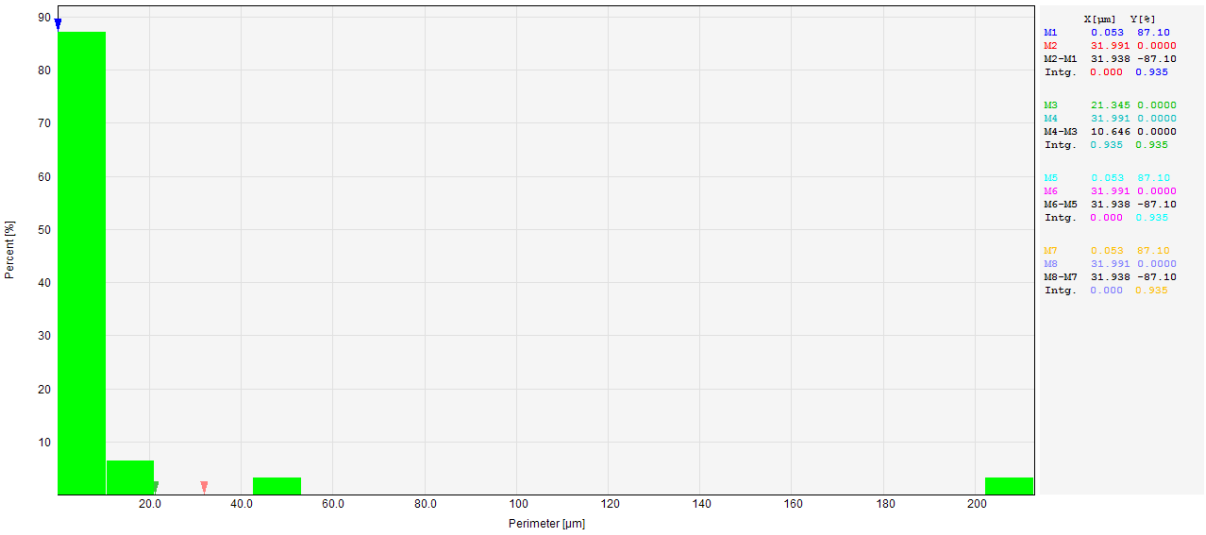

Figure V.15 Distribution of the grain boundary perimeter of 5%Ni- LSCF6428/LSCF6428-HFM end lumen side after methane conversion, data obtained by SPIP 6.0.9

V.8. EDXS results of the 5%Ni- LSCF6428/LSCF6428-HFM reactor before and after methane conversion, data discussed in Chapter 6

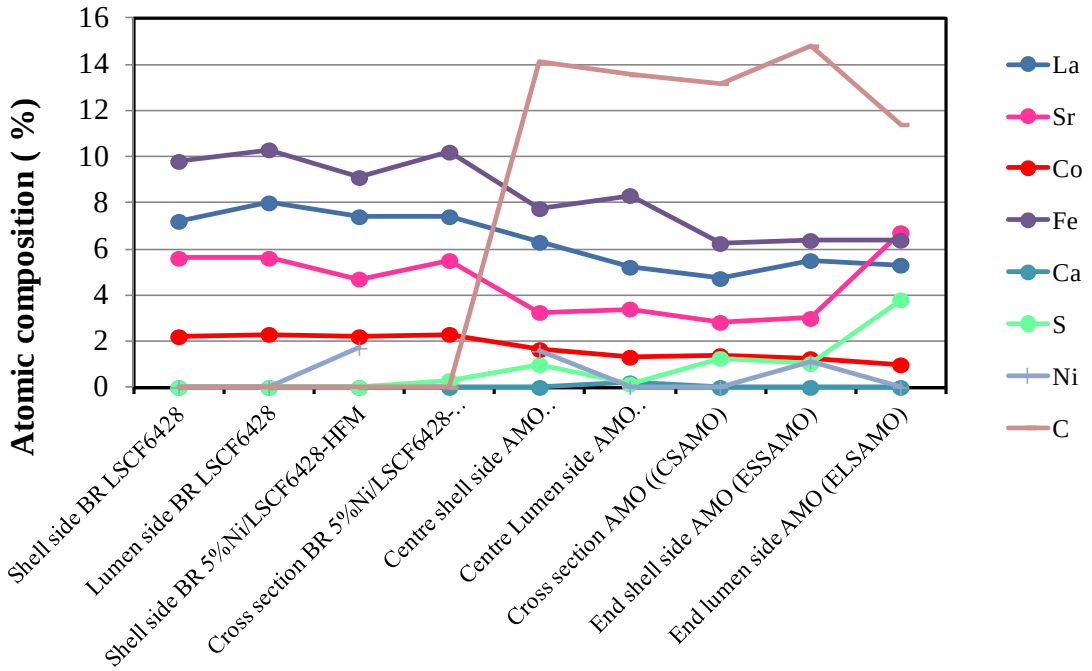

Figure V.16 EDXS results of different zones of the 5%Ni-LSCF6428-HFM module pre and post methane conversion at 850 °C.

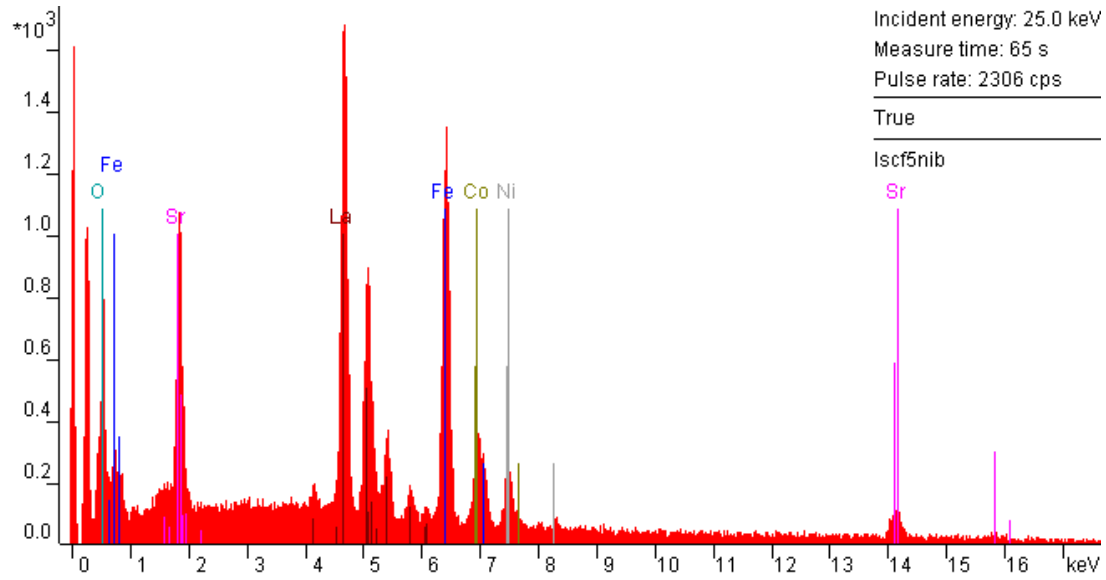

Figure V.17 EDXS profile of the shell side of 5%Ni-LSCF6428/LSCF6428-HFM before reaction.

Table V. 1 EDXS results of the shell side of 5%Ni-LSCF6428/LSCF6428-HFM before reaction

elem/line	P/B	B	F	c(atom)	confid.
O K-ser	@	1.00000	1.00000	74.92	+-13.47
La L-ser	@192.3	1.03952	1.05193	7.40	+- 0.84
Fe K-alpha	@117.0	1.04817	1.04488	9.09	+- 1.21
Co K-alpha	@ 29.2	1.05031	1.04876	2.24	+- 0.54
Ni K-alpha	@ 22.1	1.05237	1.05607	1.69	+- 0.55
Sr L-ser	46.6	1.01392	1.01496	4.66	+- 0.83
standardless				100.00	[2s]

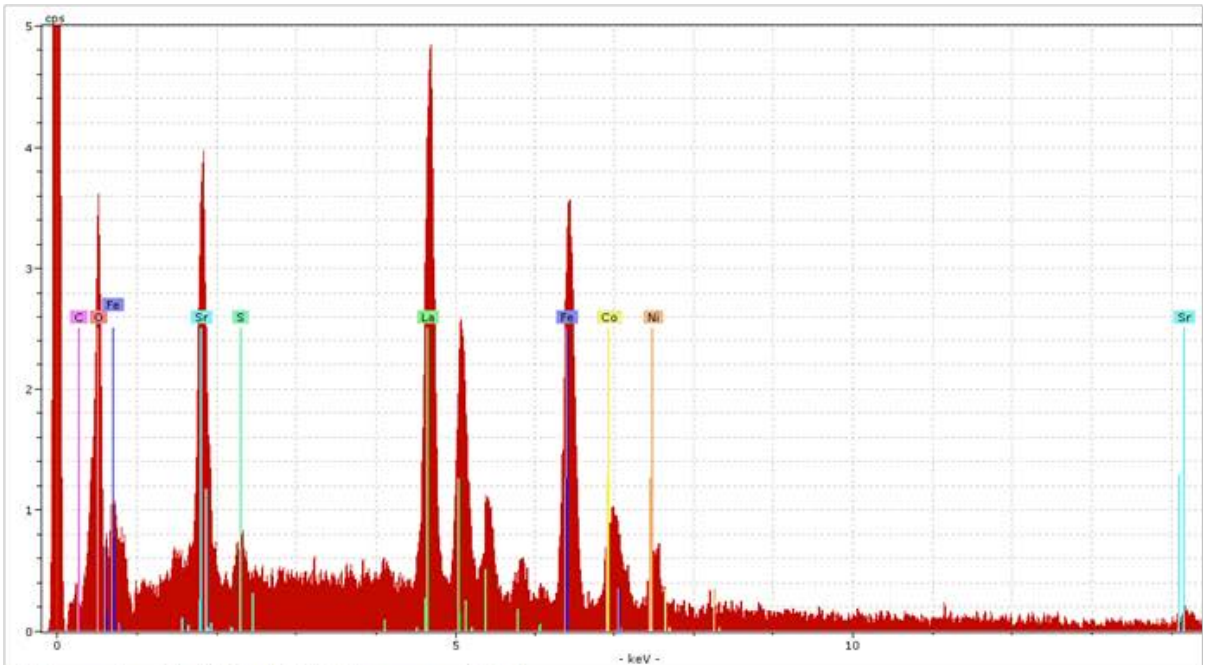

Figure V.18 EDXS profile of the centre shell side of 5%Ni-LSCF6428/LSCF6428-HFM after reaction

Table V.2 EDXS results of the 5%Ni-LSCF6428/LSCF6428-HFM centre shell side after reaction

*** PUzaf results ***					
elem/line	P/B	B	F	c(atom)	confid._h_
O K-ser	@	1.00000	1.00000	64.43	+-12.37
La L-ser	@ 192.3	1.03952	1.05193	6.29	+- 0.74
Fe K-alpha	@ 117.0	1.04817	1.04488	7.75	+- 1.20
Co K-alpha	@ 29.2	1.05031	1.04876	1.64	+- 0.54
Sr L-ser	@ 46.6	1.01392	1.01496	3.25	+- 0.92
S K-ser	@ 182.3	1.02109	1.00659	0.98	+- 3.90
Ni K-alpha	@ 22.1	1.05237	1.05607	1.57	+- 0.54
C K-ser	@ 22.3	1.00929	1.01390	14.08	+- 2.16
standardless				100.00	[2s]

Table V.3 EDXS results of the 5%Ni-LSCF6428/LSCF6428-HFM centre lumen side after reaction

*** PUzaf results ***					
elem/line	P/B	B	F	c(atom)	confid._h_
O K-ser	@	1.00000	1.00000	68.92	+-10.50
La L-ser	@ 192.3	1.03952	1.05193	5.21	+- 1.98
Fe K-alpha	@ 117.0	1.04817	1.04488	8.32	+- 1.11
Co K-alpha	@ 29.2	1.05031	1.04876	1.31	+- 0.55
Sr L-ser	@ 46.6	1.01392	1.01496	3.36	+- 2.07
S K-ser	@ 182.3	1.02109	1.00659	0.14	+- 3.92
C K-ser	@ 22.3	1.00929	1.01390	13.56	+- 2.21
Ca K-alpha	@ 1.9	1.03186	1.08325	0.48	+- 0.16
standardless				100.00	[2s]

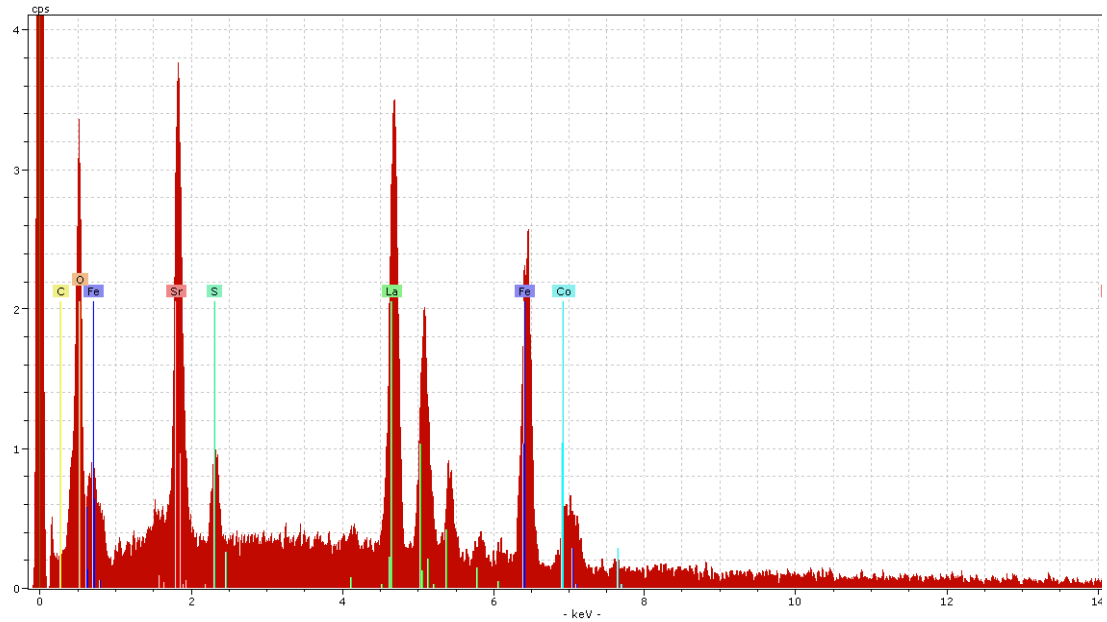

Figure V.19 EDXS profile of the cross section of 5%Ni-LSCF6428/LSCF6428-HFM after partial oxidation of methane.

Table V. 4 EDXS results of the cross section of 5%Ni-LSCF6428/LSCF6428-HFM after partial oxidation of methane.

*** PUzaf results ***					
elem/line	P/B	B	F	c(atom)	confid._h_
O K-ser	@	1.00000	1.00000	70.40	+-13.47
La L-ser	@192.3	1.03952	1.05193	4.72	+- 0.84
Fe K-alpha	@117.0	1.04817	1.04488	6.24	+- 1.21
Co K-alpha	@ 29.2	1.05031	1.04876	1.38	+- 0.54
Sr L-ser	46.6	1.01392	1.01496	2.82	+- 0.83
S K-ser	@182.3	1.02109	1.00659	.1.26	+- 3.82
C K-ser	@ 22.3	1.00929	1.01390	13.18	+- 2.21
standardless				100.00	[2s]

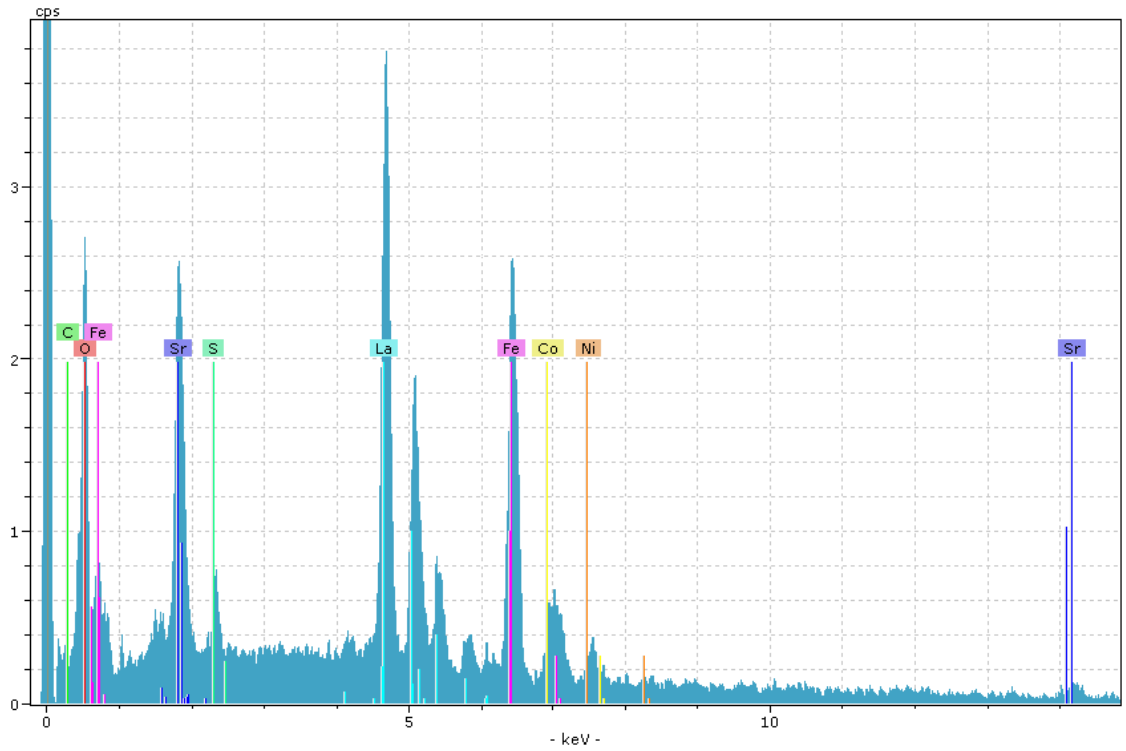

Figure V.20 EDXS profile of the end shell side of 5%Ni-LSCF6428/LSCF6428-HFM after partial oxidation of methane.

Table V. 5 EDXS results of the 5%Ni-LSCF6428/LSCF6428-HFM end shell side after partial oxidation of methane**.**

elem/line	P/B	B	F	c(atom)	confid._h_
O K-ser	@	1.00000	1.00000	66.97	+-12.97
La L-ser	@192.3	1.03952	1.05193	5.52	+- 1.44
Fe K-alpha	@117.0	1.04817	1.04488	6.37	+- 3.21
Co K-alpha	@ 29.2	1.05031	1.04876	1.25	+- 1.54
Ni K-alpha	@ 22.1	1.05237	1.05607	1.12	+- 0.75
Sr L-ser	46.6	1.01392	1.01496	2.99	+- 1.83
S K-ser	@182.3	1.02109	1.00659	1.03	+- 3.82
C K-ser	@ 22.3	1.00929	1.01390	14.75	+- 2.21
standardless				100.00	[2s]

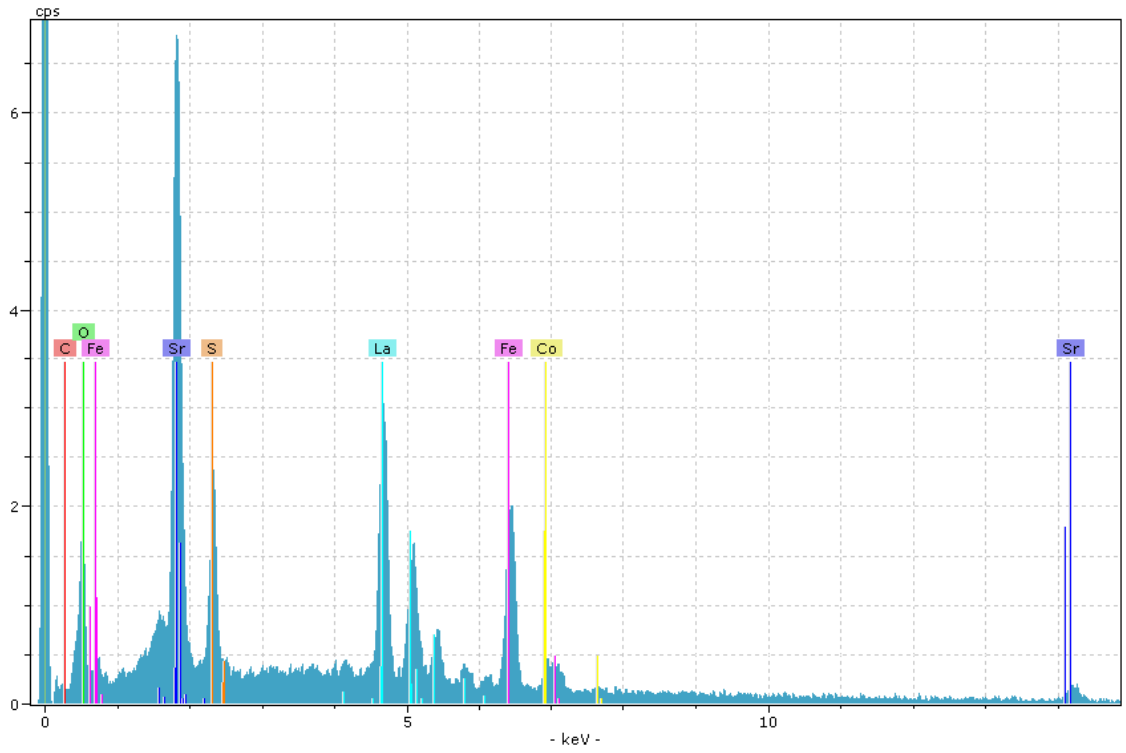

Figure V.21 EDXS profile of the end lumen side of 5%Ni-LSCF6428/LSCF6428-HFM after partial oxidation of methane.

Table V. 6 EDXS results of the end lumen side of 5%Ni-LSCF6428/LSCF6428-HFM after partial oxidation of methane.

*** PUzaf results ***					
elem/line	P/B	B	F	c(atom)	confid._h_
O K-ser	@	1.00000	1.00000	65.48	+-16.47
La L-ser	@192.3	1.03952	1.05193	5.25	+- 0.84
Fe K-alpha	@117.0	1.04817	1.04488	6.38	+- 1.21
Co K-alpha	@ 29.2	1.05031	1.04876	0.98	+- 1.54
Sr L-ser	46.6	1.01392	1.01496	6.71	+- 0.83
S K-ser	@182.3	1.02109	1.00659	3.80	+- 3.82
C K-ser	@ 22.3	1.00929	1.01390	11.40	+- 2.21
standardless				100.00	[2s]

V.9. Phases diagram for La-Fe-O and Sr-Fe-O system at different temperature.

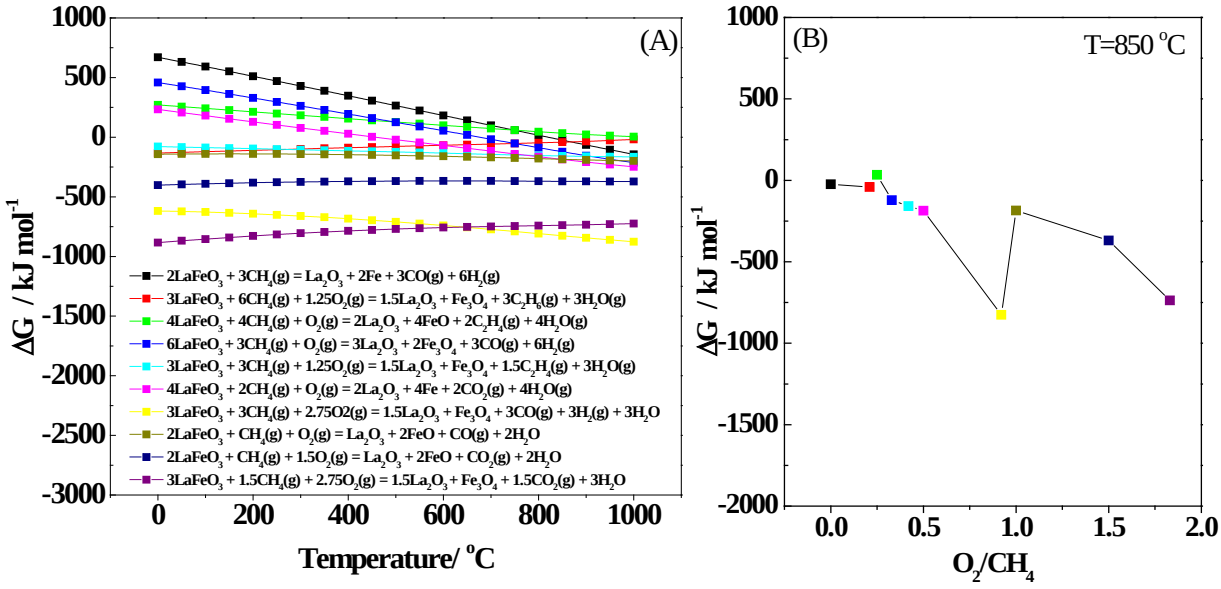

Figure V.22 Dependence of standard Gibbs free energy with temperature for various oxidations of methane reactions of the $LaFeO_3$ perovskite (A), dependence of the standard Gibbs free energy versus O_2/CH_4 ratio for $LaFeO_3$ perovskite at 850 °C (B).

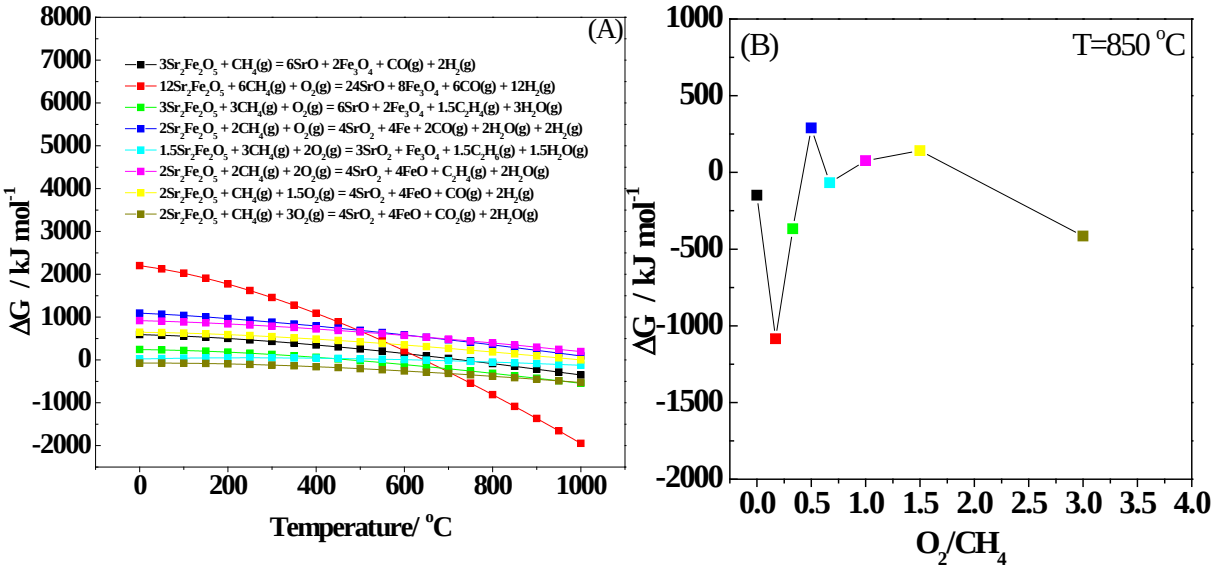

Figure V.23 Dependence of standard Gibbs free energy with temperature for various oxidations of methane reactions of the $Sr_2Fe_2O_5$ perovskite (A), dependence of the standard Gibbs free energy versus O_2/CH_4 ratio for $Sr_2Fe_2O_5$ perovskite at 850 °C (B).

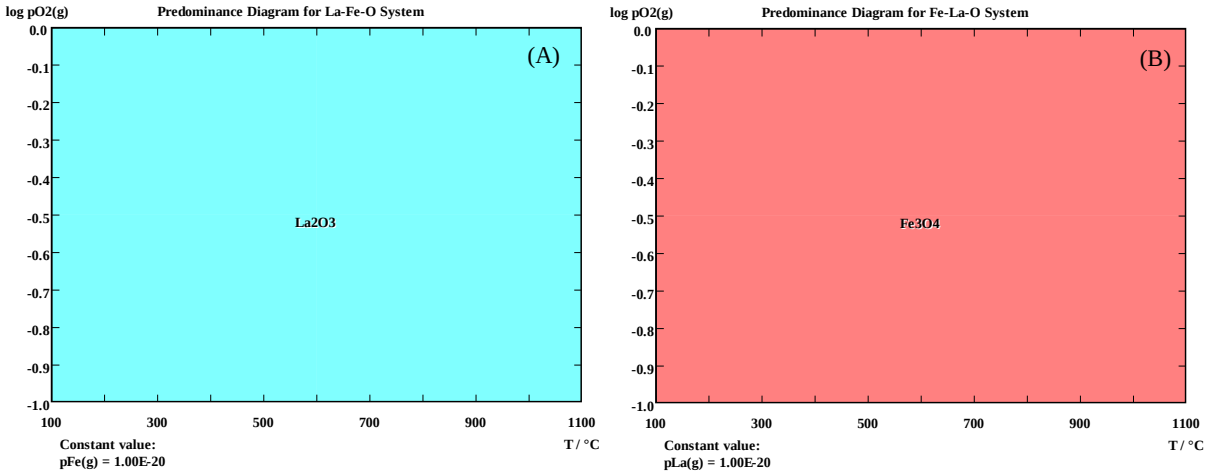

Figure V.24 Phases diagram for La-Fe-O system at different temperature.

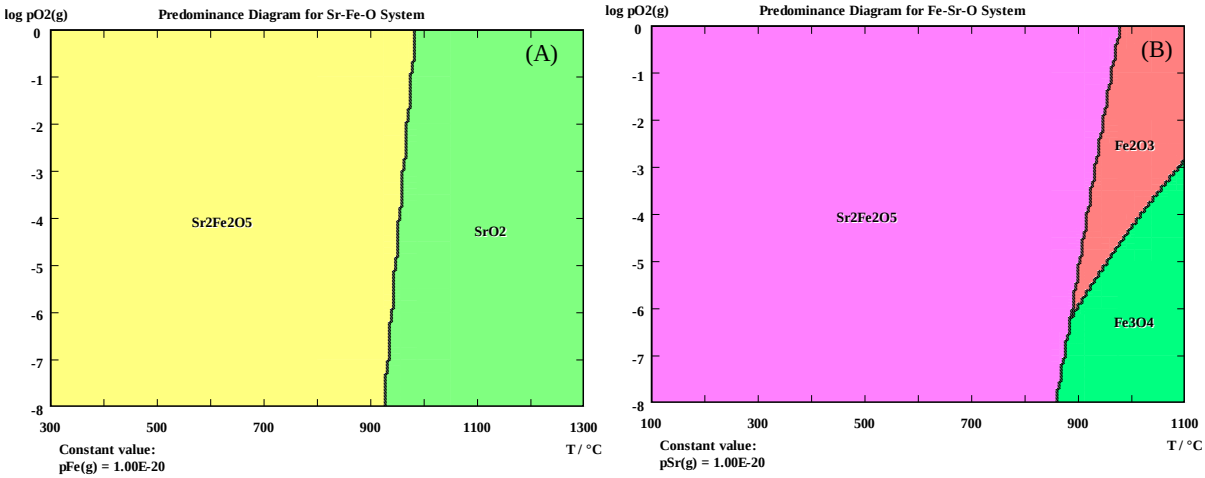

Figure V.25 Phases diagram for Sr-Fe-O system at different temperature.